UNIVERSITY OF SOUTHAMPTON

FACULTY OF MEDICINE

Cancer Sciences Unit

Dissecting the role of oncogenes and metabolism in cell survival following extracellular matrix-detachment using a 3D breast model

by

Caroline Rose Barker

Thesis for the degree of Doctor of Philosophy

September 2016

UNIVERSITY OF SOUTHAMPTON

ABSTRACT

FACULTY OF MEDICINE

Cancer Sciences

Thesis for the degree of Doctor of Philosophy

DISSECTING THE ROLE OF ONCOGENES AND METABOLISM IN CELL SURVIVAL FOLLOWING EXTRACELLULAR MATRIX-DETACHMENT USING A 3D BREAST MODEL

Caroline Rose Barker

The ability of breast cancer cells to evade cell death following detachment from the extracellular matrix (ECM) is an important feature of breast cancer development and metastasis. ECM-detachment is traditionally viewed to induce the programmed cell death pathway anoikis, however more recently a defect in metabolism has also been implicated.

The normal breast duct consists of a polarised epithelium surrounding a hollowed lumen, and the MCF-10A cell line can be cultured in 3D to form phenotypically similar acini. The hollowed lumen is formed due to luminal cell death following ECM-detachment; these acini therefore provide a more physiologically relevant setting to examine cell death upon detachment than traditional 2D culture. I utilised this system to study the role of Bcl-2 associated anthogene 1 (Bag-1) overexpression in ECM-detached cells. In addition, HER2-overexpressing MCF-10A (MCF-10A:HER2), which yield filled acini structures characteristic of a breast cancer precursor, DCIS, were used alongside non-transformed MCF-10A to examine the effect of molecular and pharmacological alteration of metabolism. Some of the work was extended to primary HMEC-derived acini to enhance understanding.

Bag-1 is an antiapoptotic protein frequently overexpressed in breast cancer and exists as three differentially localised, functionally discrete isoforms (Bag-1S, Bag-1M, Bag-1L). Overexpression of Bag-1L in stable clones led to acini with filled lumens and an external branching structure. The branching morphology correlated with the level of Bag-1L overexpression and treatment with a small-molecule inhibitor of Bag-1, Thio-2, reduced the level of branching observed. When Bag-1S or Bag-1L isoforms were individually overexpressed in retroviral pooled populations of MCF-10A it led to a temporal delay in the onset of luminal clearing however I did not observe a branching morphology.

Glycolysis and fatty acid oxidation are being targeted therapeutically in cancer as these metabolic pathways are upregulated in cancer cells to promote transformation. Metabolic inhibitors targeting glycolysis (oxamate) and fatty acid oxidation (etomoxir) reversed the HER2-driven transformation of acini. Activation of mitochondrial activity (dichloroacetate) had no effect on MCF10A:HER2 acini but drove controls towards a highly transformed phenotype. This phenotype seen in 3D was not observed in 2D culture. In addition to the pharmacological consequences of metabolic inhibition, overexpression of the metabolic sensor CtBP2 interfered with acinar morphogenesis and promoted transformation which was reversible by CtBP inhibition.

In conclusion, the identification of phenotypes in 3D that were not observed in 2D reinforces the importance of 3D culture systems to examine breast tumourigenesis and pharmacological agents. Bag-1 is able to delay the onset of luminal clearing in MCF-10A acini. In models where Bag-1 is able to fully prevent luminal clearing I propose that a second (unidentified) transformation event has occurred. Metabolic manipulation alters cell survival in ECM-detachment in MCF-10A, highlighting the relevance of metabolism in cancer development and progression and has potential for cancer therapeutics.

Table of Contents

List of Tables

List of Figures

List of Accompanying Materials

The following research publication is attached to the back of this thesis:

Papadakis, E. S., C. R. Barker, H. Syed, T. Reeves, S. Schwaiger, H. Stuppner, J. Troppmair, J. P. Blaydes and R. I. Cutress (2016). "The Bag-1 inhibitor, Thio-2, reverses an atypical 3D morphology driven by Bag-1L overexpression in a MCF-10A model of ductal carcinoma in situ." Oncogenesis 5: e215.

DECLARATION OF AUTHORSHIP

I, Caroline Rose Barker

declare that this thesis and the work presented in it are my own and has been generated by me as the result of my own original research.

Dissecting the role of oncogenes and metabolism in cell survival following extracellular matrix-detachment using a 3D breast model

I confirm that:

1. This work was done wholly or mainly while in candidature for a research degree at this University;
2. Where any part of this thesis has previously been submitted for a degree or any other qualification at this University or any other institution, this has been clearly stated;
3. Where I have consulted the published work of others, this is always clearly attributed;
4. Where I have quoted from the work of others, the source is always given. With the exception of such quotations, this thesis is entirely my own work;
5. I have acknowledged all main sources of help;
6. Where the thesis is based on work done by myself jointly with others, I have made clear exactly what was done by others and what I have contributed myself;
7. Parts of this work have been published as: Papadakis, E. S., C. R. Barker, H. Syed, T. Reeves, S. Schwaiger, H. Stuppner, J. Troppmair, J. P. Blaydes and R. I. Cutress (2016). "The Bag-1 inhibitor, Thio-2, reverses an atypical 3D morphology driven by Bag-1L overexpression in a MCF-10A model of ductal carcinoma in situ." Oncogenesis 5: e215.

Signed: .....

Date: .....

Acknowledgements

This thesis would not have been possible without the help, support, guidance and friendship of a large number of people.

Firstly thank you to all the staff involved in the Integrated PhD programme – this program originally attracted me to Southampton and helped me develop as an individual and as a scientist. Secondly to my supervisors Jeremy P Blaydes and Ramsey I Cutress for agreeing to take me on at the end of my masters and providing me with the support and guidance throughout the remaining years. Of course I am grateful also to my funding bodies, the MRC and Cancer Research UK, for making the whole thing possible.

I wish to thank all members of the laboratory who helped me along the way. Special thanks go to Manos Papadakis for his assistance, friendship and support and to Matt Darley for keeping the lab running and setting up the retrovirus room so that I could carry out my work. To Charlie Birts and Arindam Banerjee for sharing their knowledge and experience, and to the medical students Hashim Sayed and Tom Reeves whose data contributed to our research paper (Papadakis, Barker et al. 2016). Dave Johnston, from the Biomedical Imaging Unit, provided me with the necessary training for my immunofluorescence work and frequently came to my rescue when faced with technical issues.

Outside of the lab I need to extend my appreciation to everyone who kept me going at times when I was convinced I was going to leave. I must personally thank my mentor Judith Holloway – it is hard to put into words the extent of the support that Judith provided me with and for that I will be forever grateful.

Thank you to my family and friends for your support over the last four years, I would not have got through it without you. My fellow postgraduates have provided four years of fun, laughter and distraction and I will always be grateful to my gym buddy, Dannielle, and my partner, Dave, who have encouraged, listened and supported when it was most needed. I am excited to enter a future where my plans are dictated by something other than the needy demands of my cell culture.

Abbreviations

2DG	2-deoxyglucose
Bag-1	Bcl-2 associated anthogene-1
BH	Bcl-2 homology
Bim	Bcl-2 interacting mediator of cell death
CtBP	C-terminal binding proteins
CPT-1	Carnitine palmitoyltransferase I
DCIS	Ductal carcinoma *in situ*
ECAR	Extracellular acidification rate
ECM	Extracellular matrix
EGFR	Epidermal growth factor receptor
ER	Oestrogen receptor
ErbB	Epidermal growth factor family of receptor tyrosine kinases
FAO	Fatty acid oxidation
GAPDH	Glyceraldehyde-3-phosphate dehydrogenase
GLUT	Glucose transporter
HER2	Human epidermal growth factor receptor 2
HMEC	Human mammary epithelial cells
MAPK	Mitogen activated protein kinase
MCT	Monocarboxylate transporters
MTOB	4-Methylthio-2-oxobutanoic acid

NAD(H)	Nicotinamide adenine dinucleotide
NADP(H)	Nicotinamide adenine dinucleotide phosphate
OCR	Oxygen consumption rate
PI3K	Phosphatidylinositol-3-kinase
PPP	Pentose phosphate pathway
PR	Progesterone receptor
ROS	Reactive oxygen species
SDM	Site-directed mutagenesis

Chapter 1: Introduction

1.1 Anatomy of the Breast

1.1.1 The healthy breast

The female breast (Figure 1) contains the organs of milk production, the mammary glands. Comprised internally of a muscular chest wall, fatty tissue and glandular tissue, the external breast has a raised nipple surrounded by a circular, pigmented areola.

The glandular tissue in an adult female mammary gland contains 15-20 glandular lobes surrounded by adipose tissue and each lobe forms a conical mass arranged with the nipple at the apex. Each lobe has its own lactiferous duct which runs from the nipple, where it enlarges to form a small lactiferous sinus which accumulates milk during milk ejection, to the lobe, where it divides into smaller ducts which supply lobules. Within these lobules, the ducts branch further becoming smaller. In the milk-producing breast, the end of the small ducts expand to form alveoli. Alveoli are secretory sacs surrounded by myoepithelial cells; the contraction of myoepithelial cells enables the flow of milk from the secretory sacs to the nipple.

In a healthy mammary gland the ducts display a highly polarised structure with a hollowed lumen, with an inner layer of luminal epithelial cells and an outer layer of myoepithelial cells enclosed by a basement membrane (Figure 2a). In addition, the ducts are surrounded by a microenvironment which contains additional cell components including fibroblasts, the endothelium, macrophages and white blood cells. The basement membrane is a fibrous layer of extracellular matrix (ECM) components, each secreted from resident cells, which separates the epithelium from the underlying connective tissue. Fibroblasts form an important structural component of the breast and have an essential role in ECM synthesis.

The breast is also surrounded by a lymphatic system; an area of breast tissue leads into the armpit where there are many lymph nodes and a chain of lymph nodes runs up the centre of the chest (the internal mammary chain).

Breast tissue does not remain the same all through life. For example, they can change texture throughout the menstrual cycle. In addition, glandular tissue is gradually replaced by fat post menopause, making it less dense in older women. While these are natural changes that occur in the healthy female breast, changes such as fibrocystic breast disease or cancer can be detrimental to health.

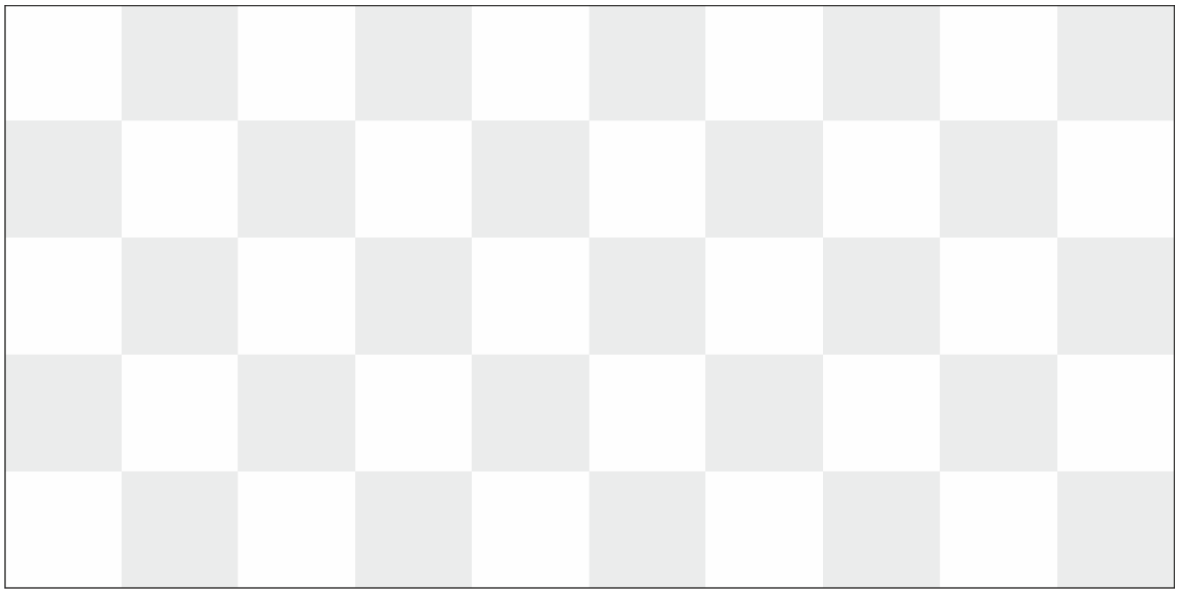

Figure 1 The anatomy of the breast
Schematic shows the anatomy of the adult breast. Taken from (OpenStax 2013).

1.1.2 Fibrocystic changes in the breast

Fibrocystic changes are benign changes in breast tissue which include the formation of fibrous tissue, fluid-filled cysts or breast hyperplasia. While not considered harmful, lumps can cause pain and discomfort in some women. With the frequency of fibrocystic breast disease increasing with age, this condition affects at least 50% of women of childbearing age (Norwood 1990).

1.1.3 Breast cancer

With an estimated 1.7 million cases a year globally, breast cancer is the most commonly diagnosed cancer after lung cancer (Ferlay, Soerjomataram et al. 2013) and, despite rising survival rates, remains the second most common cause of cancer mortality in women (National Office for Statistics 2012). The decrease in breast cancer-related mortality is attributed to earlier detection due to the introduction of screening programs, better utilisation of intervention therapies and an improved understanding of disease pathogenesis. At this time early stage breast cancer has promising survival rates, while the final stage of the disease (stage 4) is not curable and has a 15% survival rate in the UK (Cancer Research UK).

Breast cancer is a highly heterogeneous disease which can be divided into at least 10 different subtypes (Curtis, Shah et al. 2012). These subtypes define the molecular background,

pathogenesis and clinical prognosis of the disease. There are four major subtypes of breast cancer which are defined based on the status of a number of biological markers:

- Luminal A breast cancers – Luminal tumours are the most frequent subtype of breast cancer and are oestrogen receptor (ER)-positive with a similar gene expression pattern to the cells that line the lumens of the breast ducts and glands.
- Luminal B breast cancers – Luminal B cancers are like luminal A breast cancers but have a faster growth and poorer prognosis.
- HER2-positive breast cancer – these tumours have amplification and/or overexpression of the *erbB2* gene resulting in high levels of the human epidermal growth factor receptor 2 (HER2) protein. Observed in approximately 15-20% of all breast cancers, HER2 overexpression is associated with an aggressive disease, although the development of HER2-targeted medicines, such as Herceptin, have led to improved outcomes.
- Triple negative breast cancer – so called because these cells are negative for ER, progesterone receptor (PR) and HER2 overexpression. Although found at low frequency (15%), this cancer is an aggressive disease and is associated with the poorest prognosis among all breast cancer subtypes.

Another way to classify breast cancer is to divide it into pre-invasive and invasive forms. Pre-invasive forms of breast cancer are classified as ductal carcinoma *in situ* (DCIS) and lobular carcinoma *in situ*, while invasive forms of breast cancer are subdivided into invasive ductal breast carcinoma, invasive lobular breast carcinoma, inflammatory breast cancer and Paget's disease.

1.1.3.1 Genetic risk of breast cancer

5-10% of breast cancers are thought to be hereditary (Breastcancer.org), with the majority of cases of inherited breast cancer associated with mutations in BRCA1 or BRCA2. While 12% of the general population will develop breast cancer during their lifetime (Howlader, Noone et al. 2013), abnormal BRAC1 and/or BRAC2 carriers have a predicted 45-65% risk of cancer (Antoniou, Pharoah et al. 2003, Chen and Parmigiani 2007). The BRAC genes are tumour suppressor genes involved in DNA damage repair pathways. Mutations in TP53 and PTEN also significantly contribute to a woman's risk of breast cancer and genetic tests are available to women with a high risk of having mutations in these genes. Other mutations which can increase a woman's risk of breast cancer have been discovered in the genes CASP8, FGFR2, TNRCP, MAP3K1, rs4973768 and LSP1 (Cancer Research UK).

1.1.3.2 Breast cancer stem cells

Cancer stem cells are a small population of tumour cells (1-3% of the total cells) which have many characteristics of normal stem cells, including the ability to divide indefinitely and to differentiate.

Discovered in 2003, breast cancer stem cells were the first cancer stem cells identified within solid tumours (Al-Hajj, Wicha et al. 2003). It is hypothesised that these cancer stem cells persist during cancer treatment, and are responsible for remission and metastasis of breast cancer. These breast cancer stem cells are positive for the cell surface marker CD44, have little or no CD24 and are negative for Lin. In addition to cell surface markers, increased aldehyde dehydrogenase activity is a marker of cancer stem cells (Ginestier, Hur et al. 2007). The ability of stem cells to survive in a suspended culture, combined with the slow proliferation rate associated with stem cells has been utilised to isolate breast stem cell populations to further examine and characterise this populations (Pece, Tosoni et al. 2010).

1.1.4 Ductal carcinoma *in situ*

For the purposes of this work, I will be focusing further on DCIS. A carcinoma *in situ* describes an abnormal growth of cells in their normal place. In the case of DCIS, this is within the lining of the breast duct (Figure 2aii). This non-invasive disease is often considered a precursor lesion to invasive ductal carcinoma (Figure 2aiii) (Farabegoli, Champeme et al. 2002). Since the introduction of screening programs the diagnosis of early forms of breast cancer is becoming increasingly common with DCIS accounting for a quarter of breast diagnoses made through screening.

DCIS is part of a spectrum of preinvasive lesions which originate from normal breast tissue, with histological progression from atypical hyperplasia through to invasive breast cancer (Figure 2b) (Agnantis, Fatourous et al. 2004). The molecular changes involved in the pathogenesis of breast cancer are summarised in Figure 2c. The majority of these changes occur by the stage of DCIS, however it is not assumed that all forms of DCIS will progress to an invasive form of the disease. It is currently impossible to distinguish between a DCIS which will never progress to a harmful disease and one that will. While there is a distinction between benign growths and carcinomas based on biopsy reports, and many biomarker signatures help pathologists to define prognosis, there is still a need to further understand the molecular mechanisms and transformation events that drive progression from a benign mass to a life-threatening tumour. This will contribute to improved biomarkers and new therapeutic targets. A controversial systematic review in the Cochrane Database suggests that for 2000 women that were screened over 10 years, one will avoid dying of breast cancer whereas 10 healthy women will be misdiagnosed and unnecessarily treated (Gotzsche and Jorgensen 2013). A second review suggests the figures for overdiagnosis are lower, with an average of 3.4 women misdiagnosed for every life saved (Independent UK Panel of Breast Cancer Screening 2012). In addition to the added burden on the NHS, the nature of many of the treatment courses used can have detrimental effects on a patients' health.

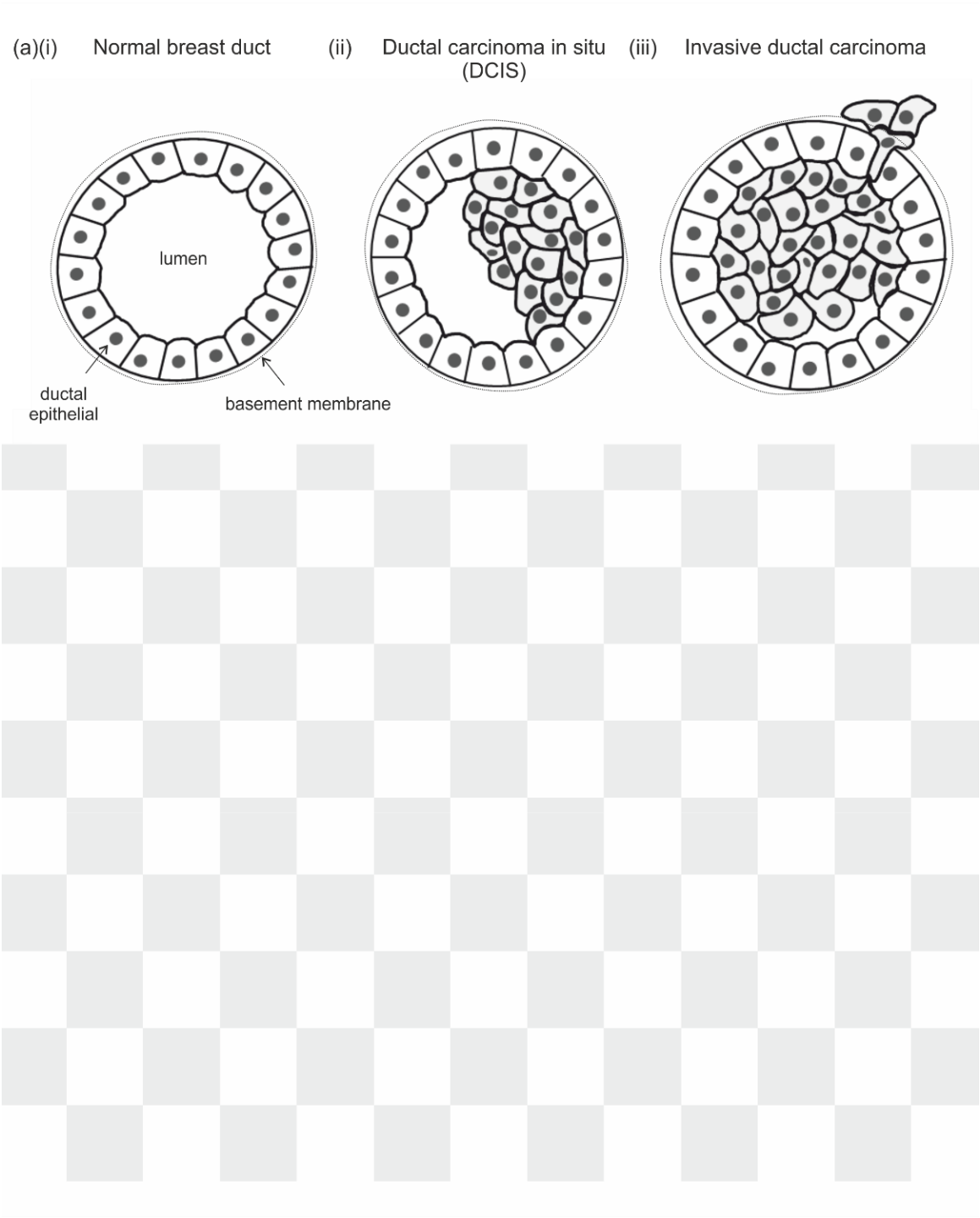

Figure 2 The different stages of ductal breast cancer

(a) Diagrammatic representation of the different stages of ductal breast cancer. While the normal breast duct consists of a hollow lumen (i), cells are present in the lumen of the duct in ductal carcinoma *in situ* (ii). As cells differentiate further they may invade through the basement membrane into the surrounding tissue, becoming an invasive carcinoma (iii). (b) Histology slices show the changing pathology of the different stages of ductal breast cancer. (c) The molecular and cellular processes that occur during transformation from a healthy tissue to an invasive carcinoma are summarised. (b,c) are taken from (Agnantis, Fatourous et al. 2004).

1.2 Modelling the Breast in the Laboratory

1.2.1 Cell lines and primary tissue

Cell lines were introduced in the 1950s and are the most widely used model to investigate the development and progression of breast cancer. Well established cell lines are easily propagated, can be genetically manipulated and under well-defined experimental conditions should yield reproducible and quantifiable results, explaining their extensive usage. However, there are also a number of disadvantages. They are prone to genotypic and phenotypic instability even with regular characterisation and replacement from cryopreserved stocks; this was well highlighted by Osborne *et al.* who showed biological differences among the MCF-7 breast cancer cell lines from different laboratories (Osborne, Hobbs et al. 1987). There have also been cases of misidentification of cell lines, with the MDA-MB-435 line being used as a breast cancer model but now shown to be derived from a M14 melanoma cell line (Rae, Creighton et al. 2007). In addition, cell lines contain genetic manipulation. For example, the MCF-10A cell line, used widely as a model of the healthy breast, contains modest genetic modifications typical of cultured breast epithelial cells (Yaswen and Stampfer 2002) including loss of $p16^{INK4a}$ (Elenbaas, Spirio et al. 2001). These disadvantages have lead researchers to question the validity of cell lines as models to study the morphogenesis of breast cancer and responses to therapies (Burdall, Hanby et al. 2003).

The use of primary cultures derived directly from patient breast samples is a viable alternative to cell lines. Mostly, these cell are maintained in culture for a finite length of time and therefore have limited chance of undergoing transformations. However, their slow population doubling rates and their finite lifespan has its limitations. Secondly, it is possible for breast tumour epithelial cells to be contaminated by normal epithelial cells and finally, for many researchers, the major limitation is tissue availability.

1.2.2 2D and 3D culture

For both cell lines and primary tissue, cultures are usually carried out in 2D on tissue culture plastic. Culture conditions are used to propagate the cells and do not necessarily match the conditions occurring in the human breast. These 2D culture conditions are easy to define, making it possible to produce readily reproducible data and providing an ideal starting point for mechanistic investigations. However, even when using primary breast cells over cell lines, there is a possibility that cells behave differently in 2D culture compared to when part of a tissue/organ. In this setting cells do not have contact with the microenvironment and are not arranged into the polarised, glandular architecture of the breast. The development of 3D culture systems has

improved the relevance of *in vitro* studies of tissue homeostasis by more accurately representing this complex microenvironment (Weaver and Bissell 1999, Vargo-Gogola and Rosen 2007, Hickman, Graeser et al. 2014). Below I will briefly describe some of the 2D and 3D culture techniques used to try to recapitulate some of the qualities of the breast environment.

1.2.2.1 2D culture techniques

1.2.2.1.1 Soft agar colony formation assay

Epithelial cells are dependent on cell signalling from the ECM for their survival, known as anchorage dependence (Meredith, Fazeli et al. 1993, Frisch and Francis 1994). In a soft agar colony formation assay, cells are grown in a semi-solid agar culture media and for a colony to form they must have the phenotype of anchorage-independent growth. This assay assesses the ability of cells to grow in anchorage-independent conditions as an indicator of transformation (Borowicz, Van Scoyk et al. 2014).

1.2.2.1.2 Growth on polyHEMA

Additional techniques to examine anchorage-dependence include the use of polyHEMA. PolyHEMA is used to coat tissue culture plastic and creates a non-adherent surface on which cells can be grown, creating a condition that mimics ECM-detachment.

1.2.2.1.3 Co-culture experiments (2D)

Many cell culture experiments involve a single cell type, and therefore lack breast epithelium-stromal interactions. The stroma, however, has important roles in breast tumour phenotype (Conklin and Keely 2012). To study some of these roles scientists utilise co-culture systems, where breast epithelial cells (from cell lines or primary tissue) are cultured with stromal cells; this is most commonly fibroblasts, but can be extended to myoepithelial cells, components of the immune system, endothelial cells and combinations of any of these cell types. These systems can be used to examine the effect of stromal cells on breast epithelium, or vice versa.

1.2.2.1.4 Growth in the presence of extracellular matrix components

In addition to stromal interactions, signalling from the ECM has a role in breast architecture and cancer morphogenesis (Hansen and Bissell 2000). Components of the ECM can be incorporated into 2D culture systems by coating of culture plastic or addition into the media. This includes the use of reconstituted basement membrane such as Matrigel or ECM proteins such as collagen.

1.2.2.1.5 Primary tumour slices

Tissue slices allows study of primary breast cells in the context of an intact microenvironment. These can be used as live tissue slices to examine tumour responses to therapies or, more frequently, are fixed and used for histology.

1.2.2.2 3D culture techniques

1.2.2.2.1 Spheroid model

Longer term culture of cells on polyHEMA, or other ultra-low attachment plates, leads to the formation of tumour spheroids – suspended multicellular 3D cultures. This is used to study cancer stem-like cells in an assay termed the mammosphere assay. Cancer stem-like cells are a population of tumour cells capable of self-renewal and proposed to be responsible for tumour initiation and development (Ponti, Costa et al. 2005, Shackleton, Vaillant et al. 2006). In the assay single cell suspensions are plated on polyHEMA dishes and incubated without disturbing the plate or changing the media for 5 days, at which point mammospheres are then counted (Shaw, Harrison et al. 2012).

In addition, this spheroid system is being utilised for high-throughput screening of new therapeutic targets (Kunz-Schughart, Freyer et al. 2004, Vinci, Gowan et al. 2012) and protocol adaptations have even enabled co-culture models to be developed (Jaganathan, Gage et al. 2014).

While the spheroid model is advantageous over 2D culture systems due to a 3D level of cell-cell interactions, this system lacks ECM interactions.

1.2.2.2.2 Culture in the presence of ECM in the ‘on-top’ assay

Breast epithelial cells can be seeded on top of a layer of ECM in media which is supplemented with a small amount of additional ECM, leading to multicellular 3D structures referred to as acini. The 3D morphology of epithelial cells in this system can be categorised as one of four distinct morphologies, with these morphologies largely correlating with gene expression profiles (Kenny, Lee et al. 2007).

1.2.2.2.3 Growth in a scaffold

In addition to signalling the ECM has an important structural role, with protein and carbohydrate components of breast tissue contributing to resistance from tensile and compressive forces respectively. To incorporate this complexity into culture systems 3D scaffolds have been

developed into which breast epithelial cells can be seeded (Rijal and Li 2016, Sokol, Miller et al. 2016).

1.2.2.2.4 Organotypics

Organotypic cultures incorporate the ECM and the cellular component of the microenvironment. Breast epithelial cells alongside myoepithelial and/or fibroblasts are cultured in an ECM gel, typically collagen (Holliday, Brouilette et al. 2009).

1.2.3 Modelling breast cancer in animal models

Breast cancer is also modelled in animals, mainly through studies in mice. These include xenograft experiments, which can involve subcutaneous or orthotopic injection of cell lines or primary tissue into the skin or mammary fat pad respectively. While xenografts have advantages over 2D culture systems because of the presence of a microenvironment, there are differences between mouse and human stroma (Hovey, McFadden et al. 1999). The differences between mice and human have been highlighted in metastasis investigations; mice breast metastasis colonise the lungs and often fail to colonise common sites of metastasis occurring in human breast cancer (Weigelt, Peterse et al. 2005). Additionally, xenografts involve immunocompromised mice and the absence of a functional immune system is likely to affect tumour development and progression.

Genetically engineered mice have contributed extensively to our understanding of genes involved in the promotion and progression of breast cancer, with studies including loss of tumour suppressor genes and gain of function mutations. In a comparison of the pathology of genetically engineered mice and human breast cancers, similarities between mouse and human tumours were identified (Cardiff, Anver et al. 2000). The conclusion overall, however, was that the histology of most genetically engineered mice does not resemble the common types of breast cancer.

1.2.4 The MCF-10A cell line

The work in this thesis utilises the MCF-10A cell line cultured in 3D in an 'on top' assay and I will therefore briefly focus on the properties of this breast line.

The MCF-10A human breast epithelial cell line is a spontaneously immortalised line arising from a patient with fibrocystic disease and is widely considered a healthy breast epithelial line. With a stable, near-diploid karyotype (Soule, Maloney et al. 1990, Yoon, Wersto et al. 2002) these cells have lost $p16^{INK4a}$ (Elenbaas, Spirio et al. 2001), have no *erbB2* amplification (Soule, Maloney et al.

1990), express wildtype p53 (Merlo, Basolo et al. 1995) and have no *Ha-ras* oncogene activating mutations (Soule, Maloney et al. 1990).

In monolayer culture MCF-10A cells grow with a cobblestone appearance characteristic of epithelial cells (Debnath, Muthuswamy et al. 2003, Imbalzano, Tatarkova et al. 2009) and, unlike transformed cells, are growth factor- and anchorage- dependent and non-tumourigenic (Soule, Maloney et al. 1990, Miller, Soule et al. 1993).

1.2.4.1 3D culture and acinar morphogenesis program

MCF-10A cells cultured 'on top' of Matrigel form spherical acini structures with hollowed lumens that are phenotypically similar to the duct of the breast (Figure 3). During acinar morphogenesis, cells undergo a well-defined program of proliferation, differentiation, apoptosis and growth arrest (Figure 3) (Debnath, Muthuswamy et al. 2003). A single MCF-10A cell proliferates to form a cluster which gains apical polarisation by day three to four. Between days five and eight of morphogenesis two populations of cells are observed – a well polarised outer layer and an inner subset of poorly polarised cells. Peripheral cells become columnar, the Golgi orientates towards the lumen, α6 integrin is observed apically and basement membrane proteins are deposited at the basal surface (Debnath, Mills et al. 2002). The central, poorly polarised inner cells undergo apoptosis between days six and ten leading to acini with a hollowed lumen. Acini growth and proliferation stops around day 12 (Debnath, Muthuswamy et al. 2003, Imbalzano, Tatarkova et al. 2009) and by day 20 the outer edges of structures are fully covered in a basement membrane (Imbalzano, Tatarkova et al. 2009).

Luminal cell apoptosis occurs both during lumen formation and also if cells proliferate into the lumen once it has been formed (Debnath, Mills et al. 2002). These cells have access to molecules as large as 40 kDa and frequent feeding of acini does not alter the apoptotic program, indicating that apoptosis is not a consequence of insufficient access to nutrients; luminal cell apoptosis is instead proposed to be driven by a lack of contact with the ECM.

Overexpression of oncogenes or anti-apoptotic proteins in MCF-10A prevents cell death following ECM-detachment and results in filled acini structures which are phenotypically similar to DCIS (Debnath, Mills et al. 2002, Anderson, Sutherland et al. 2010). MCF-10A acini therefore provide a physiologically relevant model to examine the transforming events that promote cell survival in ECM-detached conditions and drive the development and progression of early breast cancer. In this thesis I use MCF-10A acini to examine the role of cellular metabolism, Bag-1 and HER2 specifically. Below I introduce each of these in turn, explaining general principles and highlighting their roles in breast cancer.

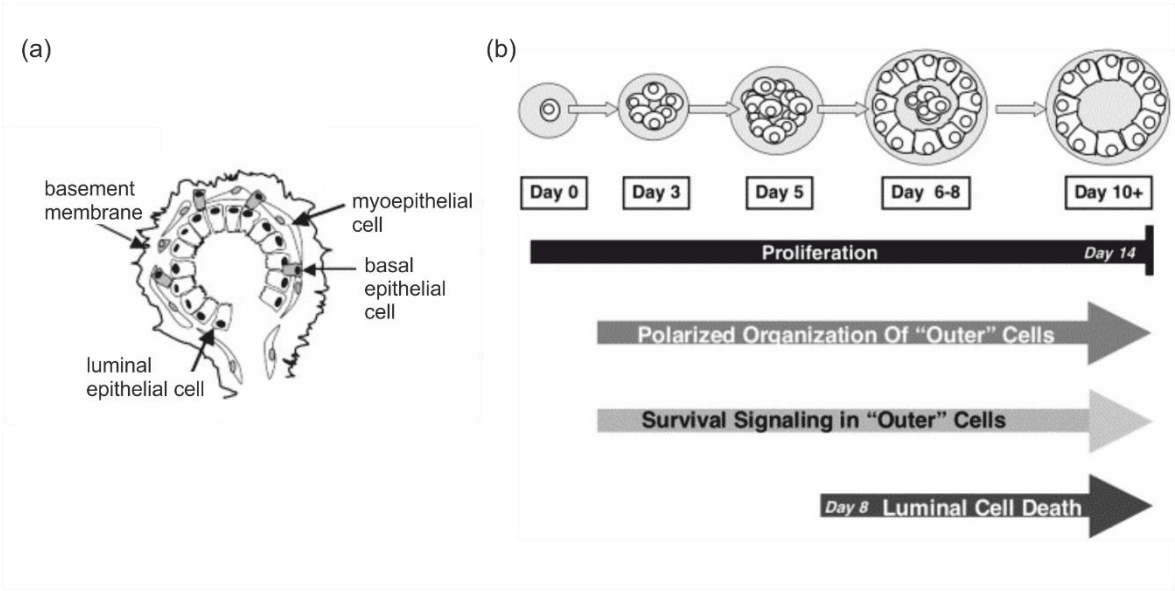

Figure 3 MCF-10A acini form structures phenotypically similar to the duct of the breast

(a) Schematic of a lobule of a mammary gland. (b) Schematic of MCF-10A acinar morphogenesis. Taken with permission from (Debnath, Muthuswamy et al. 2003).

1.3 Cellular Metabolism and Cancer

As mentioned, one of the key aims of this project was to examine the role of cellular metabolism in the MCF-10A acini model. In this section I will briefly introduce the metabolic pathways relevant for the work presented in this thesis, before discussing the role of these pathways in tumourigenesis.

Cellular metabolism encompasses all the life-sustaining chemical reactions within a cell. In addition to energy generation, metabolism also functions to generate intermediates for macromolecule biosynthesis and for elimination of waste.

1.3.1 An introduction to cell metabolism

1.3.1.1 Glycolysis: an energy-generating process

Glycolysis, the central pathway in carbohydrate metabolism, is a cytosolic, ten-stage metabolic pathway that converts glucose into pyruvate (full schematic shown in Figure 4a). Glucose enters the cell through facilitated diffusion via glucose transporters (GLUT) (Mueckler and Thorens 2013), where it is rapidly phosphorylated by hexokinase to produce glucose-6-phosphate. This phosphorylation reaction is irreversible, and prevents the diffusion of glucose out of the cells. The net reaction of glycolysis, shown below, is energy generating and produces two molecules of ATP

and two molecules of NADH. NADH can enter the electron transport chain to produce further energy.

$$Glucose + 2\ Pi + 2\ ADP + 2\ NAD^+ \rightarrow 2\ Pyruvate + 2\ ATP + 2\ NADH + 2\ H^+ + 2\ H_2O$$

Pyruvate has two fates depending on the condition of the cell. Under anaerobic conditions the enzyme lactate dehydrogenase generates lactate (Figure 4b); the conversion to lactate allows NAD^+ to be regenerated, even while the electron transport chain is not active, enabling glycolysis to continue producing ATP. Lactate can be converted back to pyruvate within the cell or exported into the blood and transported to the liver where it is converted to glucose via gluconeogenesis. Under aerobic conditions pyruvate is transported into the mitochondrial matrix by mitochondrial pyruvate carriers (Halestrap and Denton 1974, Halestrap 2012) where it is metabolised further through mitochondrial respiration. Mitochondrial respiration is divided into two pathways: the citric acid cycle and oxidative phosphorylation.

1.3.1.2 The citric acid cycle

The citric acid cycle is the common pathway for oxidation of fuel molecules, including pyruvate, fatty acids and amino acids. The first step is the irreversible conversion of pyruvate to acetyl-coA, which then enters a cyclic eight stage reaction. The full schematic is shown in Figure 5 and the net reaction is shown below. NADH and $FADH_2$ enter the electron transport chain to produce further energy.

$$AcetylCoA + 3\ NAD^+ + FAD + GDP + Pi + 2\ H_2O \rightarrow 2\ CO_2 + 3\ NADH + FADH_2 + GTP + 2\ H^+ + CoA$$

1.3.1.3 The electron transport chain

In order for aerobic respiration to continue, NAD^+ and FAD are regenerated via the electron transport chain. Also known as oxidative phosphorylation, re-oxidation of NADH and $FADH_2$ are coupled to ATP generation. Summarised in Figure 6, electrons are passed from NADH and $FADH_2$ to O_2, which is reduced to water. Protons are pumped across the inner mitochondrial membrane to generate a membrane potential and this proton motive force drives ATP synthesis through ATP synthase.

Figure 4 Schematic of glycolysis

(a) Summary schematic showing the steps of glycolysis and the enzymes involved. (b) Under anaerobic conditions, lactate dehydrogenase generates lactate from pyruvate in a reaction which generates NAD^+ from NADH. Based on information from (Berg, Tymoczko et al. 2007).

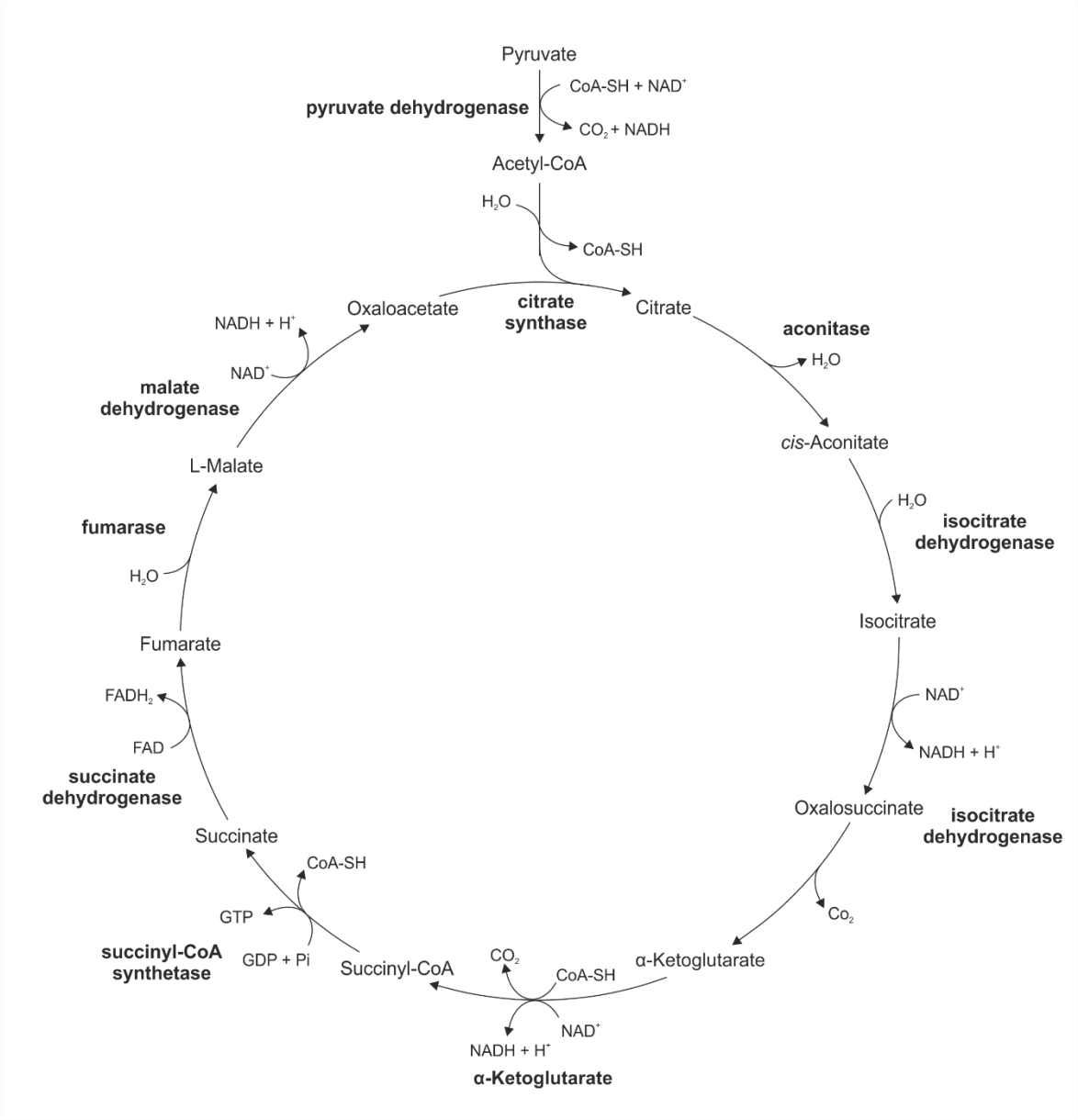

Figure 5 Schematic of the citric acid cycle

Summary schematic showing the steps of the citric acid cycle and the enzymes involved. Based on information from (Berg, Tymoczko et al. 2007).

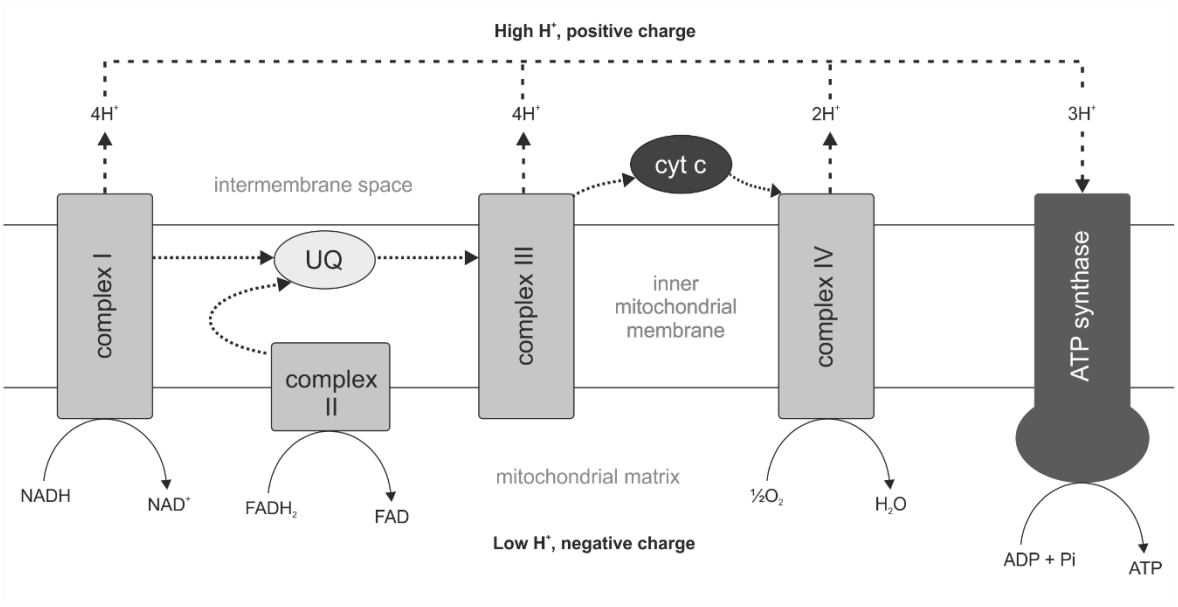

Figure 6 Overview of the electron transport chain

Summary schematic of the electron transport chain. Complexes I and II oxidise NADH and FADH2 respectively, passing electrons on to ubiquinone (UQ) and shuttling protons (H^+) across the inner mitochondrial membrane. Dotted lines show the flow of electrons while dashed lines show the flow of H^+. UQ passes electrons to complex III then onto cytochrome c (cyt c) before reducing oxygen to H_2O. The process results in a high concentration of H^+ in the intermembrane space, and this proton motive force drives ATP synthesis through ATP synthase. Based on information from (Berg, Tymoczko et al. 2007).

1.3.1.4 Fatty acid oxidation: extra ATP when required

Fatty acids are carboxylic acids with a long aliphatic chain, and within metabolism have a role in ATP generation. When compared to stored glycogen, stored fatty acids can generate over 6 times as much energy, making them the preferred nutrient for storage during times of nutrient abundance (Berg, Tymoczko et al. 2007).

Fatty acid oxidation (FAO) occurs in the mitochondrial matrix and involves a repeating sequence of four reactions (Figure 7). Fatty acids are converted into their acyl-CoA derivatives by acyl-coA synthetase in the cytoplasm (Figure 7a). Longer chain acyl-coA molecules cannot cross the inner mitochondrial membrane, and are translocated across the membrane as an acyl carnitine in a rate-limiting reaction involving carnitine palmitoyltransferase I (CPT-1) (Figure 7b) (Drynan, Quant et al. 1996). Per round, the cyclic series of FAO removes two-carbon units from the end of the acyl-CoA to generate acetyl-CoA in a process which generates $FADH_2$ and NADH (Figure 7c). $FADH_2$ and NADH enter the electron transport chain to produce ATP, while acetyl-CoA enters the citric acid cycle.

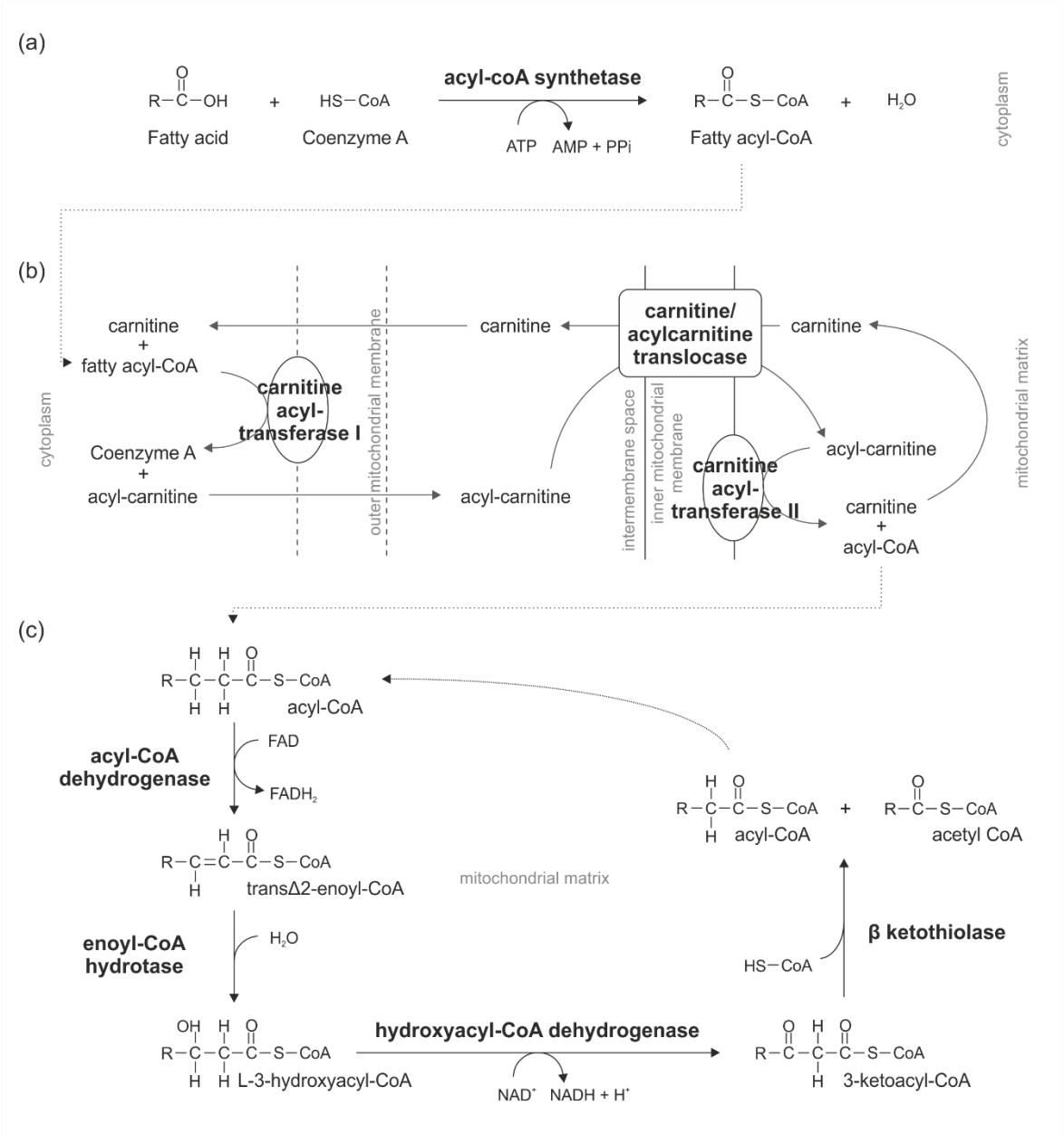

Figure 7 Summary schematic of fatty acid oxidation

(a) The fatty acid forms a thioester link with Coenzyme A (CoA) to give an acyl-CoA in a reaction that requires 1 ATP. (b) Long chain fatty acids (> 10 carbons) cannot cross the inner mitochondrial membrane. These acyl-CoA molecules are conjugated to the polar molecule carnitine by carnitine acyl-transferase I, which are translocated across the inner mitochondrial membrane by a carnitine/acylcarnitine translocase into the mitochondrial matrix. Inside the matrix, the acyl-CoA group is transferred back to CoA by a carnitine acyl-transferase II. (c) Fatty acid oxidation involves a repeating four-step reaction scheme. The acyl-CoA is oxidised to transΔ^2-enoyl-CoA by FAD, producing $FADH_2$. The transΔ^2-enoyl-CoA is hydrated to form L-3-hydroxyacyl CoA, which is oxidised to 3-ketoacyl CoA by NAD^+ in a reaction that produces NADH. 3-ketoacyl CoA undergoes thiolysis by a second CoA to give acetyl-CoA and an acyl-CoA that is shorter by 2 carbon atoms. Based on information from (Berg, Tymoczko et al. 2007).

So far I have described the energy-generating steps of metabolism; now I will focus on the additional functions of these metabolic processes.

1.3.1.5 Glycolysis: a source of precursors for biosynthesis

Many of the intermediates of glycolysis serve as precursors for biosynthesis of other critical components of the cell. The alternative fates of glycolytic intermediates are summarised in Figure 8 and include amino acid, lipid and nucleotide synthesis. Nucleotides are synthesised from the precursor ribose-5-phosphate, generated from the pentose phosphate pathway (PPP).

1.3.1.6 The pentose phosphate pathway: nucleotide synthesis and production of NADPH

The PPP occurs in the cytosol of the cell and exists in two stages – oxidative and non-oxidative. In addition to the precursor ribose-5-phosphate, this pathway also generates glycolytic intermediates which link back into the glycolytic pathway for further energy generation, and the reducing power NADPH. NADPH is generated from the oxidative stage of the PPP, summarised in Figure 9.

1.3.1.7 Fatty acid oxidation: production of NADPH

In addition to the PPP, FAO is also a source of NADPH. FAO generates one molecule of acetyl-CoA in each oxidation cycle and two in the last cycle (Figure 7c), which enters the citric acid cycle where, together with oxaloacetate, gives rise to citrate. Citrate can be exported into the cytoplasm where it can be converted into pyruvate in a two-step reaction which generates the reducing power NADPH (Figure 10).

1.3.1.8 NADPH: a reducing power

As the reduced form of nicotinamide adenine dinucleotide phosphate ($NADP^+$), NAPDH is an electron carrier with two main cellular functions; it is utilised as an electron carrier during biosynthesis reactions and provides a reducing power for neutralisation of reactive oxygen species (ROS) (Figure 11b).

1.3.1.9 Reactive oxygen species: an inducer of oxidative stress

The primary source of ROS are as a byproduct of oxygen metabolism in the electron transport chain (Figure 11a). A build-up of ROS can damage all components of the cell including lipid, proteins and DNA/RNA nucleotides. In addition to NADPH, antioxidants are also utilised to neutralise ROS and maintain the redox state of a cell. An imbalance in a cells ability to neutralise ROS or repair the consequential damage leads to a condition termed oxidative stress.

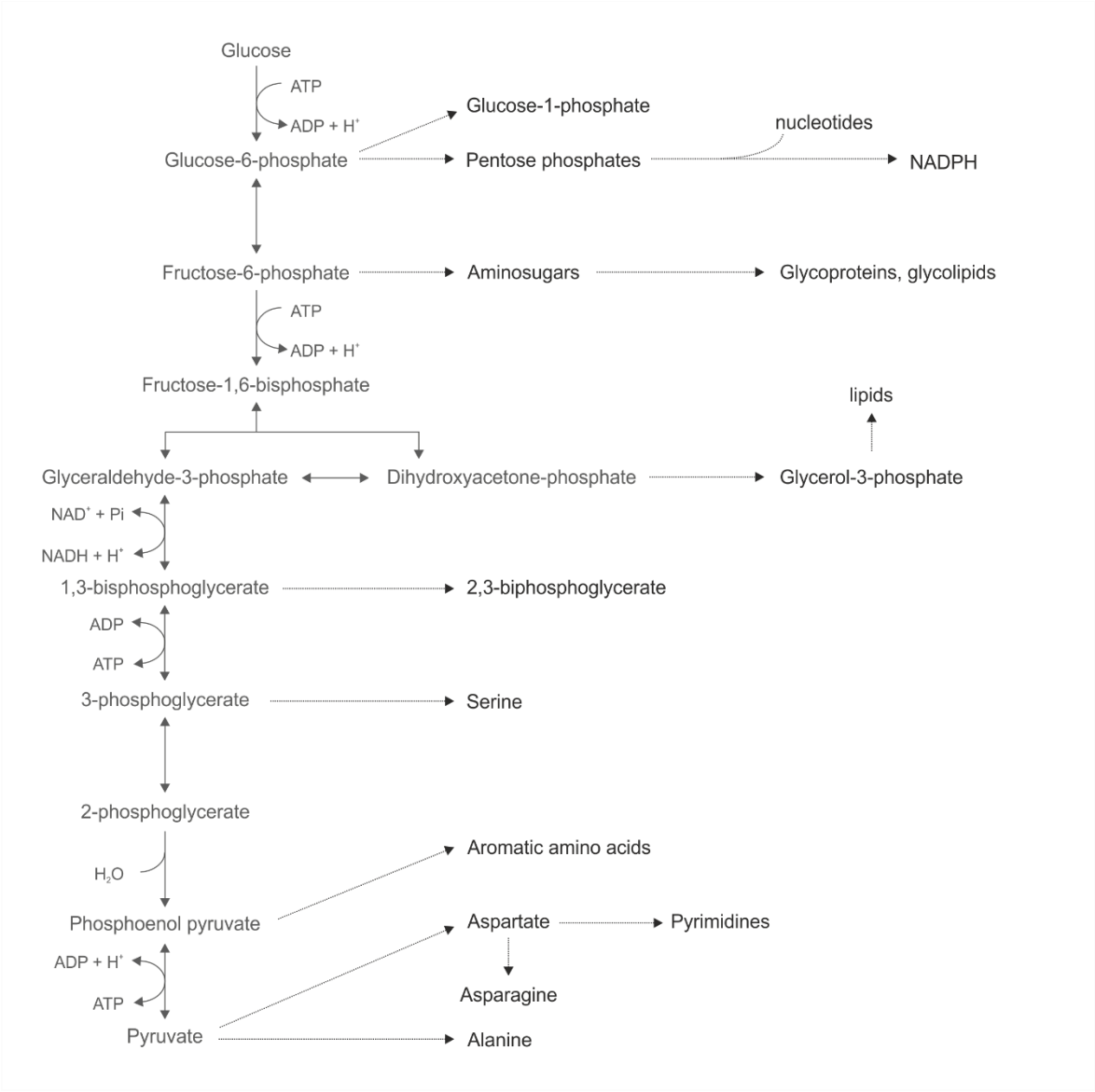

Figure 8 Summary of the alternative fates of glycolytic intermediates

Based on information from (Berg, Tymoczko et al. 2007).

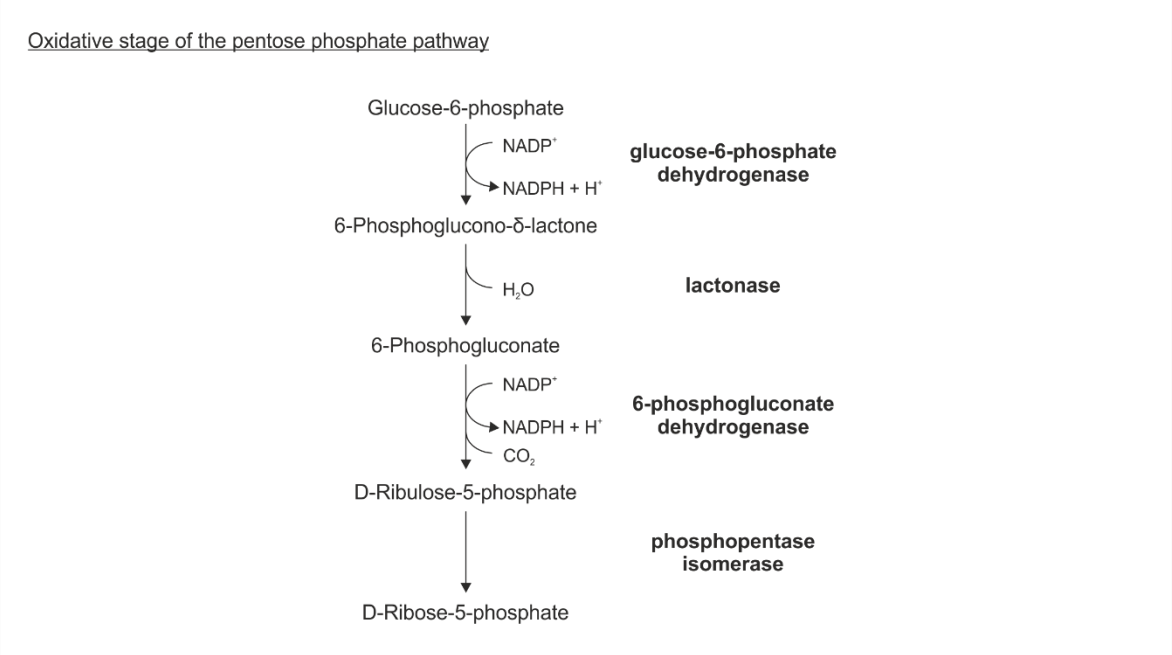

Figure 9 Summary schematic of the reactions that generate NADPH from the pentose phosphate pathway

Summary schematic showing the steps of the oxidative stage of the pentose phosphate pathway and the enzymes involved. Based on information from (Berg, Tymoczko et al. 2007).

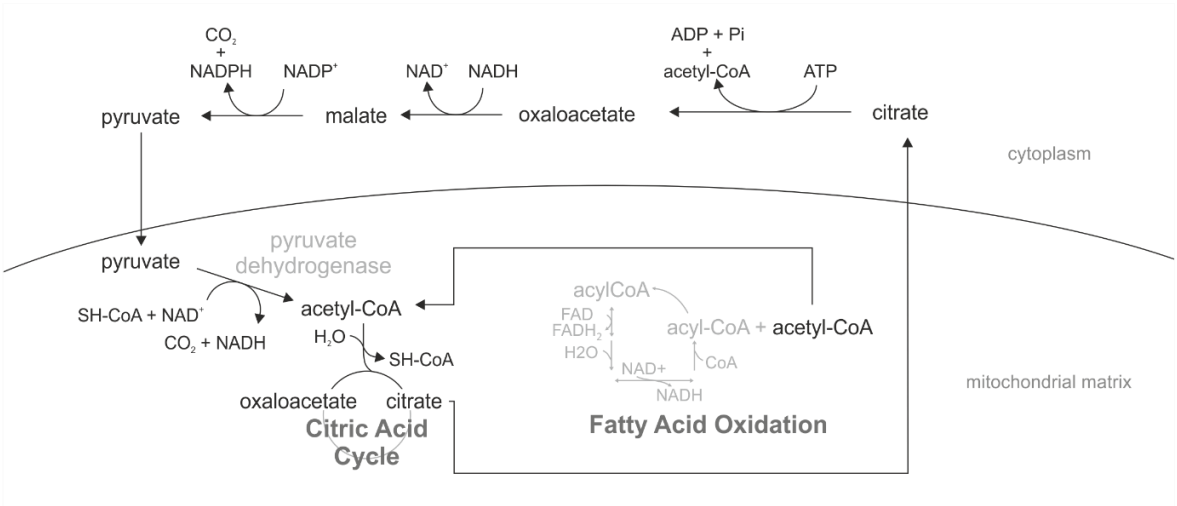

Figure 10 Summary schematic of reactions that can generate NADPH from fatty acid oxidation-derived acetyl-CoA

Acetyl-CoA generated in fatty acid oxidation enters the citric acid cycle and is combined with oxaloacetate to form citrate. Citrate is exported to the cytoplasm where it is converted to pyruvate in a three-step reaction that generates NADPH. Based on information from (Carracedo, Cantley et al. 2013).

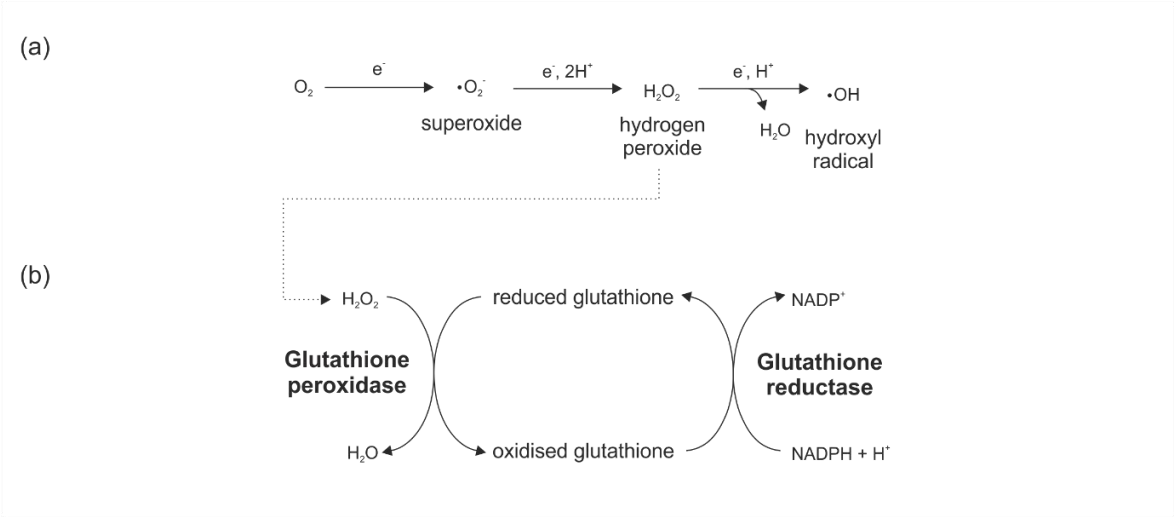

Figure 11 The importance of NAPDH to neutralise reactive oxygen species

(a) Reaction schematic of the generation of free radicals (superoxide and hydroxyl radical) from O_2. (b) Glutathione redox cycle utilises NADPH for the neutralisation of hydrogen peroxide. Based on information from (Berg, Tymoczko et al. 2007).

1.3.2 Cell metabolism and cancer

Back in 2000 Hanahan and Weinberg defined six hallmarks of cancer, which describe the properties that a cancer cell must acquire in order to transform from a healthy cell to a cancerous one (Hanahan and Weinberg 2000). This has since been expanded to include additional capabilities including a deregulation of cellular energetics (Figure 12) (Hanahan and Weinberg 2011); cancer cells must alter their metabolism in order to meet the increased demand that transformation places upon them. This has led to a therapeutic approach where we could selectively target a cancer over a healthy tissue by utilising these metabolic changes. I will now describe the metabolic transformations observed in breast cancer that are relevant for this thesis.

1.3.2.1 The Warburg effect: matching an increased growth demand

The Warburg effect describes the phenomenon by which cancer cells utilise glycolysis for ATP generation over the more efficient mitochondrial oxidative phosphorylation, even in the presence of ample oxygen supply, to facilitate enhanced generation of biomass (Vander Heiden, Cantley et al. 2009). Increased biomass generation allows the cell to meet its demand for continuous growth and proliferation.

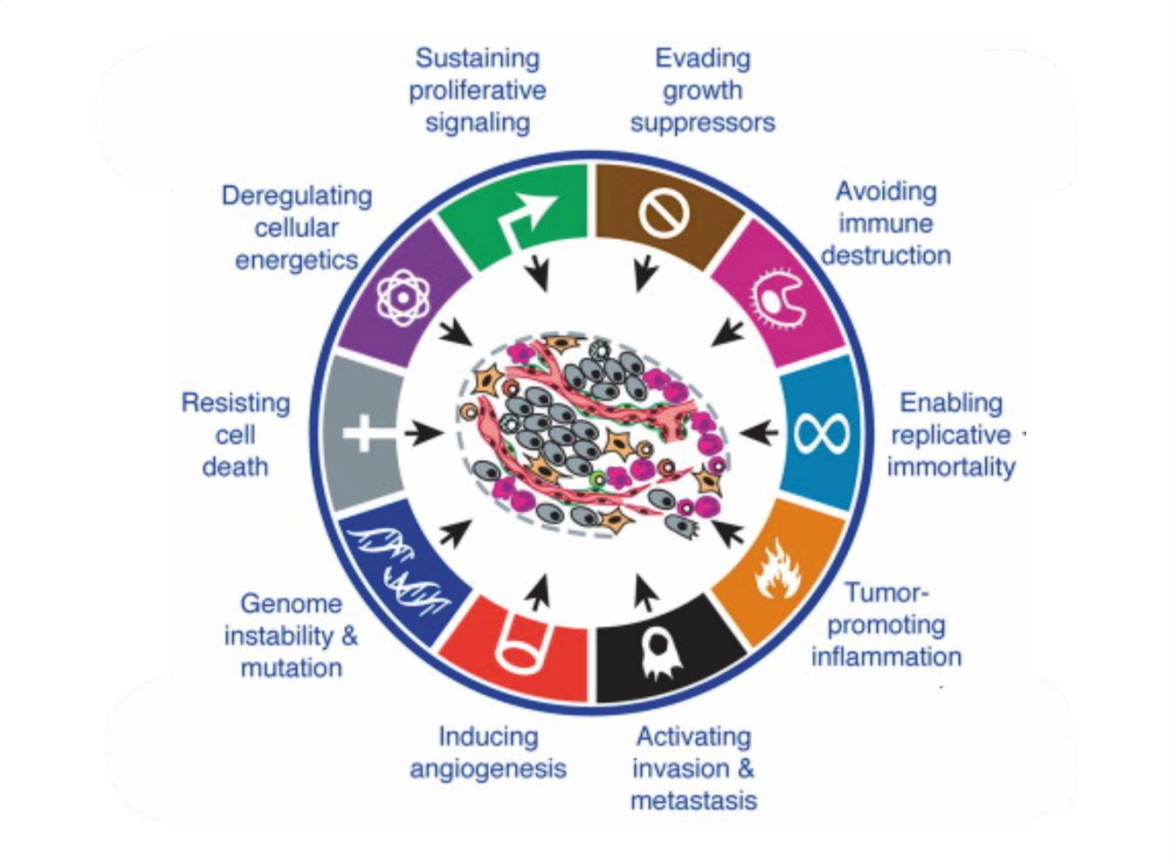

Figure 12 The Hallmarks of Cancer

This illustration shows the 10 hallmarks of cancer, describing the capabilities that are necessary for tumour growth and progression. Taken with permission from (Hanahan and Weinberg 2011).

1.3.2.1.1 Glycolysis upregulation in breast cancer

The Warburg effect is utilised clinically for metabolic positron emission tomography scanning for the detection and diagnosis of cancer (Zhu, Lee et al. 2011). Regions of increased glucose demand are highlighted during scanning through uptake of a radiolabelled glucose analogue fluoro-deoxy-glucose.

Consistent with enhanced glucose uptake, cancer cells frequently overexpress GLUT transporters and, moreover, can express a GLUT isoform that is not usually present in the respective tissue of origin (Medina and Owen 2002). In the breast, cancer cells overexpress the GLUT1 isoform (Brown and Wahl 1993) and its overexpression marks a more aggressive disease (Younes, Brown et al. 1995, Kang, Chun et al. 2002). Similarly hexokinase, specifically the hexokinase II isoform which is not typically expressed in the adult breast (Wilson 2003), is upregulated and this also correlates with a more aggressive disease (Sato-Tadano, Suzuki et al. 2013). In addition, the pyruvate kinase isoenzyme type-M2 has been shown to be essential for driving the Warburg effect (Christofk,

Vander Heiden et al. 2008) and its expression in breast cancer correlates with aggressive disease (Luftner, Mesterharm et al. 2000, Lin, Lv et al. 2015).

Finally, cancer cells upregulate the transporters which regulate pyruvate and lactate transport across the plasma membrane – monocarboxylate transporters (MCT) (Halestrap and Wilson 2012). This could be expected to enhance lactate export from the cell to prevent intracellular acidification however Hong *et al.* suggest that MCT1 is important for pyruvate, not lactate, export (Hong, Graham et al. 2016); inhibition of MCT1 in breast cancer cells reduced pyruvate but not lactate export and resulted in enhanced oxidative metabolism and reduced proliferation.

1.3.2.2 Pentose phosphate pathway

As discussed previously, the PPP is important for nucleotide synthesis and generation of NADPH. In order to continually replicate DNA, cancer cells have an increased reliance on nucleotide synthesis, while NADPH is a used as a redox power to neutralise oxidative stress, or as a co-enzyme in anabolic reactions involved in the generation of biomass.

1.3.2.2.1 Pentose phosphate pathway activity in cancer

Glucose-6-phosphate dehydrogenase catalyses the first step of the oxidative stage of the PPP in a rate-limiting reaction (Figure 9). A major modulator is the $NADP^+$/NADPH ratio, so this pathway's activity is regulated by cellular demands, however it can also be regulated at a post-translational level. Glucose-6-phosphate dehydrogenase activity can be enhanced through oncogenic signalling pathways such as phosphatidylinositol-3-kinase (PI3K), Ras or Scr signalling (Tian, Pignatare et al. 1994, Pan, World et al. 2009), or loss of p53. The tumour suppressor protein p53 can negatively regulate glucose-6-phopshate dehydrogenase, but this phenotype is restricted to wildtype p53 and tumour-associated mutants lack an inhibitory activity (Jiang, Du et al. 2011).

1.3.2.3 Fatty acid oxidation: for NADPH generation

Cancer cells utilise FAO for generation of NADPH (Carracedo, Cantley et al. 2013) which, as described for the PPP, is used to neutralise oxidative stress or as an electron carrier for biosynthesis reactions. FAO can also be important under conditions of metabolic stress where increased ATP production is required, as they can generate twice as much ATP as carbohydrates relative to their dry mass (Berg, Tymoczko et al. 2007).

1.3.2.3.1 Fatty acid oxidation and cancer

Consistent with enhanced FAO upregulation of CPT-1, the rate limiting step of this pathway, has been shown in a variety of cancers (Qu, Zeng et al. 2016), including breast (Gatza, Silva et al.

2014), and has been shown to promote cell survival (Zaugg, Yao et al. 2011, Pucci, Zonetti et al. 2016).

1.4 C-terminal Binding Proteins (CtBPs)

As part of the metabolic investigations that form part of this thesis I have manipulated the metabolic sensor, CtBP. This protein, and its link to tumourigenesis, is discussed below.

The C-terminal binding protein (CtBP) family members are well characterised as transcriptional co-regulators, but have been implicated in diverse functions. Consisting of two family members, CtBP1 and CtBP2, these genes share high levels of homology (Katsanis and Fisher 1998) with a degree of functional overlap between these two proteins. However, in addition to redundant roles, CtBP knockout mice also demonstrated unique roles for CtBP1 and CtBP2 in embryogenesis (Hildebrand and Soriano 2002) and CtBP1 is known to be involved in cytoplasmic functions such as intracellular trafficking.

1.4.1 CtBP structure and localisation

Alternative splicing of CtBP1 or CtBP2 mRNA generates two isoforms of each family member (CtBP1-S, CtBP1-L, CtBP2-S, CtBP2-L). A third CtBP2 isoform, RIBEYE, is generated from an alternative promoter of the CtBP2 gene and is expressed in synaptic ribbons and will therefore not be discussed for the purposes of this work (Schmitz, Konigstorfer et al. 2000). Excluding RIBEYE, CtBP proteins are ubiquitously expressed with all isoforms sharing a high degree of amino acid sequence similarity which is highly conserved between different species (Figure 13).

The structure of CtBPs consists of three main domains. The C-terminal region is an intrinsically unstructured domain which contains sites of post-translational modification (Nardini, Svergun et al. 2006). The substrate-binding domain recognises the consensus sequence PXDLS (Pro-X-Asp-Leu-Ser) for binding of transcription factors (Chinnadurai 2002), while the central domain is responsible for NAD (NAD^+/NADH) binding and shares strong homology with D2-hydroxyacid dehydrogenases (Kumar, Carlson et al. 2002). This central domain is responsible for dimerisation in an NAD-dependent manner, with CtBP displaying a much higher affinity for NADH than NAD^+ (Zhang, Piston et al. 2002, Fjeld, Birdsong et al. 2003, Nardini, Spano et al. 2003).

The CtBP2-L isoform contains an additional nuclear localisation sequence, making CtBP2 predominantly nuclear, while CtBP1 can be found in both nuclear and cytoplasmic compartments (Bergman, Morris et al. 2006, Birts, Harding et al. 2010). Subsequently, CtBPs have both nuclear and cytoplasmic functions which will be briefly discussed below.

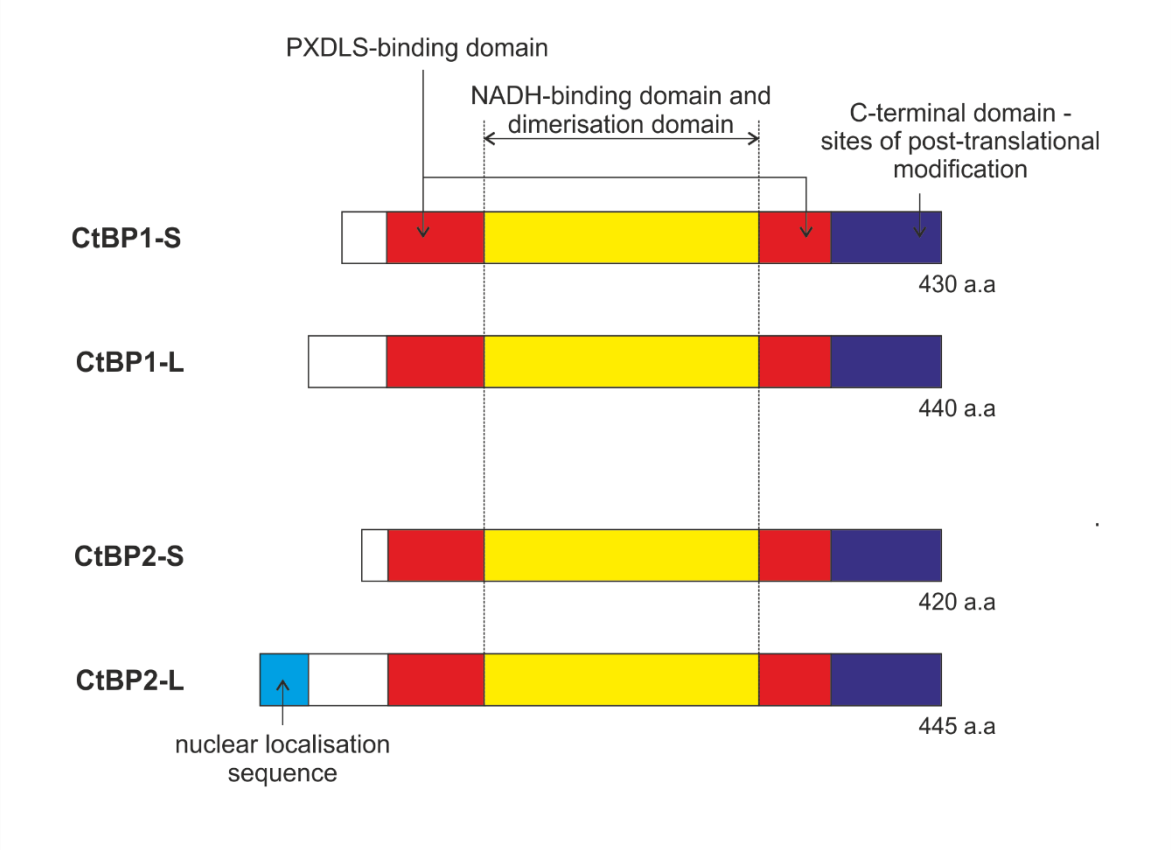

Figure 13 The structure of CtBP family members

Schematic showing the structure of the major isoforms of CtBP1 and CtBP2. Alternative splicing of the CtBP1 or CtBP2 mRNA generates short (S) and long (L) isoforms for each family member. These isoforms all share a high degree of amino acid sequence similiarity. The third CtBP2 isoform, RIBEYE, is expressed exclusively in synaptic ribbons as is not shown here. Figure adapted from (Rucka 2013).

1.4.2 Cellular functions of CtBP

1.4.2.1 CtBPs as transcriptional co-regulators

CtBPs are frequently referred to a transcriptional co-repressors due to their ability to downregulate expression of numerous CtBP target genes (Table 1), however in more recent years CtBPs have been shown to also act as transcriptional co-activators (Di, Byun et al. 2013). Studies examining the transcriptional activity of CtBP have used functional mutants to demonstrate the importance of both the NADH-dimerisation and the PXDLS-binding domain for this function (Kuppuswamy, Vijayalingam et al. 2008, Zhao, Kuppuswamy et al. 2009). NADH binding induces CtBP dimerisation and subsequent activation as a transcriptional co-regulator (Figure 14) (Nardini, Spano et al. 2003). In the dimeric state, the substrate-binding domains are exposed and binds adaptor proteins to form a co-regulator complex. CtBPs lack a DNA-binding domain and are

recruited to promoter regions of target genes by transcription factors which bind to CtBP as part of the co-regulator complex. This co-complex can include chromatic modifying enzymes such as histone deacetylases, histone demethylases and histone methyltransferases (Shi, Sawada et al. 2003, Subramanian and Chinnadurai 2003, Shi, Lan et al. 2004).

Chromatin describes the complex of DNA and histones which forms chromosomes. Histones are not only important to efficiently package DNA into a small volume, but also have roles in regulating gene expression. There are numerous ways in which histones can be modified to influence gene expression (Bannister and Kouzarides 2011), which include acetylation and methylation; acetylation generally activates transcription, while methylation can activate or repress transcription depending on the amino acid being methylated and the state of the other surrounding residues in the histone.

1.4.2.2 CtBPs as regulators of mitotic fidelity

An additional nuclear role relates to CtBPs regulation of mitotic fidelity, with CtBP knockdown resulting in mitotic defects (Bergman, Birts et al. 2009). The interaction of CtBPs with proteins via its PXDLS-binding domain is essential for maintenance of mitotic fidelity and activation of the spindle assembly checkpoint, promoting cell survival (Bergman, Birts et al. 2009, Birts, Bergman et al. 2011)

1.4.2.3 CtBPs have monomeric functions in the cytoplasm: CtBP1 and intracellular trafficking

Although the CtBP family is best characterised for their dimeric functions in epigenetic regulation of gene expression, monomeric functions of CtBP have been described. CtBPs have a cytoplasmic role in intracellular membrane trafficking, which relates mainly to the CtBP1-S isoform in its monomeric state.

The central NADH-binding domain of CtBP1-S can also bind acyl-CoA which favours a monomeric conformation and maintains a cytoplasmic localisation (Nardini, Spano et al. 2003). It is proposed that NADH and acyl-CoA binding are structurally important for switching between the alternative functions of co-repression and cytoplasmic functions. CtBP1-S was first identified as the target for brefeldin A (a fungal toxin that disrupts the Golgi complex) (De Matteis, Di Girolamo et al. 1994, Spano, Silletta et al. 1999) and later shown to be involved in Golgi tubule fission (Weigert, Silletta et al. 1999). In addition to roles in intra-Golgi fission, CtBP1-S has fission roles in transport from the Golgi and the plasma membrane (Bonazzi, Spano et al. 2005, Yang, Lee et al. 2005, Liberali, Kakkonen et al. 2008, Haga, Miwa et al. 2009).

1.4.3 CtBPs and cancer

CtBPs have been implicated in cellular transformation and tumour progression due to their ability to repress target genes which promote a malignant phenotype (Chinnadurai 2009), summarised in Table 1. CtBP activity inhibits apoptosis and promotes genomic instability, epithelial-to-mesenchymal transition, cell cycle progression and survival.

1.4.3.1 Functional link to tumorigenesis

The tumour-promoting activity of CtBPs relates to their function as transcriptional repressors, in which CtBP are in their NADH-bound dimeric state. Based on the Warburg effect, we would therefore expect cancerous cells to have higher levels of CtBP transcriptional co-regulator complexes due to higher NADH (as a result of increased glycolysis) driving dimerisation and activation. It is therefore predicted that CtBP-driven gene regulation is enhanced in cancerous cells compared to non-transformed tissue.

1.4.3.2 Expression in cancer

There have been few studies examining the expression of CtBP in cancer. In colon cancer specimens, tumour-specific CtBP overexpression was observed in 64% of samples which inversely correlated with loss of a negative regulator of CtBP (ARF) (Straza, Paliwal et al. 2010). Similarly, CtBP1 overexpression was observed in head and neck (Deng, Liu et al. 2010) and melanoma (Deng, Liu et al. 2013), while CtBP2 overexpression (Guan, Shi et al. 2013) is seen in oesophageal cancer compared to non-transformed tissue. In breast cancer specifically, CtBP1 and CtBP2 expression has been shown in all breast cell lines (six cancer and MCF-10A) and breast tumour samples examined (10) (Birts, Harding et al. 2010), but no comparison to non-transformed tissue has been made.

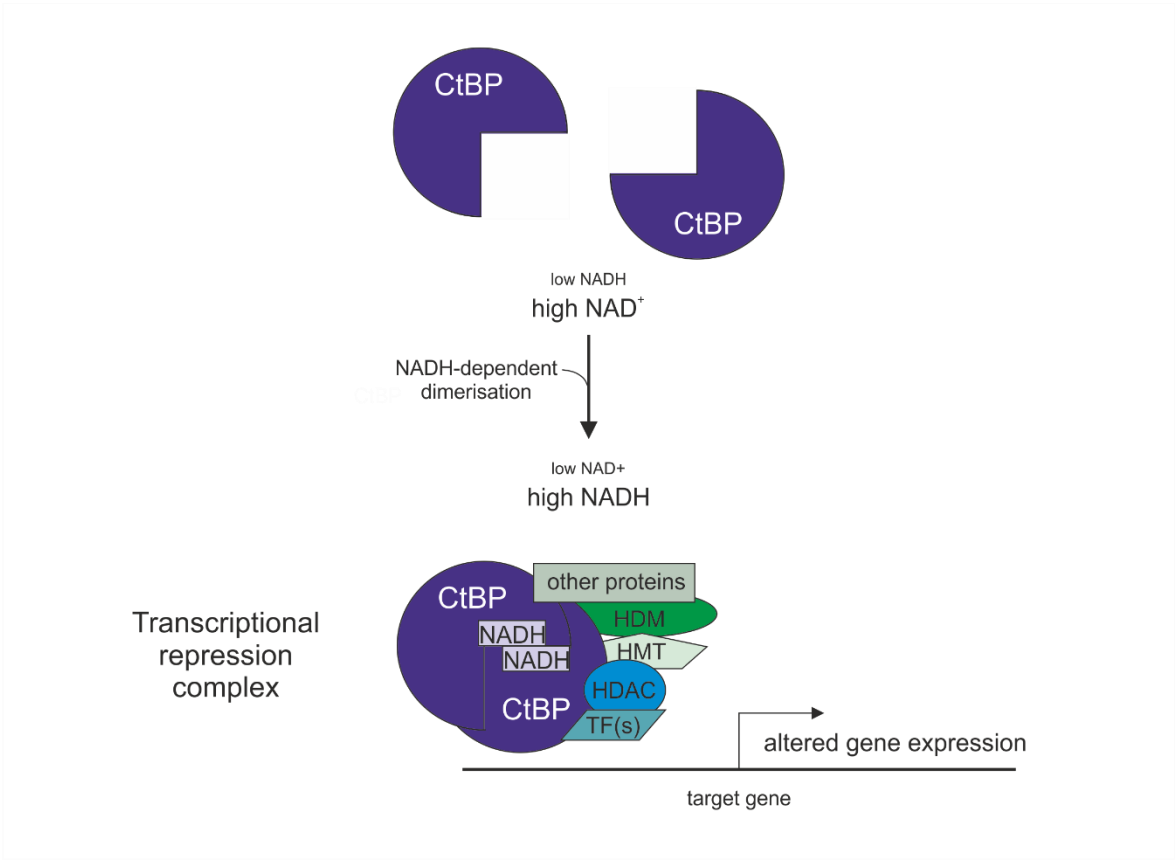

Figure 14 NADH-dependent dimerisation induces activation of the transcriptional regulator complex

In the absence of NADH binding, CtBP is in a monomeric state. Upon NADH binding, CtBPs can homo- or hetero- dimerise and recruit transcription factors (TF), histone deacetylases (HDAC), histone methyltransferases (HMT), histone demethylases (HDM) and other chromatin modifying proteins. This transcriptional regulator complex binds to target genes through transcription factors and functions to suppress or promote target gene expression. Adapted from Figure 2 of (Stankiewicz, Gray et al. 2014).

1.5 Bcl-2 Associated Anthogene-1 (Bag-1)

In addition to cellular metabolism, this project also asks research questions relating to how the anti-apoptotic protein Bag-1 and the oncogene HER2 can influence cell death following ECM-detachment in MCF-10A. I will now introduce these proteins, discussing their cellular functions and their expression and significance in breast cancer. I will also briefly mention the anti-apoptotic proteins Bcl-2 and Bim, which have relevance to the MCF-10A acini model of the breast.

Table 1 CtBP-target genes linked to cell transformation

Some of the targets of CtBP-driven transcriptional repression are listed below, with a brief summary of the consequences of gene repression on cell phenotype.

Pathway impacted	Effect of CtBP repression on pathway	Gene target	Target gene function	Reference(s)
Apoptosis	Inhibits	Bax	Pro-apoptotic members of the Bcl-2 protein family	(Grooteclaes, Deveraux et al. 2003)
		Noxa		
		PERP	Pro-apoptotic. An apoptosis-associated target of p53	
		Bik	Pro-apoptotic. BH3-only protein of the Bcl-2 superfamily	(Straza, Paliwal et al. 2010)
DNA damage repair	Inhibits DNA repair leading to genome instability	BRCA1	Tumour suppressor gene and DNA damage repair protein	(Di, Fernandez et al. 2010)
Epithelial-to-mesenchymal transition	Induces epithelial-to-mesenchymal transition	E-cadherin	Cell-cell adhesion molecule whose downregulation is associated with epithelial-to-mesenchymal transition	(Comijn, Berx et al. 2001) (Grooteclaes and Frisch 2000) (Grooteclaes, Deveraux et al. 2003) (Zhang, Wang et al. 2006) (Di, Byun et al. 2013)
Senescence/Cell cycle arrest	Enhances cell cycle progression	$p16^{INK4a}$ $p15^{INK4b}$	Tumour suppressor proteins which act as cyclin-dependent kinase inhibitors to inhibit cell cycle progression	(Mroz, Baird et al. 2008)
Survival	Promotes transformation through inhibition of PTEN tumour suppressor	PTEN	Phosphatase that inactivates Akt signalling. Role as a tumour suppressor, regulating cell cycle	(Grooteclaes, Deveraux et al. 2003)

Bcl-2 associated anthogene-1 (Bag-1) is a member of the ubiquitously expressed BAG family of proteins which all share a common C-terminal BAG domain (Kabbage and Dickman 2008). Identified independently as a novel interaction partner of the anti-apoptotic protein Bcl-2 (Takayama, Sato et al. 1995) and a binding partner of the glucocorticoid receptor, a member of the nuclear hormone receptor family (Zeiner and Gehring 1995), human Bag-1 is a multifunctional, anti-apoptotic protein existing in functionally discrete, differentially localised isoforms (Townsend, Cutress et al. 2003).

1.5.1 Multiple isoforms of Bag-1 from a single transcript

The isoforms of Bag-1 are formed from alternative translation initiation from a single mRNA and all share the same C-terminus (Figure 15a). There are three major isoforms of Bag-1, Bag-1S (36 kDa), Bag-1M (46 kDa) and Bag-1L (50 kDa) (Packham, Brimmell et al. 1997, Yang, Chernenko et al. 1998) with a fourth isoform of 29 kDa also reported (Yang, Chernenko et al. 1998). Cellular proteins are typically generated by cap-dependent translation from an AUG initiation codon within a Kozak consensus sequence (Packham, Brimmell et al. 1997). However, the Bag-1L isoform is initiated from an alternative CUG (Lys) initiation codon (Packham, Brimmell et al. 1997), while Bag-1M and Bag-1S are translated from in-frame downstream AUG (Met) codons (Packham, Brimmell et al. 1997, Yang, Chernenko et al. 1998). In addition to cap-dependent translation, Bag-1S is predominantly translated from internal ribosome entry sequence-dependent translation (Coldwell, deSchoolmeester et al. 2001), a cap-independent mechanism (Brimmell, Burns et al. 1999), making it the most abundant isoform in breast tissue and cell lines (Brimmell, Burns et al. 1999).

1.5.2 Bag-1 structure

The structure of the three major isoforms of Bag-1 is summarised in Figure 15b. The shared BAG domain is formed of three antiparallel α-helices (Briknarova, Takayama et al. 2001) and is responsible for interactions with Hsc-70/Hsp-70 and Raf-1 at an overlapping site, onto which Hsc-70/Hsp-70 and Raf-1 competitively bind (Song, Takeda et al. 2001). Helices two and three of the domain contact the ATPase domain of Hsc-70/Hsp-70 (Sondermann, Scheufler et al. 2001). The ubiquitin-like domain mediates associations with the proteasome complex (Luders, Demand et al. 2000, Alberti, Demand et al. 2002). The function of the N-terminal repeat region rich in acidic amino acid residues is not clearly defined, but may be involved in regulation of the glucocorticoid receptor (Briknarova, Takayama et al. 2001) and also contains a consensus recognition site for phosphorylation by creatine kinase 2 (Takayama, Sato et al. 1995). The unique N-terminal extension of Bag-1L contains an N-terminal nuclear localisation sequence which makes it a

predominantly nuclear isoform (Brimmell, Burns et al. 1999), while Bag-1S is predominantly cytoplasmic and Bag-1M localises to both compartments. The cellular localisation of each isoform can depend on the state of the cells, with cellular stress inducing translocation of the isoforms to different cellular compartments (Townsend, Cutress et al. 2003).

1.5.3 Cellular functions and interaction partners of Bag-1

Bag-1 influences a diverse range of cellular processes, summarised in Figure 15c. For the purposes of this work I will briefly cover the roles of Bag-1 in protein folding and degradation, transcription, proliferation and cell survival and, where relevant, will highlight any isoform specific functions.

1.5.3.1 Protein folding and degradation

As mentioned, Bag-1 interacts with Hsc-70/Hsp-70. The ubiquitous Hsc-70/Hsp-70 chaperone family are involved in a variety of cellular processes through their regulation of protein folding, maturation and turnover (Hohfeld and Jentsch 1997, Bukau, Weissman et al. 2006). For simplicity I will refer to this family as Hsc-70 from now on. The Hsc-70 protein functions to prevent aggregation of incompletely folded proteins by binding to exposed hydrophobic amino acid residues.

Hsc-70 has three major functional domains: an ATPase domain, a substrate binding domain and a C-terminal domain. The ATPase activity is weak and therefore Hsc-70 is in an ATP-bound state when not interacting with a substrate. This ATP-bound state opens up the C-terminal domain, which acts as a ‘lid’ for the substrate binding domain, allowing substrate to readily bind and release (Figure 16). The presence of peptide in the binding domain stimulates the ATPase activity of Hsc-70, activity which is enhanced further by J-domain co-chaperones, and leads to ATP hydrolysis to ADP. In the ADP-bound state the C-terminal domain ‘lid’ closes down over the substrate domain and the substrate becomes tightly bound. Nucleotide exchange factors stimulate the exchange of ADP for ATP and subsequent release of the substrate. As a nucleotide exchange factor, Bag-1 can regulate Hsc-70-dependent refolding of proteins (Hohfeld and Jentsch 1997, Sondermann, Scheufler et al. 2001). Bag-1S and Bag-1M have been shown to both stimulate or inhibit folding depending on the experimental conditions examined (Gebauer, Zeiner et al. 1997, Takayama, Bimston et al. 1997, Zeiner, Gebauer et al. 1997, Luders, Demand et al. 2000, Nollen, Brunsting et al. 2000, Gassler, Wiederkehr et al. 2001). In intact cells, Bag-1L had no effect on refolding assays (Nollen, Brunsting et al. 2000), possibly because of its nuclear localisation while the substrate used in this protein folding assay was cytoplasmic.

In addition to its influences on protein folding, Bag-1 has also been linked to protein degradation through its ubiquitin-like domain (Froesch, Takayama et al. 1998). Ubiquitination of proteins targets them for proteasomal degradation via the proteasome and is a highly conserved system across eukaryotes (Cutress, Townsend et al. 2003). The ubiquitin-like domain of Bag-1 mediates interactions with the proteasome but does not trigger rapid turnover of the protein which, when combined with the observation that Bag-1 can form trimeric complexes with Hsc-70 and the protesome, suggests that Bag-1 may form a bridge linking Hsc-70 directly with the proteosome (Townsend, Cutress et al. 2003). Bag-1 has also been shown to interact with two E3-ubiquitin ligases, Siah-1A (Wang, Takayama et al. 1996) and CHIP (Song, Takeda et al. 2001), which are involved in ubiquitination of substrates. These interactions do not alter the degradation of Bag-1, and further support a role of Bag-1 in proteasomal degradation of target proteins.

1.5.3.2 Transcription

Bag-1 influences transcription through interactions with members of the nuclear hormone receptor family (Takayama, Sato et al. 1995, Townsend, Cutress et al. 2003, Sharp, Crabb et al. 2004), which is a collection of ligand-dependent transcription factors that control the expression of genes regulating cellular processes that include proliferation, differentiation and apoptosis (Tang, Shehata et al. 1999). Bag-1 can negatively or positively regulate nuclear hormone receptors with specific isoforms modulating particular nuclear hormone receptors, summarised in Table 2. For example, only the Bag-1L isoform enhances androgen receptor (Froesch, Takayama et al. 1998) and ER function (Cutress, Townsend et al. 2003).

1.5.3.3 Proliferation

Bag-1 is also implicated in the mitogen activated protein kinase (MAPK) signalling cascade. This pathway, summarised in Figure 17, is traditionally activated by the GTPase Ras as a result of receptor tyrosine kinase activation (Avruch, Khokhlatchev et al. 2001). In the GTP-bound active state, Ras activates Raf-1 which leads to a phosphorylation and activation cascade which induces growth and proliferation signals. Bag-1 provides an alternative, Ras-independent mechanism for the activation of Raf-1, binding to the catalytic domain of Raf-1 and leading to its phosphorylation and activation (Wang, Takayama et al. 1996, Song, Takeda et al. 2001). Consistent with Bag-1 activation of Raf-1, Bag-1 overexpression is associated with activation of MAPK pathways (Kermer, Krajewska et al. 2002, Anderson, Sutherland et al. 2010).

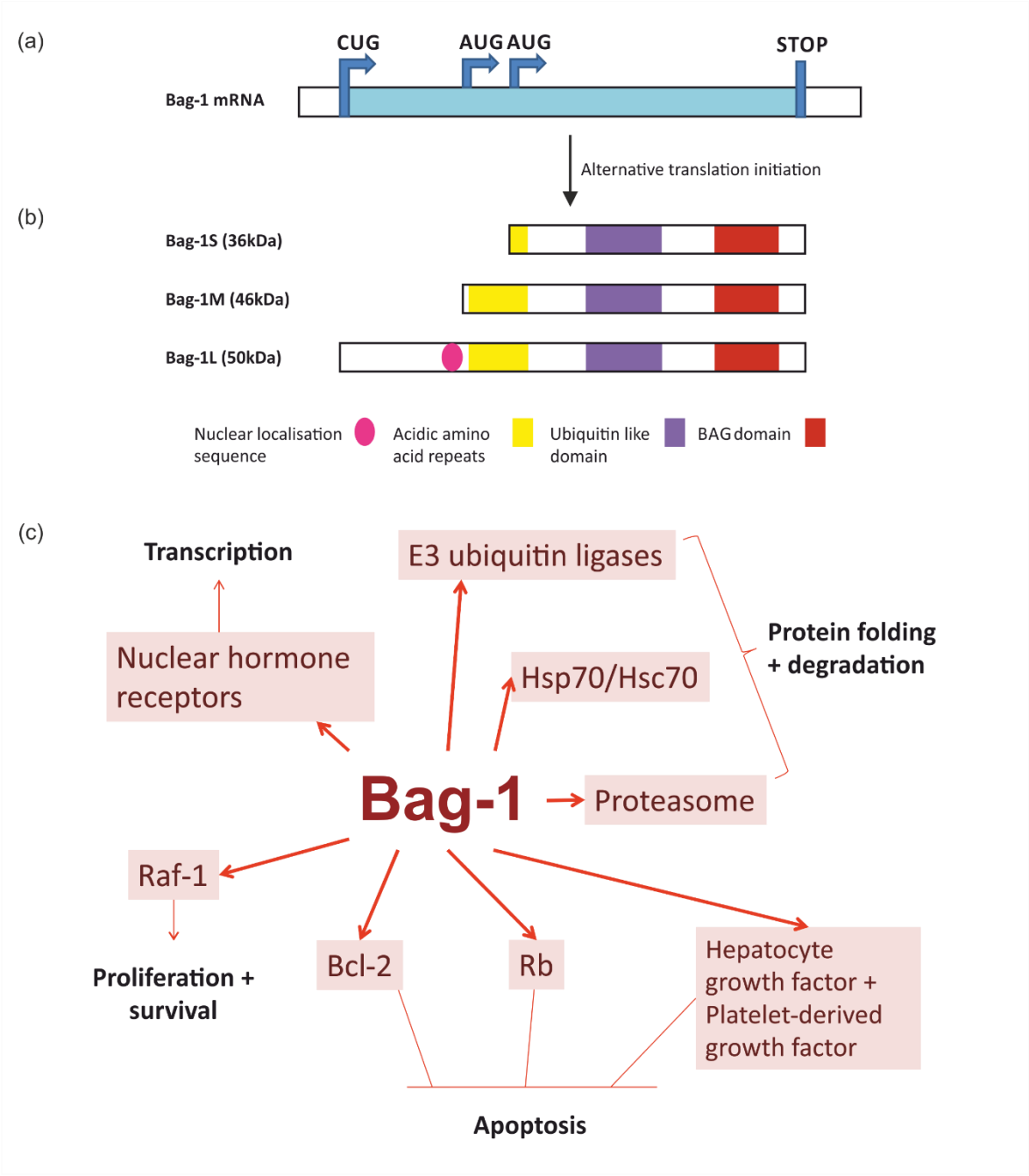

Figure 15 Bag-1 regulates a diverse range of cellular functions

(a) The three isoforms of Bag-1, Bag-1S (36 kDa), Bag-1M (46 kDa) and Bag-1L (50 kDa) are formed from alternative translation initiation from a single mRNA molecule. Bag-1L is initiated at an alternative CUG codon while Bag-1M and Bag-1L are translated from downstream inframe AUG codons. (b) Representative structure of each of the isoforms showing the functional domains. (c) A diagram of Bag-1 interactions and their influence on cellular processes. Adapted from Figure 1 and Table 1 of (Sharp, Crabb et al. 2004).

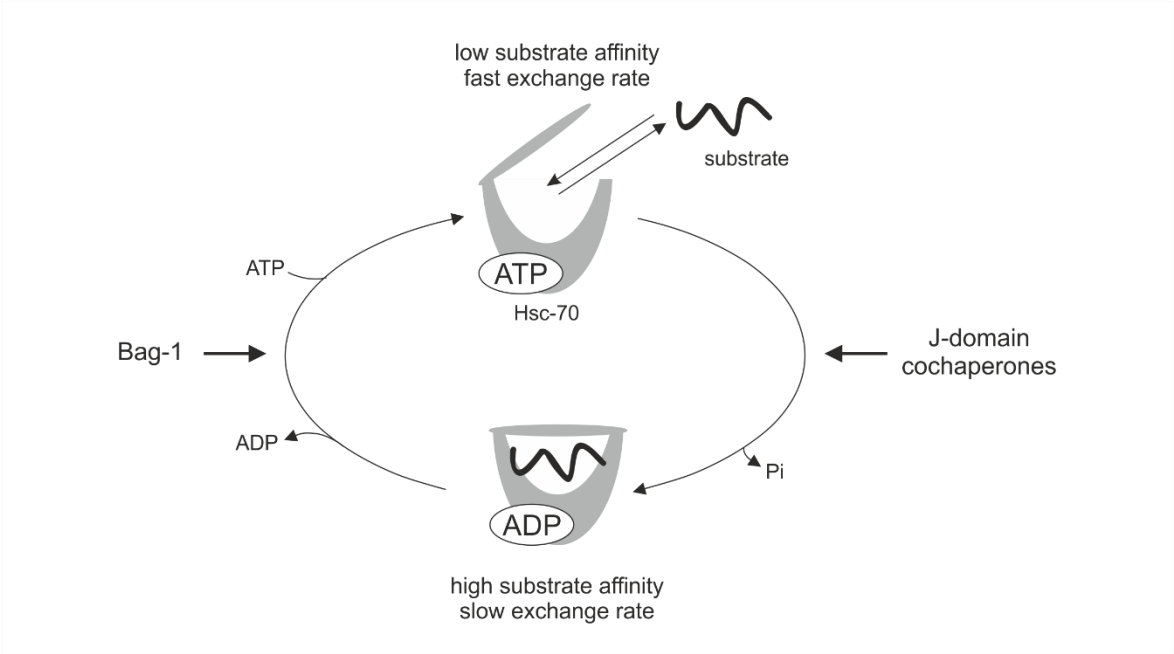

Figure 16 The Hsc-70 chaperone cycle

In an ATP-bound state the 'lid' of Hsc-70 is open allowing substrate to bind, but with low affinity. ATP hydrolysis is catalysed by J-domain co-chaperones causing the lid to close off the substrate-binding pocket. Nucleotide exchange is stimulated by Bag-1 allowing refolding and release of substrate. Adapted from Figure 6 of (Li, Hartl et al. 2013).

1.5.3.4 Cell survival

Following the original identification of Bag-1 as an anti-apoptotic protein (Takayama, Sato et al. 1995), Bag-1 has been shown to suppress apoptosis from a variety of stimuli summarised in Table 3. Bag-1 can cooperate with Bcl-2 to enhance Bcl-2 anti-apoptotic activity (Takayama, Sato et al. 1995), and it is possible that many of the effects of Bag-1 on cell survival are a consequence of its interaction with Bcl-2. Bcl-2 is an anti-apoptotic protein that is part of the Bcl-2 superfamily of apoptotic regulators which are discussed in more detail in 1.6 The Bcl-2 Superfamily. Although Bag-1 is predominantly anti-apoptotic, it should be noted that some pro-apoptotic effects of Bag-1 overexpression on cell survival have been described (Yang, Hao et al. 2000).

Table 2 Bag-1-mediated effects on nuclear hormone receptor activity

Adapted from Table 2 of (Sharp, Crabb et al. 2004).

Receptor	**Effect of Bag-1 overexpression**	**Isoform**	**Reference(s)**
Androgen receptor	Activates	Bag-1L (not Bag-1S or Bag-1M)	(Froesch, Takayama et al. 1998) (Shatkina, Mink et al. 2003)
Glucocorticoid receptor	Inhibits	Bag-1M, Bag-1L	(Kullmann, Schneikert et al. 1998) (Cutress, Townsend et al. 2001)
Mineralocorticoid receptor	No effect	Bag-1M	(Cutress, Townsend et al. 2003)
Oestrogen receptor	Activates	Bag-1L (not Bag-1S or Bag-1M)	(Cutress, Townsend et al. 2003)
Retinoic acid receptor	Inhibits	Bag-1S	(Liu, Takayama et al. 1998)
Retinoic X receptor	No effect	Bag-1S	(Liu, Takayama et al. 1998)
Thyroid hormone receptor	Inhibits	Bag-1S	(Liu, Takayama et al. 1998)
Vitamin D receptor	Activates	Bag-1L	(Guzey, Takayama et al. 2000)
	Inhibits	Bag-1L	(Witcher, Yang et al. 2001)

1.5.4 The expression and clinical significance of Bag-1 in breast cancer

Based on the interaction of Bag-1 with a number of cell pathways known to influence cell transformation, there has been considerable interest in the significance of Bag-1 in human cancer. Multiple studies have assessed the expression and the clinical significance of Bag-1 in breast cancer, the findings from which are summarised below.

Bag-1 is expressed in normal breast tissue but if frequently seen upregulated in breast cancer (Brimmell, Burns et al. 1999, Tang, Shehata et al. 1999, Turner, Krajewski et al. 2001, Nadler, Camp et al. 2008) and, importantly for this study, changes in Bag-1 expression are detected in benign lesions and in ductal carcinoma *in situ* (Brimmell, Burns et al. 1999); the high frequency of Bag-1 overexpression and the presence of overexpression in early breast cancer may implicate this protein in driving breast cancer development.

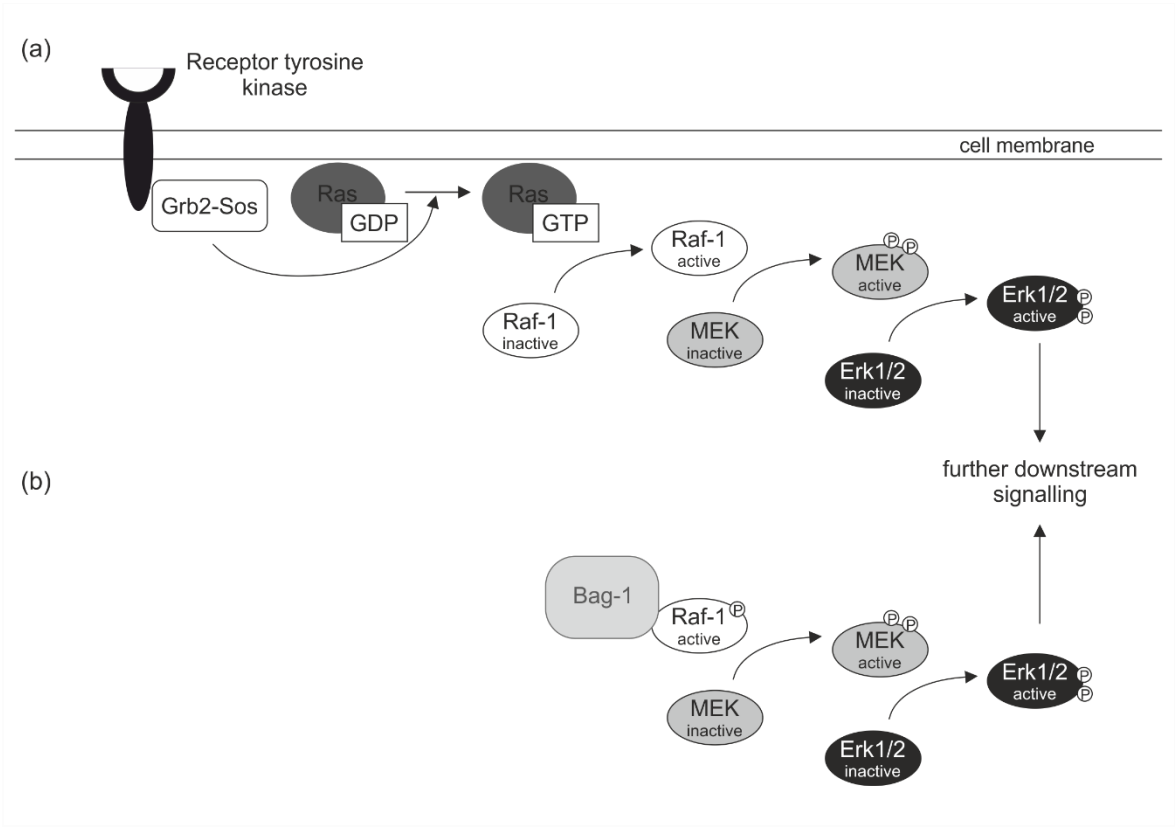

Figure 17 The MAPK signalling cascade

(a) The MAPK signalling cascade is induced following receptor tyrosine kinase activation in a Ras-dependent mechanism. (b) Bag-1 can activate Raf-1 through a Ras-independent mechanism, proposed to be through inducing auto-phosphorylation, and induce MAPK signalling. Adapted from Figure 2 of (Orton, Sturm et al. 2005).

Table 3 The role of Bag-1 in cell survival

Summary of the studies showing the anti-apoptotic properties of Bag-1. Adapted from (Cutress 2003).

Stress	**Isoform**	**Comments**	**Reference(s)**
All-trans retinoic acid	Human Bag-1S	MCF-7 and ZR-75-1 breast cancer cell lines	(Liu, Takayama et al. 1998)
Anoikis	Human Bag-1	MCF-10A	(Anderson, Sutherland et al. 2010)
	Human Bag-1S, Bag-1L	ZR-75-1	(Kudoh, Knee et al. 2002)
	Mouse Bag-1S	Gastric cancer cell line MKN74	(Yawata, Adachi et al. 1998)
Chemotherapy agents (cisplatin, paclitaxel, doxorubicin)	Human Bag-1S, 1M, 1L	C33A human cervical carcinoma cell line	(Chen, Xiong et al. 2002)
Growth factor withdrawal	Mouse Bag-1S	Mouse lymphocyte line BaF3	(Clevenger, Thickman et al. 1997)
	Mouse Bag-1S	PC12 cell line (neural cells from rat)	(Schulz, Bremen et al. 1997)
Heat shock	Human Bag-1L	3T3 fibroblasts	(Niyaz, Zeiner et al. 2001)
	Mouse Bag-1S	GM701 immortalised human fibroblasts cells but not 293 human kidney epithelial cells	(Takayama, Bimston et al. 1997)
	Human Bag-1M	DU145 prostate cancer cell line	(Zeiner, Niyaz et al. 1999)
Serum withdrawal	Mouse Bag-1S	Mesencephalic progenitor cell line CSM14.1 (neuronal)	(Kermer, Krajewska et al. 2002)
	Human Bag-1S, Bag-1L	ZR-75-1	(Kudoh, Knee et al. 2002)
	Mouse Bag-1S	Murine B16-BL6 melanoma cells	(Takaoka, Adachi et al. 1997)
	Mouse Bag-1S	Gastric cancer cell line MKN74	(Yawata, Adachi et al. 1998)
Staurosporine (ATP-competitive kinase inhibitor)	Human Bag-1S, 1M, 1L	C33A human cervical carcinoma cell line	(Chen, Xiong et al. 2002)
	Mouse Bag-1S	Jurkat T cells (human) 3T3 mouse fibroblasts	(Takayama, Sato et al. 1995)

Studies assessing the significance of Bag-1 overexpression in breast cancer reported divergent results, with overexpression of Bag-1 correlating with both improved and poor prognosis depending on the cohort and parameters examined (Tang, Shehata et al. 1999, Cutress, Townsend et al. 2001, Turner, Krajewski et al. 2001, Townsend, Dublin et al. 2002, Townsend, Cutress et al. 2003, Nadler, Camp et al. 2008, Athanassiadou, Grapsa et al. 2009). In addition, while some studies found an association between Bag-1 expression and ER (Brimmell, Burns et al. 1999, Cutress, Townsend et al. 2003, Nadler, Camp et al. 2008) and PR status (Cutress, Townsend et al. 2003, Nadler, Camp et al. 2008), other studies show no association (Tang, Shehata et al. 1999, Turner, Krajewski et al. 2001). These discrepancies may be explained, at least in part, by whether disease subtype, subcellular distribution of Bag-1, hormone receptor status and the treatment course administered was considered in analysis. In a cohort of 138 breast cancer patients treated with hormonal therapy a significant correlation between Bag-1 expression, ER and PR status was reported and nuclear, but not cytoplasmic, Bag-1 expression was correlated with improved survival (Cutress, Townsend et al. 2003). It may seem paradoxical that an anti-apoptotic protein is associated with improved responsiveness to hormonal therapy but in the case of Bag-1 this can be explained based on its role as a regulator of ER transcriptional activity (Cutress, Townsend et al. 2003, Millar, Anderson et al. 2009) and the efficacy of treatments targeting the ER.

Despite these discrepancies, in the clinical setting Bag-1 mRNA is a prognostic biomarker included within the Oncotype DX (Paik, Shak et al. 2004) and PAM50 (Parker, Mullins et al. 2009) multigene assays and high nuclear Bag-1 immunoreactivity is an independent predictor of outcome and enhances the predictive power of the IHC4 prognostic test (Afentakis, Dowsett et al. 2013). These tests are utilised to examine the risk of recurrence and to select patients who will benefit from treatment.

1.5.4.1 The role of Bag-1 in a breast cancer mouse model

Kudoh *et al.* used the ZR-75-1 breast cancer cell line in a mouse xenograft model to provide evidence that Bag-1 has a role in breast cancer growth and survival (Kudoh, Knee et al. 2002). Overexpression of Bag-1S or Bag-1L in ZR-75-1 cells injected into the mammary fat pads of female nude mice leads to a significant increase in tumour size when compared to control transfected conditions. Use of a dominant-negative deletion mutant reduced tumour size compared to controls demonstrating that endogenous Bag-1 is important in this setting and highlighting that the protective effect of Bag-1 overexpression is not an artefact of overexpression.

1.6 The Bcl-2 Superfamily

The Bcl-2 superfamily is a family of apoptotic regulators which all contain at least one Bcl-2 homology (BH) domain, regions of sequence homology of which four have been identified (BH1-4) (Petros, Olejniczak et al. 2004). Divided into anti-apoptotic and pro-apoptotic proteins, the balance of these proteins determines cell fate (Figure 18).

1.6.1 Bcl-2

Several members of the anti-apoptotic class of Bcl-2 family members, including Bcl-2, contain all four BH domains. Localised on the outer membrane of the mitochondria, these anti-apoptotic family members inhibit the activity of pro-apoptotic family members such as Bax, preventing cytochrome c release from the mitochondria and subsequent caspase activation and apoptosis (Figure 18a).

1.6.2 Bim

BH3-only proteins, including Bim, form a subclass of the pro-apoptotic proteins whose common BH3 domain is required for apoptosis initiation (Puthalakath and Strasser 2002). Two mechanisms of action are proposed for Bcl-2 interacting mediator of cell death (Bim)-induced apoptosis (Figure 18b). Firstly, Bim can interact with anti-apoptotic members of the Bcl-2 family via the BH3 domain (O'Connor, Strasser et al. 1998), sequestering them from the pro-apoptotic proteins Bak and Bax which become indirectly activated (Willis, Fletcher et al. 2007). Alternatively, Bim can interact with pro-apoptotic protein members directly inducing an activating conformational change which enhances apoptosis (Marani, Tenev et al. 2002).

Relevant to this project, BimEL, one of three major isoforms formed from alternative translation of the Bim mRNA (O'Connor, Strasser et al. 1998), can be regulated post-translationally by phosphorylation; Erk-dependent phosphorylation at Ser-69 promotes Bim ubiquitination and proteasomal degradation (Ley, Balmanno et al. 2003, Luciano, Jacquel et al. 2003, Ley, Ewings et al. 2004).

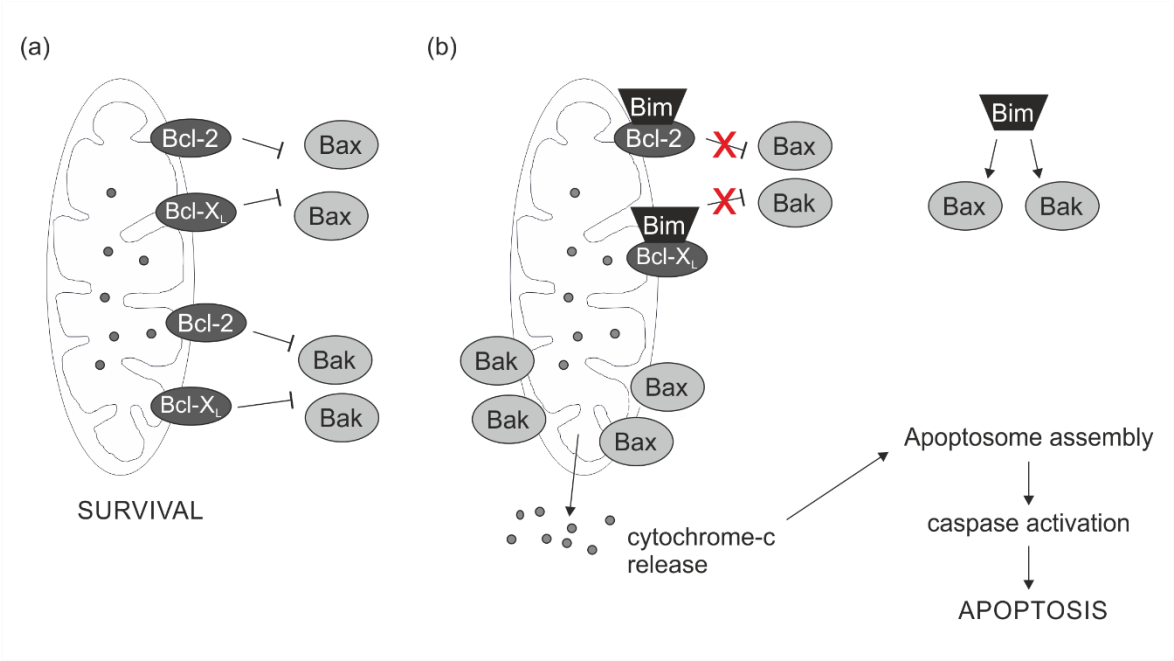

Figure 18 The balance of pro- and anti- apoptotic Bcl-2 family members determines cell fate

(a) In the absence of cellular stress the anti-apoptotic family members (Bcl-2, Bcl-X_L), localised at the outer mitochondrial membrane, inhibit the pro-apoptotic family members (Bax, Bak). (b) Following cellular stress, upregulation of BH3-only family members (Bim) leads to activation of pro-apoptotic family members. Pro-apoptotic members insert into the outer mitochondrial membrane and promote pore formation, leading to the release of cytochrome c and induction of apoptosis. BH3-only family members can activate pro-apoptotic proteins by direct binding and activation or by sequestering of anti-apoptotic family members. Adapted from Figure 1, (Lei and Davis 2003).

1.7 Human Epidermal Growth Factor Receptor 2 (HER2)

HER2 is a member of the epidermal growth factor family of receptor tyrosine kinases (ErbB). This family consists of four structurally related members: the epidermal growth factor receptor (EGFR), HER2, HER3 and HER4. With a central role in the tumourigenesis of many solid tumours, the ErbBs have essential roles in regulation of cell proliferation, survival, differentiation and cell motility (Wieduwilt and Moasser 2008).

1.7.1 Activation of the ErbB family and subsequent downstream signalling

Each receptor exists as a transmembrane protein with an extracellular ligand-binding domain, an intracellular tyrosine kinase domain and C-terminal tyrosine phosphorylation sites. ErbBs exist as monomers in the absence of ligand and upon ligand binding undergo homo- or hetero-dimerisation, inducing a conformation which activates the kinase domain and favours cross-phosphorylation of the cytoplasmic domain.

SH2-domain proteins dock onto tyrosine phosphorylation sites on the receptors via the SH2 domain (Figure 19a). These proteins either directly induce activation of further signalling molecules (PLCγ) or serve as adaptor molecules to recruit additional proteins (Grb2, Gab1). PLCγ leads to activation of protein kinase C (Figure 19a), while Grb2 leads to MAPK activation (described previously, Figure 17) and Gab1 leads to Akt (Figure 19a).

There are multiple growth factor ligands of the ErbB family, including EGF as the primary ligand for the EGFR, but no direct ligands have been identified for HER2 (Olayioye, Neve et al. 2000). It is thought to function primarily in hetero-dimerisation with other ErbB members (Figure 19b), inducing cross-phosphorylation, and HER2 overexpression increases the sensitivity of cells to growth factor signalling. HER2 can also homo-dimerise in the absence of ligand to induce cross-phosphorylation and downstream signalling.

1.7.2 The expression and clinical significance of HER2 in breast cancer

As mentioned previously (1.1.3 Breast cancer) the *erbB2* gene is amplified and overexpressed in human breast cancer and marks a subset of the disease that is associated with an aggressive disease (Kraus, Popescu et al. 1987, Slamon, Clark et al. 1987, Varley, Swallow et al. 1987, Berger, Locher et al. 1988, Guerin, Gabillot et al. 1989). Since the development of HER2-targetted therapies, the prognosis of patients with this subset of breast cancer has vastly improved (Santa-Maria, Nye et al. 2016). Overexpression enhances protein kinase C, MAPK and Akt signalling, which all contribute to tumourigenesis by enhancing growth and proliferation, inhibiting apoptosis and influencing cellular metabolism to promote transformation.

1.8 Detachment from the Extracellular Matrix

I will now describe the current understanding of the cellular signalling pathways induced following ECM-detachment in MCF-10A cells.

Anchorage-dependent cells undergo a traditional apoptosis program termed anoikis upon detachment from the ECM due to a lack of signalling through transmembrane receptors termed integrins (Meredith, Fazeli et al. 1993, Frisch and Francis 1994). In attached MCF-10A cells integrin engagement leads to EGFR stabilisation and downstream MAPK signalling (Figure 17); activated Erk phosphorylates the pro-apoptotic protein Bim promoting its degradation, and cells survive (Biswas and Greene 2002, Ley, Balmanno et al. 2003, Luciano, Jacquel et al. 2003, Ley, Ewings et al. 2004). In ECM-detached cells the lack of integrin engagement results in EGFR ubiquitination and subsequent degradation (Levkowitz, Waterman et al. 1999, Reginato, Mills et al. 2003). A lack of Erk signalling leads to upregulation of Bim which localises to the mitochondria where it

promotes apoptosis through its association and consequential inhibition of the anti-apoptotic protein Bcl-X_L (Figure 20a) (Reginato, Mills et al. 2003).

Bim-regulated anoikis drives cell death in luminal cells of MCF-10A acini (Reginato, Mills et al. 2003), supporting the hypothesis that luminal apoptosis in this model is driven by ECM-detachment. Knockdown of Bim, activation of Erk signalling or overexpression of Bcl-2 or Bcl-X_L can protect from anoikis and delay the onset of luminal clearing (Debnath, Mills et al. 2002, Reginato, Mills et al. 2005). However, the observation that anoikis suppression only delays the onset of luminal clearing implicates an additional pathway is acting to drive cell death in this setting.

Work from Schafer *et al.* has shown a metabolic defect acts alongside Bim-regulated anoikis to drive apoptosis in ECM-detached MCF-10A and attenuation of both of these pathways combined can fully prevent luminal clearing in acini (Schafer, Grassian et al. 2009). This metabolic stress relates to a defect in glucose uptake which limits flux through the PPP, limiting regeneration of the reducing power NADPH from $NADP^+$ and leading to an accumulation of ROS and cell death (Figure 20a).

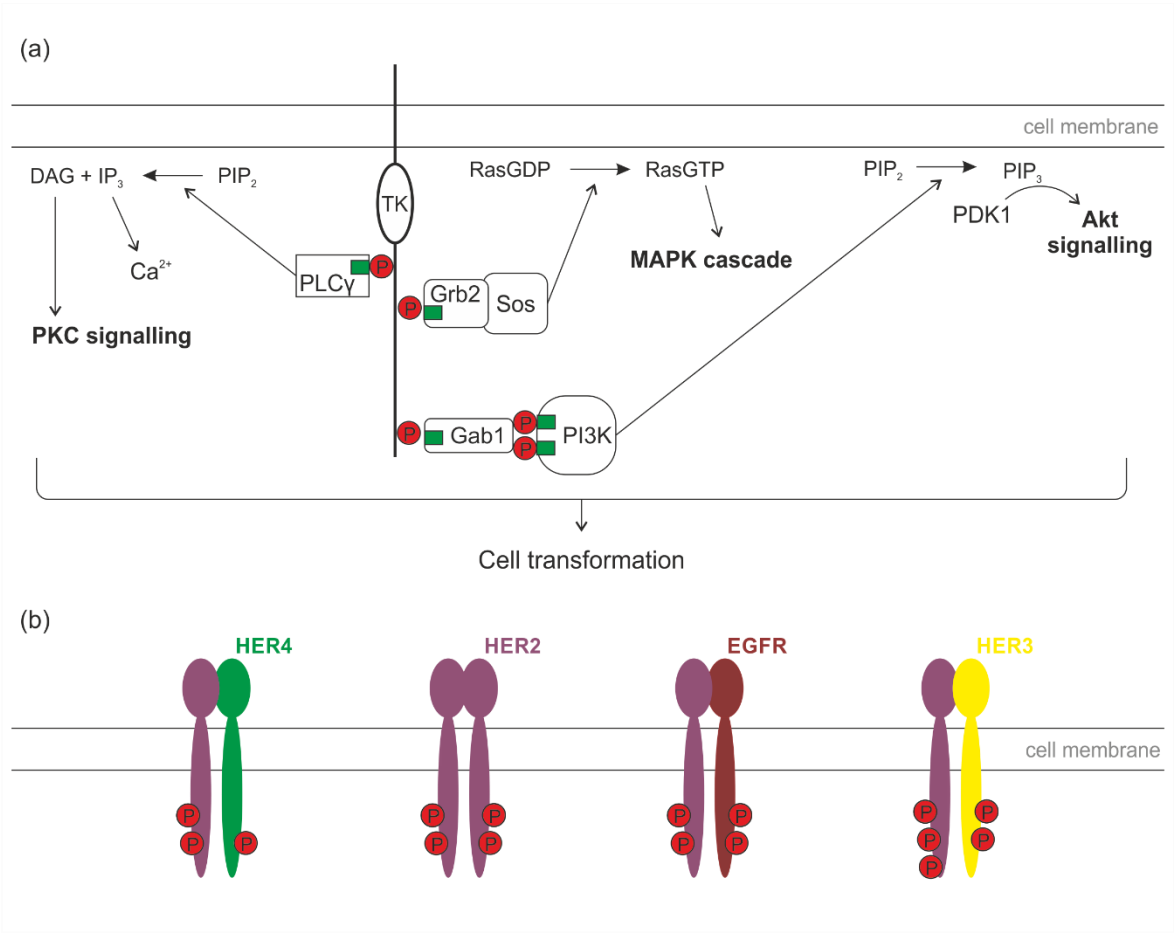

Figure 19 ErbB family signalling

(a) Summary schematic of ErbB family signalling. Following ErbB receptor dimerisation and cross-phosphorylation, phosphorylated tyrosines (Ⓟ) serve as docking sites for SH2-domain (green boxes) proteins which leads to further downstream signalling and activation of the protein kinase C (PKC), MAPK and Akt signalling pathways. (b) HER2 can homo-or hetero- dimerise with other members of the erbB family to induce cross-phosphorylation. DAG = diacylglycerol; IP_3 = inositol triphosphate; PDK1 = protein-dependent kinase I; PI3K = phosphatidylinositol-3-kinase; PIP_2 = phosphatidylinositol 4,5-bisphosphate. Adapted from Figure 1 of (Fornaro, Lucchesi et al. 2011)

1.9 Outline of Study and Aims

In this thesis I address research questions relating to the role of Bag-1 and HER2 in luminal cell survival in the MCF-10A model of the breast. Overexpression of either of these genes in MCF-10A results in filled structures (Muthuswamy, Li et al. 2001, Anderson, Sutherland et al. 2010) and the current understanding of how these proteins promote luminal cell survival is summarised in Figure 20. HER2 overexpression leads to EGFR stabilisation and downstream signalling which can attenuate both Bim upregulation and the metabolic defect associated with detachment through Erk signalling and PI3K signalling respectively (Figure 20b) (Reginato, Mills et al. 2005, Schafer, Grassian et al. 2009). As mentioned previously, Bcl-2 overexpression delays the onset of luminal clearing unless combined with an antioxidant or antioxidant enzyme where it can fully prevent luminal clearing (Figure 20c) (Schafer, Grassian et al. 2009, Davison, Durbin et al. 2013). However overexpression of the anti-apoptotic protein Bag-1 alone can fully attenuate clearing. While it has been shown that Bag-1 attenuates Bim upregulation through Erk-dependent phosphorylation (Anderson, Sutherland et al. 2010), the mechanism by which Bag-1 can overcome the metabolic defects associated with detachment remain unknown (Figure 20d).

This research set out to examine:

- How Bag-1 influences luminal clearing, and the role of individual Bag-1 isoforms in this setting.
- How metabolism influences cell survival in ECM-detached cells.
- The role of HER2 in driving the metabolic changes that support development of filled, atypical MCF-10A acini.

To address these questions the following aims were set:

- Produce HER2- and Bag-1- overexpressing MCF-10A and to characterise their behaviour in 3D.
- To determine the role of individual isoforms of Bag-1 in acinar morphogenesis.
- To investigate the role of glycolysis in HER2-overexpressing ECM-detached cells.
- To examine the phenotypic consequences of metabolic inhibition of non-transformed and transformed MCF-10A.
- To investigate the effect of CtBP overexpression on MCF-10A acini.
- To apply key findings to a second model of the breast (HMEC acini).

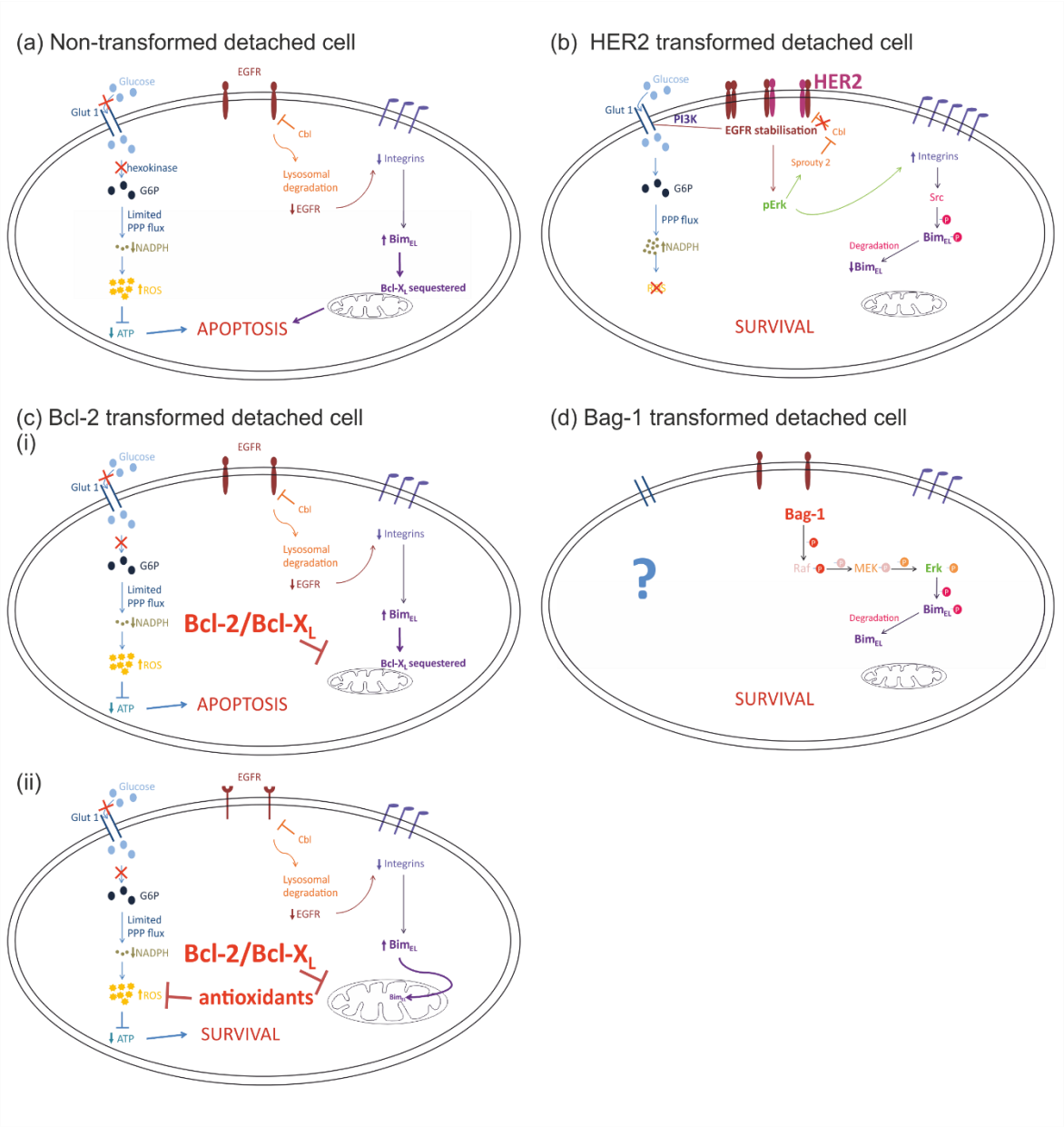

Figure 20 Oncogenes and anti-apoptotic signals regulate ECM-detachment via different mechanisms

(a) Summary of the anoikis pathway and the metabolic defects associated with detachment. (b) HER2 overexpression promotes cell survival upon detachment through stabilisation of the EGFR which inhibits Bim and the production of reactive oxygen species (ROS). (c)(i) Bcl-2/Bcl-X_L overexpression can block Bim-driven anoikis but is insufficient to fully prevent cell death due to metabolic defects unless combined with another signal (ii). (d) Bag-1 targets Bim for degradation through ERK signalling but the mechanism by which Bag-1 overcomes metabolic defects is unknown. G6P = glucose-6-phosphate; PPP = pentose phosphate pathway.

Chapter 2: Methods

2.1 DNA cloning

2.1.1 General cloning techniques

Oligonucleotides were purchased from Eurofins MWG Operon (Eurofins Genomics, Anzinger Str. 7a, Germany, Europe). Plasmids were grown in competent XL-1 Blue cells. XL-1 Blue cells were transformed with 50 ng DNA by heat shock at 42 °C for 45 s. Bacteria was grown on selective LB agar and in LB broth with 100 µg/ml ampicillin (Fisher Bioreagents, Loughborough, UK). For cloning, plasmids were isolated from LB cultures using GeneJET Plasmid Miniprep Kit (Thermo Scientific, Loughborough, UK) according to manufacturer's instructions. Plasmid preparations used for retroviral infection were isolated from LB cultures using QIAfilter^{R} Plasmid Midi Kit (Qiagen, Manchester, UK) according to manufacturer's instructions. Plasmid concentrations were determined using a NanoDrop 1000 spectrophotometer (Thermo Scientific). Before use of plasmids in retroviral infection, plasmid sequences were confirmed by Sanger sequencing (outsourced to Source BioScience LifeSciences, Nottingham, UK) using sequencing primers pBabe3' and pBabe5' extra (Table 4). Sequencing files were imported into GENtle and aligned to the appropriate DNA vector map using the 'Sequencing assistant' tool to confirm vector sequences were as intended.

Gel electrophoresis was carried out on 0.6% agarose gels with RedSafe^{TM} Nucleic Acid Staining solution (iNtRON Biotechnology, Korea) in TAE buffer. DNA was loaded with 5 µl loading dye (30% glycerol in TAE with bromophenolblue). A 1 kb DNA ladder was used. DNA gels were visualised using a GelDoc-It^{TM} Imaging System (UVP, Cambridge, UK). DNA was extracted from agarose gels using QIAquick^{R} Gel Extraction Kit (Qiagen) according to manufacturer's instructions.

2.1.2 Cloning of Bag-1 into pBABEneo

The pGEK-2T-Bag-1 vector was kindly provided by Manos Papadakis; this bacterial expression vector containing the human Bag-1 cDNA with a modification at the 5'-terminus of the Bag-1 coding region that removes the mammalian Bag-1L start site. The Bag-1 cDNA was cloned out of pGEX-2T-Bag-1 by a double digest using BamHI (Promega, Southampton, UK) and EcoRI (Promega). BamHI-EcoRI double digests were carried out in buffer E (Promega) with 1X BSA at 37 °C for 1-4 h. Following gel electrophoresis of the digest product, the Bag-1 insert (expected size 1041 bp) was extracted from the gel. The pBABEneo plasmid was double digested using BamHI and EcoRI and the corresponding cut plasmid (expected size 5330 bp) excised from a gel. The

concentration of the extracted products was estimated by running the extracted product on a gel against a gradient of known DNA concentrations. Ligation of the Bag-1 insert into pBABEneo was carried out at a 3:1 insert:vector ratio with T4 DNA ligase (Promega) and T4 DNA ligase buffer (Promega) and incubated overnight at 4 °C. The ligation product was transformed into XL-1 blue. A BamHI-EcoRI double digest was used to verify the presence of an insert, which was subsequently analysed by Sanger sequencing. The product was denoted pBABEneo-Bag-1SM.

2.1.3 Site-directed mutagenesis to generate Bag-1 variants

The principles of QuikChange® site-directed mutagenesis (Stratagene, California, USA) was utilised to generate mutants, with components purchased individually from Promega. Briefly, 50ng of target DNA was incubated with 125 ng primers, 10mM dNTPs, 1X Pfu buffer and 1 µl Pfu in 50 µl total volume. The PCR program is shown in Table 5. The PCR product was digested with Dpn1 for 1 h at 37 °C to remove methylated bacterial DNA and was transformed into XL-1 blue.

The pBABEneo-Bag-1L vector was generated from the pBABEneo-Bag1SM vector via site-directed mutagenesis using primers Bag-1L F2 and Bag-1L B2 (Table 4). Oligonucleotides were synthesised by eurofins MWG operon (85560 Ebersberg, Germany). Mutagenesis removes the BamHI site from the vector allowing colonies to be screened for successful mutagenesis. A double digest with BamHI and EcoRI causes a single cut in the pBABEneo-Bag-1L vector while removing the Bag-1 insert from the original target pBABEneo-Bag-1SM vector. Sequencing was used to confirm.

The pBABEneo-Bag1SM H3B vector and pBABEneo-Bag1L H3B vector were generated using the pBABEneo-Bag1SM and pBABEneo-Bag1L vectors respectively as a target. Primers H3B (F) and H3B (B) were used (Table 4) and successful mutagenesis confirmed by sequencing.

2.1.4 Vector design using GENTLE

The software package GENtle version 1.9.4 (Manske 2006) was utilised for the visualisation and design of DNA vector maps. The pBABEneo DNA sequence was downloaded from AddGene and stored as a sequence. The cDNA sequence of human Bag-1 (NCBI Reference Sequence: NM_004323) was downloaded from NCBI and stored as a sequence. I had information ascertaining to how the Bag-1 sequence in the provided pGEX-2T-Bag-1 vector was altered during the cloning procedure of this vector. Using the ‘Edit sequence’ function in GENtle, the necessary changes to the DNA sequence of the Bag-1 cDNA were made manually and stored as an edited transcript. The software recognises and highlights restriction enzyme sites on each vector map. The restriction enzymes BamHI and EcoRI were identified as flanking the Bag-1 insert in pGEX-2T-Bag-1 and also present in the multiple-cloning site of the target vector pBABEneo. The ‘Enzyme

Assistant' tool was utilised to identify the products of a BamHI-EcoRI double digest of pGEK-2T-Bag-1 and a copy of the Bag-1 insert DNA sequence saved as a sequence. Similarly, the linearised plasmid product of a BamHI-EcoRI double digest of pBABEneo was stored as a sequence. The 'Ligation' tool was used to generate a vector map of pBABEneo-Bag-1SM from these two sequences. The pBABEneo-Bag-1SM vector map was used as a basis to manually design primers Bag-1L F2 and Bag-1L B2 (Table 4). Using the 'Edit sequence' function, the necessary changes to the DNA sequence of pBABEneo-Bag-1SM were made manually to produce a DNA vector map for pBABEneo-Bag-1L.

2.2 Cell culture

2.2.1 Reagents and cell lines

Media components can be found detailed in Table 6 or in the relevant part of the text. Metabolic inhibitor details can be found in Table 9.

2.2.1.1 Cell lines

The MCF-10A cell line and the amphotropic Phoenix HEK-293 packaging cell line were obtained from ATCC (Middlesex, UK). Cryopreserved Clonetics™ Human Mammary Epithelial Cells (HMEC) were purchased from Lonza Walkersville, Inc (Walkersville, USA). MCF-10A clones pcDNA, Bag-1L/A and Bag-1L/B where produced by Hashim Sayed as previously described (Papadakis, Barker et al. 2016). All cell lines were routinely confirmed to be mycoplasma free.

2.2.2 Routine culture of cells

All 2D cell culture was carried out using Corning standard tissue culture treated plastic (Fisher Scientific, Loughborough, UK). Cell counts were carried out with a manual counter using a haemocytometer (Neubauer, Hawksley, Sussex, United Kingdom). Where a resistance marker is present, 2D cultures were routinely cultured for seven days in the appropriate antibiotic.

Table 4 Primer sequences for Sanger sequencing and site-directed mutagenesis (SDM)

Primer name	Function	Sequence (5' → 3')
Bag-1L F2	SDM	5'-CCTTCTCTAGGCGCCGGCCGCCATGGCTCAGCGCGGGGGG-3'
Bag-1L B2	SDM	5'-CCCCCCGCGCTGAGCCATGGCGGCCGGCGCCTAGAGAAGG-3'
H3B (F)	SDM	5'-GCCGAGTGTGCCACAGTGGAGGCGAACATCTGCCAG-3'
H3B (B)	SDM	5'-CCTGGCAGATGTTCGCCTCCACTGTGGCACACTCGG-3'
pBabe3'	Sequencing	5'-ACCCTAACTGACACACATTCC-3'
pBabe5' extra	Sequencing	5'-CCCTAAGCCTCCGCCTCC-3'

Table 5 Site-directed mutagenesis PCR program

Stage	Cycles	Temperature	Time
1	1	95 °C	30 s
2	18	95 °C	30 s
		55 °C	1 min
		68 °C	18 min
3	1	10 °C	5 min

MCF-10A cells were cultured and passaged as previously described (Debnath, Muthuswamy et al. 2003) in a 5% CO_2 humidified chamber at 37 °C. Unless otherwise stated, MCF-10A cultures were carried out in MCF-10A growth media (Table 6). Cells were subcultured at 80-90% confluence. Briefly, culture vessels were washed once with Hanks' Balanced Salt Solution (Life Technologies) (5 min, 37 °C) then incubated in 0.05% trypsin/5 mM EDTA solution (PAA) for 20-25 mins (37 °C). Following cell detachment, medium was added to neutralise trypsin; cells were split at a ratio of 1:3 to 1:10. For cryopreservation, cells (minimum 5 x 10^5 cells/vial) were resuspended in MCF-10A growth media with 10% dimethyl sulfoxide (DMSO, Sigma, Dorset, UK) and 40% fetal calf serum (FCS, GE Healthcare Life Sciences) and aliquoted into Cryo.s™ cryogenic storage vials (Grenier Bio-One GmbH, 72636 Frickenhausen, Germany). Cryovials were placed in a Mr Frosty™ (Thermo Scientific) filled with isopropanol (Fisher Scientific) and placed at -70 °C overnight to ensure gradual cooling (1 °C/min). Frozen cryovials were transferred to -180 °C within 48 h for long-term storage.

Table 6 MCF-10A media composition

	Growth media					Assay media				
Component	**Standard**	**Glucose DMEM**	**Fructose DMEM**	**Glucose Biowest DMEM – F12**	**Fructose Biowest DMEM – F12**	**Standard**	**Glucose DMEM**	**Fructose DMEM**	**Glucose Biowest DMEM – F12**	**Fructose Biowest DMEM – F12**
DMEM high glucose (GE Healthcare Life Sciences, Buckinghamshire, UK; Cat. nº. 41966-029):Ham's F12 (Lonza, Slough, UK; Cat. nº. BE12-615F)	1:1 v/v	-				1:1 v/v	-			
DMEM without glucose, L-glutamine, phenol red, sodium pyruvate and sodium bicarbonate (Sigma, Dorset, UK; Cat. nº. D5030)	-	Base		-		-	Base		-	
DMEM – F12 w/o L-Glutamine w/o Hepes w/o Glucose (Biowest, 49340 Nuaillé, France; Cat. nº. L0091-500)	-			Base		-			Base	
Sodium pyruvate (Sigma)	-	1 mM		-		-	1 mM		-	
Sodium bicarbonate (Sigma)	-	2.2 g/L		-		-	2.2 g/L		-	
D-(+)-Glucose solution (45%) (Sigma)	-	25 mM	-	25 mM	-	-	25 mM		25 mM	-
D-(-)-Fructose (Sigma)	-		10 mM	-	10 mM	-		10 mM	-	10 mM
Horse serum (Life Technologies, Paisley, UK)	5%					2%				
Epidermal growth factor (PeproTech, London, UK)	20 ng/ml					5 ng/ml				
Hydrocortisone (Sigma)	0.5 µg/ml					0.5 µg/ml				
Cholera toxin (Sigma)	100 ng/ml					100 ng/ml				
Insulin (Life Technologies)	10 µg/ml					10 µg/ml				
Penicillin/Streptomycin (Sigma)	50 U/ml					50 U/ml				
L-glutamine (Sigma)	2 mM					2 mM				
BD Matrigel basement membrane matrix (Scientific Laboratory Supplies, Yorkshire, UK)	-					2%				

Note: standard MCF-10A growth media contains a final concentration of 17.5 mM glucose (DMEM high glucose has 25 mM and Ham's F12 has 10 mM), which compares to 25 mM in glucose DMEM and glucose Biowest DMEM – F12. 10 mM fructose in fructose DMEM and fructose Biowest DMEM – F12 is based on (Reitzer, Wice et al. 1979).

Phoenix HEK-293 cells were cultured in a 10% CO_2 humidified chamber at 37 °C in DMEM high glucose (GE Healthcare Life Sciences) supplemented with 10% FCS (GE Healthcare Life Sciences), 2 mM L-glutamine (Sigma) and 50 U/ml penicillin/Streptomycin (Sigma). For cryopreservation, cells were stored in standard culture medium with 10% DMSO and 40% fetal calf serum.

HMEC were thawed, subcultured, maintained and cryopreserved according to manufacturer's instructions (Lonza) with all reagents purchased from Lonza. Briefly, cultures were initiated from cryopreserved stocks by seeding cells at a density of 2500 cells/cm^2; centrifugation was not performed as this action is more damaging than the effects of DMSO residue (based on guidance from Lonza). Growth medium (MEGM™ BulletKit™) was changed the day after seeding and every 2 days subsequently. The volume of media used was dependent on cell confluence: 1 ml/5 cm^2 for under 25% confluence, 1.5 ml/5 cm^2 for up to 45% confluence, 2 ml/5 cm^2 for over 45% confluence. Cells were subcultured at 60-80% confluence. Flasks were washed with HEPES buffered saline solution and covered with trypsin/EDTA. Following trypsinisation (approx. 4 min), trypsin was neutralised with 4 ml of trypsin neutralizing solution and detached cells transferred to a centrifuge tube. The flask was washed with HEPES buffered saline solution to collect residual cells and added to a centrifuge tube. Harvested cells were centrifuged at 220 x g for 5 minutes to pellet cells. For cryopreservation, cells were stored in growth medium with 10% DMSO and 10% FCS (minimum 5 x 10^5 cells/vial).

2.2.3 Adaptation to different sugar source

Glucose-DMEM- or fructose-DMEM- adapted populations were produced by culturing cells in glucose DMEM or fructose DMEM growth media respectively (Table 6) for 30 days, at which point cells were expanded in culture and cryopreserved. For glucose-Biowest DMEM – F12- or fructose-Biowest DMEM – F12- adapted populations cells were similarly cultured for 30 days in glucose Biowest DMEM – F12 or fructose Biowest DMEM – F12 respectively (Table 6), at which point they were expanded and cryopreserved. Adapted cells were used in experiments at low passage to prevent drift. 3D cultures were carried out in the relevant glucose or fructose assay media (Table 6).

2.2.4 Retroviral infection of MCF-10A and HMEC

The following vectors were purchased from Addgene (LGC standards, Middlesex, UK): pBABEpuro-ErbB2 vector (Greulich, Kaplan et al. 2012) (Addgene plasmid #40978); pBABEpuro-Bcl2 vector (Miura, Zhu et al. 1993) (Addgene plasmid #21144) and pMSCV-Peredox-mCherry-NLS (Hung, Albeck et al. 2011) (Addgene plasmid #32385). The following vectors were produced in the

laboratory by Matt Darley: pBABEneoRiCtBP2mh; pBABEneoRiCtBP2mh G189 and pBABEneoRiCtBP2mh H312L. A full description of the pooled populations produced is given in Table 7.

The Phoenix HEK-293 packaging cell line was utilised to package retroviral vectors. 2 µg vector was transfected into Phoenix HEK-293 using FuGene HD transfection reagent (Promega) using a FuGene:DNA ratio of 3:1. Media was changed at 24 h and viral supernatant collected at 48 h post transfection. Supernatant was passed through a 0.45 µm filter to remove cell debris. Subconfluent target cultures were infected as previously described (Debnath, Muthuswamy et al. 2003) using a 1:4 viral supernatant to media ratio. Selection began 48 h post transfection for seven days; the antibiotic(s) used for each pooled population are shown in Table 7; puromycin (Calbiochem®, Merck Chemicals Lyd, Nottingham, UK) was used at 0.5 µg/ml while geneticin (Sigma) was used at 100 µg/ml.

2.3 2D functional assays

2.3.1 Colony forming assays

For colony forming assays cells (50/well) were seeded into 6-well plates and incubated for 7 days, with media replaced on day 4. On day 7 colonies were fixed in 50% ice cold methanol (10 min) and stained with 0.02% crystal violet with 20% methanol (10 min). Colonies were manually counted and expressed as a percentage of the number of cells seeded.

2.3.2 Proliferation assay

For cell proliferation assays, cells (10,000 or 20,000/well) were seeded into 12-well plates and incubated for the indicated number of days. Cells were fixed in 50% ice cold methanol (10 min) and stained with 0.02% crystal violet with 20% methanol (10 min). Stain was dissolved in 0.5 ml 20% acetic acid and 100 µl of stain transferred to a 96-well plate. Absorbance at 595 nm was recorded using a Varioskan Flash plate reader (Thermo Scientific).

Table 7 Details of the host cell, vector and antibiotic utilised to generate pooled populations

Pooled clone notation	Host cells	Vector	Antibiotic selection	Notes
neo	MCF-10A	pBABEneo	Geneticin	Vector control for 1SM, 1L, 1SM H3B, 1L H3B
1SM	MCF-10A	pBABEneo-Bag-1SM		Predominantly Bag-1S overexpression
1L	MCF-10A	pBABEneo-Bag-1L		Optimised for Bag-1L overexpression
1SM H3B	MCF-10A	pBABEneo-Bag-1SM H3B		Bag-1 mutant which prevents Hsc-70 binding but does not alter Raf-1 binding
1L H3B	MCF-10A	pBABEneo-Bag-1L H3B		
puro	MCF-10A	pBABEpuro	Puromycin	Vector control for HER2 and Bcl-2
HER2	MCF-10A	pBABEpuro-ErbB2		HER2 overexpressing
Bcl-2	MCF-10A	pBABEpuro-Bcl2		Bcl-2 overexpressing
puro neo	puro	pBABEneo	Puromycin and Geneticin	Dual vector control for puro CtBP2, puro G189A and puro H312L
puro CtBP2	puro	pBABEneoRiCtBP2mh		CtBP2 overexpression
puro G189A	puro	pBABEneoRiCtBP2mh G189A		NADH-insensitive CtBP2 mutant (Mirnezami, Campbell et al. 2003, Thio, Bonventre et al. 2004)
puro H312L	puro	pBABEneoRiCtBP2mh H312L		Dehydrogenase CtBP2 mutant (Thio, Bonventre et al. 2004)
HER2 neo	HER2	pBABEneo		HER2 overexpressing vector control for HER2 CtBP2, HER2 G189A and HER2 H312L
HER2 CtBP2	HER2	pBABEneoRiCtBP2mh		HER2 and CtBP2 overexpression
HER2 G189A	HER2	pBABEneoRiCtBP2mh G189		HER2 and NADH-insensitive CtBP2 mutant
HER2 H312L	HER2	pBABEneoRiCtBP2mh H312L		HER2 and dehydrogenase CtBP2 mutant
HMEC puro	HMEC	pBABEpuro	Puromycin	Vector control for HMEC HER2
HMEC HER2	HMEC	pBABEpuro-ErbB2		HER2 overexpressing HMEC

2.3.3 Growth factor sensitivity assay

Growth factor sensitivity assays were carried out in serum free media and cells were serum- and growth factor- starved for 24 h prior to assay. Cells (20,000/well) were grown in growth factor-containing or growth factor-free media for 48 h. Wells were fixed in 50% ice cold methanol (10 min), stained with 0.02 % crystal violet with 20% methanol (10 min) and the stain dissolved in 0.5 ml 20% acetic acid (10 min). 100 µl of stain was transferred to a 96-well plate and the absorbance at 595 nm red on a Varioskan Flash plate reader. The response to growth factors was expressed as the growth relative to the growth factor-free condition.

2.3.4 Bag-1 inhibition

To examine the effect of Thio-2 (Enthammer, Papadakis et al. 2013) on signalling cell monolayers were rinsed with phosphate-buffered saline and kept for 4 h in growth factor-free media containing reduced horse serum (0.5%). Cells were subsequently treated with 50 µM compound for 1 h and cells harvested following stimulation with 10% horse serum (10 min). Unstimulated cells were used as a negative control for protein activation, with 25 µM U0126 (Promega) included as a positive control for inhibition of Erk signalling.

2.3.5 Seahorse Extracellular Flux (XF) Analyser

2.3.5.1 Principles of Seahorse Analyser

The Seahorse XF96 Analyser (Seahorse Bioscience, Agilent technologies) simultaneously measures glycolysis and mitochondrial respiration in live cells, in real time, in a 96-well plate assay. This is done by measuring proton release into and O_2 consumption from the media immediately surrounding the cell (extracellular flux). Lactate, the primary source of free protons in the media of cultured cells, is generated from glycolysis. The acidification of the media, as a direct consequence of proton release, is measured to monitor glycolytic activity (extracellular acidification rate, ECAR). An injection of 2-deoxyglucose (2DG) enables examination of the ECAR that is a consequence of glycolysis (Figure 21a). In addition O_2, used in mitochondrial respiration, is utilised to monitor mitochondrial respiration by measuring the rate of O_2 consumption from the media (oxygen consumption rate, OCR). Injections of oligomycin followed by antimycinA and rotenone enable examination of the OCR that is a consequence of mitochondrial ATP production and proton leak respectively (Figure 21b).

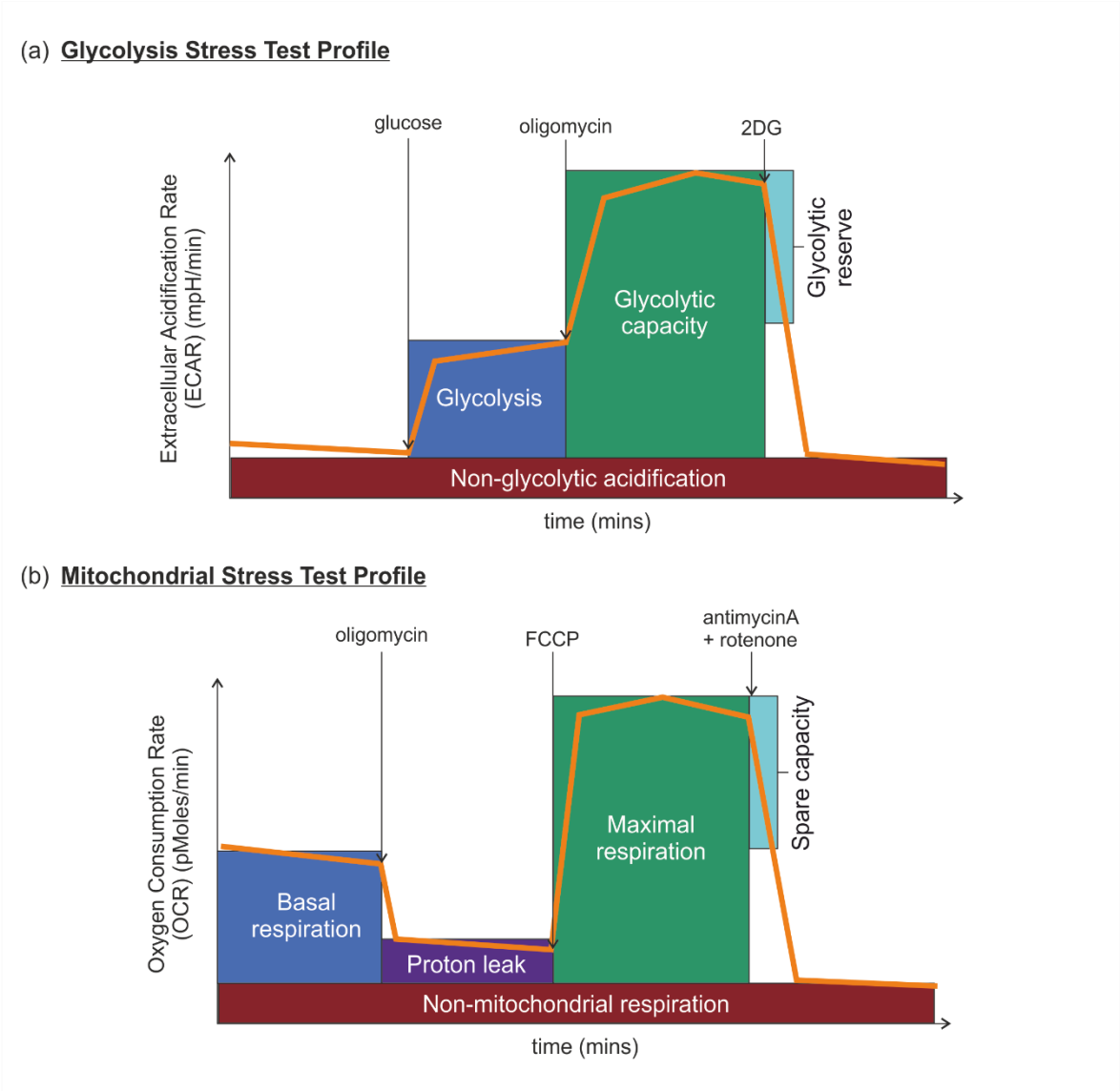

Figure 21 Schematic of glycolysis and mitochondrial stress profiles that can be generated using the Seahorse Analyser

(a) Glycolysis stress test profile showing the measurements that can be obtained relating to glycolytic activity following glucose, oligomycin and 2-deoxyglucose (2DG) injections. (b) Mitochondrial stress test profile showing the measurements that can be obtained relating to mitochondrial activity following oligomycin, FCCP and antimycinA and rotenone injections.

2.3.5.2 Seahorse Analyser set up

18 h prior to seeding, cells ($2.5x10^5$/well) were seeded in 80 µl of growth medium in a V3-PS XF96 cell culture microplate (Seahorse Bioscience) and cultured at 37 °C in a 5% CO_2 humidified chamber. XF96 extracellular flux assay kits (Seahorse Bioscience) were prepared by adding 200 µl of XF Calibrant (pH 7.4) (Seahorse Bioscience) to immerse the probes and incubated overnight at 37 °C in a non-CO_2 humidified chamber.

Running media was prepared using glucose-free DMEM supplemented with 2 mM L- glutamine and 50 U/ml penicillin/Streptomycin and the pH adjusted to pH 7.4 (at 37 °C). Glycolytic stress tests were carried out in standard running media, with port B and port C injections prepared in running media supplemented with 10 mM glucose. Mitochondrial stress tests and drug titration experiments were carried out in running media supplemented with 10 mM glucose and 1 mM pyruvate. Injection ports for each experiment were loaded as described in Table 8. Dichloroacetate and Vitamin C compounds were adjusted to pH 7.4 before use in Seahorse assays.

On the day of the run, injection drugs were diluted in running media to the desired concentrations and loaded into the relevant injection ports of the probe cartridge. Once ports were loaded the probe cartridge was incubated at 37 °C in a non-CO_2 humidified chamber for 30 mins, then loaded into the instrument and calibration of the probes initiated (automated process done by the Seahorse Analyser). During probe calibration the assay plate was washed once with 180 µl running medium (at 37 °C) then the cells were incubated in 180 µl running medium at 37 °C in a non-CO_2 humidified chamber for 15-45 mins. Cells were given a final wash with 180 µl running medium then the plate loaded into the machine. The Seahorse Analyser was programmed to record OCR and ECAR for a 2 min period every 5 mins, with mixing occurring in between measurements. At the end of the run the cell culture plate was removed from the machine and running media removed from the wells; the dry plate was wrapped in saran wrap and placed at -20 °C.

Table 8 Details of port injections for Seahorse Analyser metabolic tests

Test		**Port**	**Injection**	**Port concentration**	**Volume of injection /µl**	**Final concentration**
Glycolytic stress test		A	Glucose	100 mM	20	10 mM
		B	Oligomycin (Sigma)	10 µM	22	1 µM
		C	2-deoxyglucose	1 M	24	100 mM
Mitochondrial stress test		A	Oligomycin	10 µM	20	1 µM
		B	FCCP (Seahorse Bioscience)	3 µM	22	0.3 µM
		C	AntimycinA and rotenone (Sigma)	10 µM	24	1 µM
Drug titration experiments	Glycolytic test	A	Drug	10X	20	as stated
		B	2-deoxyglucose	1 M	22	100 mM
		C	Running medium	n/a	24	n/a
	Mitochondrial test	A	Drug	10X	20	as stated
		B	Oligomycin	10 µM	22	1 µM
		C	AntimycinA and rotenone	10 µM	24	1 µM

2.3.5.3 Bradford Assay for Seahorse normalisation

To determine the concentration of protein per well a Bradford assay was carried out on plates from Seahorse assays. Plates were removed from -20 °C storage and lysed in 20 µl/well of seahorse lysis buffer (250 mM Tris, pH 7.4, 0.1 % Triton-X-100) and incubated for 15 min on a plate rocker. 130 µl/well dilution buffer (250 mM Tris, pH 7.4) was added to dilute the Triton-X-100. 150 µl/well of 2X Bradford Reagent (Bio-Rad, Hertfordshire, UK) was added with mixing, and 200 µl of each sample transferred to a 96-well plate. Absorbance at 595 nm was recorded on a Varioskan plate reader and protein concentration determined by referencing to a BSA standard curve.

2.3.5.4 Data analysis for Seahorse

Data files were opened using the Seahorse Bioscience XFReader96 software version 1.4.0.11. Normalisation values calculated from the Bradford assay (2.3.5.3 Bradford Assay for Seahorse normalisation) were applied to wells. A series of quality control steps were carried out for each run. Normalisation values were examined in detail. Any well which had a normalisation range that was far from the average was excluded; this is because the confluency of a well alters the cells metabolic responses, and the normalisation count is a rough indicator of confluency (a higher reading indicates a higher confluency). Raw O_2 readings were examined; levels typically sat within 90-160 mmHg. The pH during the run was examined, to assess whether the starting pH was within an acceptable range (pH 6.6-7.4) and to confirm that the injections did not alter the pH. In addition, ECAR or OCR following injection of drugs from the glycolytic or mitochondrial stress tests respectively were examined to check that the drug was behaving as expected. A representative set of quality control data is shown in Figure 22.

Subsequent experimental analysis was carried out on normalised data. Data was analysed using group well mode, where a group included all wells relating to a single condition, and exported to excel reporting the mean, standard deviation (SD) and number of samples (N) for each group. For drug titration experiments, all data was baselined to the values for OCR and ECAR at the point of injection of the drug (injection port A).

(a) Normalisation count

	1	2	3	4	5	6	7	8	9	10	11	12
A	0.00	0.00	0.00	0.00	0.00	0.00	0.00	0.00	0.00	0.00	0.00	0.00
B	0.00	8.78	8.40	8.06	8.51	8.90	9.30	9.37	8.78	9.46	9.18	0.00
C	0.00	9.63	7.91	8.77	8.51	8.56	9.26	9.44	8.79	9.48	9.19	0.00
D	0.00	9.64	8.55	8.20	8.07	8.79	9.21	8.98	8.85	9.24	9.09	0.00
E	0.00	10.84	10.07	10.34	10.13	10.90	10.68	10.85	10.73	10.78	10.88	0.00
F	0.00	11.56	9.82	10.12	10.02	10.63	10.50	10.71	10.75	10.56	11.02	0.00
G	0.00	11.02	10.36	9.88	10.08	10.56	10.62	10.91	11.00	10.93	10.56	0.00
H	0.00	0.00	0.00	0.00	0.00	0.00	0.00	0.00	0.00	0.00	0.00	0.00

(b) Raw O_2 readings

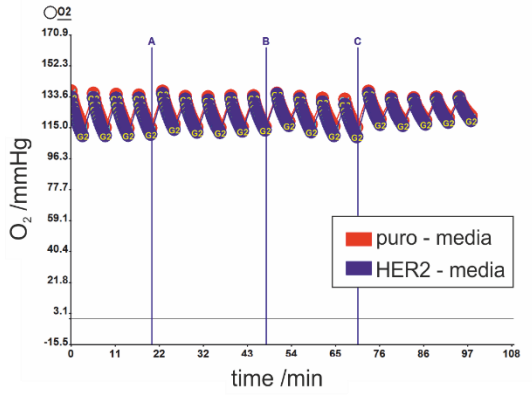

(c) Raw pH readings

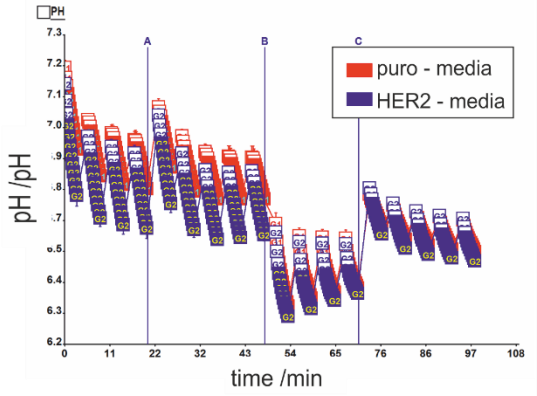

(d) OCR following injections

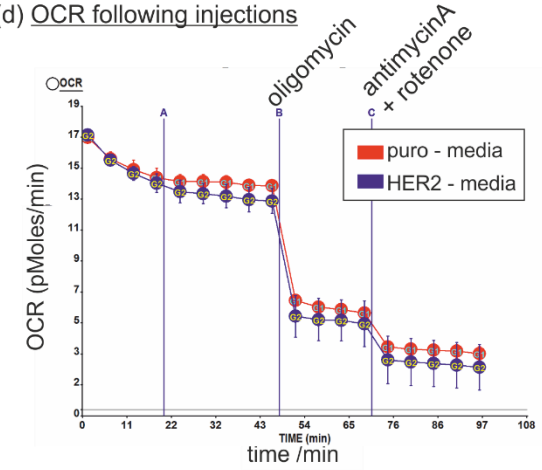

(e) ECAR following injections

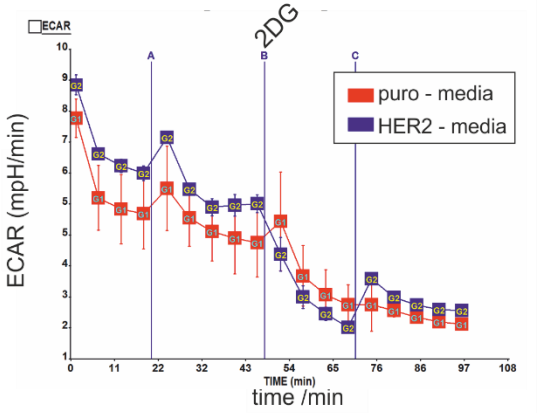

Figure 22 Representative data set to show Seahorse quality control checks

A series of quality control checks were carried out for each Seahorse experiment prior to analysis. Data shown here is from an etomoxir drug titration experiment. For simplicity, only puro and HER2 cells in media alone wells are shown. (a) Normalisation values were examined to check that all wells had a similar level of protein (as an indicator of confluency). (b) Raw O_2 readings were assessed to monitor the range of O_2 across wells. (c) pH was examined to confirm that the starting pH range was within an acceptable range and that drug injections were not immediately influencing pH levels (to confirm that effects on ECAR are a consequence of metabolic inhibition and not due to the drug influencing the media pH of the well). OCR (d) and ECAR (e) were also examined to confirm that oligomycin, antimycinA and rotenone and 2-deoxyglucose (2DG) injections behaved as expected. Data in (b-e) is not normalised for protein levels.

The following equations were used as part of analysis:

Mitochondrial stress test:

$$Mitochondrial\ ATP\ production = basal\ OCR - \ OCR\ following\ oligomycin\ injection$$

Glycolytic stress test:

$$Glycolysis = ECAR\ in\ the\ presence\ of\ glucose - ECAR\ following\ 2DG\ injection$$

Normal Difference Distribution:

Standard deviations for mitochondrial and glycolytic stress tests were adjusted using the rule for normal difference distribution. For variates X and Y with means and variances (μ_x, σ_x) and (μ_y, σ_y), the difference of these variants is given by:

mean $\mu_{x-y} = \ \mu_x - \ \mu_y$ and variance ${\sigma^2}_{x-y} = \ {\sigma^2}_x + \ {\sigma^2}_y$

Metabolic inhibitor analysis:

$$Fold\ change\ in\ glycolysis = \frac{(OCR\ in\ presence\ of\ inhibitor - OCR\ in\ the\ presence\ of\ 2DG\ *)}{(OCR\ in\ the\ absence\ of\ inhibitor - OCR\ in\ the\ presence\ of\ 2DG\ *)}$$

* values are taken as the average OCR in the presence of 2DG across all conditions for that pool. In cases where a particular condition significantly alters OCR following 2DG, this condition was excluded from the average OCR in the presence of 2DG. Where this is the case it will be stated in the figure legend.

$$Fold\ change\ in\ mitochondrial\ ATP\ production = \frac{(ECAR\ in\ presence\ of\ inhibitor - ECAR\ in\ presence\ of\ oligomycin\ **)}{(ECAR\ in\ the\ absence\ of\ inhibitor - ECAR\ in\ the\ presence\ of\ oligomycin\ **)}$$

** values are taken as the average ECAR in the presence of oligomycin across all conditions for that pool. In cases where a particular condition significantly alters ECAR following oligomycin, this condition was excluded from the average ECAR in the presence of oligomycin. Where this is the case it will be stated in the figure legend.

2.3.6 Attachment versus detachment cell viability assays

Cells (15,000/well) were seeded in 100 µl of media onto standard tissue-culture plastic or polyHEMA-coated (12 mg/ml) dishes for 24 h or 48 h at which point cell viability was assessed by an alamarBlue® assay (Thermo Fisher) and cellular ATP examined using the ATPlite luminescence

assay kit (Perkin Elmer, Buckinghamshire, UK). AlamarBlue® reagent (10 µl/well) was added 6 h prior to 24 h or 48 h time point; fluorescence was read on a Varioskan Flash plate reader using an excitation wavelength of 570 nm and an emission wavelength of 595 nm. For the ATPlite assay, mammalian lysis buffer (25 µl/well) was added and incubated for 15 min on a rocking platform. ATPlite buffer was used to reconstitute lyophilised substrate solution. Substrate solution (25 µl/well) was added to a white, flat bottomed 96-well plate (Perkin Elmer). 50 µl of lysed media suspension was transferred to the white plate pre-loaded with substrate solution and incubated for 15 min on a rocking platform in the dark; luminescence was monitored using a Varioskan Flash plate reader.

2.4 3D functional assays

2.4.1 3D acinar culture in an 'on top' assay

Standard 3D morphogenesis assays were carried out on BD falcon 8 well culture slides (Scientific Laboratory Supplies) coated with BD Matrigel basement membrane matrix (Scientific Laboratory Supplies). Culture slides were coated with Matrigel (30-40 µl/chamber) and incubated at 37 °C in a 5% CO_2 humidified chamber for 30 min to allow the Matrigel to polymerise. Debnath *et al.* report that care should be taken to ensure Matrigel does not form a meniscus (Debnath, Muthuswamy et al. 2003). This forms when Matrigel is dragged to the walls of the chamber and settles around the sides of the chamber. While acini tend to form across the surface of a chamber when there is no meniscus, acini cluster around the edges of the chamber where there is a meniscus because the Matrigel is thicker here (Figure 23). Under certain conditions, particularly when growing HMECs, the Matrigel layer was found to float off the surface of the chamber slide during feeds or the fixing process – chambers were therefore seeded with a deliberate meniscus to minimise loss and allow me to carry out analysis on these acini. Cells were seeded onto the Matrigel bed in 400 µl of media containing 2 % Matrigel at 1000 cells/chamber (MCF-10A) or 2500 cells/chamber (HMEC). The day cells were seeded was designated day zero and media was replenished every four days. MCF-10A 3D cultures were carried out in MCF-10A assay media (Table 6). HMEC 3D cultures were carried out in HMEC growth medium with 2% Matrigel added just prior to use.

2.4.2 3D Thio-2 experiments

For Bag-1 inhibition in 3D experiments cells were pre-treated with 25 µM Thio-2 in 2D for 24 h before seeding in compound-free assay media in 3D. Acini were fed with 50 µM compound-containing assay media on days 4 and 8 of morphogenesis.

2.4.3 3D acini metabolic inhibitor experiments

Metabolic inhibitors were included in assay media feeds at day six of acinar morphogenesis, and every two subsequent days. The concentration of each metabolic inhibitor used in summarised in Table 9. For drugs reconstituted in DMSO, control acini were treated with DMSO at the same concentration as present in wells containing drug.

2.4.3.1 Analysis of acini experiments

The percentage of incompletely cleared acini was calculated using the equation shown below:

$$Incompletely\ cleared\ acini\ (as\ a\ \%\ of\ total\ acini\ scored) = \frac{number\ of\ acini\ scoring\ as\ filled + number\ of\ acini\ scoring\ as\ partially\ filled}{total\ number\ of\ acini\ scored}\ x\ 100$$

When examining the effect of oncogene overexpression on luminal status, the mean percentage of incompletely cleared acini from each independent experiment was taken and used for analysis.

When analysing metabolic inhibitor data which combined multiple independent experiments, each independent experiment was adjusted for experimental drift in luminal filling within an individual pool (ie puro and HER2 were analysed separately). For example:

$$Adjusted\ value\ for\ puro = \frac{Incompletely\ cleared\ acini\ (as\ a\ \%\ of\ total\ acini\ scored)}{\sum(no.\ of\ puro\ acini\ scoring\ as\ filled\ or\ partially\ filled\ across\ whole\ experiment)}$$

All subsequent analysis was carried out on adjusted values. A combined mean percentage of incompletely cleared acini for the experimental control (media or DMSO) for that pool was calculated from across all three experiments.

$$Combined\ mean\ for\ control = \frac{\overline{x}\mathrm{exp.}\,1 + \overline{x}exp.\,2 + \overline{x}exp.\,3}{3}$$

Values were divided by the combined mean for control, giving data that was expressed relative to the experimental control for puro or HER2.

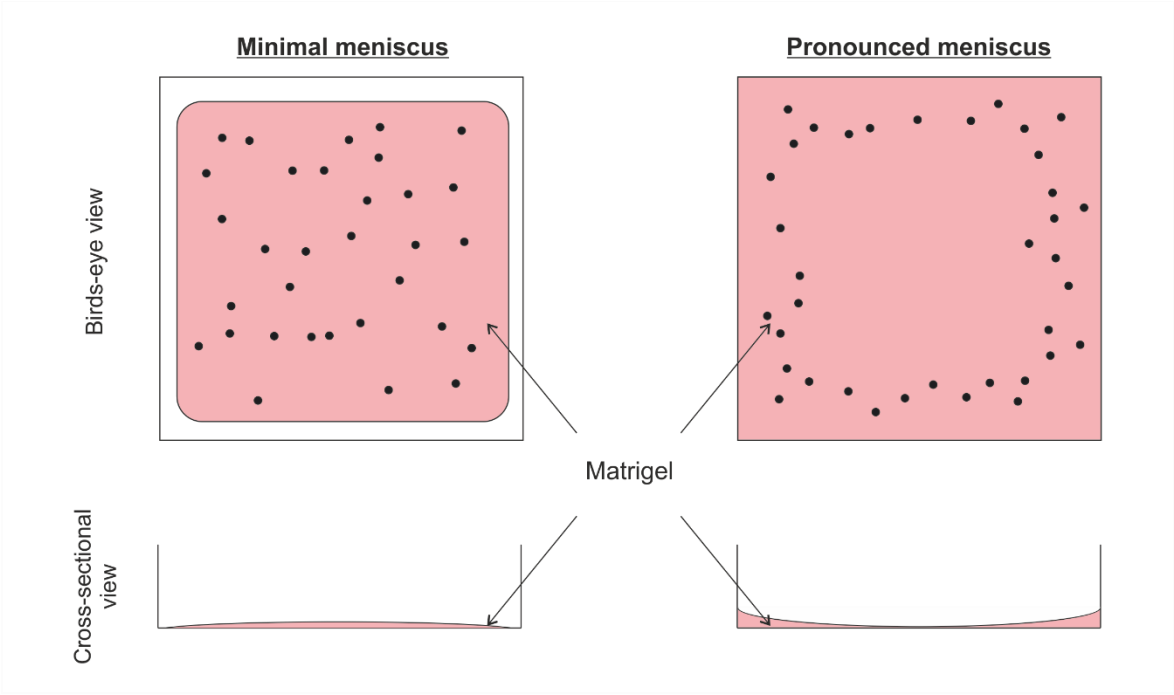

Figure 23 Diagrammatic representation of the two ways to coat Matrigel onto a chamber slide

Schematic shows the suggested way of coating the chamber slides surface (left) (Debnath, Muthuswamy et al. 2003). Matrigel does not touch the walls of the chamber, but the majority of the well is coated; a minimal meniscus results and acini form with an even distribution across the slide. When Matrigel is dragged to the walls of the chamber slide, the whole chamber is coated, however a pronounced meniscus forms with Matrigel settling around the edges of the chamber. Acini distribution tends to cluster at the edges where Matrigel is thickest. Under certain conditions the minimal meniscus Matrigel layer can float off the chamber slide during the course of an experiment, the pronounced meniscus approach was therefore favoured in this setting.

Table 9 Metabolic inhibitor details, including concentrations used in 3D acini experiments

All drug stocks were stored at -20 °C except for dichloroacetate which was made fresh for each experiment and stored at 4 °C.

				Conc. for 3D assays		
Metabolic inhibitor	**Also known as**	**Reconstituted in**	**Stock conc.**	**Dilution factor**	**Final conc.**	**Target of inhibition**
L-ascorbic acid (Sigma)	Vitamin C, VitC	dH_2O	10 mg/ml	113.6X	500 µM	Antioxidant (ROS neutralisation)
Chloroquine diphosphate salt (Sigma)	Chloroquine	dH_2O	20 mM	1000X	20 µM	Autophagy (lysosomal acidification)
2-deoxyglucose (ACROS Organics, Thermo Fisher)	2DG	dH_2O	1 M	100X	10 mM	Glycolysis (hexokinase and phosphoglucose isomerase)
1,1-Dimethylbiquanidine hydrochloride (Sigma)	Metformin	dH_2O	50 mM	1000X	50 µM	Electron transport chain (complex I)
(+)-Etomoxir sodium salt (Sigma)	Etomoxir, Ethyl-2-[6-(4-chlorophenoxy)hexyl] oxirane-2-carboxylate	dH_2O	10 mM	100X	100 µM	Fatty acid oxidation (CPT-1)
Iodoacetic acid, sodium salt, 99% (Thermo Fisher)	Iodoacetate, IAA	dH_2O	0.1 M	as stated	as stated	Glycolysis (GAPDH)
Lactate Dehydrogenase A Inhibitor, FX11 – Calbiochem	FX11	DMSO	9 mM	1000X	9 µM	Glycolysis (lactate dehydrogenase)
3-methyladenine (Sigma)	3MA	DMSO	67 mM	149X	10 mM	Autophagy (autophagosome formation)
α-Keto-γ-(methylthio)butyric acid sodium salt (Sigma)	MTOB	dH_2O	250 mM	62.5X	4 mM	Metabolic sensor (CtBP inhibitor)
Perhexiline maleate salt (Sigma)	Perhexiline	DMSO	10 mM	1000X	10 µM	Fatty acid oxidation (CPT-1)
Phenformin hydrochloride (Sigma)	Phenformin	dH_2O	2 mM	1000X	2 µM	Electron transport chain (complex I)
Sodium dichloroacetate (Santa Cruz Biotechnology, Heidelberg, Germany)	Dichloroacetate, DCA	dH_2O	50 mg/ml	33X	10 mM	Activator of mitochondrial actvitiy (activator of pyruvate dehydrogenase)
Sodium oxamate (Sigma)	Oxamate	dH_2O	0.5 M	20X	25 mM	Glycolysis (lactate dehydrogenase)

2.4.4 3D alamarBlue® assays

To examine viability of acini in 3D, 200 cells were seeded in MCF-10A standard assay media into wells of a 96-well plate which had been pre-coated with Matrigel (30 µl, 30 mins, 37 °C) (day 0). Acini were cultured as previously described with inhibitors present from day 6 of morphogenesis (2.4.3 3D acini metabolic inhibitor experiments). On day 12 of morphogenesis, alamarBlue® (10 µl) was added to each well and incubated at 37 °C in a 5% CO_2 humidified chamber for 6 h. Fluorescence was red on a Varioskan Flash plate reader using an excitation wavelength of 570 nm and an emission wavelength of 595 nm. For each condition a no cell well was included which gave a background reading; background was subtracted from each well prior to analysis.

2.5 Molecular and cellular imaging techniques

2.5.1 Immunoblotting

For 2D cultures cell pellets were collected by cell scraping from subconfluent dishes, which were lysed in denaturing urea lysis buffer (7 M Urea, 0.05% Triton X-100, 25 mM NaCl, 20 mM 1M HEPES pH 7.6, 100 mM DTT). For 3D cultures cells were lysed directly in ice cold radioimmunoprecipiation assay buffer (20 mM Tris-HCl pH 7.4, 150 mM NaCl, 1 mM EDTA pH 7.4, 1 mM EGTA pH 7.4, 1% NP-40, 0.1% SDS, 1% sodium deoxycholate, 25 mM sodium pyrophosphate, 1 mM β-glycerophosphate, 1 mM Na_3VO_4, 1:100 dilution protease inhibitor cocktail (Sigma)). SDS-PAGE and Western immunoblotting procedures were carried out using Bio-Rad equipment according to standard procedures (Green and Sambrook 2012). The protein concentration of samples from 2D lysates were determined by a Bradford assay (Bio-Rad) and samples adjusted to a set protein concentration/well prior to loading. For 3D lysates the presence of Matrigel in the lysate means a Bradford assay cannot be used. The maximum volume of lysate was loaded/well and blots probed for the loading control β-actin. Densitometry on β-actin (2.5.1.1 Immunoblot image acquisition and analysis) was used to determine the relative protein abundance per lane and an additional immunoblot ran with adjusted volumes of sample to give the same concentration of sample/well, which was then probed for the target protein. The PageRuler Prestained Protein Ladder (Thermo Scientific) was used. Membranes were blocked in 5% milk in PBS with 0.1% Tween20. Antibodies were diluted in 3% milk in PBS with 0.1% Tween20. A full list of antibodies and their dilution can be found in Table 10. SuperSignalR West Pico or Femto Chemiluminescent substrates (Thermo Scientific) were used for detection.

2.5.1.1 Immunoblot image acquisition and analysis

Immunoblot images were acquired on a BioRad Fluor-S^{TM} MultiImager using the Quantity One analysis software, version 4.6.3. Quantification of bands was performed using the volume tools in Quantity One analysis software, version 4.6.9, where a volume is the sum of the intensities of the pixels within the volume boundary times by the pixel area. Analysis was carried out on bands pre-saturation. All bands were adjusted for global background volume. Protein abundance was calculated by normalising bands for actin, and expressed relative to a stated control. The Bag-1 antibody used is monoclonal recognising a single epitope; where Bag-1L isoform bands were not present in all conditions on an immunoblot, Bag-1L isoforms were expressed relative to Bag-1S abundance.

2.5.2 Immunofluorescence

2.5.2.1 2D immunofluorescence

For 2D immunofluorescence cells were plated on glass coverslips coated with 10 µg/ml type I rat tail collagen (Corning, Flintshire, UK). Immunofluorescence staining was carried out as previously described (Debnath, Muthuswamy et al. 2003). Briefly cells were fixed in 4% paraformaldehyde in PBS, pH 7.4 (15 min), rinsed in 100 mM glycine in PBS (10 min), permeabilised with 0.5% Triton-X-100 in PBS (10 min) and blocked in 10% FCS in PBS (30 min). All antibody incubations were carried out in 0.6% BSA in PBS (1 h). A full list of antibodies and their dilutions can be found in Table 10. DAPI was included in the secondary antibody incubation step as a DNA counterstain. A secondary antibody only condition was included for each species of antibody used to exclude the possibility of non-specific binding. Slides were mounted on glass coverslips with fluorescence mounting medium (Dako), allowed to dry overnight and stored at 4 °C.

2.5.2.2 3D immunofluorescence

3D immunofluorescence was carried out as described for 2D (2.5.2.1, 2D immunofluorescence) with acini being fixed and stained directly in chamber slides. A full list of antibodies and their dilutions can be found in Table 10. Slides were fixed in 2% compared to 4% paraformaldehyde.

Table 10 Antibody or stain applications and dilutions

Full details of antibodies and stains used for immunofluorescence (IF) or immunoblotting (IB)

Antibody or Stain	Source	Species	Application	Dilution
4'6-diamidino-2-phenylindole (DAPI)	Sigma	n/a	IF	1:1000
Bag-1 antibody (3.10G3E2)	Santa Cruz Biotechnology	Mouse	IB	1:1000
HER2/ErbB2 antibody #2242	Cell Signalling, Hertfordshire, UK	Rabbit	IB	1:500
			IF	1:250
monoclonal anti-β-actin peroxidase	Sigma	Rabbit	IB	1:5000
Monoclonal Mouse Anti-Human BCL2 Oncoprotein clone 124	Dako, Cambridge UK	Mouse	IB	1:1000
Phalloidin-TRITC	Dako	n/a	IF	1:5000
polyclonal goat anti-mouse immunoglobulins/HRP	Dako	Goat	IB	1:1000
polyclonal goat anti-rabbit immunoglobulins/HRP	Dako	Goat	IB	1:1000
Swine anti-Rabbit Immunoglobulins/TRITC	Dako	Swine	IF	1:100-1:300
Swine anti-Mouse Immunoglobulins/TRITC	Dako	Swine	IF	1:100-1:300
TB3 Bag-1	Made in house (Brimmell, Burns et al. 1999)	Rabbit	IF	1:300
Anti-E Cadherin antibody [HECD-1]	AbCam	Mouse	IB	1:2000
Phospho-Akt (Ser473) Antibody #9271	Cell Signalling	Rabbit	IB	1:1000
Akt Antibody #9272	Cell Signalling	Rabbit	IB	1:1000
p44/42 MAPK (Erk1/2) Antibody #9102	Cell Signalling	Rabbit	IB	1:1000
Phospho-p44/42 MAPK (Erk1/2) (Thr202/Tyr204) (20G11) Rabbit mAb #4376	Cell Signalling	Rabbit	IB	1:1000
Anti-6His Rabbit polyclonal IgG	AbCam	Rabbit	IF	1:1000
CtBP Antibody (E-12): sc-17759	Santa Cruz	Mouse	IF	1:200
Purified Mouse Anti-CtBP2	BD Bioscience, Oxford, UK	Mouse	IF	1:500
Monoclonal Mouse Anti-Human BCL2 Oncoprotein Clone 124	Dako	Mouse	IB	1:2500

2.5.3 Microscopy image acquisition and analysis

All images of fixed samples were taken at room temperature. Monolayer cultures were imaged on an Olympus IX81 microscope using xcellence pro version 1.1 (Olympus Soft Imaging Solutions GmbH, 48149 Münster, Germany). Immunofluorescence images from 3D morphogenesis assays were acquired on a Leica SP5 scanning confocal microscope using the Leica LAS EZ software, version 3.0, and image analysis carried out using the LEICA LAS AF version 2.6.0 (Leica, London, UK). Slides for acinar morphology scoring were photographed using an Olympus BX51 microscope with automated slide scanning and high resolution pictures covering the entire sample were captured and automatically montaged using dotslide TMA (Olympus software imaging solutions, GmbH). Images were opened using OlyVIA software version 2.4 (Olympus software imaging solutions).

2.5.4 Scoring of acini

Acinar luminal status was scored on the stated day of morphogenesis by observing acini counterstained for DAPI and phalloidin-TRITC on the Leica SP5 confocal microscope using the Leica LAS EZ software. A minimum of 60 acini across at least three chambers were scored for each condition. Luminal status was scored in four categories: filled, partially filled, nearly hollowed and completely hollowed; nearly hollowed acini were perceived to have over 80% space in the lumen (Figure 24).

Morphology scoring slides were fixed on the stated day of morphogenesis by adding an equal volume of 4% paraformaldehyde in PBS directly onto the media (2% paraformaldehyde final concentration) and left at room temperature overnight. This minimised the number of acini becoming dislodged and lost during washing and fixation steps. Images were captured using the slide scanner. All acini were manually scored with a minimum of three chambers scored per condition; acini that did not display the spherical structure characteristic of parental MCF-10A were defined as atypical, including multiacinar, abnormal and branching structures (Figure 25).

2.6 Statistical analysis

Statistical analysis was carried out using the statistical package GraphPad Prism version 6.00 for Windows (GraphPad Software, San Diego, USA). The number of technical repeats within an independent experiment, and the number of independent experiments contributing to a graph are stated within the figure legend. Unless otherwise stated, data are presented as mean ± SEM; analysis of two groups was done using an unpaired t-test and analysis of more than two groups using a two-way ANOVA with Fishers LSD test. Results which were significantly significant from the control group were marked with asterisks, where * $p \leq 0.05$, ** $p \leq 0.01$ and *** $p \leq 0.001$.

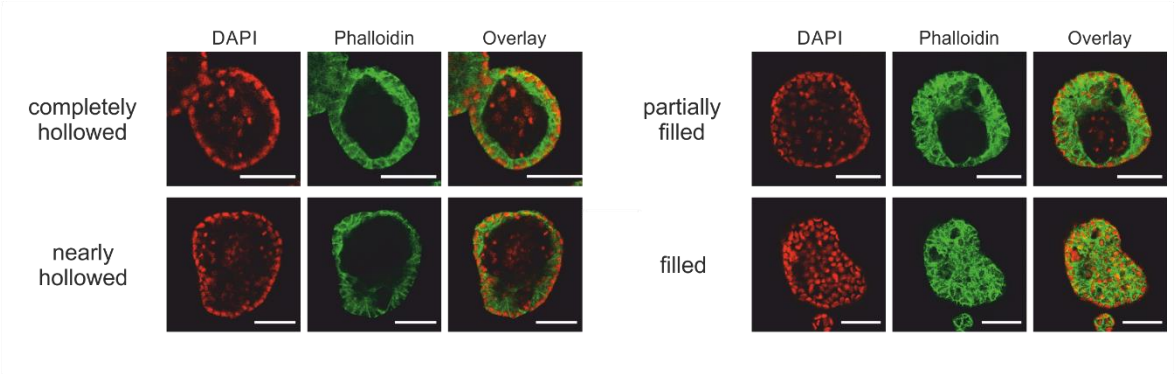

Figure 24 Representative images for each scoring category of acinar luminal status

At the relevant time point during culture acini were fixed and stained with DAPI (red) and phalloidin-TRITC (green). Confocal microscopy was utilised to score luminal status. Looking through all focal planes, acini were scored as filled, partially filled, nearly hollowed or completely hollowed. Representative images of each of the scoring categories are shown; scale bars show 50 µm.

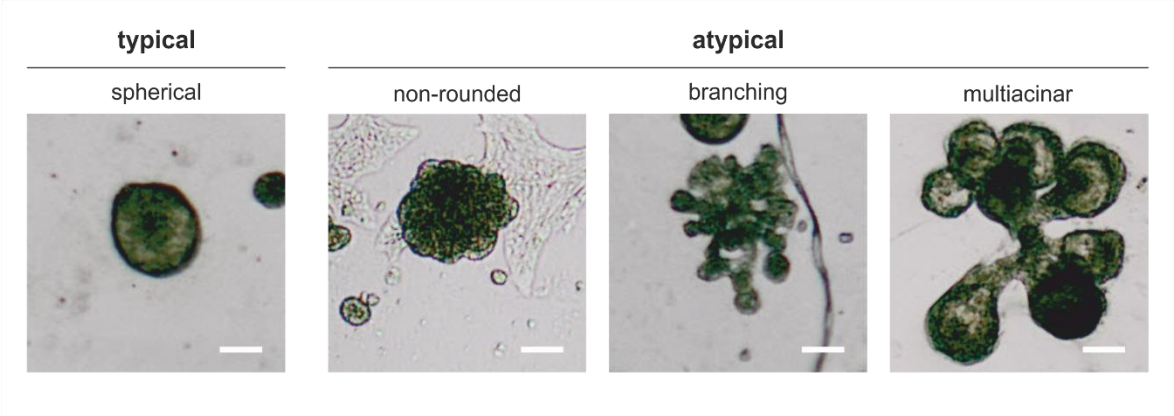

Figure 25 Representative images of the four acinar morphologies observed

At the relevant time point during culture acini were fixed directly to minimise acini loss in wash steps (2% PFA final concentration) and mounted. High resolution pictures covering the entire slide were captured and all acini within a chamber scored manually. Morphology was scored as typical or atypical, where atypical acini includes non-rounded, branching and mulitacinar. Representative images of each of the scoring categories are shown; scale bars show 100 µm.

Chapter 3: The Bag-1 inhibitor, Thio-2, reverses an atypical 3D morphology driven by Bag-1L overexpression in an MCF-10A model of ductal carcinoma in situ

The multifunctional, anti-apoptotic protein Bag-1 is expressed in most human tissues (Takayama, Krajewski et al. 1998) and is frequently seen overexpressed in invasive breast carcinoma and in the preinvasive DCIS (Takayama, Krajewski et al. 1998, Brimmell, Burns et al. 1999, Tang, Shehata et al. 1999, Turner, Krajewski et al. 2001, Tang, Beck et al. 2004). Proof-of-principle studies from the Cutress laboratory have shown that targeting of Bag-1 protein-protein interactions using synthetic peptides and small-molecular compounds like Thioflavin S and its biologically active component Thio-2 can restrict breast cancer cell growth, implicating Bag-1 in the progression of this disease (Sharp, Crabb et al. 2009, Sharp, Cutress et al. 2009, Enthammer, Papadakis et al. 2013). However little is known about the role of Bag-1 in initiating premalignant change in the breast.

Bag-1 exists as three major isoforms, Bag-1S, Bag-1M and Bag-1L (Packham, Brimmell et al. 1997, Yang, Chernenko et al. 1998), which have functionally distinct roles (1.5.3 Cellular functions and interaction partners of Bag-1) and, in the case of the Bag-1L isoform, a nuclear rather than cytoplasmic localisation (Brimmell, Burns et al. 1999). This isoforms' unique cellular functions include enhancement of transcription of the androgen receptor (Froesch, Takayama et al. 1998, Knee, Froesch et al. 2001, Shatkina, Mink et al. 2003), the vitamin D receptor (Lee, Crabb et al. 2007) and the ER (Cutress, Townsend et al. 2003). Within a xenograft model, Bag-1L overexpression drives growth of breast tumours formed by oestrogen-responsive ZR-75-1 breast cancer cells in an oestrogen-dependent manner (Kudoh, Knee et al. 2002). In the clinical setting, high nuclear Bag-1 immunoreactivity is an independent predictor of outcome (Turner, Krajewski et al. 2001, Cutress, Townsend et al. 2003, Nadler, Camp et al. 2008, Millar, Anderson et al. 2009) and enhances the predictive power of IHC4 score (a multigene prognostic test) (Afentakis, Dowsett et al. 2013). The distinct cellular functions and prognostic implications of Bag-1L overexpression highlights the importance of isoform-specific studies of Bag-1 overexpression in breast cancer disease initiation and progression.

Culture of cell lines on plastic creates an environment that differs markedly from the breast microenvironment, providing a non-physiological setting to examine the regulation of apoptosis in mammary cells (Weaver and Bissell 1999) (1.2 Modelling the Breast in the Laboratory). In contrast, the MCF-10A acini 3D model of the breast enables study of mammary tissue

homeostasis in a more physiologically relevant setting. Of particular relevance for this work, lumen formation in MCF-10A acini is due to central cell death following ECM-detachment; this is therefore an ideal model for us to examine the role of Bag-1L in luminal cell survival during early breast cancer development. While Anderson *et al.* have shown that co-overexpression of all three isoforms of Bag-1 can lead to the formation of filled acini, through an Erk-dependent attenuation of Bim-regulated anoikis (Anderson, Sutherland et al. 2010), this is the first study looking at the ability of individual Bag-1 isoforms to regulate acinar morphogenesis.

The work in this chapter forms the basis of the data presented in the paper 'The Bag-1 inhibitor, Thio-2, reverses an atypical 3D morphology driven by Bag-1L overexpression in a MCF-10A model of ductal carcinoma *in situ*' (Papadakis, Barker et al. 2016). Where work has been carried out by someone other than myself it is highlighted within the figure legend or text.

3.1 Characterisation of Bag-1L/A and Bag-1L/B in 2D

To examine the role of Bag-1L in breast tumorigenesis, Bag-1L-overexpressing MCF-10A stable clones were generated by lipid-based transfection (Hashim Sayed, MMedSci report). The relative expression of Bag-1L within each stable clone was examined by immunoblotting. Two clones were identified as overexpressing Bag-1L compared to pcDNA3 controls (Figure 26a); Bag-1L/A overexpressed Bag-1L to a low extent and Bag-1L/B overexpressed Bag-1L at a high extent. Clone 1 of the pcDNA3 control (denoted pcDNA) was used as the control in all future experiments.

Immunofluorescence staining for Bag-1 was used to confirm overexpression and to examine the subcellular location of Bag-1 (Figure 26b). Bag-1 staining revealed higher Bag-1 expression in the nucleus of both clones compared to pcDNA and was more intense in Bag-1L/B. The unavailability of isoform specific antibodies prevents examination of individual isoforms via immunofluorescence, but high nuclear staining is consistent with overexpression of the predominantly nuclear Bag-1L isoform (Brimmell, Burns et al. 1999, Weaver and Bissell 1999). Bag-1 staining was heterogeneous across all clones, with the presence of heterogeneity in pcDNA controls implying this protein is heterogeneously expressed within MCF-10A cells. To this end I examined Bag-1 expression in parental MCF-10A cells via immunofluorescence and confirmed heterogeneity of Bag-1 expression (Figure 27).

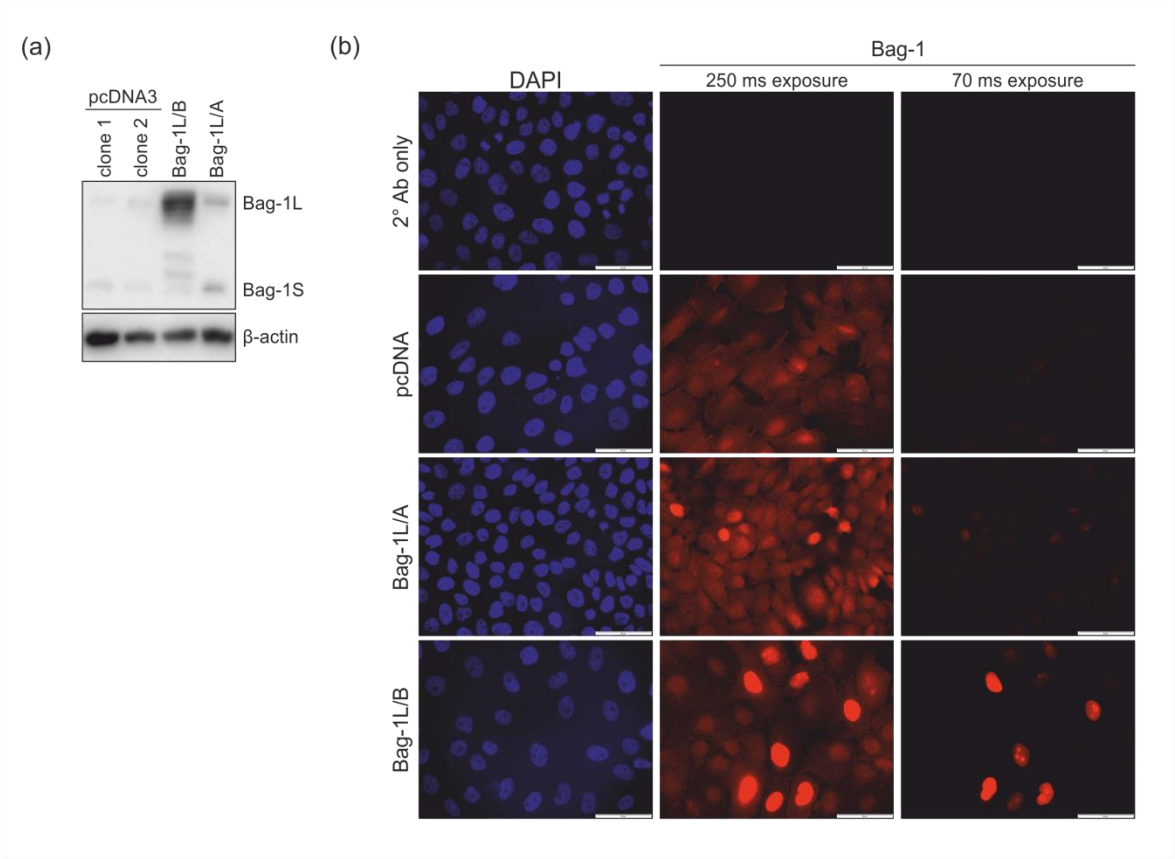

Figure 26 Bag-1L abundance and localisation in Bag-1L/A and Bag-1L/B clones

(a) Representative immunoblot of Bag-1 expression; β-actin was included as a loading control. (b) Representative images of immunofluorescence staining for Bag-1 (red) and DAPI counterstain (blue) in monolayer cultures. Two exposures times are shown for Bag-1 staining. Scale bars show 50 µm. Immunoblotting analysis (a) was carried out by Hashim Sayed (MMedSci report).

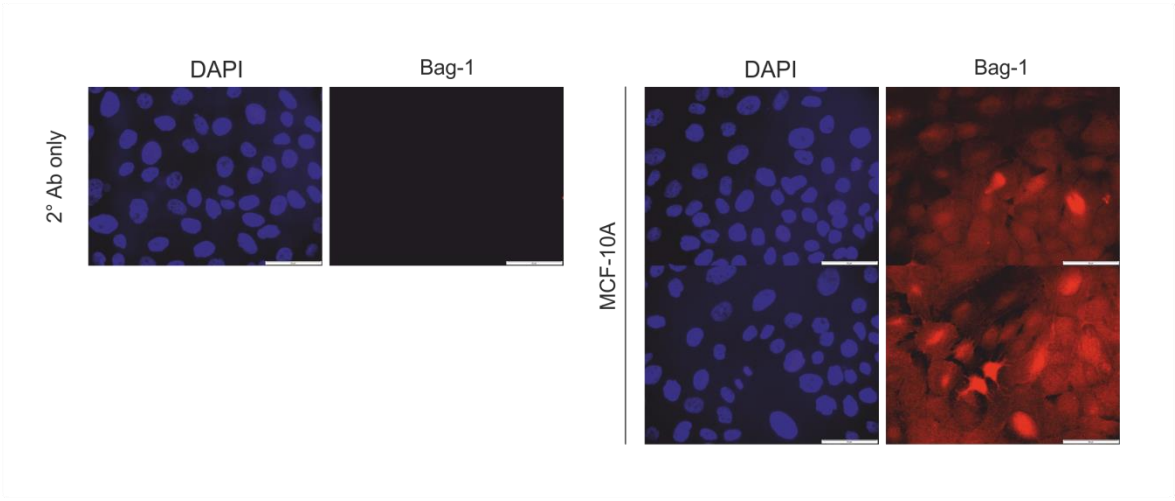

Figure 27 Bag-1 staining is heterogeneous in parental MCF-10A

Representative images of immunofluorescence staining for Bag-1 (red) and DAPI counterstain (blue) in monolayer cultures; scale bars show 50 µm.

We sought to characterise the effect of Bag-1L overexpression in 2D culture, examining cell morphology, colony forming efficiency and proliferation. Clones adopted a cobblestone appearance, with lamellipodia extending from the edges of clusters, typically observed in parental MCF-10A cells (Figure 28a) (Debnath, Muthuswamy et al. 2003). Overexpression of Bag-1L did not alter colony forming efficiency (Figure 28b) and did not support anchorage-independence growth *in vitro* or tumour growth *in vivo* (data not show, work carried out by Manos Papadakis), features characteristic of parental MCF-10A cells (Soule, Maloney et al. 1990, Miller, Soule et al. 1993). However high but not low Bag-1L overexpression statistically significantly ($p \leq 0.05$) decreased proliferation when examined using a crystal violet assay (Figure 28c), shown by a 38% reduction in crystal violet absorbance in Bag-1L/B compared to pcDNA.

3.2 Characterisation of Bag-1L/A and Bag-1L/B in 3D

To confirm Bag-1L overexpression was maintained following 3D culture, acinar lysates were harvested at day 12 of morphogenesis for immunoblotting (Figure 29a). Bag-1L protein levels were 9-fold and 16-fold higher in Bag-1L/A and Bag-1L/B acini respectively compared to pcDNA.

Luminal status of acini was examined on day 20 of morphogenesis, when parental acini display growth arrested structures and an evidently hollowed lumen (Debnath, Muthuswamy et al. 2003). As expected, the majority of pcDNA acini were hollowed with only 9% of acini displaying an incompletely cleared phenotype (Figure 29b,c). In contrast, Bag-1L overexpression statistically significantly increased the number of filled acini ($p \leq 0.05$), with 26% and 86% of Bag-1L/A and Bag-1L/B acini respectively scoring as incompletely cleared. Moreover, examination via phase-contrast microscope revealed a branching morphology present in Bag-1L-overexpressing acini that resembled an atypical phenotype reported previously in breast cancer cells (Figure 29d,e) (Kenny, Lee et al. 2007). While only 3% of controls scored as atypical, low or high Bag-1L overexpression resulted in a 5- or 29-fold increase respectively in atypical acini compared to controls, with 86% of high Bag-1L-overexpressing acini scoring as atypical.

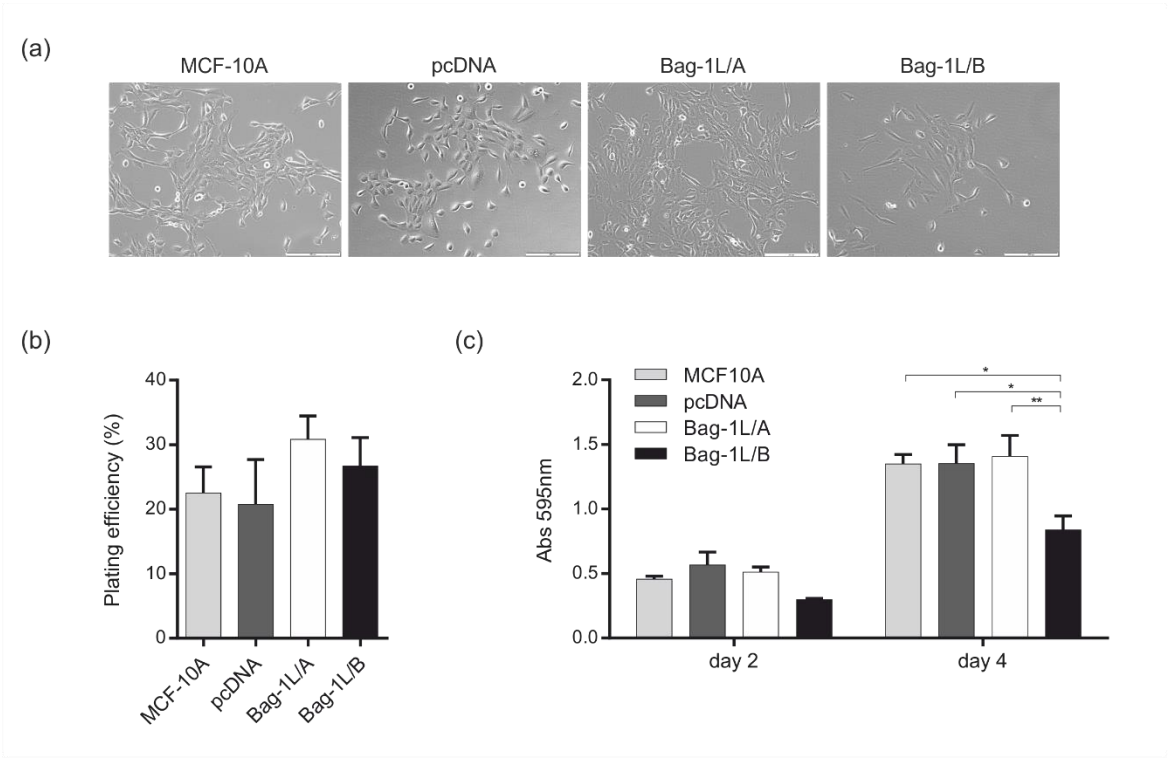

Figure 28 Effect of Bag-1L overexpression on MCF-10A 2D cultures

(a) Phase contrast images reveal that Bag-1L-overexpressing cells adopt a cobblestone appearance typical of MCF-10A; scale bars show 200 µm. (b) The colony-forming efficiency of MCF-10A Bag-1L clones was assessed in a clonogenic assay and expressed as the plating efficiency. (c) Proliferation was measured at days 2 and 4 of culture. Cells (20,000 per well) were plated at day 0 and were fixed in methanol and stained with crystal violet. Stain was dissolved in 20% acetic acid and absorbance at 595 nm recorded. Bar graphs represent the mean ± SEM from three independent experiments, each with three technical repeats. * $p \leq 0.05$, ** $p \leq 0.01$ as determined by two-way ANOVA with Bonferroni's multiple comparisons test. Phase contrast images (a) were collected by Hashim Sayed (MMedSci report) and clonegenic assay (b) was carried out by Tom Reeves (MMedSci report). Proliferation assay (c) was carried out in collaboration with Manos Papadakis.

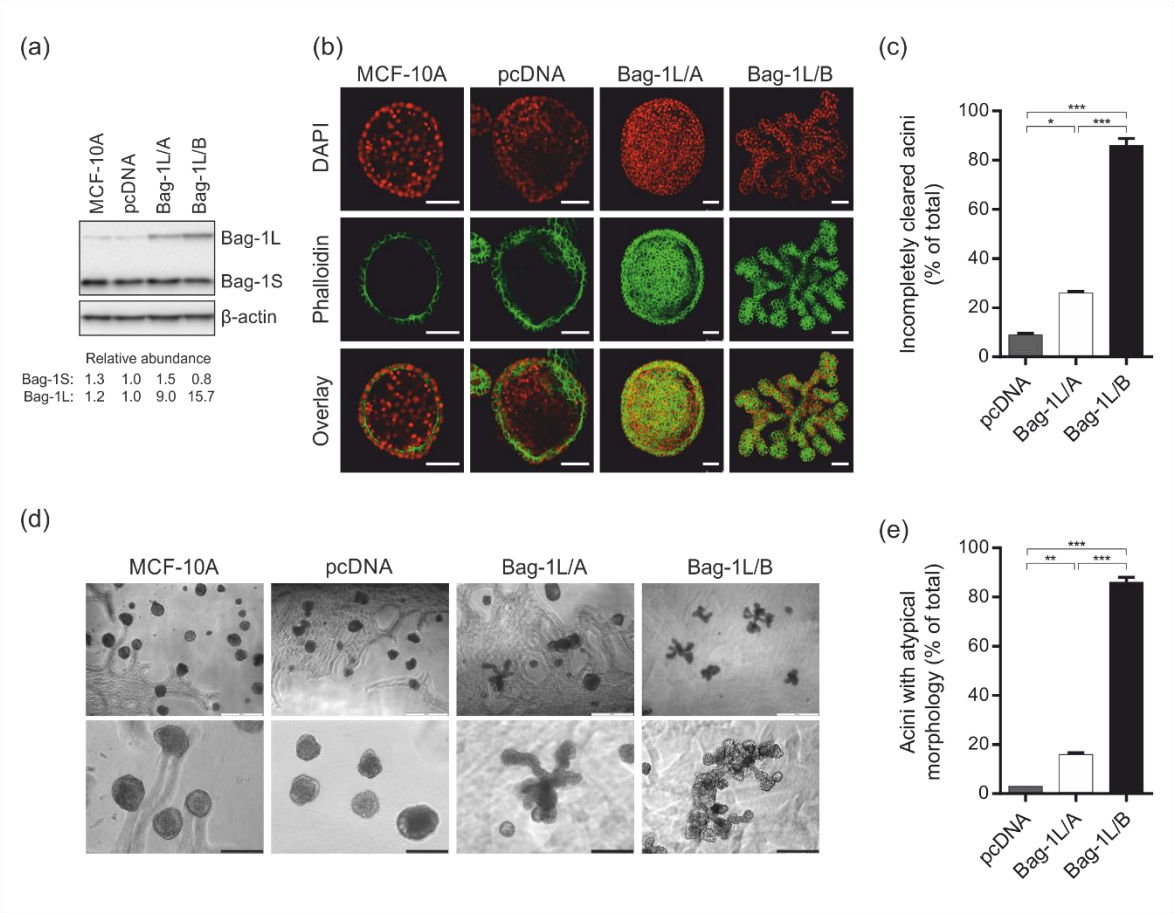

Figure 29 Bag-1L overexpression attenuates luminal clearing and promotes an atypical acinar morphology

(a) Immunoblot analysis of Bag-1 expression in lysates harvested from MCF-10A acini clones cultured in 3D for 12 days; β-actin was included as a loading control. Densitometry analysis shows the abundance of Bag-1S and Bag-1L protein isoforms relative to pcDNA control. (b) Representative confocal immunofluorescence images show the centre of MCF-10A acini at day 20 of morphogenesis. Cells were stained with DAPI (red) and phalloidin-TRITC (green); scale bars show 100 µm. (c) Acini with incompletely cleared lumens at day 20 of morphogenesis were counted and their numbers expressed as a percentage of total acini. (d) Representative phase-contrast images of acini at day 20 of morphogenesis reveal an atypical external morphology in Bag-1L-overexpressing acini. Two magnifications are shown; white scale bars show 500 µm, black scale bars show 200 µm. (e) Acini with an atypical morphology were counted at day 20 of morphogenesis and their numbers expressed as a percentage of total acini. Bar graphs represent the mean ± SEM from at least three independent experiments, each with two technical repeats. * $p \leq 0.05$, ** $p \leq 0.01$, *** $p \leq 0.001$ as determined by a one-way ANOVA with Bonferroni's multiple comparisons test. All data presented here was produced by Hashim Sayed (MMedSci report), excluding immunoblot analysis (a) which was carried out by myself.

To further characterise the effect of Bag-1L overexpression on acinar morphogenesis, cell proliferation and apoptosis were examined by immunofluorescence staining (Figure 30). During parental MCF-10A acinar morphogenesis, cells undergo a well-defined program of proliferation, differentiation, apoptosis and growth arrest (Figure 3) (Debnath, Mills et al. 2002); central cells undergo apoptosis from around day 8, with acinar proliferation stopping around day 12 (Debnath, Mills et al. 2002, Imbalzano, Tatarkova et al. 2009). Proliferation was examined on day 6 and day 20 of morphogenesis using the cell protein marker of proliferation Ki67, which detects a nuclear antigen present in all stages of the cell cycle associated with proliferation, but absent from growth-arrested cells (Gerdes, Schwab et al. 1983). Apoptosis was examined on day 12 of morphogenesis using M30, which recognises caspase-cleaved cytokeratin 18 (Leers, Kolgen et al. 1999). Parental MCF-10A acini and pcDNA controls stain positive for proliferation in ECM-attached cells located at the periphery of acini at day 6 of culture; at day 20 of culture acini exhibited minimal Ki67 staining consistent with a growth arrested structure (Figure 30a). While the Bag-1L/A clone showed Ki67 staining consistent with the pattern observed for controls, Bag-1L/B acini stained positive for proliferation throughout the acini structure at day 6; this effect was lost by day 20, with acini exhibiting minimal Ki67 staining. At day 12 of culture, luminal, ECM-detached cells stained positive for apoptosis in control acini (Figure 30b). Both Bag-1L-overexpressing clones had almost undetectable levels of M30 staining.

3.3 Effect of HER2 overexpression on acinar morphogenesis and a comparison between HER2- and Bag-1L-overexpressing MCF-10A cells

3.3.1 Generation of HER2-overexpressing pooled population

I was interested in comparing the morphogenesis of Bag-1L-overexpressing acini with a described and recognised model of MCF-10A transformation by HER2 overexpression. HER2 overexpression in MCF-10A acini promotes filled lumens and an atypical structure (Muthuswamy, Li et al. 2001), similar to that observed in Bag-1L-overexpressing clones. A pooled population of MCF-10A overexpressing HER2 (denoted HER2) were generated by retroviral infection using a pBABEpuro-ErbB2 vector. A pooled population using an empty pBABEpuro construct was generated as an experimental control (denoted puro). HER2 overexpression was confirmed by immunoblotting (Figure 31a) and localisation examined by immunoblotting (Figure 31b). HER2 protein was not detected in MCF-10A or puro cells under these experimental conditions. Across the HER2 population, HER2 staining is positive in cells with more intense staining observed at the periphery.

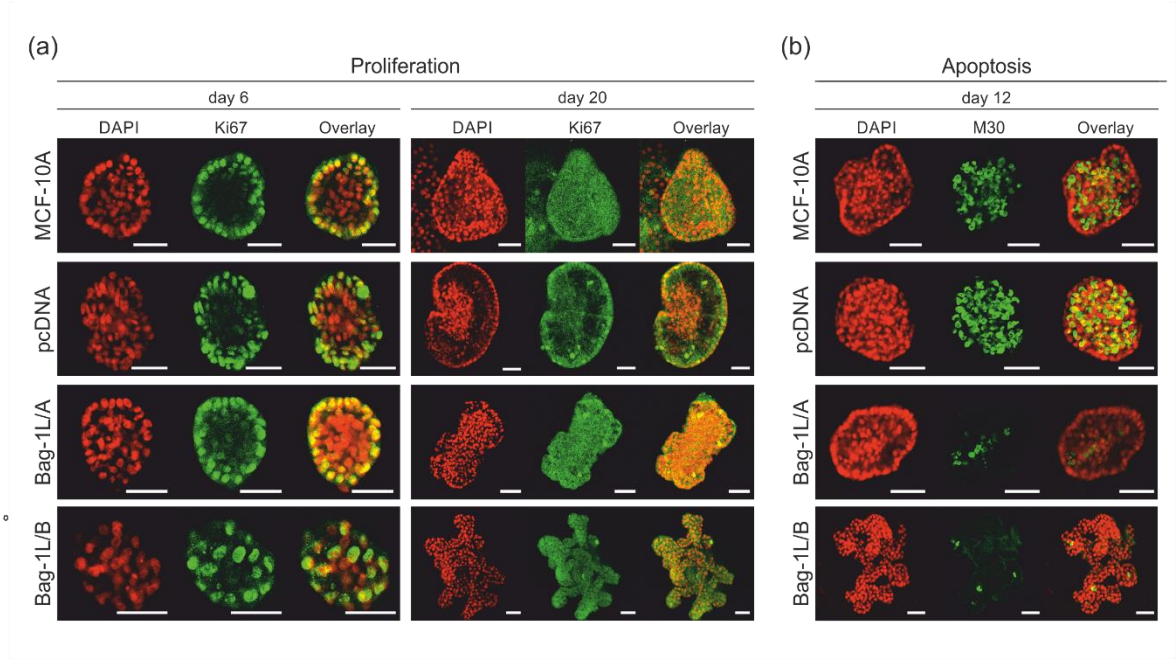

Figure 30 Bag-1L does not prevent cell cycle arrest but attenuates luminal apoptosis during acinar morphogenesis

Representative confocal immunofluorescence images show the centre of MCF-10A acini at the indicated time points of morphogenesis. Cells were stained with DAPI (red) and either Ki67 (green) to examine proliferation (a) or M30 (green) to examine apoptosis (b); scale bars show 50 µm. All data presented here was produced by Hashim Sayed (MMedSci report).

3.3.2 Characterisation of HER2 pooled populations in 3D culture

Acini were scored for luminal status on day 12 of morphogenesis, when parental acini display an evidently hollowed lumen (Debnath, Muthuswamy et al. 2003). Puro behaved characteristically of parental acini, with the majority of acini having undergone luminal clearing and just 20% of acini displaying an incompletely cleared phenotype (Figure 32a,b). In contrast 80% of the HER2 acini scored as incompletely cleared, indicating HER2 overexpression is attenuating luminal clearing.

To examine acinar morphology, acini were scored on day 20 of morphogenesis. At this time point of acinar morphogenesis parental acini have undergone growth and proliferation arrest and the morphology observed is therefore their final morphology (Muthuswamy, Li et al. 2001, Debnath, Mills et al. 2002). The puro population behaved characteristically of MCF-10A acini with only 14% of acini adopting an atypical structure (Figure 32c,d). HER2 display a statistically significantly increased ($p \leq 0.001$) number of atypical acini, with a 4-fold increase in atypical structures compared to controls (Figure 32d). Two types of atypical structures were observed, a branching structure and a non-rounded structure (Figure 32c).

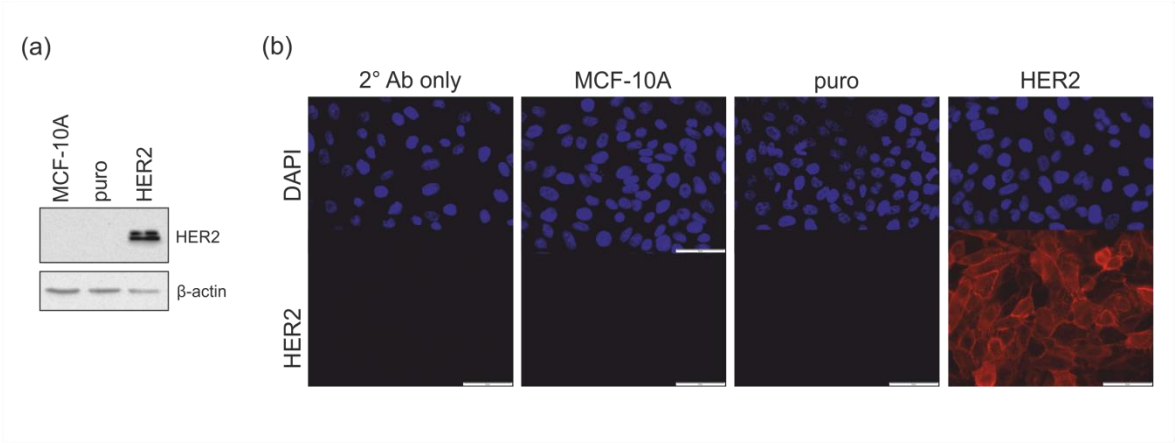

Figure 31 HER2 abundance and localisation in MCF-10A pooled populations

(a) Representative immunoblot of HER2 expression in retrovirally transduced MCF-10A pooled populations; β-actin was included as a loading control. (b) Representative images of immunofluorescence staining for HER2 (red) and DAPI counterstain (blue) in monolayer cultures; scale bars show 50 µm.

This work confirmed that HER2 overexpression can attenuate luminal clearing and drive an atypical morphology in my model, in agreement with the literature (Muthuswamy, Li et al. 2001, Debnath, Mills et al. 2002). Based on the phenotypic similarities between HER2- and Bag-1L-overexpressing MCF-10A acini I investigated whether these models shared a metabolic transformation documented for HER2 overexpression, which may drive the 3D phenotype, by using a 2D growth factor-responsiveness assay.

3.4 Comparison of 2D growth response to growth factors between Bag-1L- and HER2- overexpressing MCF-10A cells

MCF-10A cells display growth factor-dependence (Soule, Maloney et al. 1990) requiring insulin-like growth factor 1, which is chemically and functionally similar to insulin (Rechler and Nissley 1985), for growth (Ram, Kokeny et al. 1995). Overexpression of HER2 metabolically transforms MCF-10A cells, enhancing glucose uptake even in the absence of insulin-like growth factor 1 receptor activity and promoting insulin-independent proliferation (Ignatoski, Lapointe et al. 1999, Schafer, Grassian et al. 2009, Bollig-Fischer, Dewey et al. 2011). Within the 3D HER2 acini model, this metabolic transformation is described to attenuate the metabolic stress induced from ECM-detachment, overcoming a detachment induced accumulation of ROS which is a consequence of reduced glucose uptake (Schafer, Grassian et al. 2009); this enables HER2 transformed cells to survive in the lumen of an acinus. I investigated whether the similar to HER2 atypical phenotype

of Bag-1L-overexpressing acini could be associated with a loss of insulin-dependence using a 2D assay to examine growth-factor responsiveness.

Cells were cultured in insulin-free or insulin-containing media, using HER2 as a positive control for insulin-independent growth. No statistically significant difference in the growth of HER2 was observed in these conditions (Figure 33a), indicative of a loss of insulin responsiveness and consistent with previous studies (Bollig-Fischer, Dewey et al. 2011). In contrast, puro and pcDNA controls showed a statistically significant ($p \leq 0.05$) approximately 1.4-fold increase in growth in the presence of- compared with the absence of- insulin. Similarly, growth increases of approximately 1.6- and 1.5-fold were observed in the presence compared with the absence of insulin in Bag-1L/A and Bag-1L/B respectively, indicating responsiveness to this hormone. All cell lines were responsive to EGF for growth (Figure 33b) as previously reported (Ignatoski, Lapointe et al. 1999).

3.5 Effect of Bag-1 inhibition on 2D culture and acinar morphogenesis

We sought to examine the effect of Bag-1 inhibition on acinar morphogenesis using the small molecule inhibitor of Bag-1 protein-protein interactions Thioflavin S (Sharp, Crabb et al. 2009) and the biologically active constituent Thio-2 (Enthammer, Papadakis et al. 2013). We examined the viability of MCF-10A clones to Thioflavin S and Thio-2 in 2D and confirmed the previously published finding that Thio-2 was more active than Thioflavin S (Enthammer, Papadakis et al. 2013) (Figure 34a); Thio-2 statistically significantly ($p \leq 0.001$) decreased growth across all clones at 50 µM and 100 µM, while Thioflavin S had no effect in the concentration range tested. Thio-2 was therefore used for subsequent experiments.

We tested whether the atypical morphology of Bag-1L-overexpressing acini could be pharmacologically reversed by Thio-2. Cells were cultured in 2D and pre-treated with 50 µM Thio-2 for 24 h before seeding onto Matrigel, with additional 25 µM Thio-2 treatments administered on days 4 and 8 of 3D culture; the concentration of Thio-2 administered to 3D cultures was lowered due to increased toxicity observed in 3D compared to 2D culture (data not shown, work done by Tom Reeves). Thio-2 treatment statistically significantly ($p \leq 0.05$) reduced the number of atypical acini by 17% in Bag-1L/A and 29% in Bag-1L/B compared with DSMO control (Figure 34b). In addition, acini displaying the atypical branching morphology exhibited reduced levels of branching following Thio-2 treatment (Figure 34c).

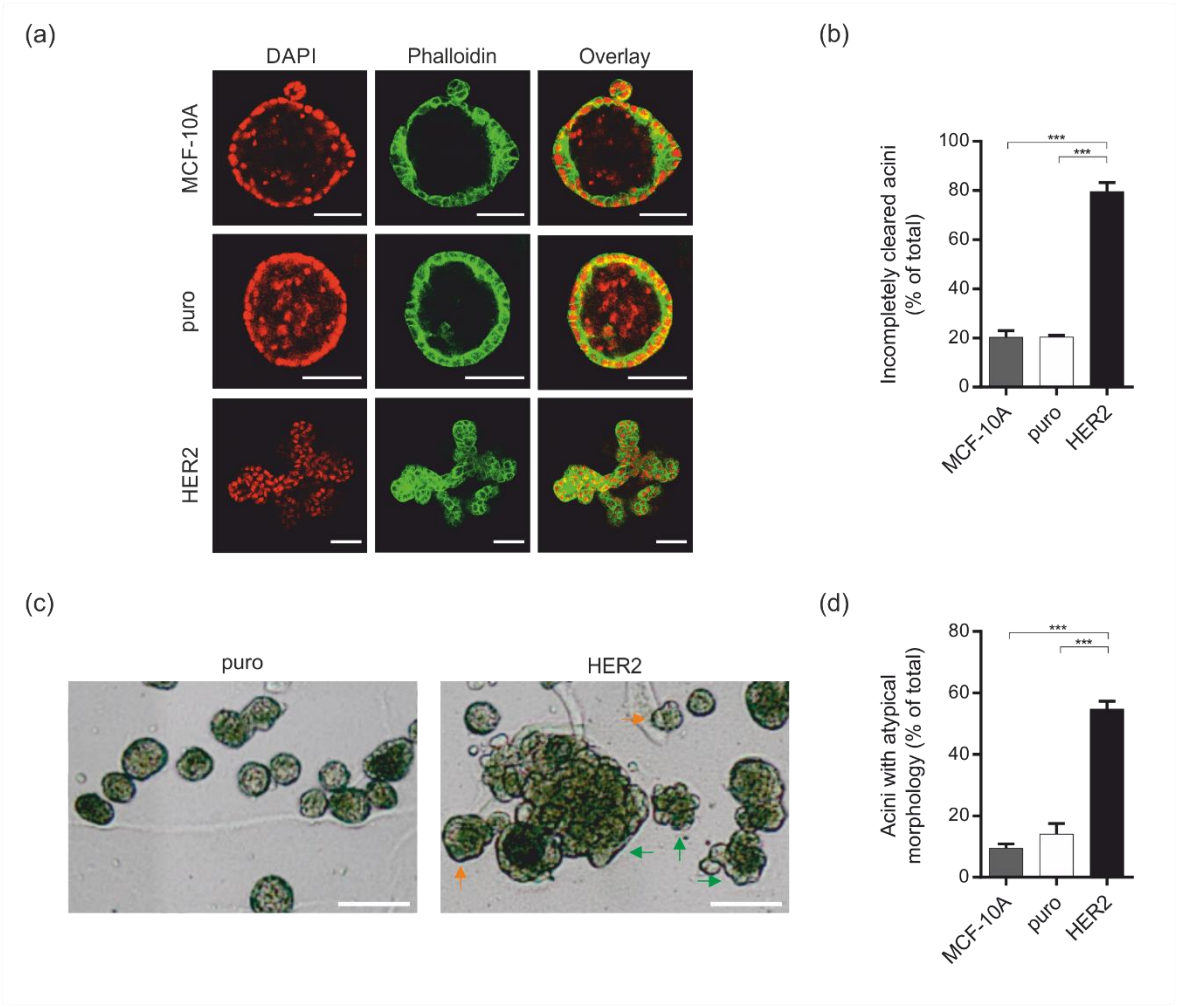

Figure 32 HER2 overexpression promotes an incompletely cleared, atypical MCF-10A acinar morphology

(a) Representative confocal immunofluorescence images show the centre of MCF-10A acini at day 12 of morphogenesis. Cells were stained with DAPI (red) and phalloidin-TRITC (green); scale bars show 50 µm. (b) Acini with incompletely cleared lumens at day 12 of morphogenesis were counted and their numbers expressed as a percentage of total acini. (c) Representative phase-contrast images of acini at day 12 of morphogenesis reveals two atypical externals morphology in HER2-overexpressing acini; arrows indicate branching (green) and non-rounded (orange) acini structures. Scale bars show 200 µm. (d) Acini with an atypical morphology were counted at day 12 of morphogenesis and their numbers expressed as a percentage of total acini. A minimum of 150 acini were present in each technical repeat. Bar graphs represent the mean ± SEM from three independent experiments, each with four technical repeats. *** $p \leq 0.001$ as determined by a one-way ANOVA with Bonferroni's multiple comparisons test.

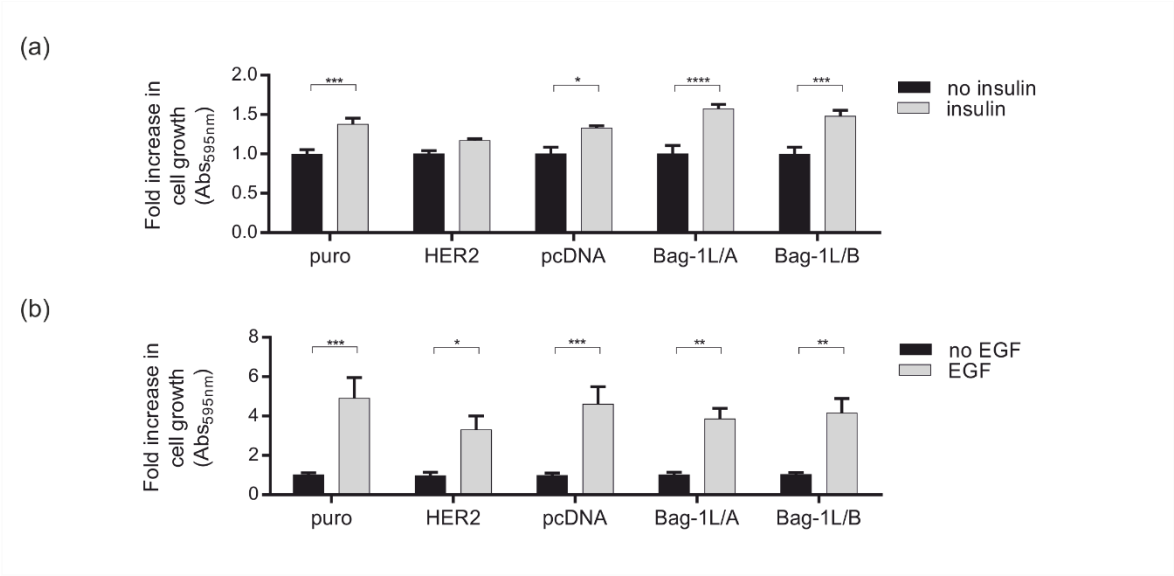

Figure 33 Bag-1L-overexpressing MCF-10A clones display growth factor-responsiveness in 2D cultures

Insulin and EGF sensitivity was assessed over 48 h (following a 24 h serum starvation) in 2D, serum-free culture conditions. Following treatment with the indicated growth factor, cells were fixed in methanol and stained with crystal violet. Stain was dissolved in 20% acetic acid and absorbance at 595 nm recorded. Bar graphs represent the mean fold change ± SEM in absorbance for each cell line, relative to growth in growth factor-free media. Data are from three independent experiments, each with three technical repeats. * $p \leq 0.05$, ** $p \leq 0.01$, *** $p \leq 0.001$ as determined by two-way ANOVA with Bonferroni's multiple comparisons test.

To investigate the potential signalling pathways involved in the atypical acinar morphology we examined the role of Thio-2 on the activities of Erk and Akt. Signalling was examined by immunoblotting of lysates harvested following serum stimulation of serum-starved cells in 2D culture (Figure 35). Any signalling inhibition observed following Thio-2 inhibition in 2D culture is a good pathway to examine in the more complex 3D system as a potential pathway which may be contributing to the atypical morphology which Thio-2 is capable of reversing. Consistent with previous reports (Anderson, Sutherland et al. 2010), pErk levels were upregulated in Bag-1L-overexpressing cells compared to pcDNA controls; pErk upregulation correlated with Bag-1L expression levels. pAkt levels were also upregulated in Bag-1L/B, but not Bag-1L/A, compared to pcDNA. There was no noticeable effect on Erk and Akt activation following Thio-2 treatment when examined in this setting. UO126, a MEK inhibitor, was included in this assay as a positive control for pErk inhibition and resulted in reduced levels of pErk1/2 compared to DMSO controls.

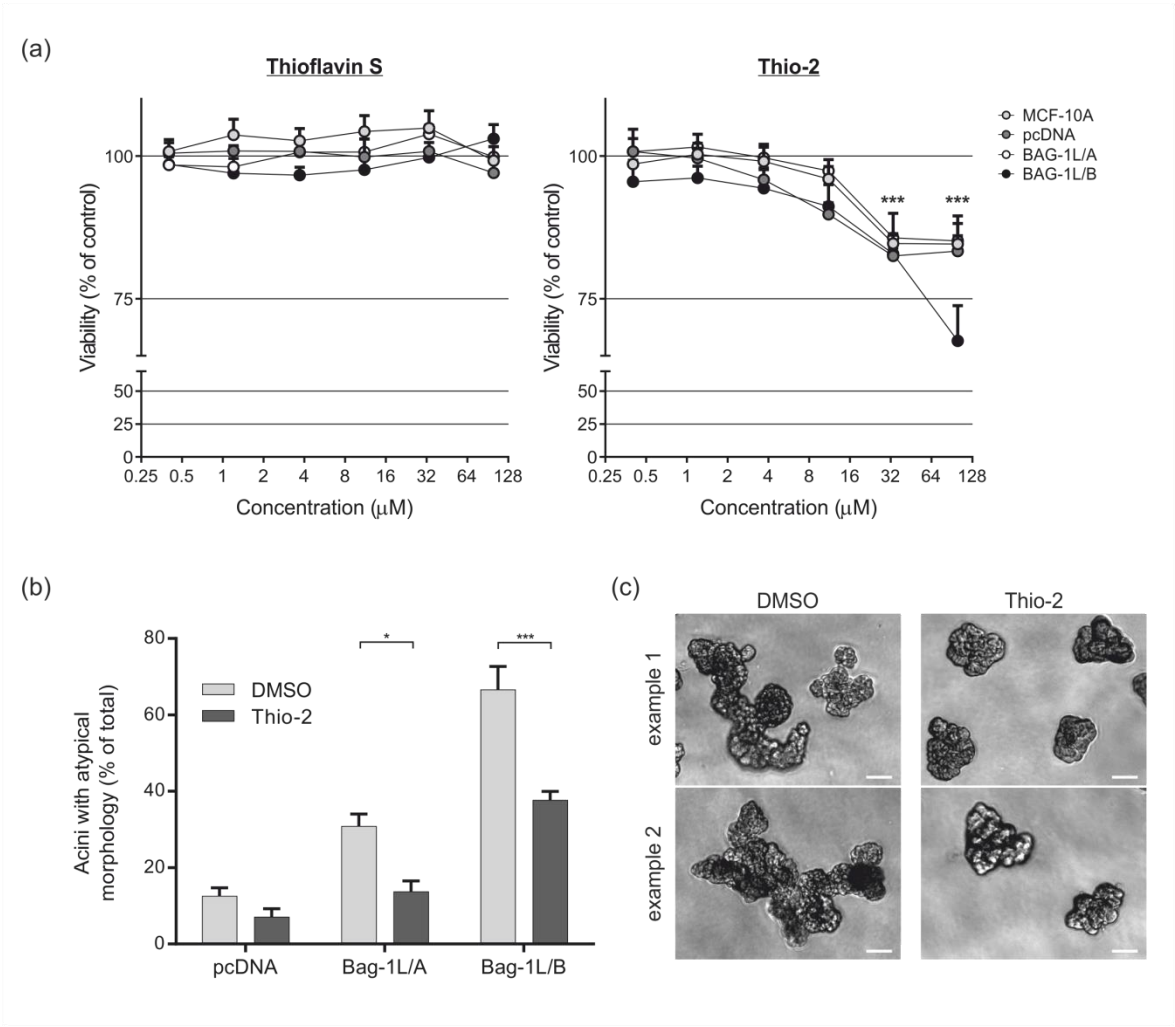

Figure 34 Thio-2 can partially reverse the atypical acinar morphology associated with Bag-1L overexpression

(a) MCF-10A cells were treated with Thioflavin S or Thio-2 at the indicated concentration for 5 days and viability assessed by CellTiter Aqueous One solution assay. Values represent the mean ± SD as a percentage of DMSO-treated cells. (b) MCF-10A cells were treated for 24h with Thio-2 (50 μM) or DMSO (0.5% v/v) before seeding in 3D morphogenesis assays. Acini were allowed to form for 14 days, with further Thio-2 (25 μM) or DMSO (0.25% v/v) treatment administered on days 4 and 8 of culture. Acini with an atypical morphology were counted and their numbers expressed as a percentage of total acini. Bar graphs represent the mean ± SEM from four independent experiments each with two technical repeats. (c) Representative phase-contrast images of Bag-1L/B acini show the atypical external morphology in the presence of DMSO or Thio-2; scale bars show 50 μm. * $p \leq 0.05$, *** $p \leq 0.001$ as determined by two-way ANOVA with Bonferroni's multiple comparisons test. Viability assay (a) was carried out by Manos Papadakis, atypical morphology scoring (b) was carried out by Tom Reeves (MMedSci report). Representative images of morphology (c) were collected by me.

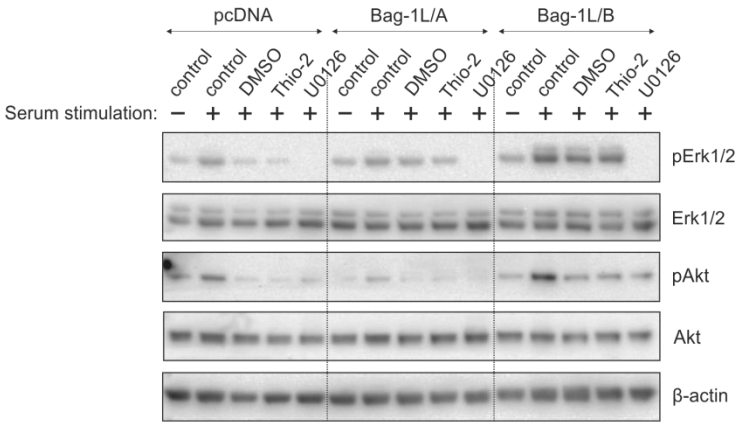

Figure 35 Thio-2 treatment in 2D culture does not inhibit Erk or Akt signalling

Immunoblot analysis shows the effect of serum stimulation alone (10%) or in the presence of DMSO (0.5%), Thio-2 (50 µM) or U0126 (25 µM) on the activation of Erk and Akt in serum-starved cells; β-actin was included as a loading control. This work was carried out in collaboration with Manos Papadakis.

3.6 Bag-1L overexpression results in E-cadherin downregulation

Preliminary data suggested Bag-1L overexpression in Bag-1L/B may result in a reduction in E-cadherin (Hashim Sayed, MMedSci report). Kenny *et al*. categorised the 3D cell culture phenotypes of human breast cancer cell lines into four distinct morphologies with these morphologies largely correlating with the gene expression profiles (Kenny, Lee et al. 2007). The grape-like morphology described is characterised by reduced cell-cell adhesions, with eight out of nine of the cell lines isolated from metastases, suggestive that this morphology marks cells with a migratory potential. As Bag-1L/B fits closest into the grape-like morphology status, and E-cadherin is a cell-cell adhesion molecule whose loss is associated with increased invasiveness and metastases (Canel, Serrels et al. 2013), I looked to confirm the role of Bag-1L overexpression in E-cadherin regulation (Figure 36) and migration (data not shown, reported in my MRes rotation project C report).

E-cadherin levels were reduced in Bag-1L-overexpressing clones and densitometry analysis showed a statistically significant ($p \leq 0.05$) reduction in E-cadherin levels of over 50% in Bag-1L/A and Bag-1L/B compared to pcDNA controls; the extent of E-cadherin downregulation increased with increasing Bag-1L overexpression (Figure 36a). To determine whether this phenotype is unique to MCF-10A cells grown in 3D culture, E-cadherin levels in MCF-10A clones grown in monolayer cultures were analysed by immunoblotting. Similarly to the 3D culture, E-cadherin

expression inversely correlated with Bag-1L expression in monolayer cultures (Figure 36b). E-cadherin is a marker of the epithelial-to-mesenchymal transition so I next examined the role of Bag-1L in migration. Bag-1L overexpression was found to have no effect on the migration of MCF-10A cells to collagen I in transwell migration assays (data not shown, reported in my MRes rotation project C report).

3.7 Discussion

This study examined the role of Bag-1L in acinar morphogenesis, the first time isoform specific roles of Bag-1 have been investigated in this setting. Our data demonstrate that overexpression of the Bag-1L isoform alone is sufficient to suppress luminal apoptosis and drive the formation of branched, atypical MCF-10A acini. This branching, atypical structure was reversible by treatment with a Bag-1 protein-protein interaction inhibitor, Thio-2. In addition, Bag-1L acini were phenotypically similar to the transformed acini formed following overexpression of HER2, which have been published by others (Muthuswamy, Li et al. 2001, Pradeep, Zeisel et al. 2012) and generated here by myself. However, in contrast to HER2 acini, Bag-1L-overexpressing MCF-10A retain insulin responsiveness.

Bag-1 expression is heterogeneous in MCF-10A

Bag-1 expression was shown to be heterogeneous in the stable clones (Figure 26) and in parental MCF-10A cells (Figure 27). Heterogeneous expression of endogenous Bag-1 in parental cells confirms that the heterogeneity of expression is not a consequence of the cloning procedure or the subsequent antibiotic selection, but a phenotype of the cell line. The presence of heterogeneity within a genetically identical population implicates a post-translational modification in the modulation of Bag-1 levels within MCF-10A.

The role of Bag-1L in proliferation of 2D cultures

Our data shows that Bag-1L overexpression results in decreased MCF-10A cell growth in 2D cultures. While this was only seen in the highest Bag-1L-overexpressing clone (Figure 28c), it supports previous observations in non-tumourigenic HaCaT skin epidermal keratinocytes, who show that overexpression of either of the three isoforms of Bag-1 reduced growth rate (Hinitt, Wood et al. 2010).

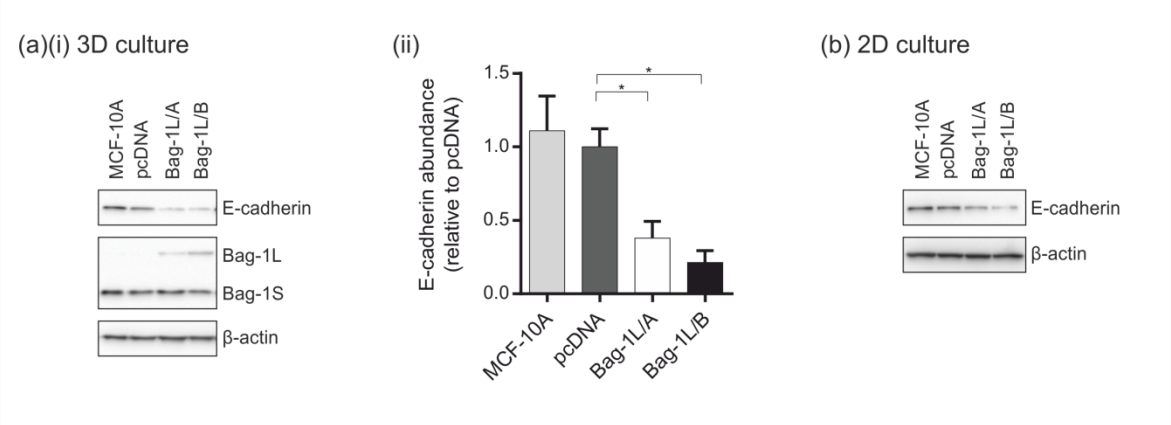

Figure 36 E-cadherin is downregulated in Bag-1L-overexpressing clones

(a) Representative immunoblot (i) of E-cadherin expression in lysates harvest from MCF-10A acini clones cultured in 3D for 12 days, with relative protein abundance for E-cadherin (ii) expressed relative to pcDNA control. Bar graphs represent the mean protein abundance ± SEM relative to E-cadherin levels in pcDNA from two independent experiments with two technical repeats; all four data sets were plotted. * $p \leq 0.05$ as determined by a one-way ANOVA with Bonferroni's multiple comparisons test. (b) Immunoblot of E-cadherin expression in lysates harvested from MCF-10A clones cultured in 2D. Lysates were harvest directly from the dish (no trypsinisation). β-actin was included as a loading control. E-cadherin was examined in 2D culture in a single experiment.

Bag-1L prevents luminal clearing in the MCF-10A acini model

Bag-1L overexpression was shown to suppress lumen formation, driving formation of acini with a filled phenotype (Figure 29b,c). Anderson *et al.* showed that co-expression of Bag-1S, Bag-1M and Bag-1L can result in attenuation of the luminal apoptosis pathway (Anderson, Sutherland et al. 2010). Similarly, staining for apoptosis and proliferation markers (Figure 30) indicate that overexpression of Bag-1L does not prevent eventual cell cycle arrest but does attenuate luminal apoptosis during acinar morphogenesis. In line with the mechanism of luminal filling described for HER2 acini (Debnath, Mills et al. 2002), our findings imply that the filled phenotype is a consequence of apoptosis inhibition, and not due to continual proliferation of cells which enter the luminal space.

MCF-10A acinar morphogenesis is a highly regulated sequence of events (Figure 3) (Debnath, Muthuswamy et al. 2003). ECM-detachment induces luminal clearing through anoikis driven by Bim_{EL} (Debnath, Mills et al. 2002, Reginato, Mills et al. 2005, Schafer, Grassian et al. 2009); this proapoptotic protein accumulates due to a downregulation of Erk signalling (Figure 19a) (Reginato, Mills et al. 2003). Anderson *et al.* have shown that Bag-1 overexpression results in activation of Erk signalling, impeding luminal apoptosis by targeting Bim_{EL} for proteosomal degradation (Anderson, Sutherland et al. 2010). We also observed an upregulation of pErk in the Bag-1L-overexpressing clones compared to pcDNA that correlated with the level of Bag-1L

overexpression (Figure 35) and which, taken together with the literature, implies that Erk signalling has a role in the Bag-1L-driven phenotype of luminal filling. Although it has previously been shown that Thio-2 can downregulate the activity of Erk in MCF7 cells this was not the case in the MCF-10A model (Figure 35). We therefore did not pursue the use of Thio-2 to examine the mechanism by which Bag-1L-overexpression can overcome luminal clearing pathways.

Anoikis suppression alone is insufficient to prevent luminal clearing, with overexpression of an anti-apoptotic protein reported to delay but not completely prevent luminal clearing (Debnath, Mills et al. 2002). A metabolic defect upon ECM-detachment also promotes clearing (Schafer, Grassian et al. 2009). While luminal apoptosis begins around day 8 of parental acinar morphogenesis (Debnath, Muthuswamy et al. 2003), luminal filling following Bag-1L overexpression was observed at a late time point of morphogenesis (day 20, Figure 29b,c). This indicates that Bag-1L overexpression is able to protect from both anoikis and metabolic stress. In the case of the well characterised HER2 acini, an upregulation of glucose uptake upon ECM-detachment prevents the induction of metabolic stress (Schafer, Grassian et al. 2009). This can be examined in 2D culture by monitoring the insulin-responsiveness of cells; HER2 transformation enhances glucose uptake independently of insulin-like growth factor 1 or insulin leading to insulin insensitivity (Bollig-Fischer, Dewey et al. 2011). Despite the phenotypic similarities in HER2 and Bag-1L acini relating to luminal filling and morphology, Bag-1L-overexpressing clones retained insulin responsiveness (Figure 33a). This suggests that Bag-1L overexpression overcomes the metabolic defects associated with detachment via a different transforming mechanism to HER2.

Bag-1L drives a branching, atypical structure in the MCF-10A acini model

Although Anderson *et al.* did not report an atypical branching morphology following co-expression of Bag-1S, Bag-1M and Bag-1L (Anderson, Sutherland et al. 2010), here we report a Bag-1L-driven branching, atypical structure (Figure 29d,e). This was reversible upon targeting Bag-1 with a protein-protein interaction inhibitor (Thio-2) (Figure 34b,c), providing evidence to support the observation that the atypical phenotype is a consequence of Bag-1L overexpression. The level of Bag-1L overexpression correlated with the phenotypic effect of compound treatment, with the Bag-1L/B clone showing the greatest reversal in morphology in response to Thio-2 treatment (Figure 34b). The fact that this phenotype was not observed by Anderson *et al.* could be because the level of expression of Bag-1 was insufficient to induce the phenotype (Anderson, Sutherland et al. 2010). Alternatively it could be contributed to regulatory balance exerted by the combined activities of individual Bag-1 isoforms, considering also that Bag-1S will be the predominant isoform overexpressed. For example, Hinitt *et al.* measured single-cell movement from small colonies of HGF-stimulated HaCaT cells using scatter assays and showed that Bag-1L

overexpression resulted in greater than 2-fold cell-to-cell dissociation, whereas Bag-1S and Bag-1M retain their cell-to-cell contacts and exhibit no scattering (Hinitt, Wood et al. 2010).

The reduction in branching following Thio-2 treatment implicates Bag-1 protein-protein interactions in the Bag-1L-driven changes in morphology. We observed no noticeable inhibitory effects of Thio-2 on the activities of Erk and Akt when examined in this setting (Figure 35), implying that these signalling pathways may not be involved.

Bag-1L overexpression promotes E-cadherin downregulation in the MCF-10A clones

The atypical branching structure described for the Bag-1L/B clone most closely resembles the grape-like morphological structures described by Kenny *et al.*, which are characterised by poor cell-cell adhesions and display lower levels of E-cadherin than the structures which have robust cell-cell adhesions (Kenny, Lee et al. 2007). Consistent with this observation, a convincing down-regulation of E-cadherin protein levels has been shown following Bag-1L overexpression in our clones, which is relative to the level of Bag-1L overexpression and is not specific to the 3D culture system (Figure 36). This is of potential interest because E-cadherin down-regulation is causally associated with epithelial-to-mesenchymal transition, a hallmark of cancer metastasis (Lee, Dedhar et al. 2006). The mechanism of E-cadherin downregulation was not examined and could be at a transcriptional or translational level or be the result of enhanced protein turnover. While Bag-1 has already been formerly linked to transcriptional and proteosomal degradation pathways (Figure 15), regulation of E-cadherin is a previously unreported function of Bag-1 and may be promoting the atypical morphology observed.

In addition to the phenotypic similarities shared between Bag-1L and HER2 acini relating to luminal filling and morphology, HER2 MCF-10A also display a downregulation of E-cadherin which correlated with increased invasive and migratory potential (Kim, Yong et al. 2009). Based on the well published role of E-cadherin in migration and invasion of breast cancers (Frixen, Behrens et al. 1991, Vleminckx, Vakaet et al. 1991, Siitonen, Kononen et al. 1996, Meiners, Brinkmann et al. 1998), we hypothesised that E-cadherin loss may promote a higher migratory potential in Bag-1L-overexpressing clones. However, E-cadherin downregulation did not correlate with an increased migratory potential when examined in this setting. It is important to note that cells were under growth factor-free and serum-starved conditions in this assay, but Katz *et al.* showed that MCF-10A migration through transwell membranes is dependent on the presence of EGF in the lower chamber (Katz, Amit et al. 2007).

Conclusion

In summary our data describes a role for Bag-1L in driving phenotypic changes that are associated with a premalignant state in a 3D model of the breast. The ability of Thio-2 to reverse some of these transformations highlights the potential of this model to test the efficacy of other inhibitors of breast tumour initiation; such changes seen in 3D may not be observed in traditional 2D culture.

Chapter 4: The role of isoform-specific Bag-1S- or Bag-1L-overexpression on MCF-10A acinar morphogenesis

To follow on from the work presented in Chapter 3: 'The Bag-1 inhibitor, Thio-2, reverses an atypical 3D morphology driven by Bag-1L overexpression in an MCF-10A model of ductal carcinoma *in situ*' I was interested in further examining the individual roles of Bag-1 isoforms during acinar morphogenesis. While lipid based transfection generated two Bag-1L-overexpressing stably transfected clones (Bag-1L/A and Bag-1L/B), attempts to produce Bag-1S-overexpressing stable clones were unsuccessful (work done by Hashim Sayed and Tom Reeves during MMedSci placements). I therefore looked to move into retroviral infection using an amphotropic viral packaging system.

While transient transfection followed by appropriate antibiotic selection can generate chromosomal integrants, viral-mediated infection is a more efficient means to generate sustainable expression of a transgene due to viral-driven integration into the host genome (Kim and Eberwine 2010). In addition, transduction by virus-based vectors tends to result in uniform delivery of the vector into cells. This compares to the non-uniformity that can be seen with lipid based transfection, where some cells may carry a single plasmid copy and others carry multiple.

An amphotropic viral packing system is advantageous over the ecotropic system utilised by Anderson *et al.* to examine Bag-1 overexpression in retroviral pools (Anderson, Sutherland et al. 2010) as it enables direct infection of parental MCF-10A cells. I opted to use pooled populations over selecting individual clones because of the random nature of plasmid integration, which can disrupt another gene, and the existence of random genetic drift. Both of these can lead to a phenotype which is not a direct result of overexpression of the transgene. In pooled populations, while both of these effects can still occur within a clone in that population, the effect is minimised when examining the population as a whole.

The use of pooled, retroviral-transduced populations overexpressing Bag-1S or Bag-1L will allow me to collect further evidence to support our findings relating to the role of Bag-1L in acinar morphogenesis, while also enabling a direct comparison between the role of Bag-1S and Bag-1L isoforms in this setting.

4.1 Generation of Bag-1-overexpressing pooled populations

For this work I needed to produce Bag-1 coding vectors optimised for Bag-1S or Bag-1L expression with an appropriate retroviral vector backbone (pBABEneo).

4.1.1 Generation of Bag-1 vectors

A Bag-1S optimised overexpression vector (denoted pBABEneo-Bag-1SM) was generated by a four step cloning strategy summarised in Figure 37. A pGEX-2T bacterial expression vector containing the human Bag-1 cDNA with a modification at the 5'-terminus of the Bag-1 coding region that removes the mammalian Bag-1L start site was provided by Manos Papadakis. Through restriction enzyme double-digests the Bag-1 coding region was firstly removed from pGEX-2T-Bag-1 (Figure 37a) and, in a separate digest, the pBABEneo vector was linearised (Figure 37b). Reaction products were run on an agarose gel and bands corresponding to the relevant sizes of the Bag-1 insert or linearised vector were extracted from the gel (Figure 37c). Products were ligated together to generate the pBABEneo-Bag-1SM plasmid (Figure 37d). This plasmid has no Bag-1L start site and unaltered translation initiation start sites of Bag-1S and Bag-1M.

To produce a Bag-1L-optimised vector (denoted pBABEneo-Bag-1L) site-directed mutagenesis of the pBABEneo-Bag-1SM vector was utilised to introduce a Bag-1L-optimised start site, summarised in Figure 38. The primer pair Bag-1L F2 and Bag-1L B2 (Figure 38a) was designed to introduce an ATG site with a flanking Kozak sequence at the appropriate site within the Bag-1 coding region. Whereas mammalian Bag-1L is translated from an atypical CUG site (Packham, Brimmell et al. 1997), a sub-optimal start site, the introduction of an ATG and Kozak sequence maximises the level of overexpression of Bag-1L attainable. A sequence alignment of the Bag-1L start site of pBABEneo-Bag-1L is shown compared to pBABEneo-Bag-1SM, the Kozak consensus sequence and the pcDNA3-Bag-1L vector used to generate Bag-1L/A and Bag-1L/B clones (Figure 38b).

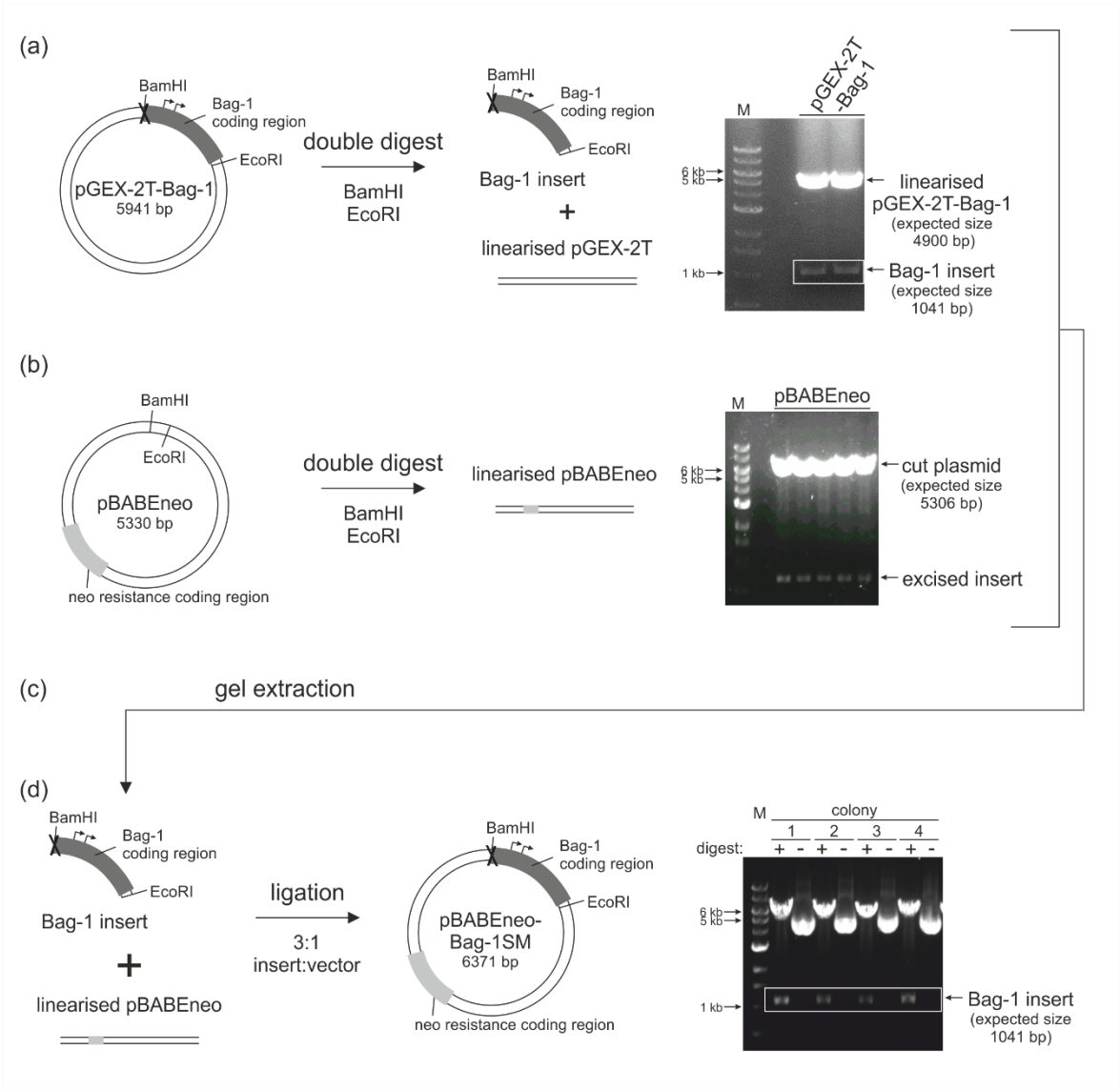

Figure 37 Summary schematic of the cloning strategy to produce the pBABEneo-Bag-1SM vector

(a) Bag-1 cDNA was cloned out of pGEX-2T-Bag-1 vector by a double digest using BamHI and EcoRI. ↱ marks translational start sites of Bag-1M and Bag-1S; 'X' marks the site where the translational start site of Bag-1L is missing. (b) The pBABEneo target plasmid was double digested using BamHI and EcoRI. (c) Bands corresponding to the relevant sizes of the Bag-1 insert (a) and the linearised pBABEneo plasmid (b) were gel extracted. (d) Ligation of the Bag-1 insert into pBABEneo was carried out at a 3:1 insert:vector ratio to generate the pBABEneo-Bag-1SM plasmid. Colonies were screened for successful ligation by double digest using BamHI and EcoRI.

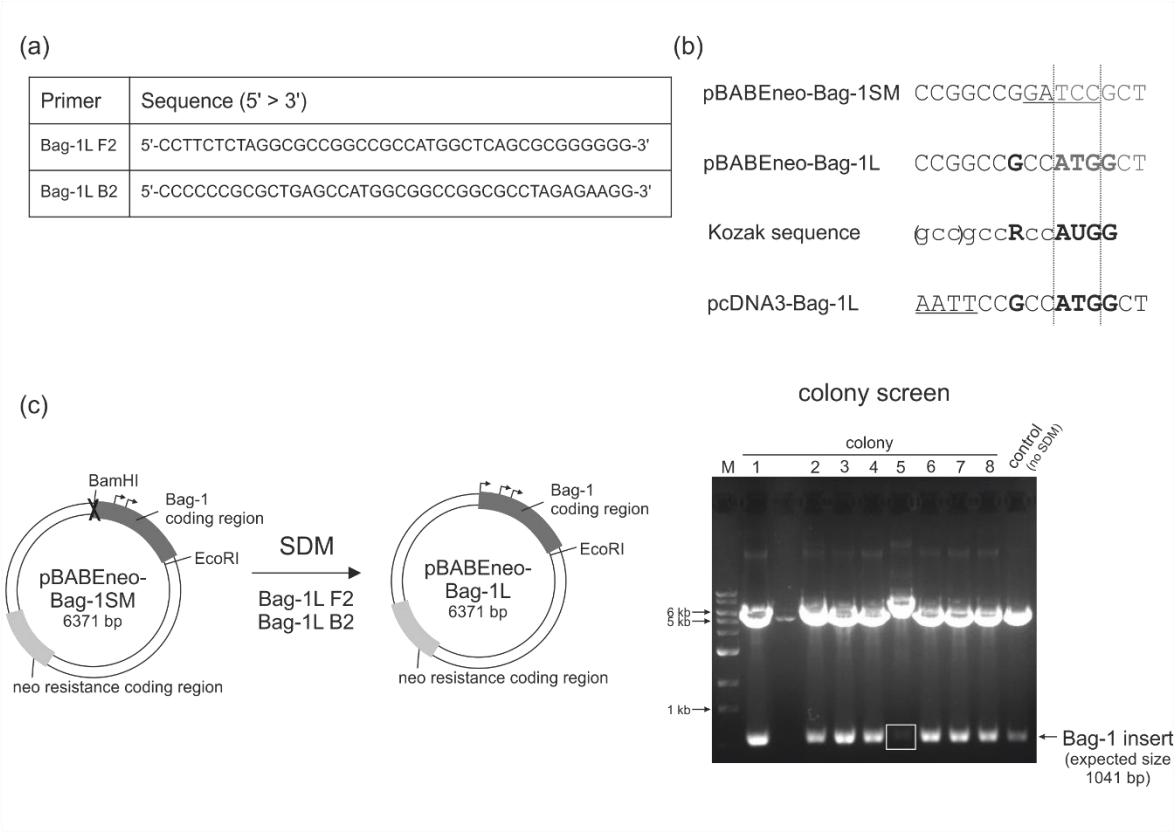

Figure 38 Summary of the cloning strategy to produce the pBABEneo-Bag-1L vector

(a) Table showing site-directed mutagenesis (SDM) primers used to produced pBABEneo-Bag-1L from pBABEneo-Bag-1SM. (b) Sequence alignments of the region surrounding the Bag-1L translational start site aligned to the Kozak sequence (Kozak 1987). Underlined sequences highlight where sequences differ from the sequence introduced into the pBABEneo-Bag-1L vector. In the Kozak sequence, uppercase letters denote a highly conserved base and R represents a purine. Lower case letters are the most common base seen in that position but the base can vary. The sequence in brackets is of unclear significance. pBABEneo-Bag-1L contains a guanine residue at position - 6 so is closer to the consensus sequence than pcDNA3-Bag-1L, the vector used to generate the Bag-1L/A and Bag-1L/B stably transfected clones. (c) The pBABEneo-Bag-1SM plasmid was subjected to 18 cycles of site-directed mutagenesis PCR in the presence of primers Bag-1L F2 and Bag-1L B2. Colonies were screened for successful mutagenesis by a double digest using BamHI and EcoRI. SDM product should not contain a BamHI site and will run as a nicked plasmid with no insert (colony 5). ↱ marks translational start sites of Bag-1 isoforms; 'X' marks the site where the translational start site of Bag-1L is missing from pBABEneo-Bag-1SM.

Bag-1 is a multifunctional protein with a wide range of interaction partners impacting on diverse signalling pathways (Figure 15) (Cutress, Townsend et al. 2002). Identifying the specific Bag-1 interactions involved in promoting a Bag-1-driven phenotype can help elucidate a mechanism of action so I decided to investigate this by generating a mutant of Bag-1 which is incapable of interacting with Hsc-70. Helix two and three of the Bag-1 domain are involved in Hsc-70 interactions (Sondermann, Scheufler et al. 2001) and mutations within these helices have been shown to disrupt Hsc-70 binding and interfere with Bag-1 functions (Briknarova, Takayama et al.

2001, Song, Takeda et al. 2001, Townsend, Cutress et al. 2003, Townsend, Cutress et al. 2004). If a phenotype is found to be partially reversed or altered in a mutant compared to wildtype Bag-1 this would imply that the interaction is involved in driving that phenotype. Site-directed mutagenesis of the Bag-1SM and Bag-1L vector was used to produce vectors coding for Bag-1 H3B mutants (denoted pBABEneo-Bag-1SM H3B and pBABEneo-Bag-1L H3B respectively) using previously designed primers (Cutress 2003). This mutant is unable to interact with Hsc-70 but retains its' ability to bind to and activate Raf-1 (Briknarova, Takayama et al. 2001, Song, Takeda et al. 2001). In human Bag-1S these mutations are D208A, Q212A and in Bag-1L these are D323A, Q327A.

4.1.2 Production of Bag-1-overexpressing pooled populations

Pooled populations of MCF-10A cells overexpressing different Bag-1 variants were generated by retroviral infection using the described vectors. Pooled populations generated from the pBABEneo-Bag-1SM or pBABE-neo-Bag-1L vectors were denoted 1SM and 1L respectively. Pooled populations generated from the H3B mutant vectors pBABEneo-Bag-1SM H3B or pBABEneo-Bag-1L H3B were denoted 1SM H3B and 1L H3B respectively. A pooled population using an empty pBABEneo construct was produced as an experimental control and denoted neo.

The relative protein abundance of each Bag-1 isoform in the pooled populations was examined by immunoblotting (Figure 39). The 1SM and 1SM H3B pools had high levels of expression of Bag-1S compared to neo and parental MCF-10A (denoted 10A). The relative abundance of Bag-1S in 1SM and 1SM H3B was 5.6- and 9.8- fold higher respectively than in neo. Bag-1M levels are upregulated compared to controls but not to the levels of Bag-1S, and Bag-1L levels were unaltered.

The 1L and 1L H3B pools had high levels of expression of Bag-1L compared to controls whilst not altering Bag-1M and Bag-1S expression levels (Figure 39a). As there is little-to-no expression of Bag-1L detected in neo and 10A controls it is difficult to determine the relative protein abundance of this isoform in 1L with respect to Bag-1L levels in controls. Immunoblotting utilised a monoclonal antibody which recognises a single epitope on Bag-1. Assuming that this epitope on Bag-1 will be recognised and bound with equal intensity across the isoforms I have expressed the abundance of Bag-1L molecules relative to those of Bag-1S in neo. The relative abundance of Bag-1L in 1L and 1L H3B was 6.8- and 5.0- fold higher respectively than Bag-1S levels in neo, compared to Bag-1L abundance in neo which was 0.97-fold lower than Bag-1S levels.

As I will be using the data collected using the Bag-1L/B stably transfected clone as a reference the expression levels of Bag-1 in this clone was compared to the retroviral pooled populations and showed that the Bag-1L isoform is expressed at a higher level in 1L than in Bag-1L/B (Figure 39c).

Immunofluorescence staining for Bag-1 was used to examine Bag-1 localisation and the heterogeneity of overexpression in the retroviral pooled populations (Figure 39b). Endogenous Bag-1 protein was detected in neo, which was heterogeneously expressed and is consistent with the heterogeneous immunofluorescence staining seen in parental MCF-10A cells (3.1 Characterisation of Bag-1L/A and Bag-1L/B in 2D). Heterogeneous staining for Bag-1 was also seen in the Bag-1-overexpressing pooled populations. Comparing 1SM to neo the population showed higher staining across the cytoplasm and nucleus (Figure 39b). Across the 1L pooled population cytoplasmic and nuclear staining is increased compared to neo (Figure 39b). Cytoplasmic staining levels are similar to those seen in 1SM while nuclear staining is enhanced. The staining patterns for 1SM H3B and 1L H3B were consistent with the staining patterns of 1SM and 1L respectively.

4.2 Characterisation of Bag-1 pooled populations in 2D culture

I sought to characterise the effect of isoform specific Bag-1 overexpression in 2D culture examining cell morphology, colony forming efficiency and proliferation. Bag-1-overexpressing pooled populations adopted a cobblestone appearance, with lamellipodia extending from the edges of clusters as typically observed in parental MCF-10A cells (Figure 40a) (Debnath, Muthuswamy et al. 2003). Overexpression of Bag-1S resulted in a statistically significantly higher ($p \leq 0.01$) colony forming efficiency compared to control with 99% of the 1SM cells seeded forming colonies compared to 74% of neo (Figure 40b). This phenotype was not observed with overexpression of the Hsc-70 binding mutant with 72% of cells forming colonies in 1SM H3B. Overexpression of Bag-1L or Bag-1L H3B had no effect on the colony forming efficiency (1L 74%; 1L H3B 72%). Overexpression of either Bag-1S or Bag-1L had no effect on proliferation when examined using a crystal violet assay (Figure 40c).

A downregulation of E-cadherin relative to pcDNA control was previously reported in the Bag-1L/A and Bag-1L/B stably transfected clones which was proportional to the level of Bag-1L overexpression (3.6 Bag-1L overexpression results in E-cadherin downregulation). Observing a downregulation of E-cadherin in the pooled population overexpressing Bag-1L would support a role for this protein in the regulation of this tumour suppressor. To this end expression of E-cadherin across the retroviral pooled Bag-1 clones was examined (Figure 41). E-cadherin levels were not downregulated compared to 10A or neo in either 1SM or 1L pooled populations.

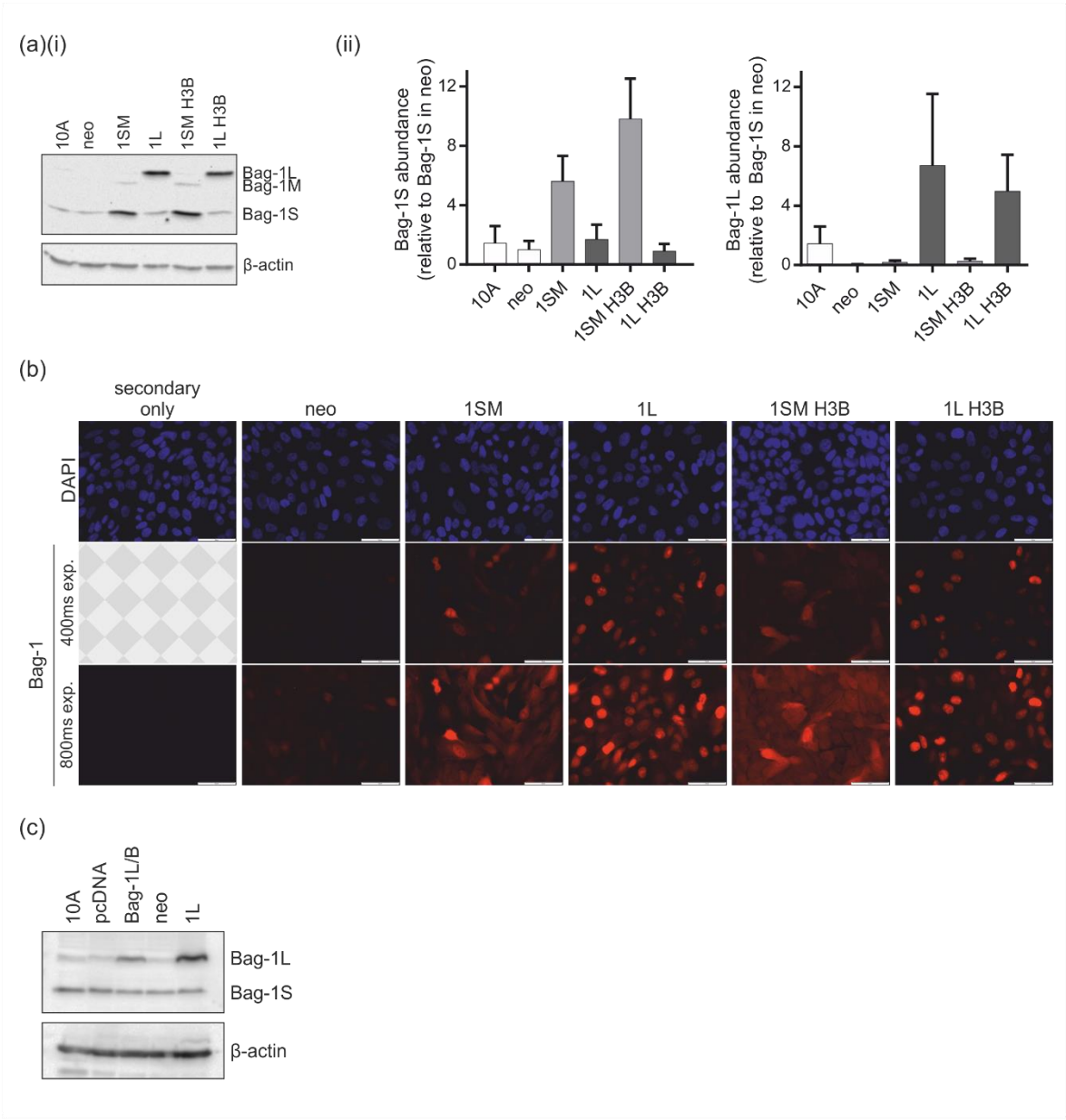

Figure 39 Bag-1 abundance and localisation in retroviral MCF-10A pooled populations

(a) Representative immunoblot (i) of Bag-1 expression with relative protein abundance for Bag-1S and Bag-1L isoforms (ii). Bag-1S and Bag-1L were independently quantified from the blots and protein abundance expressed relative to Bag-1S levels in neo. Bar graphs represent the mean protein abundance ± SEM from three independent experiments. (b) Representative images of immunofluorescence staining for Bag-1 (red) and DAPI counterstain (blue) in monolayer cultures; scale bars show 50 µm. (c) Immunoblot showing expression levels of Bag-1 in retroviral pooled populations compared to the stably transfected clone Bag-1L/B.

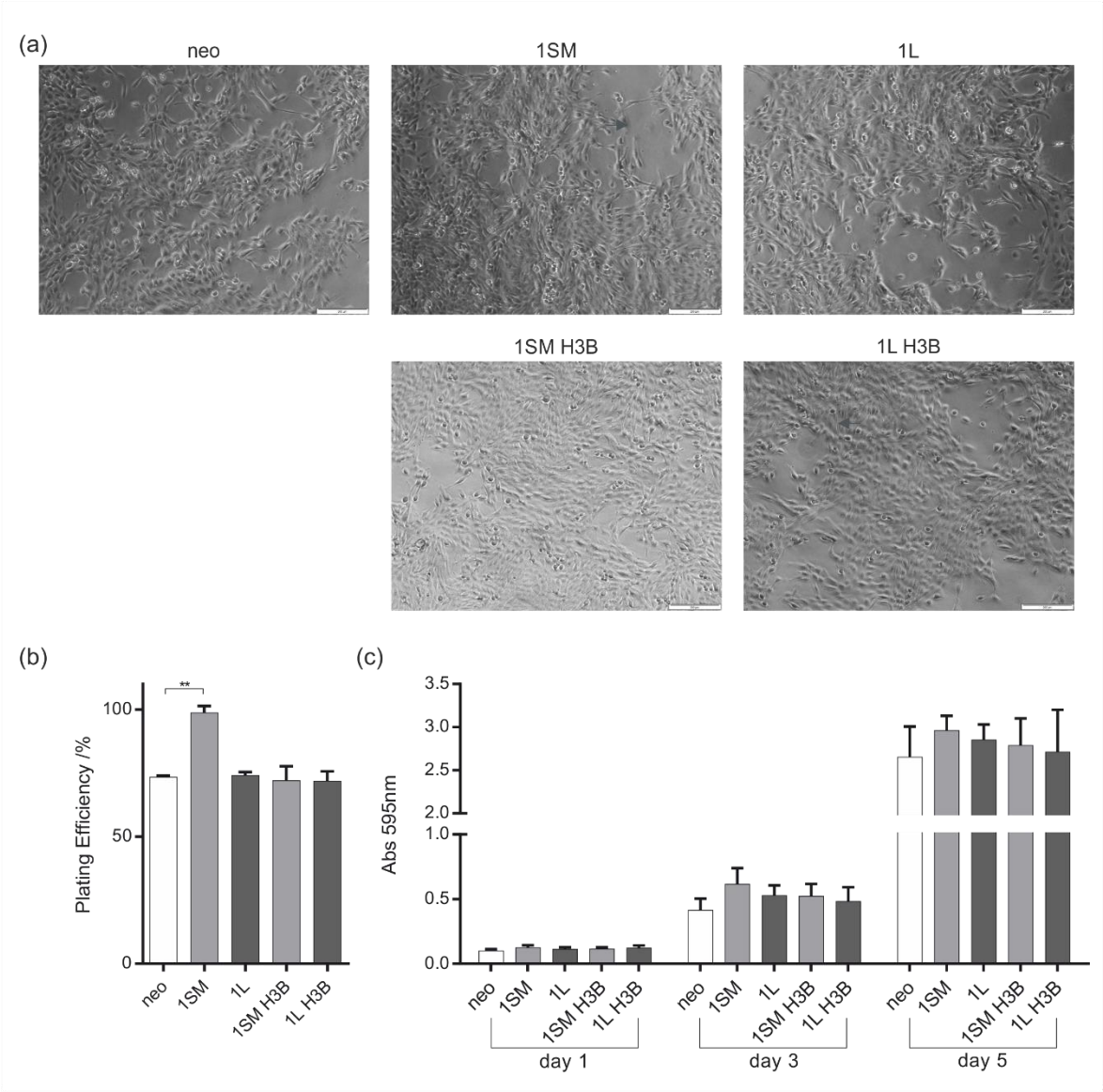

Figure 40 Effect of Bag-1 on retroviral MCF-10A pooled populations in 2D culture

(a) Phase contrast images reveal that Bag-1 pooled populations adopt a cobblestone appearance typical of MCF-10A cells. Scale bars show 200 µm. (b) The colony-forming efficiency of MCF-10A Bag-1 pooled populations was assessed in a clonogenic assay and expressed as the plating efficiency; 50 cells were plated per well in a 6-well dish. (c) Proliferation was measured at days 1, 3 and 5 of culture. Cells (10,000 per well) were plated at day 0 and were fixed in methanol and stained with crystal violet. Stain was dissolved in 20% acetic acid and absorbance at 595 nm recorded. Bar graphs represent the mean ± SEM from three independent experiments, each with three technical repeats. ** $p \leq 0.01$ as determined by one-way ANOVA with Fisher's LSD test.

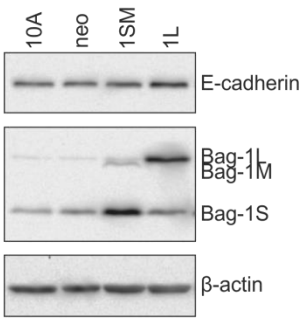

Figure 41 E-cadherin expression levels are unaltered in Bag-1-overexpressing retroviral MCF-10A pooled populations

Immunoblot of E-cadherin and Bag-1 levels in lysates collected from 2D culture; β-actin was included as a loading control.

4.3 Characterisation of Bag-1 pooled populations in 3D culture

To validate our reported role of Bag-1L in the attenuation of luminal filling and the acquisition of an atypical, branching morphology (Papadakis, Barker et al. 2016) I sought to examine the effect of Bag-1L overexpression using the 1L pool. In addition the Bag-1L H3B mutant was included in the study to provide evidence to support or exclude a role for Bag-1-Hsc-70 interactions in driving the observed phenotype. Growth of the 1SM pool and its corresponding H3B mutant population, was the first time that the role of the Bag-1S isoform specifically had been examined in acinar morphogenesis.

Immunoblotting of acinar lysates harvested at day 12 of morphogenesis confirmed that Bag-1 overexpression was maintained following 3D culture (Figure 42). Bag-1S was upregulated in 1SM compared to neo, with Bag-1M and Bag-1L bands not showing up with the exposure time used. Bag-1L was expressed in the 1L pool with no upregulation of Bag-1S.

Luminal status of acini was examined on day 12 of morphogenesis when parental acini display an evidently hollowed lumen (Debnath, Muthuswamy et al. 2003). As expected the majority of neo acini were hollowed or nearly hollowed (Figure 43a,b). Across the Bag-1 pooled populations the majority of acini were hollowed but there was a shift towards a less cleared phenotype compared to controls. Wildtype isoforms 1SM and 1L displayed 30% and 28% incompletely cleared acini compared to 17% in neo. The Bag-1 H3B mutants scored with a higher percentage of incompletely cleared acini than their respective wildtypes with 34% in 1SM H3B and 38% in 1L H3B. The consistent trend towards reduced clearing in all four Bag-1-overexpressing pools suggests that

overexpression of Bag-1 may be attenuating luminal clearing in these models, although statistical significance was not reached in these series of experiments at this time point.

Acinar morphology was scored on day 18 of morphogenesis. Neo acini adopted a spherical structure characteristic of non-transformed MCF-10A acini (Debnath, Muthuswamy et al. 2003) with only 19% atypical (Figure 43c,d). The 1SM clone had statistically significantly ($p \leq 0.05$) more acini displaying an atypical structure compared to neo with 37% of acini atypical (Figure 43d). The 1L pooled clone had a smaller, non-statistically significant increase in atypical acini with just 25% atypical. The 1SM H3B and 1L H3B mutants had 31% and 24% atypical acini respectively, which was not statistically significantly different to neo or their respective wildtype isoforms. The atypical acini observed in this setting tended to have a multiacinar structure (Figure 43c).

I hypothesised that Bag-1 may be acting to delay but is unable to fully prevent the onset of luminal clearing in these models. To test this I examined the luminal status of pools at an earlier stage of morphogenesis, as day 12 may be too late in the program to see the effect of a delay. At day nine of morphogenesis, acini had not yet undergone luminal clearing with controls presenting with 94% of acini incompletely cleared (Figure 44a,b). At day ten of morphogenesis the majority of acini still presented as incompletely cleared, with 67% of neo incompletely cleared, but there was a statistically significantly ($p \leq 0.05$) higher percentage of incompletely cleared acini in 1SM (81%) and 1L (78%) (Figure 44c,d).

4.4 Generation of Bcl-2-overexpressing pooled population

Similar to Bag-1 in these MCF-10A pools, Bcl-2 overexpression in MCF-10A acini is reported to delay, but not fully attenuate, luminal clearing (Debnath, Mills et al. 2002); this is therefore a good model for me to include as a positive control when examining whether Bag-1 can delay the onset of clearing.

4.4.1 Production of Bcl-2-overexpressing pooled population

An MCF-10A pooled population overexpressing Bcl-2 (denoted Bcl-2) was generated by retroviral infection using a pBABEpuro-Bcl-2 vector, a vector coding for the murine Bcl-2 protein. The empty vector control for Bcl-2 is the puro pooled population described for HER2 (3.3.1 Generation of HER2-overexpressing pooled population). Bcl-2 overexpression was confirmed by immunoblotting (Figure 45a). Bcl-2 protein was undetectable in 10A or puro cells under this experimental condition.

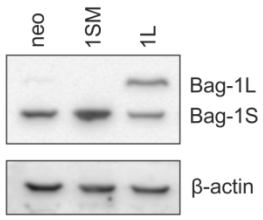

Figure 42 Bag-1 overexpression is maintained in 1SM and 1L acini

Immunoblot of Bag-1 expression in lysates harvested at day 12 of acinar morphogenesis; β-actin was included as a loading control.

4.4.2 Establishment of Bcl-2-overexpressing positive control – 2D culture

To characterise the effect of Bcl-2 overexpression in 2D culture cell morphology, colony forming efficiency and proliferation were examined. The Bcl-2-overexpressing pool adopted a cobblestone appearance typically observed in parental MCF-10A cells (Figure 45b) (Debnath, Muthuswamy et al. 2003). Bcl-2 overexpression did not alter the colony forming efficiency (Figure 45c) or the proliferation of MCF-10A cells (Figure 45d).

4.4.3 Establishment of Bcl-2-overexpressing positive control – 3D culture

To confirm my Bcl-2-overexpressing MCF-10A pool behaved as reported in the literature I examined its effect on acinar morphogenesis. At day 12 of morphogenesis Bcl-2 overexpression led to a statistically significant ($p \leq 0.05$) increase in incompletely cleared acini compared to controls with 32% of Bcl-2-overexpressing acini scoring as incompletely cleared compared to 21% of puro (Figure 46a,b). This confirmed that Bcl-2 overexpression was sufficient to interfere with the luminal clearing program and I therefore sought to examine if Bcl-2 still prevented luminal clearing a late time point of morphogenesis. I found that at day 18 Bcl-2 overexpression still results in a statistically significant ($p \leq 0.05$) increase in the percentage of acini that are incompletely cleared compared to controls (Figure 46c,d).

Looking at acinar morphology, the Bcl-2 pooled clone displayed 42.1% of atypical acini, statistically significantly ($p \leq 0.05$) more than puro (Figure 46e), when scored on day 18 of morphogenesis; atypical acini displayed a multiacinar structure (Figure 46f).

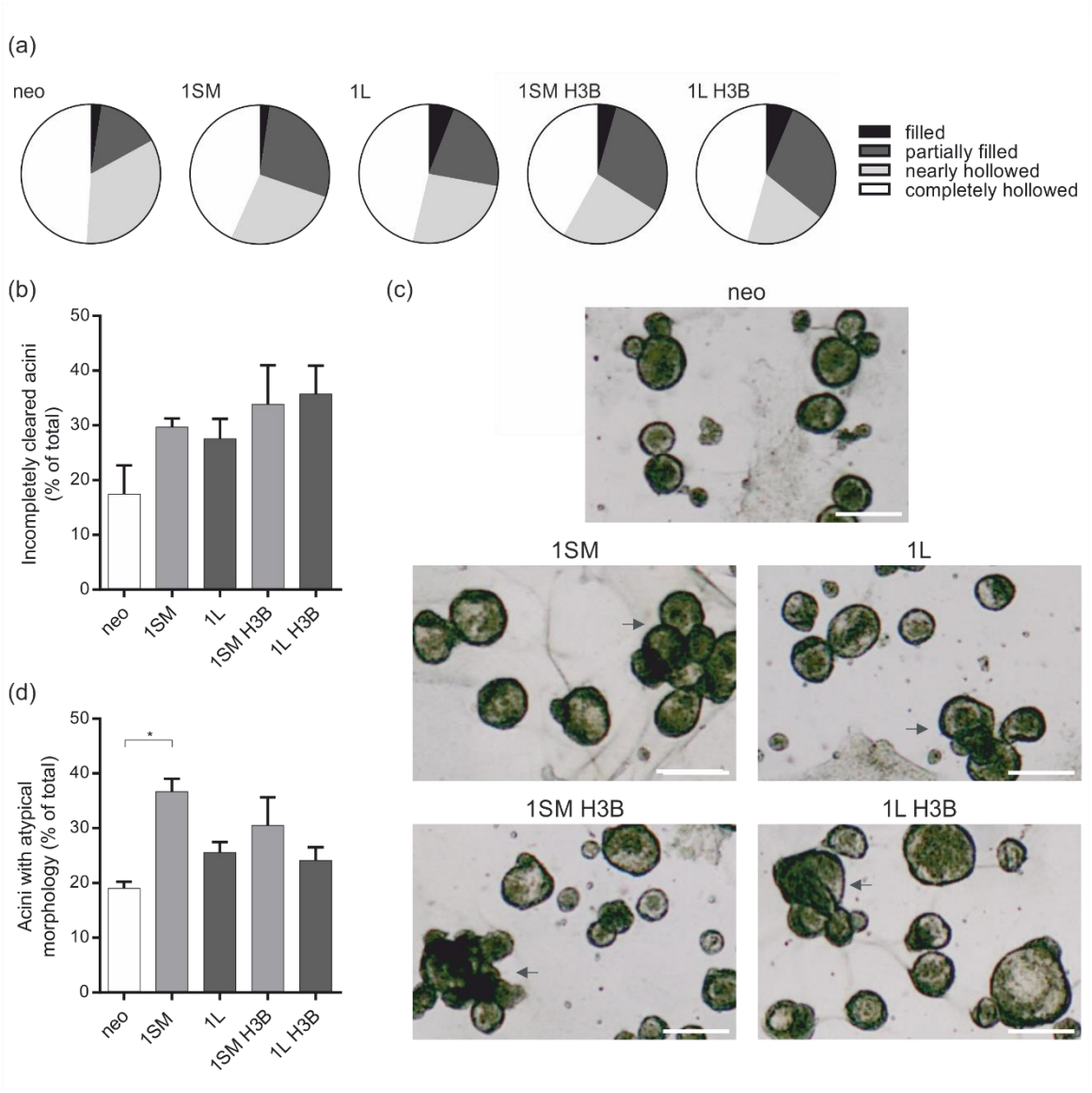

Figure 43 The role of Bag-1 isoforms in MCF-10A acinar morphogenesis

Acini were cultured for 12 days and stained with DAPI (red) and phalloidin-TRITC (green). Confocal microscopy was utilised to score luminal status; looking through all focal planes, acini were scored as filled, partially filled, nearly hollowed or completely hollowed. (a) Pie chart representation shows the proportions of acini scoring in each category. (b) The number of acini scoring as incompletely cleared (filled or partially filled) was expressed as a percentage of the total acini scored. A minimum of 60 acini were scored for each condition within an independent experiment across three chambers. (c) Acini were cultured for 18 days, fixed directly to minimise acini loss in wash steps (2% PFA final concentration) and mounted. High resolution pictures covering the entire slide were captured and all acini within a chamber scored manually. (c) Representative images of acinar morphology are shown; scale bars show 200 µm. (d) Morphology was scored as normal or atypical, where atypical includes multiacinar, branching and non-rounded acini. The number of acini scoring as atypical was expressed as a percentage of the total acini scored. A minimum of 100 acini were present in each well. Bar graphs represent the mean ± SEM from three independent experiments, each with three technical repeats. * $p \leq 0.05$ as determined by a one-way ANOVA with Fisher's LSD test.

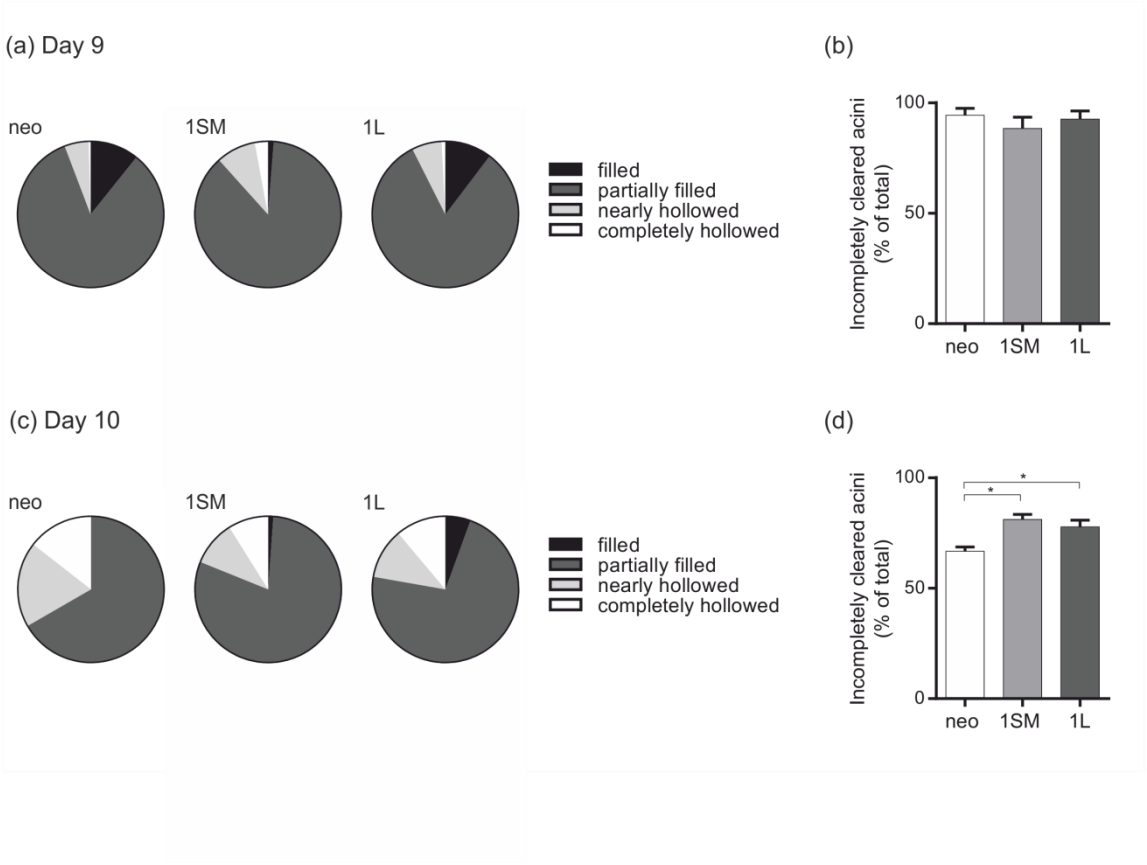

Figure 44 At an earlier stage of the luminal clearing program Bag-1 overexpression significantly alters luminal status

Acini were cultured for the indicated number of days and stained with DAPI and phalloidin-TRITC. Confocal microscopy was utilised to score luminal status; looking through all focal planes, acini were scored as filled, partially filled, nearly hollowed or completely hollowed. Pie chart representation shows the proportion of acini scoring in each category at day 9 (a) or day 10 (c) of morphogenesis. The number of acini scoring as incompletely cleared (filled or partially filled) at day 9 (b) or day 10 (d) was expressed as a percentage of the total acini scored. (a,b) is a separate experiment to (c,d). For (a,b) a minimum of 80 acini were scored for each condition within an independent experiment across two chambers. Bar graphs represent the mean ± SEM from three independent experiments each with two technical repeats. For (c,d) a minimum of 90 acini were scored for each condition across three chambers. Bar graphs represent the mean ± SEM from an independent experiment with three technical repeats. * $p \leq 0.05$ as determined by a one-way ANOVA with Fisher's LSD test.

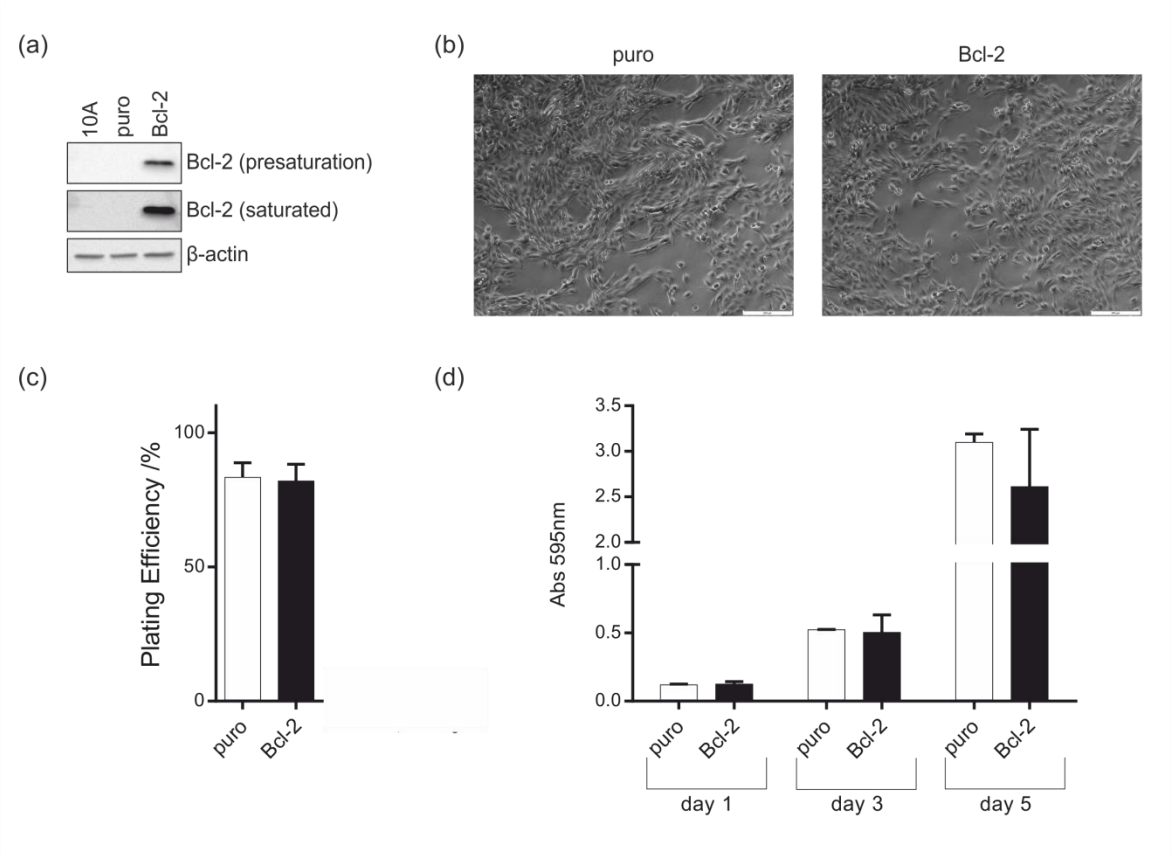

Figure 45 Effect of Bcl-2 overexpression on MCF-10A 2D culture

(a) Immunoblot of Bcl-2 overexpression in retroviral MCF-10A pooled populations. (b) Phase contrast images reveal the Bcl-2 pooled population adopts a cobblestone appearance typical of MCF-10A cells; scale bars show 200 µm. (c) The colony-forming efficiency was assessed in a clonogenic assay and expressed as the plating efficiency. (d) Proliferation was measured at days 1, 3 and 5 of culture. Cells (10,000 per well) were plated at day 0 and were fixed in methanol and stained with crystal violet. Stain was dissolved in 20% acetic acid and absorbance at 595 nm recorded. Bar graphs represent the mean ± SEM from three independent experiments, each with three technical repeats.

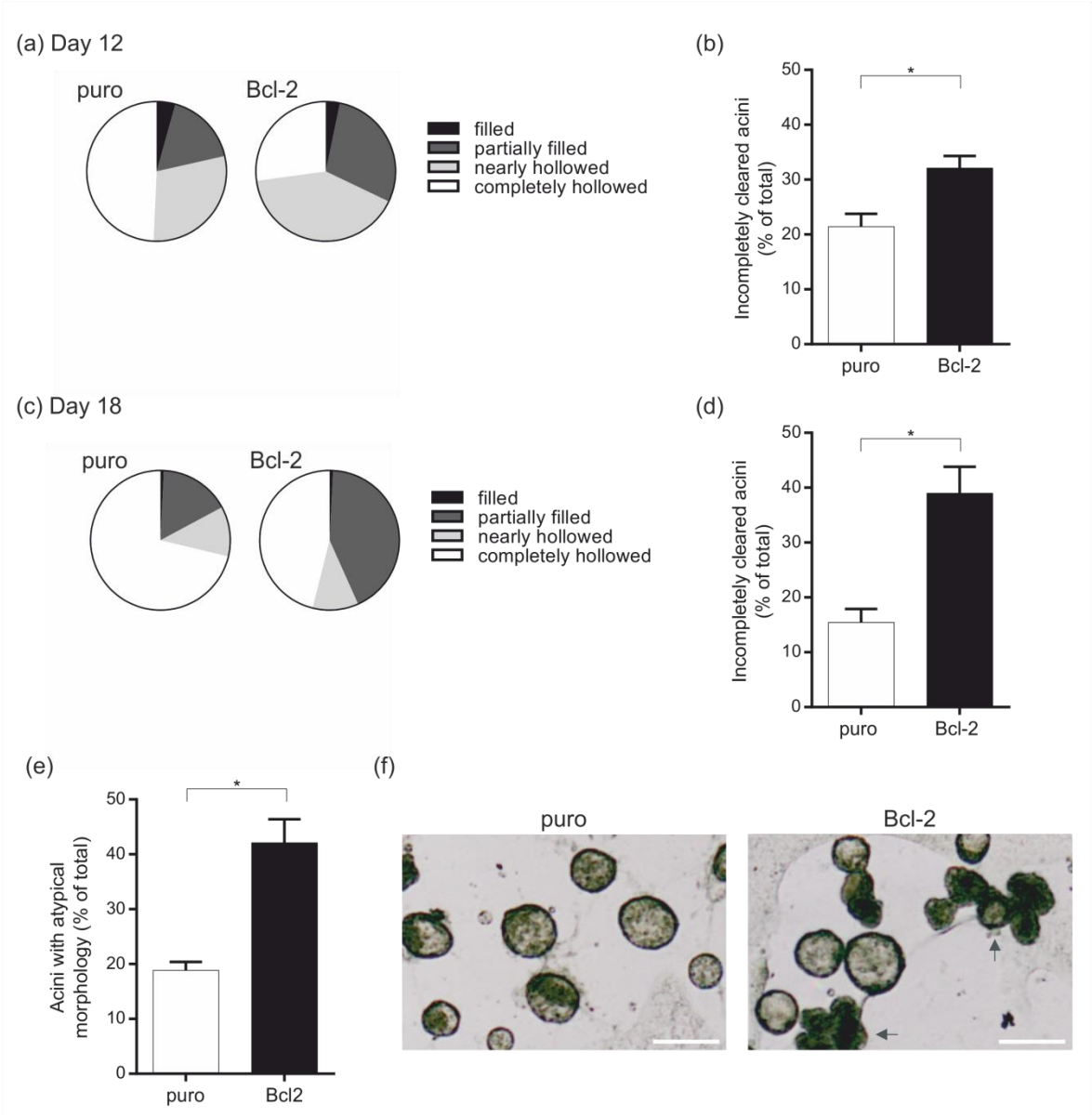

Figure 46 The role of Bcl-2 in MCF-10A acinar morphogenesis

Acini were cultured for the indicated number of days and stained with DAPI and phalloidin-TRITC. Confocal microscopy was utilised to score luminal status; looking through all focal planes, acini were scored as filled, partially filled, nearly hollowed or completely hollowed. Pie chart representation shows the proportion of acini scoring in each category at day 12 (a) or day 18 (c) of morphogenesis. The number of acini scoring as incompletely cleared (filled or partially filled) at day 12 (b) or day 18 (d) was expressed as a percentage of the total acini scored. (a,b) is a separate experiment to (c,d). A minimum of 60 acini were scored for each condition within an independent experiment across three chambers. (e) Acini were cultured for 18 days, fixed directly to minimise acini loss in wash steps (2% PFA final concentration) and mounted. High resolution pictures covering the entire slide were captured and all acini within a chamber scored manually. Morphology was scored as normal or atypical, where atypical includes multiacinar, branching and non-rounded acini. The number of acini scoring as atypical was expressed as a percentage of the total acini scored. A minimum of 100 acini were present in each well. (f) Representative images of acinar morphology are shown; scale bars show 200 µm. Bar graphs represent the mean ± SEM from three independent experiments, each with three technical repeats. * $p \leq 0.05$ as determined by a paired t-test.

4.5 Characterisation of the full time course of acinar morphogenesis

Work leading up to this point has implicated that there is a level of variation in the luminal clearing program across experiments; this may be that the onset of clearing alters from experiment to experiment or because the duration of the clearing programme can be increased or decreased depending on conditions. Conditions such as media composition and Matrigel batch may be contributing to this variability. Due to this, the time point at which Bag-1 influences luminal status may shift from experiment to experiment, making it difficult to analyse data combined from multiple independent experiments. I therefore sought to examine the role of Bag-1 overexpression across all stages of clearing by setting up a time course experiment. All time points were seeded simultaneously with culture conditions, media and Matrigel batch all identical. The Bcl-2- and HER2- overexpressing models were also included for comparison. With this experimental set up the morphogenesis program of all of the acini will be occurring in synchronicity; this enables me to robustly examine the role of Bag-1 in luminal clearing, and to compare the effect of Bag-1 overexpression to other, well characterised models. Within the same time course experiment slides were set up to examine the morphology of Bag-1S- and Bag-1L-overexpressing acini compared to Bcl-2- and HER2- overexpressing acini.

Examining morphology at day 18 of morphogenesis the majority of control acini scored as spherical, the typical morphology observed for MCF-10A acini (Debnath, Muthuswamy et al. 2003), with just 15% of neo and 19% of puro exhibiting an atypical morphology (Figure 47). Bag-1S and Bag-1L did not promote an atypical morphology in this setting, with both 1SM and 1L scoring with 14% of acini atypical. Bcl-2 promoted a statistically significant ($p \leq 0.01$) approximately 1.4-fold increase in acini with an atypical morphology compared to puro, while HER2 overexpression resulted in a statistically significant ($p \leq 0.001$) 2.1-fold increase in acini with an atypical morphology.

Luminal status was examined in Bag-1S-, Bag-1L- and Bcl-2- overexpressing acini every day between days nine and 12 of morphogenesis, the stages at which the majority of parental acini undergo luminal clearing, and at the late time point of day 18; HER-2-overexpressing acini were included as a positive control for incompletely cleared acini at days 12 and 18.

Representative images of control acini (neo) show the full time course of non-transformed acinar morphogenesis with acini moving from a filled to a hollowed phenotype (Figure 48). At early time points, acini stain for phallodin in central, luminal cells; this corresponds to a highly filled phenotype in neo (Figure 49) with 93% of acini scoring as incompletely cleared at day 9 of morphogenesis and 83% at day 10, dropping to approximately 61% at day 11 (Figure 50). The majority of clearing occurred between days 10 and 12 of morphogenesis, with over 50% of acini

moving from an incompletely cleared phenotype to a more hollowed phenotype within this time frame. From day 12 of morphogenesis onwards neo acini show a distinct, hollowed structure (Figure 48, Figure 49). Just 33% of acini score as incompletely cleared at day 12, dropping further to 18% at day 18 (Figure 50).

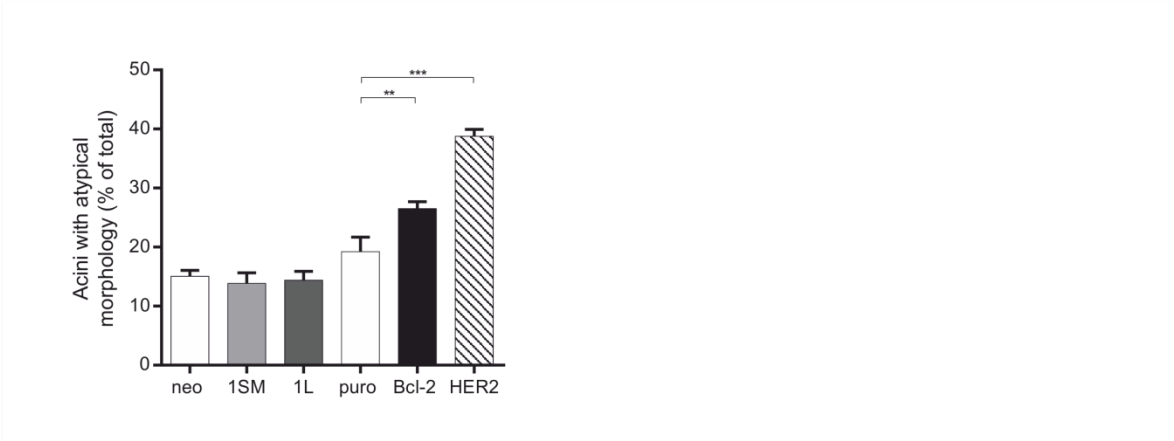

Figure 47 The role of Bag-1 in external MCF-10A acinar morphology

All acini were seeded together (day 0), cultured for 18 days of morphogenesis, fixed directly to minimise acini loss in wash steps (2% PFA final concentration) and mounted. High resolution pictures covering the entire slide were captured and all acini within a chamber scored manually. Morphology was scored as normal or atypical, where atypical includes multiacinar, branching and non-rounded acini. The number of acini scoring as atypical were expressed as a percentage of the total acini scored. Bar graphs represent the mean ± SEM from an independent experiment with three technical repeats. ** $p \leq 0.01$, *** $p \leq 0.001$ as determined by one-way ANOVA with Fisher's LSD test. A minimum of 100 acini were present in each well.

Similarly to neo, Bag1S-, Bag-1L-, Bcl-2- and HER2- overexpressing acini all progress from a filled to a hollowed phenotype over time but at varying rates compared to each other and to their relevant vector control (Figure 49).

1SM and 1L score similarly to neo at days nine and 10 of morphogenesis, with over 90% of incompletely cleared acini at day nine and over 80% at day 10 (Figure 50). At day 11 of morphogenesis 1SM and 1L show an approximately 7% and 9% increase in the number of incompletely cleared acini respectively compared to neo, although statistical significance was not reached at this time point. In contrast to neo, where 66% of acini had undergone luminal clearing by day 12 of morphogenesis, approximately 40% of acini had cleared in 1SM and 1L. At this time point both 1SM and 1L showed a statistically significant ($p \leq 0.001$) increase in the number of acini scoring as incompletely cleared compared to neo. 1SM acini showed a 1.75-fold increase in the number of incompletely cleared acini compared to neo and 1L showed a 1.88-fold increase. The 0.13-fold increase in the number of incompletely cleared acini in 1L compared to 1SM did not reach statistical significance. By day 18 of morphogenesis Bag-1 acini had no statistically significant differences in the percentage of incompletely cleared acini compared to neo controls; 1SM acini had 25% of incompletely cleared acini compared to 18% in neo, while 1L acini had 20%.

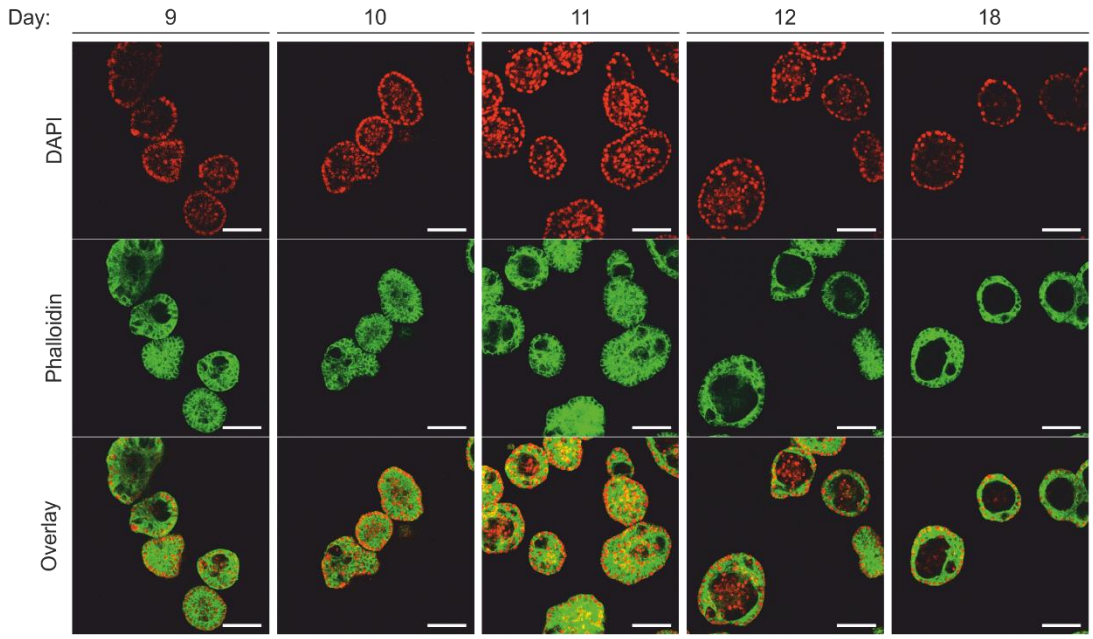

Figure 48 Characterisation of the full time course of MCF-10A acinar morphogenesis
Representative confocal immunofluorescence images show the centre of MCF-10A acini at the indicated time point of morphogenesis. All acini were seeded together (day 0) and fixed and stained with DAPI (red) and phalloidin-TRITC (green); scale bars show 100 µm.

Bcl-2-overexpressing acini progress through the clearing program slower than 1SM and 1L (Figure 49). At day nine of morphogenesis Bcl-2 acini score similarly to puro controls with 97% of acini scoring as incompletely cleared compared to 92% in puro (Figure 50). At all later time points examined Bcl-2 had statistically significantly ($p \leq 0.001$) more incompletely cleared acini compared to puro. At day 12 of morphogenesis, Bcl-2 acini displayed a 2.8-fold increase in the number of incompletely cleared acini compared to control which compares to the 1.75-fold and 1.88-fold increase seen in 1SM and 1L respectively at the same time point. By day 18 of morphogenesis Bcl-2 acini scored as 47.5% of incompletely cleared compared to 20% of puro.

At day 12 of morphogenesis HER2 acini scored with a statistically significant ($p \leq 0.001$) increase in the percentage of incompletely cleared acini compared to controls with 70.8% of acini scoring as incompletely cleared (Figure 50). This is lower than the percentage of Bcl-2 acini scoring as incompletely cleared at this time point but higher than scores for 1SM and 1L. By day 18 of morphogenesis the majority of acini (64%) still remain as incompletely cleared, a statistically significant ($p \leq 0.001$) increase compared to puro controls; an approximately 7% drop in the number of incompletely cleared acini occurred over the six days of morphogenesis. At this time point HER2 acini score higher than Bcl-2 acini, reversing the trend seen at day 12.

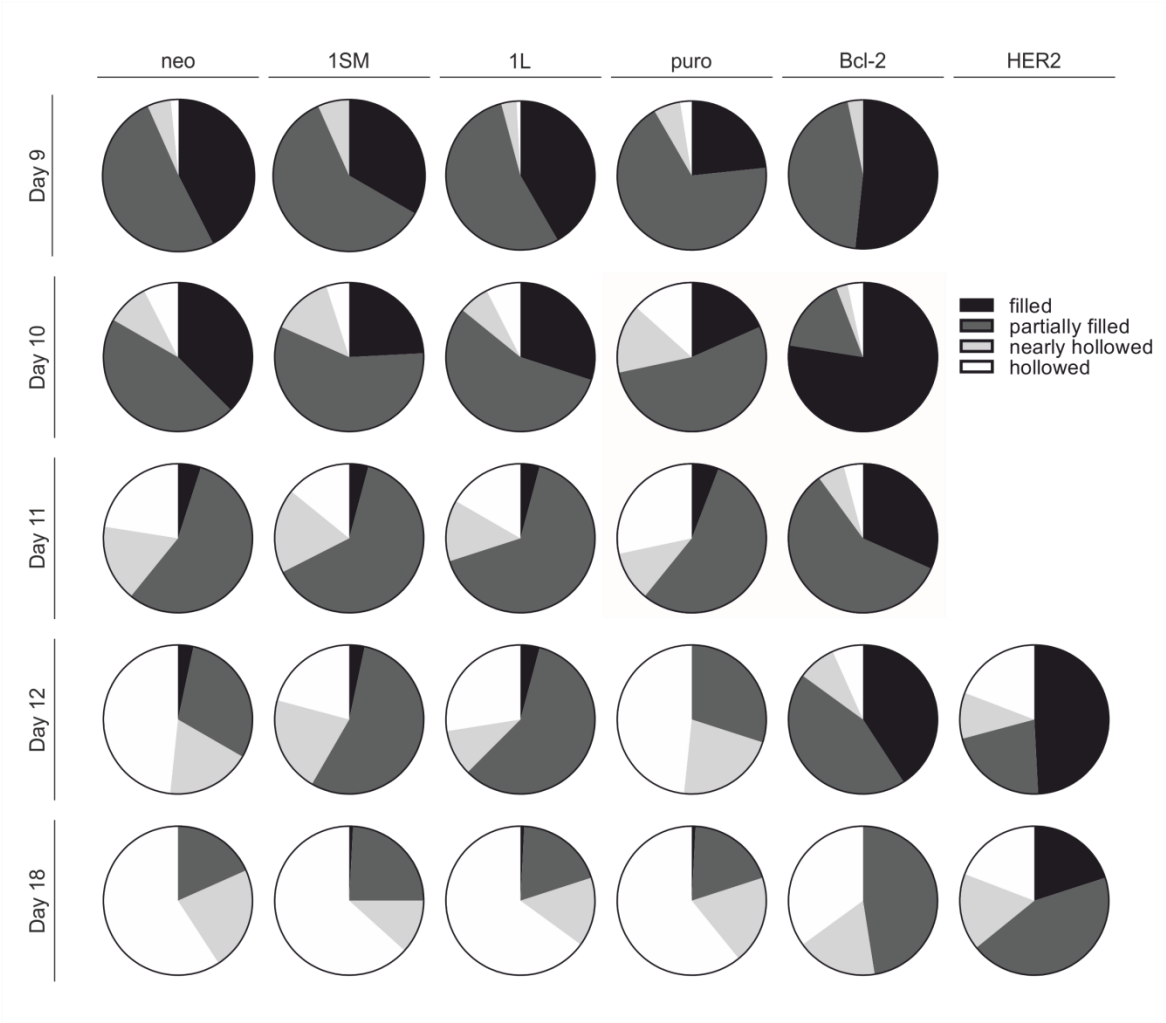

Figure 49 The role of Bag-1 in MCF-10A acinar morphogenesis - luminal status over time

All acini were seeded together (day 0), fixed at the indicated time point and stained with DAPI and phalloidin-TRITC. Confocal microscopy was utilised to score luminal status. Looking through all focal planes, acini were scored as filled, partially filled, nearly hollowed or completely hollowed. Pie chart representation shows the proportions of acini scoring in each category at the indicated time point. Data are from an independent experiment with three technical repeats. A minimum of 120 acini were scored for each condition across three chambers.

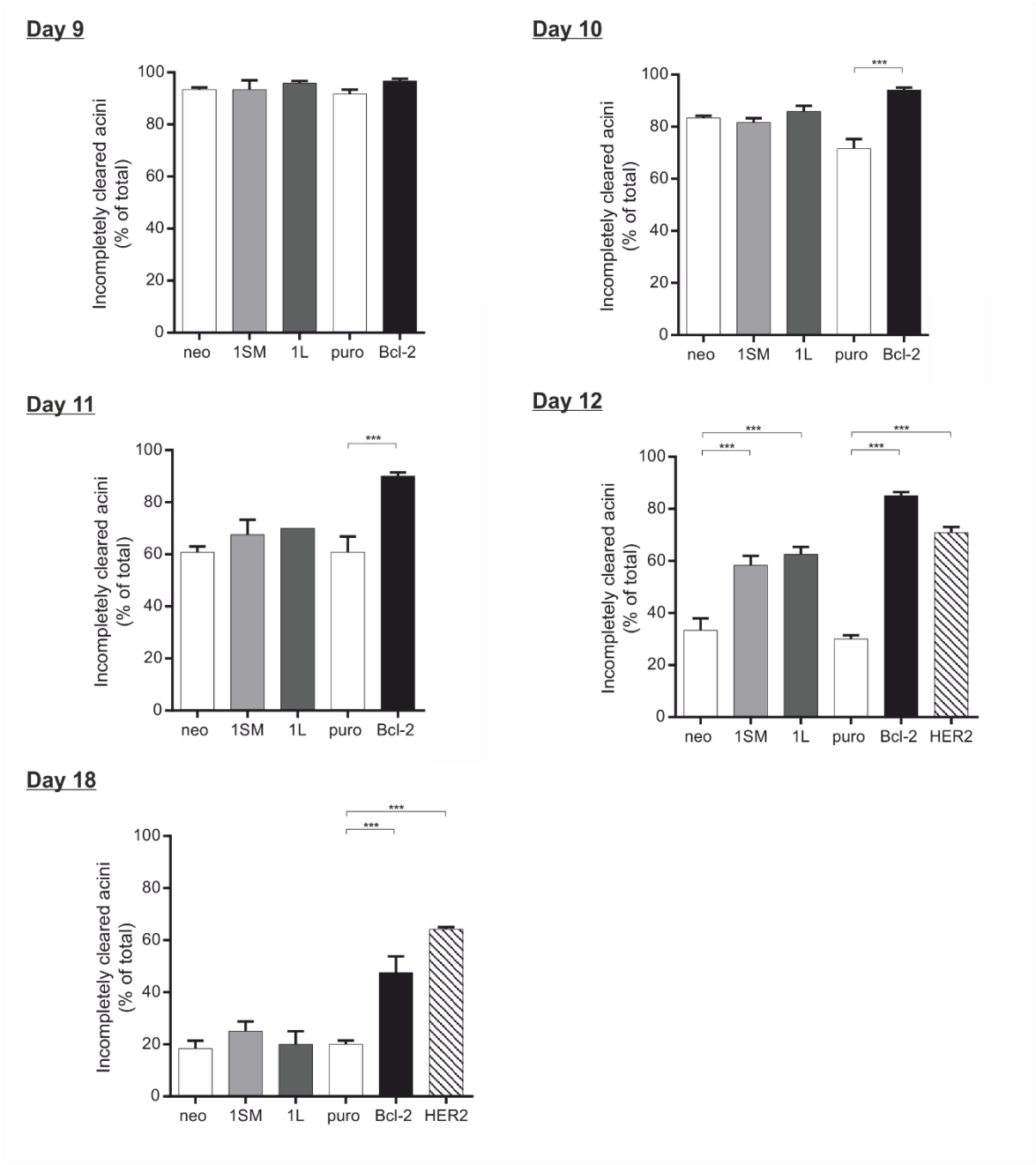

Figure 50 Isoform specific Bag-1S- or Bag-1L- overexpresssion can delay the onset of luminal clearing

All acini were seeded together (day 0), fixed at the indicated time point and stained with DAPI and phalloidin-TRITC. Confocal microscopy was utilised to score luminal status. Looking through all focal planes, acini were scored as filled, partially filled, nearly hollowed or completely hollowed. The number of acini scoring as incompletely cleared (filled or partially filled) was expressed as a percentage of the total acini scored. Bar graphs represent the mean ± SEM from an independent experiment with three technical repeats. *** $p \leq 0.001$ as determined by one-way ANOVA with Fisher's LSD test. A minimum of 120 acini were scored for each condition across three chambers.

4.6 Discussion

In this chapter I report further characterisation of the isoform-specific functions of Bag-1 in MCF-10A acinar morphogenesis. Bag-1S- and Bag-1L- overexpressing MCF-10A were compared to the more characterised Bcl-2- and HER2- overexpressing models. Bag-1S or Bag-1L- overexpression was shown to interfere with the luminal clearing program of MCF-10A but did not induce a branching, atypical morphology.

Successful generation of predominantly Bag-1S- and predominantly Bag-1L-overexpressing retroviral pooled populations

The pBABEneo-Bag-1SM and pBABEneo-Bag-1L vectors were designed to have optimal overexpression of Bag-1S or Bag-1L respectively. The pBABEneo-Bag-1SM vector lacked a mammalian start site for Bag-1L; I did not opt to remove the Bag-1M start site as internal ribosome entry sequence-dependent translation of Bag-1S (Coldwell, deSchoolmeester et al. 2001) should make Bag-1S the predominant isoform expressed. Consistent with this, Bag-1S was the predominant isoform present in 1SM and 1SM H3B populations (Figure 39a). In addition, immunostaining for Bag-1 was predominantly cytoplasmic, consistent with overexpression of Bag-1S (Figure 39b) (Packham, Brimmell et al. 1997, Takayama, Krajewski et al. 1998, Yang, Chernenko et al. 1998). This confirmed that the translational start sites coded for in the pBABEneo-Bag-1SM vector behaved as expected.

I designed the pBABEneo-Bag-1L start site to have a highly optimised Bag-1L site, introducing an ATG and Kozak sequence to maximise the level of Bag-1L expression attainable (Figure 38b). This optimised start site compares to the atypical CUG site of mammalian Bag-1L (Packham, Brimmell et al. 1997), a sub-optimal site. Although internal ribosome entry sequence-dependent translation of Bag-1S can still occur in the pBABEneo-Bag-1L vector, ribosomes translating the mRNA from the highly optimised Bag-1L start site should displace initiating complexes forming at the Bag-1M and Bag-1S sites limiting expression of these isoforms. Indeed I saw high levels of Bag-1L overexpression in 1L and strong nuclear immunofluorescence staining, consistent with overexpression of the predominantly nuclear 1L isoform (Packham, Brimmell et al. 1997, Takayama, Krajewski et al. 1998, Yang, Chernenko et al. 1998), with little change in Bag-1S and Bag-1M levels compared to neo controls (Figure 39a,b).

The Bag-1L optimised start site in pBABEneo-Bag-1L contains a guanine residue at position minus six so is closer to the consensus Kozak sequence than the start site in the pcDNA3-Bag-1L vector (Figure 38b); this should result in a higher level of Bag-1L expression from the pBABEneo-Bag-1L vector than can be achieved from the pcDNA3-Bag-1L vector used to generate the stably

transfected Bag-1L/A and Bag-1L/B clones. However it must be considered that virus-based vectors tend to be uniformly delivered into the cell, with a single plasmid copy per cell, while lipid based transfection can result in cells with multiple copies. While pBABEneo-Bag-1L is better optimised it may not achieve higher levels of expression than multiple copies of pcDNA3-Bag-1L. To assess the level of expression of Bag-1L in 1L versus the stably transfected Bag-1L/B clone I carried out an immunoblot of Bag-1 expression and showed that 1L has an enhanced level of Bag-1L overexpression compared to Bag-1L/B (Figure 39c).

The role of Bag-1 in 2D culture

In the retroviral pooled populations 1SM and 1L I observed no statistically significant effects on cellular proliferation upon overexpression of Bag-1S or Bag-1L (Figure 40c). This is inconsistent with previously reported findings; Bag-1L overexpression was shown to statistically significantly inhibit proliferation in the Bag-1L/B stably transfected clone (Figure 28) and individual overexpression of Bag-1S, Bag-1M or Bag-1L in keratinocytes has been shown to inhibit proliferation (Hinitt, Wood et al. 2010). I did, however, observe a statistically significant increase in the colony forming efficiency of 1SM cells compared to neo controls (Figure 40b). Clonegenic assays are an *in vitro* cell survival assay based on the ability of a single cell to form a colony (Puck and Marcus 1956); this data therefore suggests that Bag-1SM overexpression enhances the ability of single MCF-10A cells to survive and proliferate.

A downregulation of E-cadherin was reported in the Bag-1L-overexpressing stably transfected clones Bag-1L/A and Bag-1L/B (Figure 36). I was interested in confirming this result based on the role of this tumour suppressor in the epithelial-to-mesenchymal transition (Canel, Serrels et al. 2013). If Bag-1 can regulate E-cadherin levels this highlights a previously unreported function of this protein and implicates Bag-1 in driving features associated with the epithelial-to-mesenchymal transition. The use of the 1SM and 1L pools allowed me to first examine whether Bag-1L overexpression altered E-cadherin levels in this setting, while also assessing whether overexpression of Bag-1SM had a similar consequence. I did not see a downregulation of E-cadherin in the 1L pool (Figure 41). I have shown that 1L overexpresses Bag-1L to a higher extent than the Bag-1L/B stably transfected clone (Figure 39c) suggesting that the absence of a phenotype is not due to Bag-1L overexpression being too low. I also saw no effect on E-cadherin expression in the 1SM pool (Figure 41) suggesting that Bag-1S overexpression does not affect E-cadherin levels. Although the level of E-cadherin downregulation in the Bag-1L stable clones correlated with Bag-1L overexpression (Figure 36), Bag-1 knockdown experiments in the Bag-1L/A and Bag-1L/B stably transfected clones were unable to reverse E-cadherin downregulation (data not shown, carried out by Tom Reeves during a summer placement). There may be an additional

transformation in the Bag-1L/A and Bag-1L/B stable clones that is promoting E-cadherin downregulation. 1SM and 1L are pooled populations which should minimise the effect of a phenotype being observed that is not a direct result of overexpression of Bag-1L. Taken together this data indicates that Bag-1 does not directly regulate E-cadherin levels in MCF-10A.

Bag-1 delays the onset of luminal clearing without fully preventing it

In the initial experimental set up examining luminal status following Bag-1 overexpression at day 12 of morphogenesis, I did not observe a statistically significant Bag-1-driven attenuation of luminal apoptosis following either Bag-1S- or Bag-1L- overexpression when analysing data from three independent experiments (Figure 43a,b). Although Bag-1L overexpression in 1L is higher than the level of overexpression seen in Bag-1L/B (Figure 39c) the phenotypic consequences of Bag-1L overexpression on acinar morphogenesis are different. I detected a 77% increase in the number of filled acini in the Bag-1L/B clone compared to its control at day 20 of morphogenesis (Papadakis, Barker et al. 2016). While the work with the Bag-1 pooled populations was carried out independently and so direct comparisons cannot be accurately made, based on our findings in the Bag-1L/B clone I did expect to see a more pronounced effect of Bag-1L overexpression on luminal status than the non-statistically significant 10% increase in incompletely cleared acini in 1L compared to controls at day 12 of morphogenesis.

I hypothesised that Bag-1 was able to delay but not fully prevent luminal clearing in this experimental setting. However, at day 12 of morphogenesis the majority of acini had undergone luminal clearing (Figure 43a,b) and this could make identification of a delay in the clearing program less pronounced. I therefore examined early time points of morphogenesis and found that at day 10 of acinar morphogenesis 1SM and 1L acini displayed a statistically significant increase in the number of incompletely cleared acini. At this time point the majority of control neo acini were incompletely cleared (67%) suggesting that Bag-1 exerts an effect on luminal clearing during the main luminal clearing program and supporting a role for Bag-1 in the delay of luminal clearing.

To this end I generated Bcl-2 acini, reported to be able to delay but insufficient to fully prevent luminal clearing (Debnath, Mills et al. 2002). The delay in the onset of clearing following Bcl-2 overexpression is due to inhibition of Bim-regulated anoikis (Reginato, Mills et al. 2005) but clearing is described to occur as a result of a metabolic defect characterised by ROS production (Figure 20ci) (Schafer, Grassian et al. 2009). Antioxidant treatment (Schafer, Grassian et al. 2009) or overexpression of an antioxidant enzyme (Davison, Durbin et al. 2013) combined with Bcl-2 attenuation of Bim-upregulation can fully attenuate luminal clearing (Figure 20cii). The Bcl-2 model was included to serve as a positive control for the delay of luminal clearing in experiments

assessing the role of Bag-1 in luminal clearing. Similarly, HER2 acini were included as a positive control for luminal filling. The inclusion of a positive control for luminal filling allowed me to confirm that the luminal clearing observed in the Bag-1 pools was not a consequence of a change in experimental conditions that promoted luminal clearing.

HER2 acini behaved as previously reported (Muthuswamy, Li et al. 2001, Debnath, Mills et al. 2002, Papadakis, Barker et al. 2016) with the majority of acini scoring as incompletely cleared at day 18 of morphogenesis (Figure 50). In contrast Bcl-2 acini showed a statistically significant increase in the percentage of incompletely cleared acini at day 12 of morphogenesis as well as at day 18 (Figure 46b,d), a late time point compared to the period in which luminal clearing occurs in parental acini (days 9-12) (Debnath, Muthuswamy et al. 2003). In the experimental setting examined Bcl-2 is fully preventing luminal clearing rather than delaying clearing. However, while only 7% of HER2 acini progressed from an incompletely cleared phenotype to a more hollowed phenotype from day 12 to day 18, 38% of Bcl-2 acini progressed during the same time frame and, by day 18 of morphogenesis, Bcl-2 overexpression resulted in less acini with an incompletely cleared status than in HER2 (Figure 50); it is possible that Bcl-2 acini are still undergoing luminal clearing at day 18 of morphogenesis and a later time point still is required.

Work has indicated that there is a level of variation in the morphogenesis program between individual experiments; this is highlighted by data from three independent experiments relating to the luminal status of Bcl-2. Initial experiments during the establishment of the Bcl-2 pooled population show Bcl-2 scoring with 32% of acini incompletely cleared at day 12 of morphogenesis (Figure 46a,b). However in a separate experiment Bcl-2 acini score with a higher 39% of incompletely cleared acini at day 18 (Figure 46c,d). Further showing inconsistencies in the luminal clearing program, in the full time course characterisation experiment including Bag-1, Bcl-2 acini scored with 85% of acini incompletely cleared at day 12 (Figure 50). While acini all go through the luminal clearing program, it seems that the time point at which this process begins and/or the duration of the clearing can vary from experiment to experiment. It is therefore very difficult to compare data across independent experiments.

To fully examine the role of Bag-1 in luminal clearing it was necessary to carry out a full time course characterisation experiment (Figure 48, Figure 49, Figure 50). Here I seeded all time points simultaneously and included Bcl-2- and HER2- overexpressing models for comparison. All experimental conditions were identical, ensuring the morphogenesis program of all acini occurs in synchronicity. Under these conditions Bag-1 resulted in a statistically significant increase in the number of incompletely cleared acini compared to neo at day 12 of morphogenesis (Figure 49). This robust examination of Bag-1 in luminal clearing provided further evidence to support a role

for Bag-1S- and Bag-1L in promoting a delay in luminal clearing, although eventual clearing still occurred in this model. HER2 acini still remained filled at day 18 within this experiment, providing a positive control for luminal filling.

Interfering with Bag-1-Hsc-70 interactions does not reverse Bag-1-driven inhibition of luminal clearing

Bag-1 has a diverse range of interaction partners which impact on a range of signalling pathways (Cutress, Townsend et al. 2002) (Figure 15). This can make it difficult to decide where to begin mechanistic investigations into any Bag-1-driven phenotype. I successfully generated retroviral pools overexpressing the Bag-1SM or the Bag-1L H3B mutant; this variant contains a mutation in helix three of the Bag-1 domain which prevents binding to Hsc-70 while retaining its ability to bind to and activate Raf-1 (Briknarova, Takayama et al. 2001). This allows me to investigate whether Hsc-70 interactions and subsequent downstream signalling influences Bag-1 function in MCF-10A acini. If a phenotype was found to be partially reversed or altered in a mutant compared to wildtype Bag-1 this would imply that the Hsc-70 interaction is involved in the phenotype. The H3B mutants scored with a higher percentage of incompletely cleared acini compared to their relevant wildtype controls, although statistical significance was not reached (Figure 42a,b). Disrupting the Hsc-70 interaction appears to be further attenuating luminal clearing. Raf-1 and Hsc-70 compete for binding on Bag-1 (Song, Takeda et al. 2001) and, in MCF-10A acini, Bag-1 has been shown to interfere with luminal apoptosis through Raf-1 activation (Anderson, Sutherland et al. 2010). In the context of a developing acini Bag-1 interactions with Hsc-70 may be blocking pro-survival signalling through Raf-1 by competing with Raf-1 for binding on Bag-1. Bag-1 mutants which cannot bind Hsc-70 proteins may therefore have an enhanced pro-survival effect through increased Raf-1 binding and activation.

The Bag-1L/B stably transfected clone may have an additional transformation which, combined with Bag-1L, drives acini transformation

I detected a different phenotype in the retroviral pooled population 1L than we observed in the Bag-1L/A and Bag-1L/B stably transfected clones. While Bag-1L-overexpression in Bag-1L/A and Bag-1L/B clones fully prevented luminal clearing (Papadakis, Barker et al. 2016), I propose that Bag-1L can only delay the onset of clearing in the 1L model. Bag-1L-overexpression in 1L is higher than in Bag-1L/B, so the different phenotype is not a consequence of insufficient Bag-1L levels (Figure 39c). This would implicate an additional transformation event in the Bag-1L/A and Bag-1L/B stably transfected clones which, when combined with Bag-1L-overexpression, is able to fully attenuate luminal clearing. The use of a pooled population in 1L will have minimised the chance of an additional transformation driving a phenotype that was observed when examining the pooled

population as a whole. Anderson *et al.* also used pooled clones but utilised a modified version of the MCF-10A line expressing an ecotropic retroviral receptor, MCF-10A/EcoR (Anderson, Sutherland et al. 2010). Although the appropriate control was used in experiments it is possible that, similarly to in the Bag-1L/A and Bag-1L/B clones, the MCF-10A/EcoR line contains an additional transformation which is insufficient alone to interfere with acinar morphogenesis but when combined with Bag-1 results in further attenuation of luminal clearing.

Bag-1 does not induce a branching, atypical structure in the 1SM and 1L pools

A statistically significant increase in the percentage of atypical acini was seen in 1SM acini compared to neo controls (Figure 43d), however in the full time course experiment there was no difference in atypical 1SM or 1L acini compared to neo controls (Figure 47). Those acini that did present as atypical tended to have a multiacinar morphology (Figure 43e). I also observed a multiacinar structure in Bcl-2 acini (Figure 46f) which has not been previously reported. When examined by confocal microscopy these multiacinar structures were formed from individual, hollowed acini. The variation in morphogenesis program between independent experiments described previously also related to morphology. It was noted that high passage cells tended to form multiacinar structures at a higher frequency than lower passage cells (data not shown).

I did not see evidence of Bag-1 driving a branching, atypical structure in the 1SM and 1L pools. This is different to the phenotype we detected in the Bag-1L/A and Bag-1L/B stably transfected clones (Papadakis, Barker et al. 2016). The reversibility of this branching, atypical structure upon treatment with a Bag-1 protein-protein interaction inhibitor indicates that Bag-1L does have a role in driving this phenotype. However this phenotype was not seen in the 1L pooled population which further suggests the presence of an additional transformation in the Bag-1L/A and Bag-1L/B stably transfected clones which, when combined with Bag-1L-overexpression, is driving transformation.

Conclusion

In summary my data suggests that Bag-1S- or Bag-1L- overexpression is able to delay, but not fully prevent, luminal clearing within this 3D model. This is in contrast to the filled, atypical acini observed in the Bag-1L/A and Bag-1L/B model implicating the presence of an additional transformation in these clones. This work also highlights that there is variability in the time line of the MCF-10A luminal clearing program which must be considered when planning experiments using this acini model.

Chapter 5: The role of metabolism in MCF-10A acinar morphogenesis

Cancer cells alter their metabolism in association with the increased demand that transformation places upon them and this phenotype has been described as one of the hallmarks for cancer (Hanahan and Weinberg 2011). Cancer cells upregulate glycolysis in order to generate biomass and sustain enhanced proliferation and growth (1.3.2.1 The Warburg effect: matching an increased growth demand) (Vander Heiden, Cantley et al. 2009) and, in addition, enhance PPP flux for the generation of NADPH (1.3.2.2 Pentose phosphate pathway). NADPH is also generated through FAO and cancer cells show an increased dependence on this metabolic pathway (1.3.2.3 Fatty acid oxidation: for NADPH generation) (Carracedo, Cantley et al. 2013). NADPH acts as an electron carrier for biosynthesis and, importantly for this project, is a reducing agent for the neutralisation of ROS. An accumulation of ROS can induce oxidative stress and cell apoptosis and it is therefore essential that a cancer cell maintains the ability to neutralise these species for its survival.

Targeting these alterations in cellular metabolism within cancer is receiving attention as a new therapeutic approach and should be able to selectively target a cancer cell over healthy tissue. However metabolism is a highly complex integration of a number of pathways, many of which occur in equilibrium with each other. For example, the flux of the PPP is limited, but not exclusively, by the rate of glycolysis and the regeneration of $NADP^+$ from NADPH. It is therefore important that we increase our understanding of the metabolic pathways promoting a transformed phenotype and how targeting of these pathways may affect healthy, benign and malignant tissue.

HER2-overexpressing MCF-10A acini fail to undergo luminal clearing leading to the presentation of filled structures which are characteristic of early breast cancer (Muthuswamy, Li et al. 2001, Debnath, Mills et al. 2002, Reginato, Mills et al. 2005, Papadakis, Barker et al. 2016). Both traditional anoikis (Debnath, Mills et al. 2002, Reginato, Mills et al. 2005) and a metabolic defect (Schafer, Grassian et al. 2009) act within the central, ECM-detached cells of parental acini, promoting cellular apoptosis and subsequent luminal clearing (Figure 20a). However HER2 overexpression is able to overcome both of these programs (Figure 20b).

The role of HER2 in overcoming the metabolic stress of cellular detachment has been examined in 2D by growing cells in conditions that mimic ECM-detachment. Schafer *et al.* show that HER2-driven rescue of detachment-induced inhibition of ATP production is through upregulation of glucose uptake; rescue was dependent on both PPP and FAO (Schafer, Grassian et al. 2009). A

dichotomy of NAD(P)H native fluorescence observed across a developing acini, which is reversible by antioxidant treatment, suggests that HER2 inhibits ROS accumulation through enhanced NADPH production. Furthermore, Carracedo *et al.* show that overexpression of the tumour suppressor protein promyelocytic leukemia induces luminal filling in a FAO-dependent manner (Carracedo, Weiss et al. 2012), supporting a role for FAO in acinar morphogenesis.

The work presented in this chapter utilises HER2 acini as a model of early breast cancer and the vector control (puro) as a model of healthy breast acini to further study the role of cellular metabolism in acinar morphogenesis. I investigated the importance of sugar source availability for acinar development. In addition, I used these models to test the effect of some of the metabolic inhibitors which are receiving attention as potential anti-cancer therapeutics.

5.1 HER2-overexpression in MCF-10A alters cell metabolism

I began investigations by directly comparing the metabolism of HER2-overexpressing cells to controls.

5.1.1 HER2 overexpression promotes a more glycolytic phenotype

The Seahorse XF96 Analyser simultaneously reports glycolysis and mitochondrial respiration in live cells by measuring proton release into the media and O_2 consumption from the environment immediately surrounding the cell. Full details of this assay are described in 2.3.5.1 Principles of the Seahorse Analyser. Glycolysis is reported as the extracellular acidification rate (ECAR) and mitochondrial activity reported as oxygen consumption rate (OCR). HER2 overexpression was shown to statistically significantly ($p \leq 0.01$) increase ECAR that was a direct consequence of glycolysis in MCF-10A cells (Figure 51a), while statistically significantly ($p \leq 0.001$) decreasing OCR that is a direct consequence of mitochondrial respiration (Figure 51b).

5.1.2 HER2-overexpression enhances cell viability and ATP levels following 48 h detachment

To compare the metabolism of HER2-overexpressing cells to controls in the 2D setting cell viability and intracellular ATP levels were examined over a 24 h and 48 h period in attached and detached cells. Detached cells were grown on poly-HEMA coated dishes to mimic ECM-detachment. Cell viability was examined using an alamarBlue® assay, a metabolic read out of viability which assesses the reducing ability of a cell.

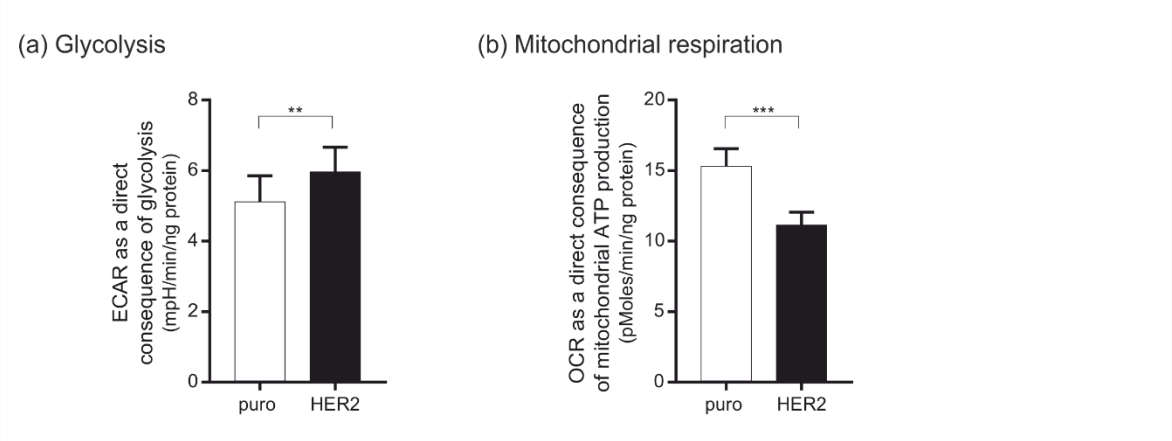

Figure 51 The effect of HER2 overexpression on MCF-10A metabolism

Cells (25,000 per well) were seeded into a Seahorse PET plate 18 h prior to experiment. The Seahorse Analyser simultaneously measured extracellular acidification rate (ECAR) and oxygen consumption rate (OCR) of puro and HER2 MCF-10A cells. (a) ECAR that is a consequence of basal glycolysis. (b) OCR that is a consequence of basal mitochondrial ATP production. Bar graphs represent the mean ± SEM from an independent experiment with twelve technical repeats. ** $p \leq 0.01$; *** $p \leq 0.001$ as determined by an un-paired t-test.

In puro and HER2 cells detachment resulted in a statistically significant ($p \leq 0.001$) reduction in cell viability compared to attachment at both 24 h and 48 h (Figure 52a). The fold-reduction in cell viability following detachment was more pronounced at 48 h than 24 h. Puro cells displayed a 0.40- and 0.48- fold reduction in viability following detachment at 24 h and 48 h respectively while HER2 cells displayed a smaller 0.18- and 0.25- fold reduction. Looking at the relative viability of puro versus HER2 cells, HER2 overexpression resulted in a statistically significant ($p \leq 0.001$) increase in viability (Figure 52b); this increase was of a similar magnitude at 24 h and 48 h, with a 1.48- fold and 1.52-fold increase in viability respectively.

Similarly to cell viability, ATP levels were statistically significantly ($p \leq 0.001$) reduced in detached versus attached conditions in puro and HER2 cells at 24 h and 48 h (Figure 52c). The fold-reduction in ATP levels following detachment was more pronounced at 48 h than 24 h. Puro cells displayed a 0.46- and 0.76- fold reduction in ATP levels following detachment at 24 h and 48 h respectively, while HER2 cells displayed a 0.45- and 0.63- fold reduction. At 24 h HER2 overexpression had no statistically significant effects on ATP levels in detachment compared to controls while at 48 h, HER2 resulted in a statistically significant ($p \leq 0.01$) increase in ATP levels (Figure 52d).

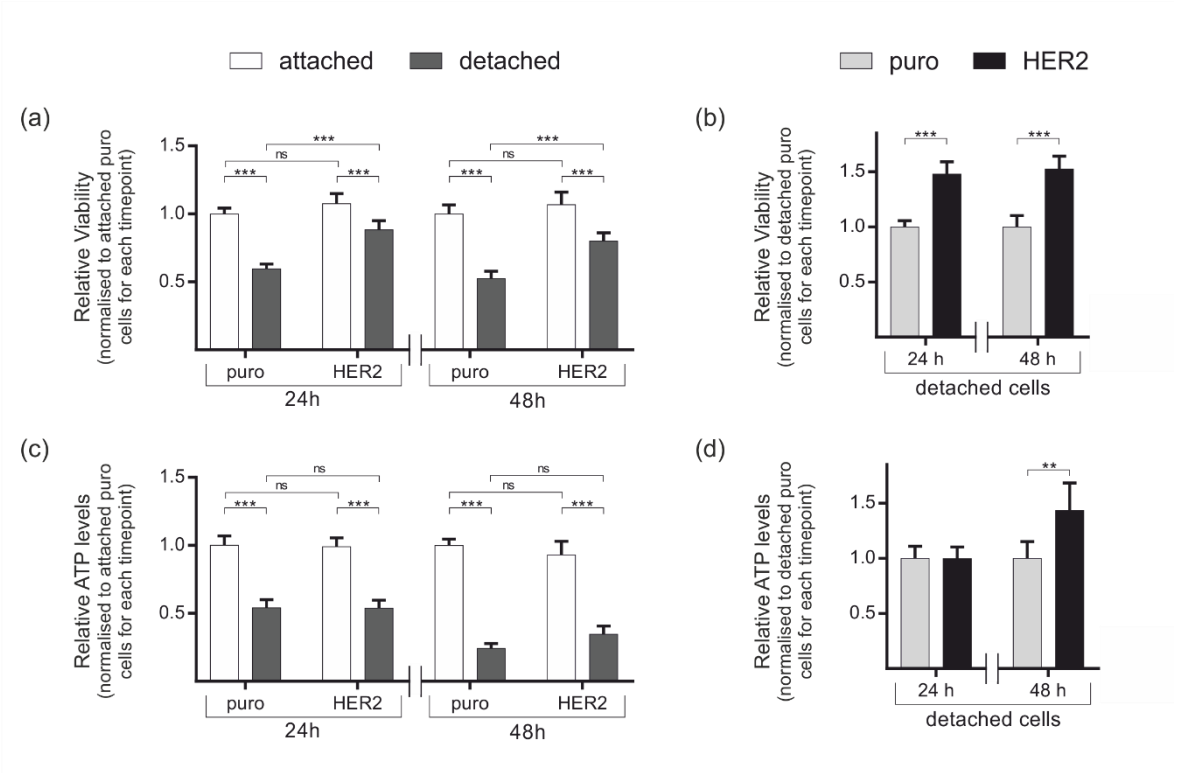

Figure 52 The effect of HER2 overexpression on cell viability in 2D

Cells (15,000 per well) were seeded onto standard tissue culture plates (attached) or polyHEMA-coated plastic (detached) for 24 h or 48 h. (a,b) Cell viability was examined using alamarBlue® reagent which was added to conditions 6 h prior to data collection. Fluorometric data was normalised for experimental variation and expressed relative to attached puro cells (a) or to detached puro cells (b) for each time point. (c,d) ATP levels were examined using the ATPlite assay. Luminescence data was normalised for experimental variation and expressed relative to attached puro cells (c) or to detached puro cells (d) for each time point. Bar graphs represent the mean ± SEM from six independent experiments each with three technical repeats. ns = nonsignificant, ** $p \leq 0.01$, *** $p \leq 0.001$ as determined by a two-way ANOVA with Fisher's LSD test.

5.1.3 HER2 overexpression results in a small, non-significant increase in alamarBlue® readings in 3D acini

To further compare HER2 to puro I carried out an alamarBlue® assay on 3D acini to assess the reducing ability. Due to experimental limitations of the alamarBlue® assay acini needed to be cultured in a 96-well plate rather than in the traditional chamber slides. Matrigel, cell seeding densities and media volumes were adjusted accordingly; phase contrast images confirm that acini culture in these conditions (Figure 53a). In this setting HER2 acini displayed a 1.08-fold increase in cell viability compared to puro which did not reach statistical significance (Figure 53b).

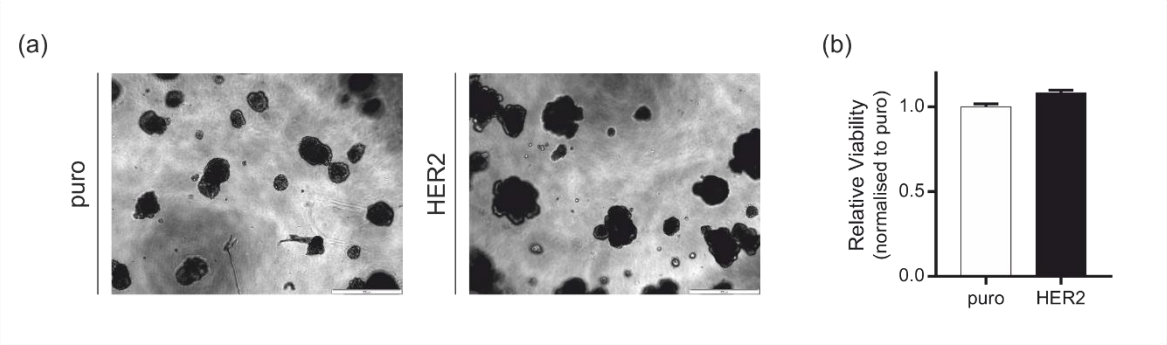

Figure 53 The effect of HER2 overexpression on 3D cell viability

Cells (200 per well) were seeded in 96-well plates which had been pre-coated with Matrigel and cultured in 3D for 12 days. (a) Representative phase contrast images of acini growing in 96-well plate confirm that acini will form under these culture conditions; scale bars show 500 µm. (b) Cell viability was examined using alamarBlue® reagent which was added to conditions 6 h prior to data collection. Fluorometric data was adjusted for background, normalised for experimental variation and expressed relative to puro. Bar graphs represent the mean ± SEM from five independent experiments each with four technical repeats.

5.2 Sugar source availability influences acinar morphogenesis.

Investigations into the role of metabolism in the HER2-driven phenotype of luminal filling relate to short term effects of HER2 overexpression in response to acute metabolic stress. By substituting glucose for fructose within cell medium we can limit the glycolytic ability of a cell (Reitzer, Wice et al. 1979). This is a consequence of slower fructose utilisation because its import and retention are limited by the high Km of its transporter (GLUT5) and the Km of hexokinase for fructose. Relative enzyme kinetics of glucose-6-phosphate dehydrogenase and phosphofructokinase mean that the PPP draws what it needs and dictates that fructose-6-phosphate concentrations in fructose-cultured cells are too low to drive the lower stages of glycolysis (Figure 54); therefore fructose-cultured cells utilise glutamine for energy generation and anaplerosis (Reitzer, Wice et al. 1979). The culture of glucose- versus fructose- adapted MCF-10A acini will enable study of the long term consequences of HER2-driven changes in cell metabolism on MCF-10A morphogenesis.

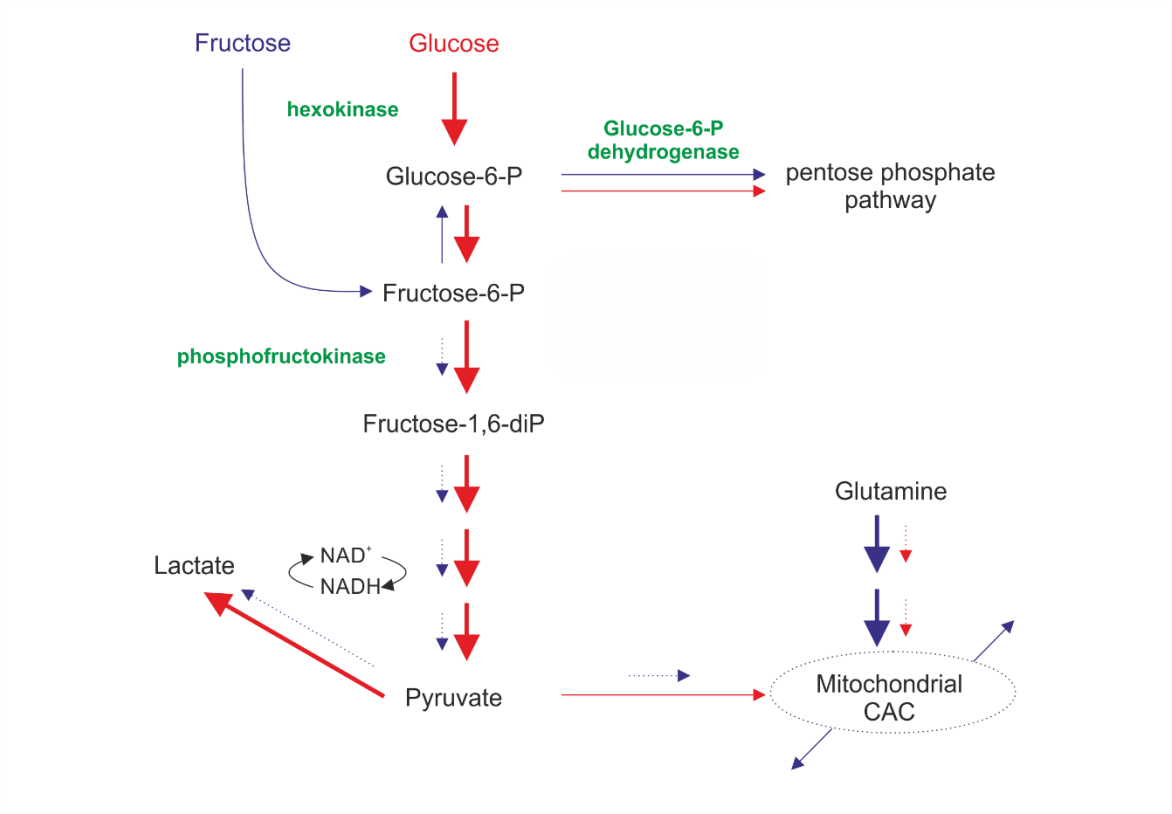

Figure 54 Fructose-cultured cells have lower levels of glycolysis than glucose-cultured cells

Enzyme kinetics dictates that fructose (blue arrows) is drawn into the pentose phosphate pathway and fructose-6-phosphate levels remain too low to drive the phosphofructokinase-dependent lower stages of glycolysis. Fructose-cultured cells instead rely on glutamine for energy generation. CAC = citric acid cycle.

5.2.1 Altering the sugar-source available alters MCF-10A acinar morphogenesis when grown in DMEM media

Puro and HER2 pooled populations were routinely cultured in glucose- or fructose-containing, supplemented DMEM media for a period of 30 days before use in experiments to ensure adaptation to the new sugar source. This media differed from standard MCF-10A culture media as it lacked Ham's F12 base; media still contained all additional MCF-10A media supplements (Table 6). At day 12 of acinar morphogenesis puro acini grown in glucose-DMEM (denoted Glu-DMEM puro) had 92% of acini scoring as incompletely cleared (Figure 55b,c) and 75% of acini scoring as morphologically atypical (Figure 55d,c). Fructose-DMEM adapted puro acini (denoted Fru-DMEM puro) had statistically significantly less ($p \leq 0.001$) acini scoring as incompletely cleared compared to Glu-DMEM puro (Figure 55b,c), with 57% of incompletely cleared acini and 40% atypical (Figure 55d,c). For HER2-overexpressing glucose- or fructose- adapted pools acini displayed the reverse trend to puro. 27% more fructose-DMEM adapted acini (denoted Fru-DMEM HER2) scored as

incompletely cleared compared to glucose-DMEM adapted HER2 (denoted Glu-DMEM HER2) (Figure 55b,c), with 23% more Fru-DMEM scoring as atypical compared to Glu-DMEM HER2 (Figure 55c,d).

The Glu-DMEM puro condition was expected to mimic standard MCF-10A culture conditions. At day 12 of morphogenesis the majority of non-transformed acini should have undergone luminal clearing and acini should adopt a spherical structure (Debnath, Muthuswamy et al. 2003). The high percentage of filled acini, combined with the high percentage of acini displaying a transformed morphology, suggests the Glu-DMEM media is driving a transformation. This transformation could be due to the absence of Ham's F12 base. However sugar source availability did significantly alter acinar morphogenesis in this setting and I therefore sought to examine these findings in a glucose-free Biowest DMEM – F12 media. This media was purchased from a different supplier than the standard DMEM – Hams' F12 media used for typical MCF-10A culture (Table 6).

5.2.2 Acini fail to form in glucose-Biowest DMEM – F12

Puro and HER2 MCF-10A cells, cultured from early passaged cryopreserved stocks and which had not undergone any previous adaptation, were cultured in glucose- or fructose- Biowest DMEM – F12 for a period of 30 days of adaptation before use in experiments. 2D cultures grew as expected, requiring subculturing at the expected frequency of parental MCF-10A (data not shown). When seeded in 3D at the standard density (1000 cells/well) little to no acini formed across three repeats (data not shown). One repeat had no acini at all, while two had no acini in the glucose-Biowest DMEM – F12 condition and less than 20 acini/well present in the fructose-Biowest DMEM – F12 condition.

The glucose-Biowest DMEM – F12 media should be the same media as cells grown in standard culture media. The inability of acini to grow during culture may be due to a transformation occurring during the adaptation stage that limits the cells ability to form acini. Alternatively, there may be a difference in media composition or preparation between the two suppliers that is incompatible for 3D culture. To examine these possibilities in detail puro cells which had always been cultured in standard MCF-10A media were seeded into 3D culture alongside glucose- and fructose- Biowest DMEM – F12 adapted cells. Puro cells from standard culture were seeded in either traditional MCF-10A assay media or the glucose-Biowest DMEM – F12 media used for glucose-adaptation. As little to no acini formed when cells were seeded at 1000 cells/well in the Biowest DMEM – F12 media, the seeding density of glucose- and fructose-adapted cells was doubled. 3D acinar culture is analogous to 2D culture in that too sparse a seeding density results in a failure of cells to propagate, and too high a density can also be detrimental. It may be that the

Biowest DMEM – F12-adapted cells have a reduced ability to form colonies compared to the standard DMEM – Hams' F12 media, and increasing the seeding density may therefore promote acini formation.

Consistent with the previous experiment, glucose- and fructose- Biowest DMEM – F12 adapted acini did not form at the expected density in Biowest DMEM – F12 assay media (Figure 56). 3D structures grew out from monolayers in the puro population adapted to glucose-Biowest DMEM – F12 but these did not mimic traditional acini structures. In the fructose-Biowest DMEM – F12 puro population branching acini structures were seen at a low number. Puro and HER2 populations from standard culture (no adaptation) grew as expected in their standard assay media (Figure 57). However, similarly to as described for the adapted populations, growth of standard culture puro and HER2 in glucose-Biowest DMEM – F12 assay media resulted in a reduced number of 3D structures which grew out of monolayers and did not mimic traditional structures.

5.3 Inhibition of fatty acid oxidation accelerates luminal clearing and attenuates HER2-driven luminal filling

Glucose- or fructose- adaptation faced experimental limitations when moving from 2D to the 3D culture system. However, data collected using glucose- or fructose- DMEM media did suggest that metabolic manipulation can alter acinar morphogenesis. I therefore looked to use small molecule inhibitors to examine how metabolic interference influences acinar morphogenesis.

As FAO has previously been implicated in cell survival of MCF-10A I began by examining the role of this pathway in MCF-10A morphogenesis. Overexpression of a tumour suppressor molecule, promyelocytic leukemia, has been shown to induce MCF-10A luminal filling in a FAO-dependent manner (Carracedo, Weiss et al. 2012) which, combined with the findings by Schafer *et al.* in 2D culture showing that HER2-overexpression in MCF-10A rescues the ATP defect seen upon matrix detachment in a FAO-dependent manner (Schafer, Grassian et al. 2009), implicates FAO in HER2-driven luminal filling.

For each metabolic inhibitor examined I first sought to confirm the metabolic consequences of inhibitor treatment in 2D, to assess whether the inhibitors are behaving as expected, and carry out a dose response to determine an appropriate concentration to take forward for further experiments. Following this I assessed the consequences of inhibitor treatment on cell viability in 2D and, finally, I examined the consequence of inhibitor treatment on 3D morphogenesis.

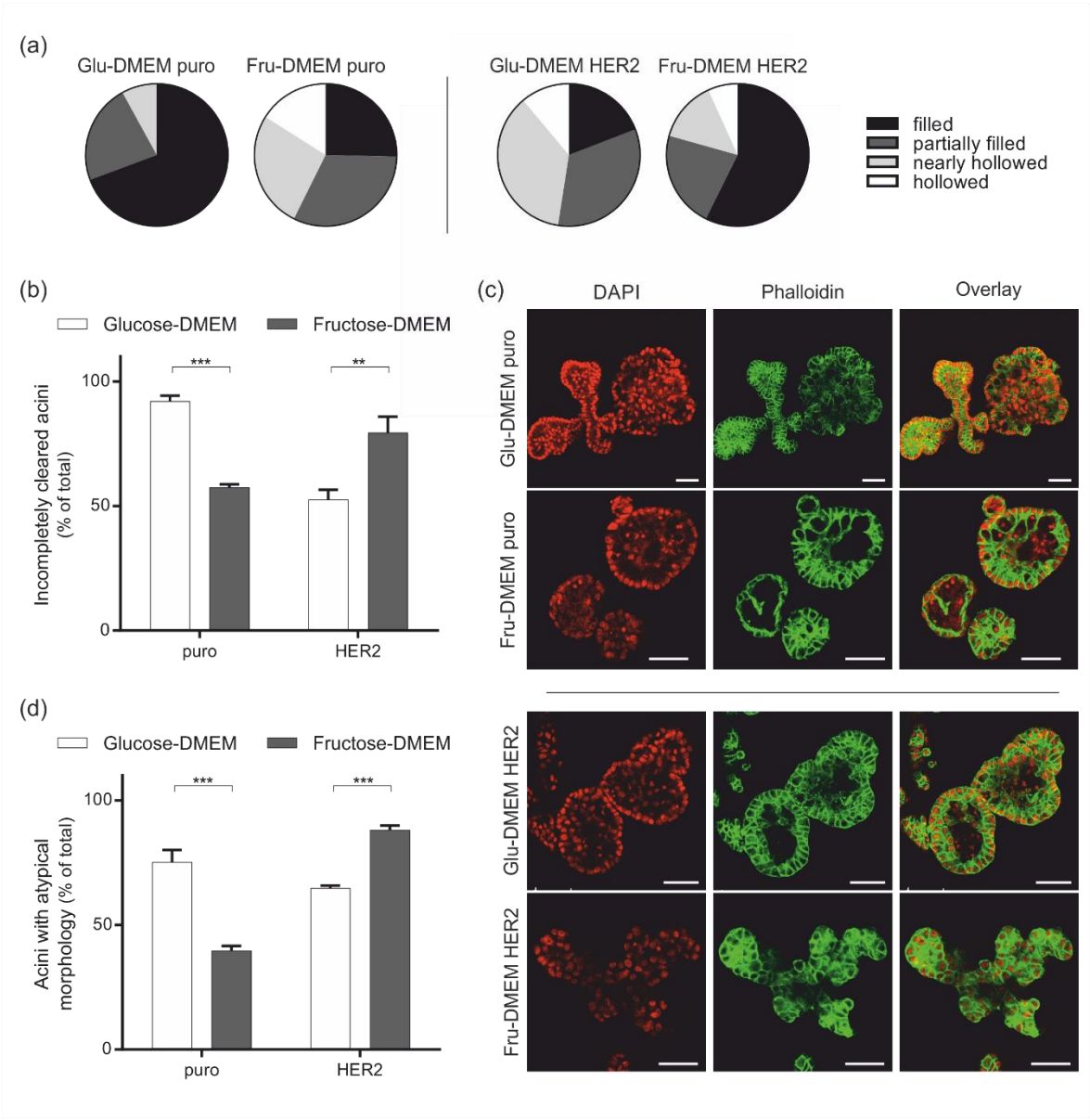

Figure 55 Sugar source availability alters the morphogenesis of MCF-10A

Acini adapted to glucose- or fructose- DMEM were cultured in their adapted assay medium for 12 days of morphogenesis and stained with DAPI (red) and phalloidin-TRITC (green). Confocal microscopy was utilised to score luminal status; looking through all focal planes, acini were scored as filled, partially filled, nearly hollowed or completely hollowed. (a) Pie chart representation shows the proportions of acini scoring in each category. (b) The number of acini scoring as incompletely cleared (filled or partially filled) was expressed as a percentage of the total acini scored. Bar graphs represent the mean ± SEM from an independent experiment with three technical repeats. A minimum of 75 acini were scored for each condition. (c) Representative confocal immunofluorescence images show the centre of MCF-10A acini at day 12 of morphogenesis; scale bars show 50 µm. (d) Acini with an atypical morphology were counted at day 18 of morphogenesis and their numbers expressed as a percentage of total acini. Bar graphs represent the mean ± SEM from three independent experiments each with four technical repeats. A minimum of 50 acini were present in each technical repeat. ** $p \leq 0.01$; *** $p \leq 0.001$ as determined by a two-way ANOVA with Fisher's LSD test.

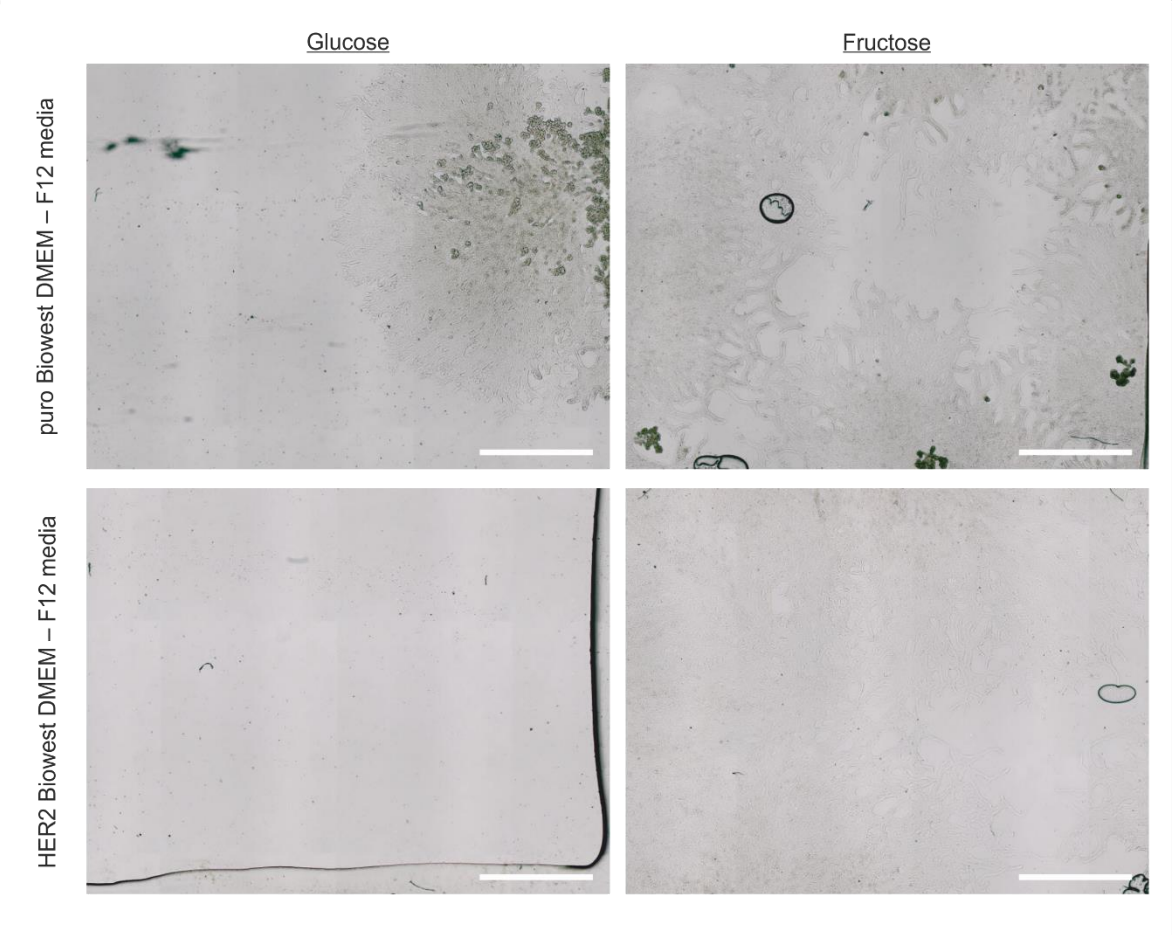

Figure 56 Acini growth is disrupted when cultured in glucose- or fructose- Biowest DMEM - F12 glucose free media

Cells adapted to glucose- or fructose- Biowest DMEM – F12 were cultured in their adapted assay media for 12 days of acinar morphogenesis at which point they were fixed directly to minimise acini loss in wash steps (2% PFA final concentration) and mounted. High resolution pictures covering the entire slide were captured. Representative images of a whole chamber for each condition are shown; scale bars show 2 mm.

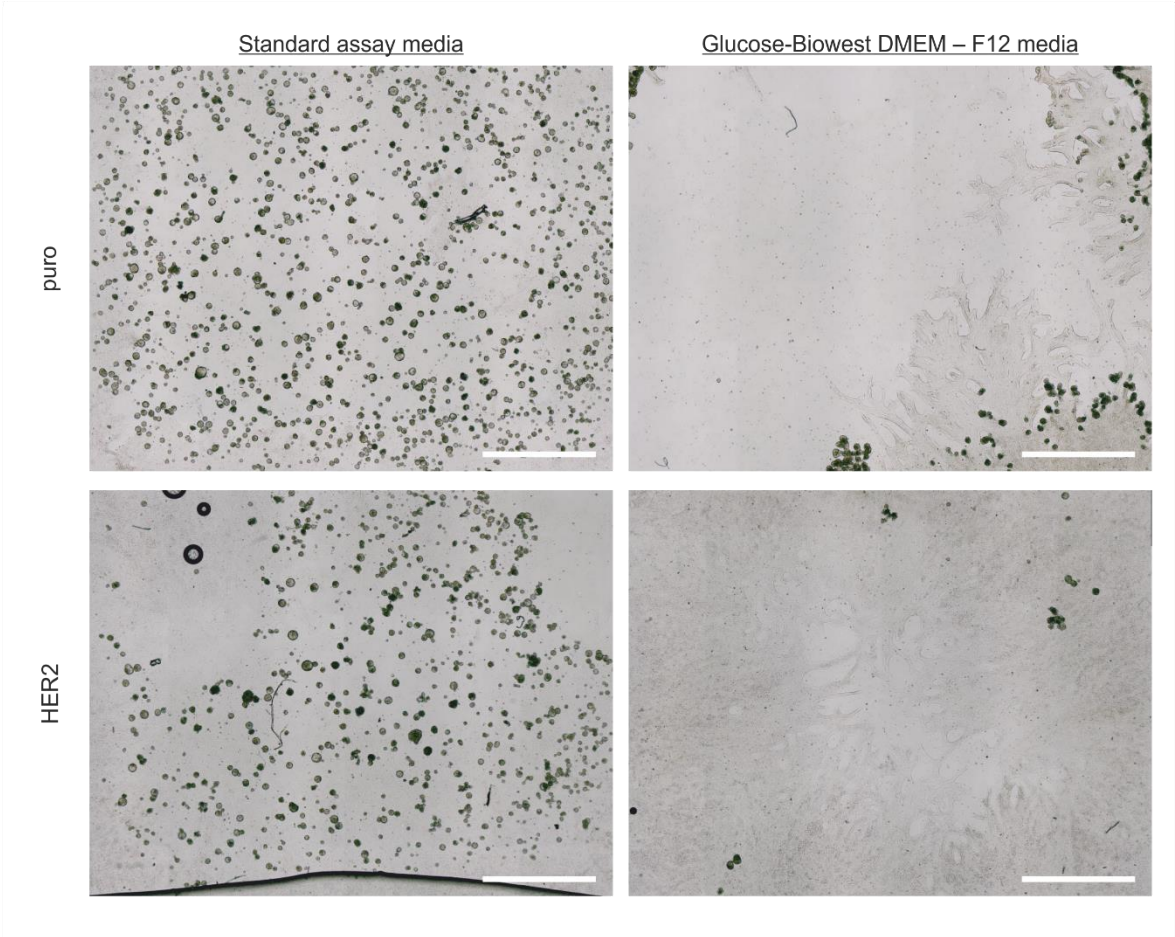

Figure 57 Acini which have been pre-cultured in 2D in standard growth MCF-10A media fail to form typical acini when grown in glucose- Biowest DMEM - F12

Cells that had always been cultured in 2D in standard MCF-10A growth media were cultured in 3D in standard assay media or glucose-Biowest DMEM – F12 for 12 days at which point acini were fixed directly to minimise loss in wash steps (2% PFA final concentration) and mounted. High resolution pictures covering the entire slide were captured. Representative images of a whole chamber for each condition are shown; scale bars show 2 mm.

5.3.1 Etomoxir

I began inhibitor studies by looking at etomoxir which inhibits FAO by irreversibly inhibiting CPT-1) (Table 11) (Eistetter and Wolf 1986). CPT-1 is a mitochondrial membrane protein which catalyses the formation of acyl-carnitine from acyl-coA and carnitine to allow passage of long chain fatty acids from the cytosol into the intermembrane space (Figure 7b).

5.3.1.1 Metabolic consequences of etomoxir treatment

The inhibitory effect of etomoxir on cellular glycolysis and mitochondrial respiration was examined in a 2D assay utilising the Seahorse Analyser equipment. For this assay baseline ECAR and OCR readings were recorded and all readings were expressed relative to baseline readings at

the point of drug injections. Following drug injections wells were then injected with either 2-deoxyglucose (100 mM) or oligomycin followed by antimycinA and rotenone (Figure 21). This concentration of 2-deoxyglucose completely inhibits glycolysis, allowing me to determine the ECAR that is a consequence of glycolysis (Figure 21a). Oligomycin inhibits ATP synthase while antimycinA and rotenone inhibit complexes III and I of the electron transport chain respectively, allowing me to examine the OCR that is a consequence of proton leak and non-mitochondrial respiration and thus calculate OCR that is a direct consequence of mitochondrial ATP production (Figure 21b).

In both puro and HER2 pools etomoxir significantly ($p \leq 0.01$) increases ECAR plateauing at higher concentrations to give an ECAR that is approximately 135% of media controls (Figure 58a). Etomoxir had no statistically significant effect on ECAR following 2-deoxyglucose injection (Figure 58c) indicating that effects observed on ECAR were a consequence of glycolytic activity. In addition etomoxir significantly ($p \leq 0.001$) inhibits OCR in a dose-dependent manner (Figure 58b). At lower etomoxir concentrations (25-100 µM) etomoxir had no statistically significant effect on OCR values following oligomycin or antimycinA and rotenone injections (Figure 58d,e), indicating that the effects observed on OCR are a consequence of reduced mitochondrial activity. At the highest etomoxir concentrations (150 µM, 200 µM) OCR was significantly ($p \leq 0.001$) reduced following oligomycin injection indicating that an extent of the decrease in OCR observed following 150 µM or 200 µM etomoxir is due to a decrease in proton leak and not mitochondrial ATP production (Figure 58d). However no statistically significant differences were seen following antimycinA and rotenone treatment indicating that non-mitochondrial oxygen consumption is not altered (Figure 58e). 100 µM etomoxir was selected to use in future experiments; this concentration of etomoxir was used by Carracedo *et al.* to fully inhibit FAO in mouse embryonic fibroblasts and primary hepatocytes (Carracedo, Weiss et al. 2012). In the Seahorse assay this concentration inhibited mitochondrial ATP production by 0.60- and 0.68-fold in puro and HER2 respectively while increasing glycolysis by 1.73- and 1.46-fold respectively (Figure 58a,b).

5.3.1.2 The effect of etomoxir treatment on 2D cultured cells

To examine the effect of etomoxir on 2D cultured cells, cell viability and intracellular ATP levels were examined over a 24 h and 48 h period in attached and detached cells (Figure 59). Examining cell viability etomoxir increases cell viability in both attached and detached conditions with statistical significance ($p \leq 0.05$) reached in puro cells at 24 h and in HER2 and detached puro cells at 48 h (Figure 59a). Looking at intracellular ATP there is a trend towards reduced ATP following etomoxir treatment, excluding in HER2 attached cells at 48 h, although statistical significance was not reached in any conditions (Figure 59b).

5.3.1.3 The effect of etomoxir treatment on 3D acini

In acini etomoxir treatment pushes acini towards a less filled phenotype with a significantly ($p \leq 0.001$) reduced number of acini scoring as incompletely cleared at day 12 of morphogenesis (Figure 60a,b,c); etomoxir reversed the phenotype of HER2-driven luminal filling with less incompletely cleared acini in HER2 compared to puro (Figure 60b). A 0.44-fold reduction in incompletely cleared acini was observed following etomoxir treatment in puro with a 0.85-fold reduction in incompletely cleared HER2 acini (Figure 60d). Acini were observed to be typically rounded with a hollowed lumen (Figure 60c). A reduction in HER2-driven branching would be indicative of reduced transformation and is consistent with the attenuation of luminal filling following etomoxir treatment and was examined further (Figure 61). Morphology scoring confirmed that etomoxir treatment led to a significant ($p \leq 0.05$) decrease in the number of atypical acini in HER2 acini (Figure 61b).

To further examine the effect of etomoxir treatment on 3D acini I carried out an alamarBlue® assay to assess acini viability (Figure 62). Etomoxir treatment of puro acini significantly ($p \leq 0.01$) increased cell viability when examined in this assay, while no statistically significant effects where observed on HER2 acini.

5.3.2 Perhexiline

My data relating to luminal status in puro and HER2 acini following etomoxir treatment supports reported findings implicating FAO in luminal cell survival (Schafer, Grassian et al. 2009, Carracedo, Weiss et al. 2012) and highlights a novel finding relating to the role of FAO in acinar morphology. To examine this further I tested the effect of a second CPT-1 inhibitor, perhexiline (Table 11) (Kennedy, Unger et al. 1996), on puro and HER2.

5.3.2.1 Metabolic consequences of perhexiline treatment

The metabolic consequences of perhexiline treatment were examined using the Seahorse Analyser (Figure 63). I aimed to assess the perhexiline concentration that would induce a similar fold-reduction in mitochondrial activity seen with 100 µM etomoxir; 100 µM etomoxir was therefore included for comparison. Lower concentrations of perhexiline were included than those examined during the etomoxir titration, based around findings from Stäubert *et al.* who had treated BT-474 and HCC1954 cells with etomoxir or perhexiline and found similar fold-changes in ATP production following treatment of 30 µM etomoxir and 2.5 µM perhexiline.

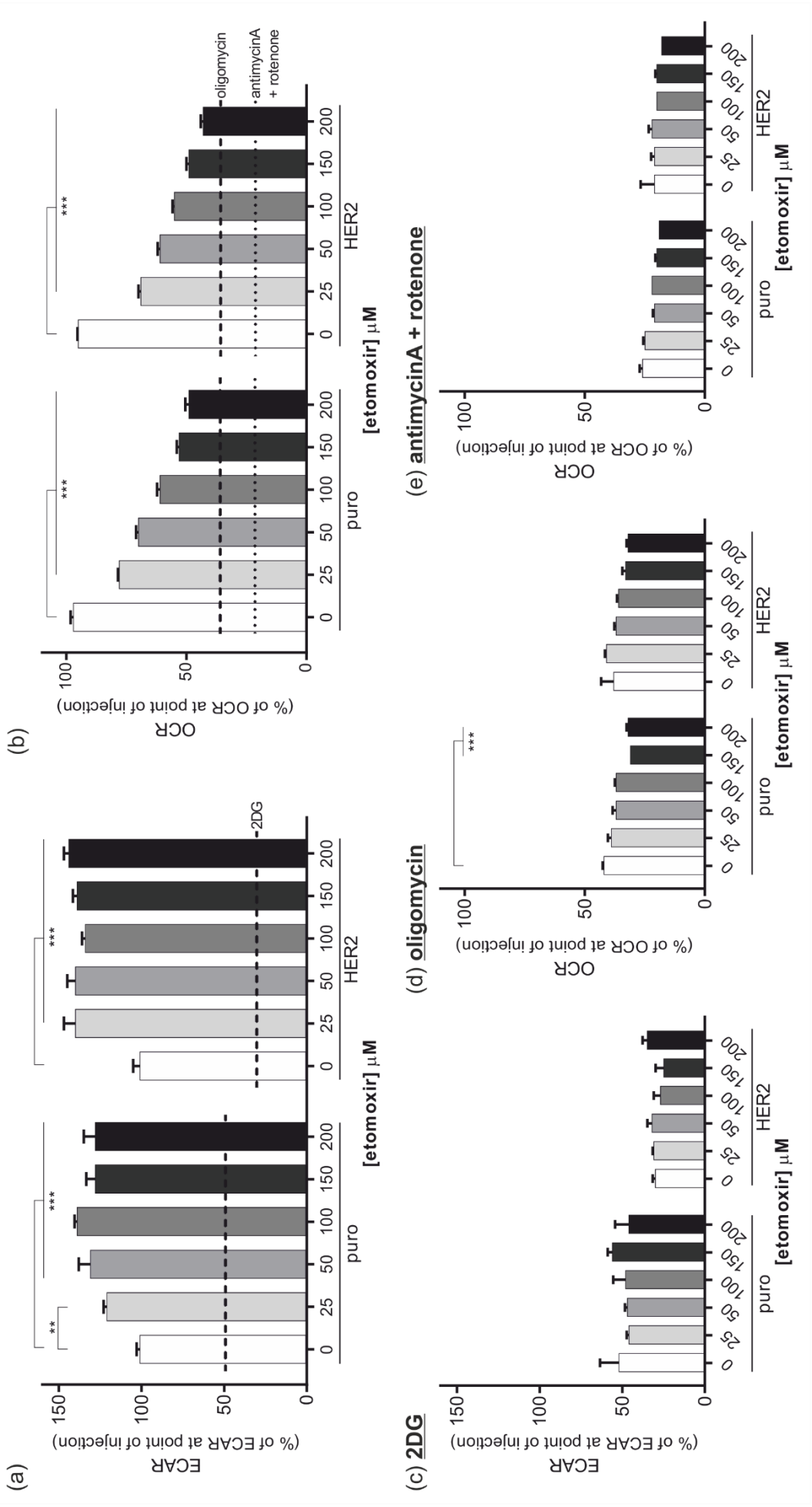
(a)
ECAR
(% of ECAR at point of injection)
150
100
50
0
**
***
***
2DG
0
25
50
100
150
200
puro
HER2
[etomoxir] μM
(b)
OCR
(% of OCR at point of injection)
100
50
0
***
***
oligomycin
antimycinA
+ rotenone
(c) 2DG
(d) oligomycin
(e) antimycinA + rotenone

Figure 58 Metabolic responses to etomoxir treatment

Cells (25,000 per well) were seeded into a Seahorse PET plate 18 h prior to experiment. The Seahorse Analyser simultaneously measured extracellular acidification rate (ECAR) and oxygen consumption rate (OCR) following injection of the stated etomoxir concentration. Following etomoxir treatment wells were injected with either 100 mM 2-deoxyglucose (2DG) or 1 µM oligomycin followed by 1 µM antimycinA and 1 µM rotenone. All data was baselined to the values for ECAR and OCR at the point of injection of the drug (0 min). (a) ECAR following etomoxir treatment; dashed lines show the average ECAR for puro or HER2 cells following 2DG. Bar graphs represent the mean ± SEM from an independent experiment with four technical repeats. (b) OCR following etomoxir treatment. Dashed lines show the average OCR for puro or HER2 cells following oligomycin injection; dotted lines show the average OCR for puro or HER2 cells following antimycinA and rotenone injection. Bar graphs represent the mean ± SEM from an independent experiment with four technical repeats. (c) ECAR following 2DG; bar graphs represent the mean ± SEM from an independent experiment with two technical repeats. (d,e) OCR following oligomycin (d) followed by antimycinA and rotenone (e). Bar graphs represent the mean ± SEM from an independent experiment with two technical repeats. ** $p \leq 0.01$; *** $p \leq 0.001$ as determined by a two-way ANOVA with Fisher's LSD test.

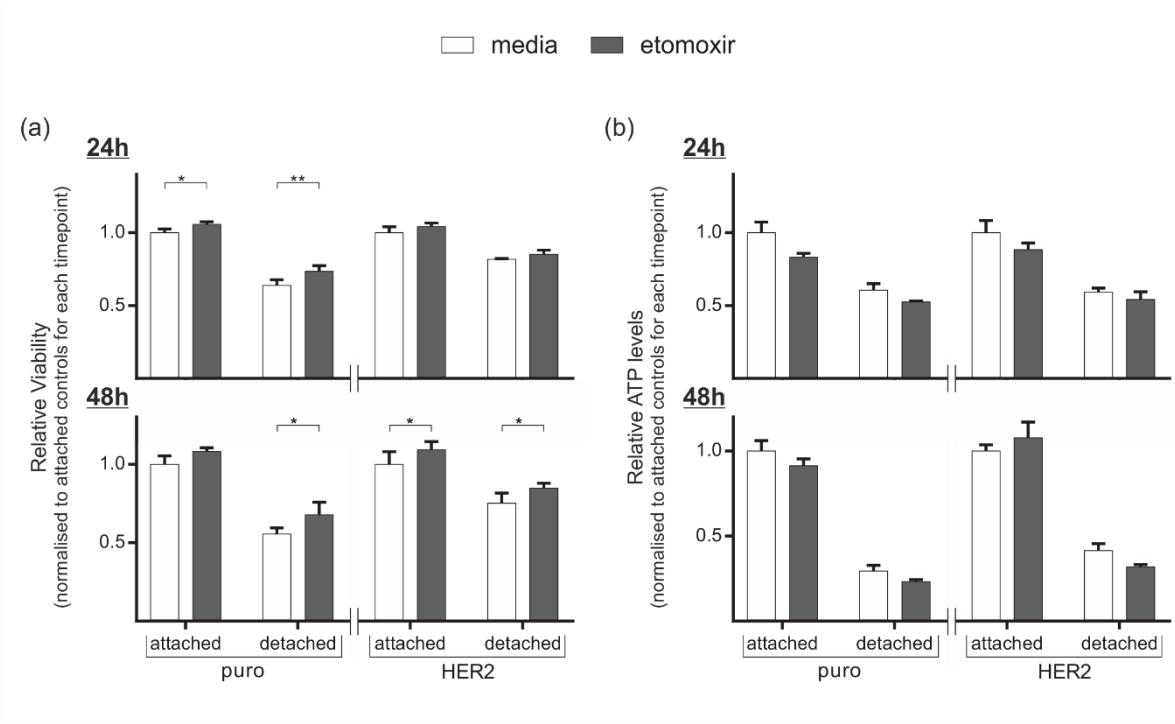

Figure 59 The effect of etomoxir on cell viability in 2D

Cells (15,000 per well) were treated with media or etomoxir (100 µM) and seeded onto standard tissue culture plates (attached) or polyHEMA-coated plastic (detached) for 24 h or 48 h. (a) Cell viability was examined using alamarBlue® reagent which was added to conditions 6 h prior to data collection. (b) ATP levels were examined using the ATPlite assay. Fluorometric (a) or luminometric data (b) was normalised for experimental variation and expressed relative to the appropriate media control in attached conditions (puro or HER2). Bar graphs represent the mean ± SEM from three independent experiments, each with three technical repeats. * $p \leq 0.05$, ** $p \leq 0.01$ as determined by a two-way ANOVA with Fisher's LSD test.

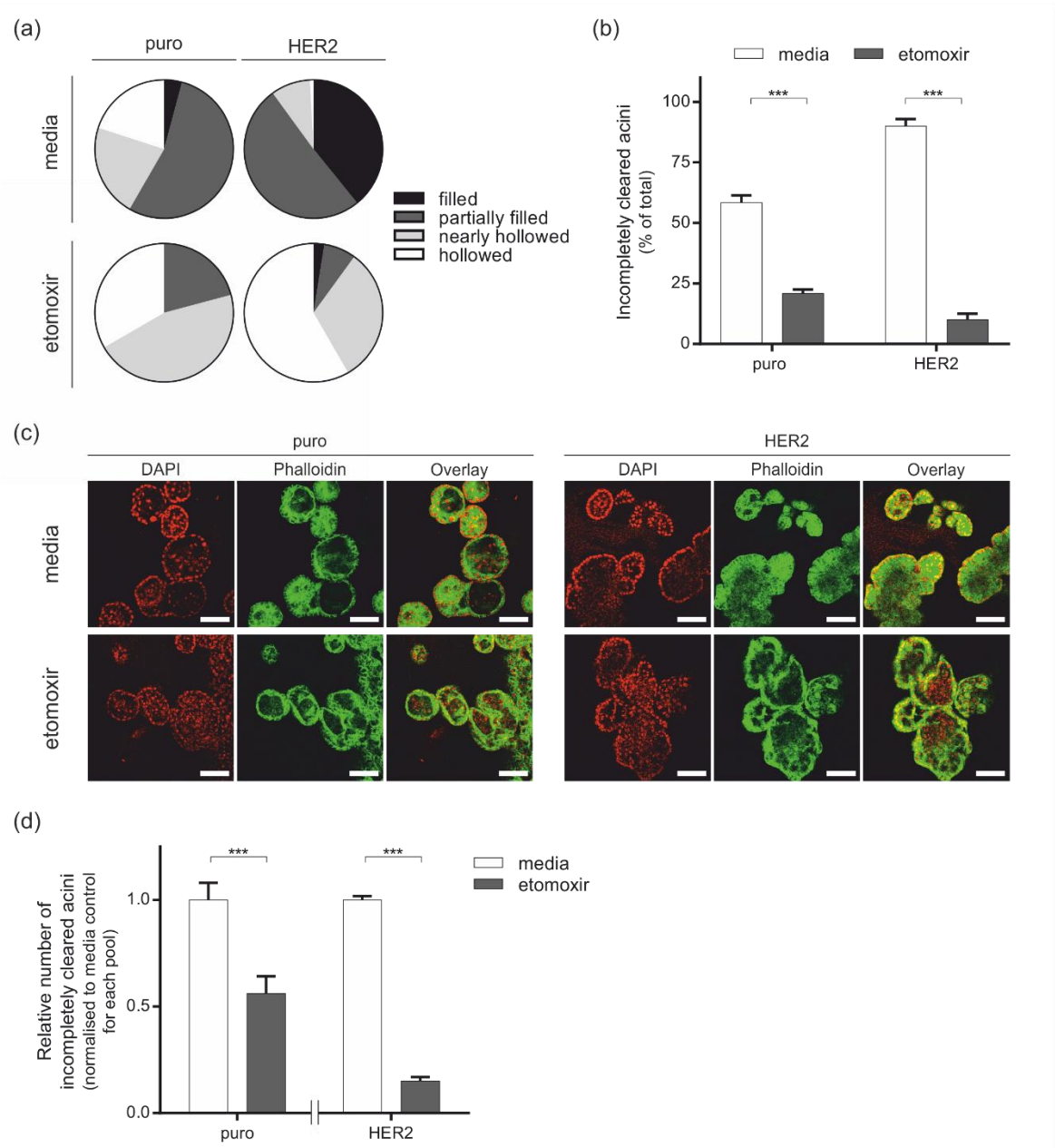

Figure 60 The effect of etomoxir on 3D acini

Acini were treated with media or etomoxir (100 µM) every 2 days from day 6 of morphogenesis. At day 12 acini were fixed and stained with DAPI (red) and phalloidin-TRITC (green). Confocal microscopy was utilised to score luminal status; looking through all focal planes, acini were scored as filled, partially filled, nearly hollowed or completely hollowed. (a) Pie chart representation shows the proportion of acini scoring in each category from a representative experiment. (b) The number of acini scoring as incompletely cleared (filled or partially filled) in (a) was expressed as a percentage of the total acini scored. A minimum of 120 acini were scored for each condition across three replicates. Bar graphs represent the mean ± SEM from three technical repeats. (c) Representative confocal immunofluorescence images show the centre of acini following etomoxir treatment; scale bars show 100 µm. (d) Combined data from three independent experiments shows the relative number of incompletely cleared acini in the presence of etomoxir compared to media controls. Within an independent experiment values were adjusted for the total number of incompletely cleared acini for each pool. Adjusted values were normalised to the mean adjusted values for media across all three experiments. *** $p \leq 0.001$ as determined by two-way ANOVA with Fisher's LSD test.

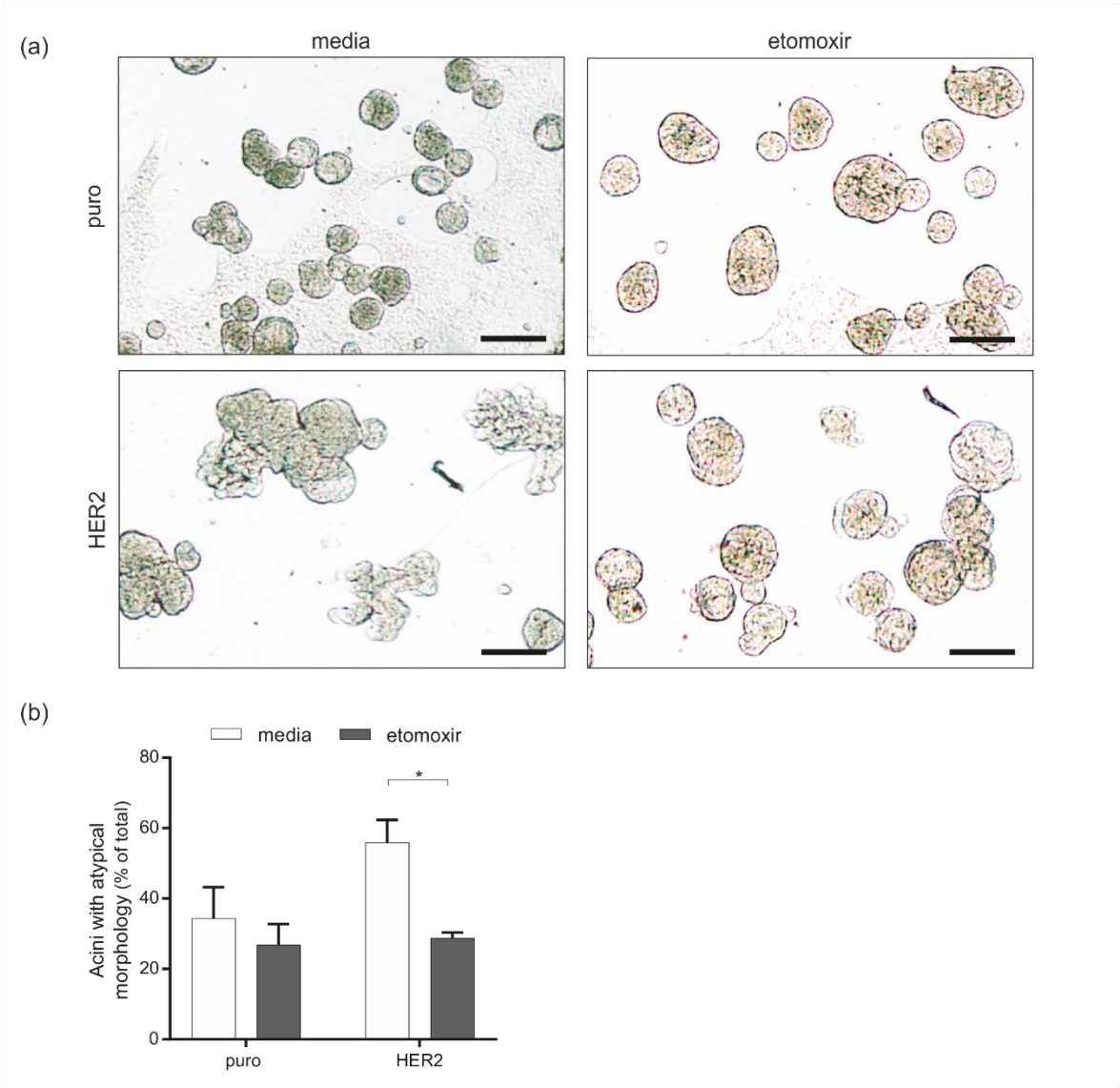

Figure 61 The effect of etomoxir on 3D acinar morphology

Acini were treated with media or etomoxir (100 µM) every 2 days from day 6 of morphogenesis. At day 12 acini were fixed directly to minimise acini loss in wash steps (2% PFA final concentration) and mounted. High resolution pictures covering the entire slide were captured and all acini within a chamber scored manually. (a) Representative phase contrast images of acini morphology are shown; scale bars show 200 µm. (b) Morphology was scored as normal or atypical, where atypical includes multiacinar, branching and non-rounded acini. The number of acini scoring as atypical was expressed as a percentage of the total acini scored. A minimum of 140 acini were present in each well. Bar graphs represent the mean ± SEM from three independent experiments, each with three technical repeats. * $p \leq 0.05$ as determined by a two-way ANOVA with Fisher's LSD test.

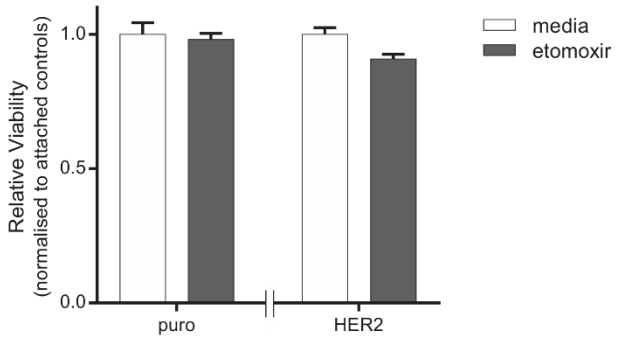

Figure 62 The effect of etomoxir on 3D acini viability

Cells (200 per well) were seeded in 96-well plates which had been pre-coated with Matrigel and cultured in 3D for 12 days. Acini were treated with media or etomoxir (100 µM) every 2 days from day 6 of morphogenesis. Cell viability was examined using alamarBlue® reagent which was added to conditions 6 h prior to data collection. Fluorometric data was adjusted for background, normalised for experimental variation and expressed relative to the appropriate media control (puro or HER2). Bar graphs represent the mean ± SEM from three independent experiments each with four technical repeats. ** $p \leq 0.01$ as determined by a two-way ANOVA with Fisher's LSD test.

Perhexiline had variable effects on ECAR and OCR compared to DMSO control. Looking at glycolysis, perhexiline significantly ($p \leq 0.05$) inhibits ECAR at 5 µM, 100 µM and 200 µM while significantly ($p \leq 0.001$) increasing ECAR at 25 µM in both puro and HER2 cells (Figure 63a). ECAR in puro and HER2 following 2-deoxyglucose injection were significantly ($p \leq 0.01$) reduced in the presence of 50 µM perhexiline and above (Figure 63c). Mitochondrial activity was increased following treatment of perhexiline at concentrations of up to 25 µM (Figure 63b). OCR following oligomycin injections were significantly ($p \leq 0.05$) increased in puro cells treated with 25 µM perhexiline and in HER2 cells treated with 10 µM perhexiline (Figure 63d), but statistical significance is lost following antimycinA and rotenone injections (Figure 63e) indicating that perhexiline is interfering with proton leak but not non-mitochondrial O2 consumption. At higher concentrations ($\geq$ 50 µM) perhexiline significantly ($p \leq 0.001$) reduces OCR in a dose dependent manner (Figure 63b). OCR following oligomycin or antimycinA and rotenone are not statistically significantly different to DMSO controls at 50 µM perhexiline (Figure 63d,e); however at 100 µM and 200 µM perhexiline the oligomycin and antimycinA and rotenone data suggests that perhexiline is interfering with proton leak and non-mitochondrial O_2 consumption.

100 µM etomoxir significantly ($p \leq 0.001$) reduced OCR compared to media controls (Figure 63b), consistent with previous findings. While OCR inhibition was only observed at perhexiline concentrations of 50 µM and above, these concentrations were found to impact on ECAR and OCR

measurements following 2-deoxyglucose, oligomycin or antimycinA and rotenone injections indicating that they are having unintended effects. This makes them undesirable for use in further experiments as I cannot ascertain whether a consequence is due to the intended inhibition of FAO or due to off-target effects.

Stäubert *et al.* used a 12-fold lower concentration of perhexiline than etomoxir in their experimental conditions (Staubert, Broom et al. 2015). The nearest concentration I examined in the Seahorse titration is 10 µM; this concentration had no significant effects on ECAR (Figure 63a) but a significant ($p \leq 0.01$) increase in OCR was observed in HER2, but not puro, cells (Figure 63b). While this concentration is not having the desired effect, this 2D metabolic assay is not directly comparable to the 3D system due to the length of the drug exposure; in the Seahorse Analyser measurements are recorded within 1 h of inhibitor exposure compared to a 6 day exposure in 3D acini. Despite being unable to be confident of the metabolic effects of perhexiline I decided to examine the effect of 10 µM perhexiline in my system.

5.3.2.2 The effect of perhexiline treatment on 2D cultured cells

Cell viability and intracellular ATP levels were examined over a 24 h and 48 h period in attached and detached cells (Figure 64). Perhexiline had no statistically significant effects on cell viability when examined via alamarBlue® except for in HER2 attached cells following 24 h treatment where perhexiline significantly ($p \leq 0.05$) decreased viability (Figure 64a). Similarly, perhexiline treatment had no statistically significant effects on ATP except for in HER2 attached cells following 24 h treatment where perhexiline significantly ($p \leq 0.05$) decreased ATP (Figure 64b).

5.3.2.3 The effect of perhexiline treatment on 3D acini

In 3D acini 10 µM perhexiline pushed acini towards a less filled phenotype when scored at day 12 of morphogenesis (Figure 65a,b,c) however statistical significance was not reached when analysing data from individual independent experiments (Figure 65b). When combining data from three independent experiments, adjusted for luminal filling and expressed relative to the number of incompletely cleared acini in DMSO condition, a significant ($p \leq 0.05$) 0.17-fold reduction in the number of incompletely cleared puro acini was observed following perhexiline treatment (Figure 65c). HER2 acini showed a 0.11-fold reduction in the number of incompletely cleared acini but statistical significance was not reached.

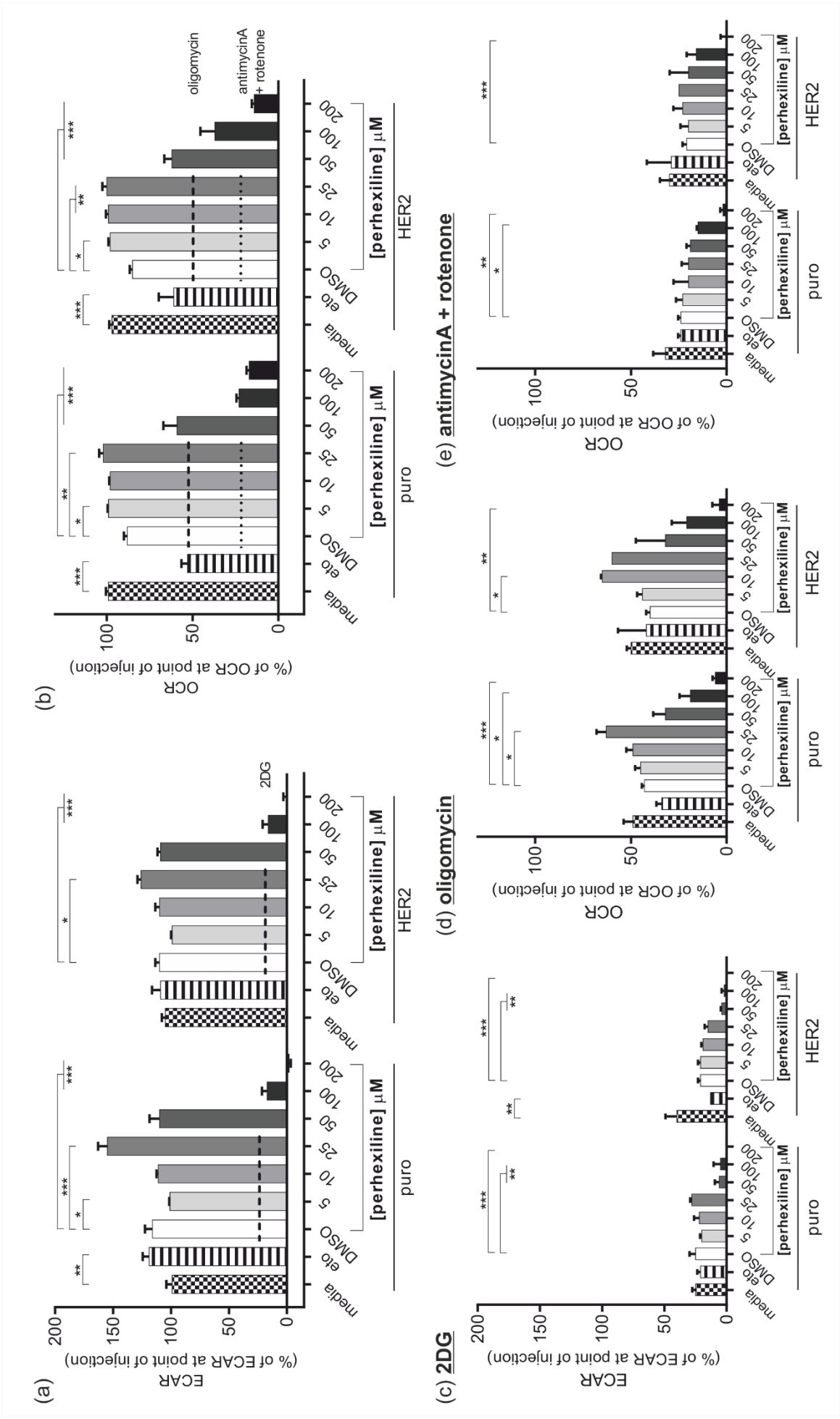
(a)
ECAR
(% of ECAR at point of injection)
200
150
100
50
0
media
etoDMSO
5
10
25
50
100
200
[perhexiline] µM
puro
HER2
2DG
(b)
OCR
(% of OCR at point of injection)
100
50
0
oligomycin
antimycinA + rotenone
(c) 2DG
(d) oligomycin
(e) antimycinA + rotenone

Figure 63 Metabolic responses to perhexiline treatment

Cells (25,000 per well) were seeded into a Seahorse PET plate 18 h prior to experiment. The Seahorse Analyser simultaneously measured extracellular acidification rate (ECAR) and oxygen consumption rate (OCR) following injection of 100 µM etomoxir (eto) or the stated perhexiline concentration. Following inhibitor treatment wells were injected with either 100 mM 2-deoxyglucose (2DG) or 1 µM oligomycin followed by 1 µM antimycinA and 1 µM rotenone. All data was baselined to the values for ECAR and OCR at the point of injection of the drug (0 min). (a) ECAR following inhibitor treatment; dashed lines show the average ECAR for puro or HER2 cells following 2DG (eto data and concentrations of 50 µM perhexiline and above were excluded from this analysis). Bar graphs represent the mean ± SEM from an independent experiment with four technical repeats. (b) OCR following etomoxir or perhexiline treatment. Dashed lines show the average OCR for puro or HER2 cells following oligomycin injection; dotted lines show the average OCR for puro or HER2 cells following antimycinA and rotenone injection (eto data and concentrations of 50 µM perhexiline and above were excluded from this analysis). Bar graphs represent the mean ± SEM from an independent experiment with four technical repeats. (c) ECAR following 2DG; bar graphs represent the mean ± SEM from an independent experiment with two technical repeats. (d,e) OCR following oligomycin (d) followed by antimycinA and rotenone (e). Bar graphs represent the mean ± SEM from an independent experiment with two technical repeats. * $p \leq 0.05$, ** $p \leq 0.01$; *** $p \leq 0.001$ as determined by a two-way ANOVA with Fisher's LSD test.

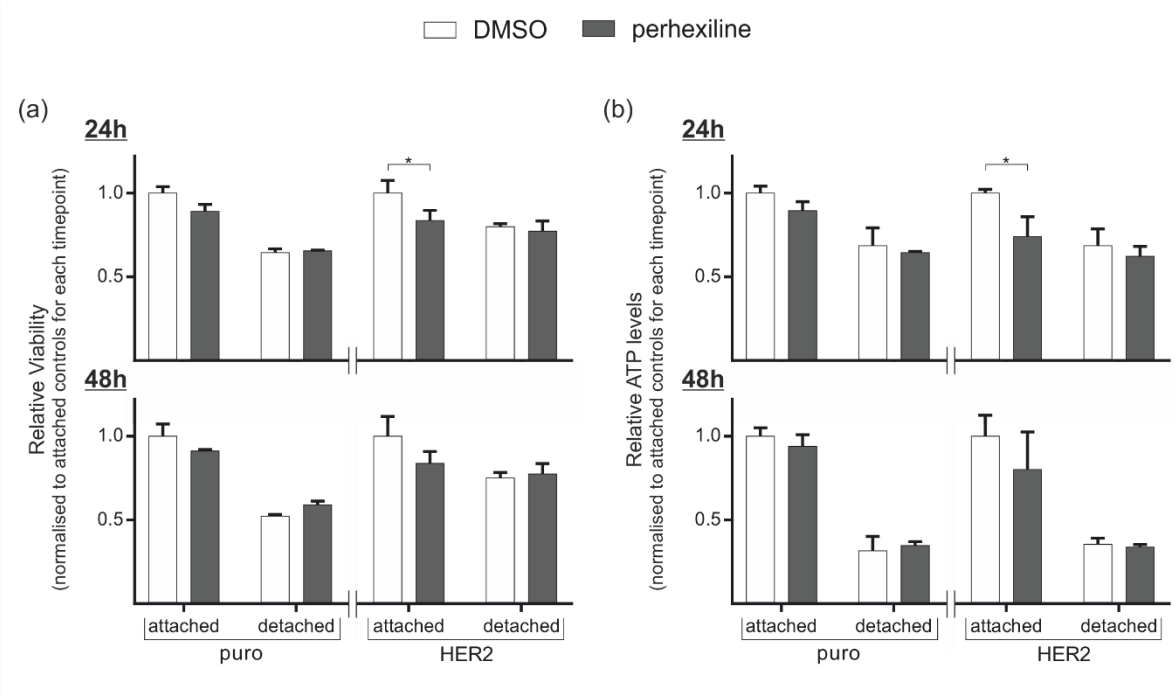

Figure 64 The effect of perhexiline treatment on 2D cell viability

Cells (15,000 per well) were treated with media or perhexiline (10 µM) and seeded onto standard tissue culture plates (attached) or polyHEMA-coated plastic (detached) for 24 h or 48 h. (a) Cell viability was examined using alamarBlue® reagent which was added to conditions 6 h prior to data collection. (b) ATP levels were examined using the ATPlite assay. Fluorometric (a) or luminometric data (b) was normalised for experimental variation and expressed relative to the appropriate media control in attached conditions (puro or HER2). Bar graphs represent the mean ± SEM from three independent experiments each with three technical repeats. * $p \leq 0.05$ as determined by a two-way ANOVA with Fisher's LSD test.

The effects on luminal status observed with 10 µM perhexiline were not comparable to the clear reversal of the HER2-driven luminal filling observed with 100 µM etomoxir (Figure 60). In the Seahorse assay 10 µM perhexiline did not inhibit OCR compared to controls while etomoxir significantly inhibited OCR (Figure 63b). This indicates that 10 µM perhexiline is not inhibiting FAO to the same extent as observed with 100 µM etomoxir. I therefore examined whether increasing the concentration of perhexiline would lead to a more distinct phenotype when monitoring luminal status in 3D. A 25 µM perhexiline treatment was administered however acini were dead by day 12 of morphogenesis and failed to stain for DAPI and phalloidin following fixation (data not shown, from an independent experiment with four technical repeats).

5.4 Targeting glycolysis can alter the acinar morphogenesis program

Having examined the role of FAO in acinar morphogenesis, I then investigated how targeting the Warburg affects acinar morphogenesis. The upregulation of glycolysis in cancer cells is a well-documented phenotype (1.3.2.1 The Warburg effect: matching an increased growth demand) (Vander Heiden, Cantley et al. 2009). In HER2 MCF-10A Schafer *et al.* have shown that enhanced glucose uptake is important for the rescue of ATP following detachment (Schafer, Grassian et al. 2009) while, within the acini setting, data relating to glucose- and fructose- DMEM adapted pools suggests that glycolysis manipulation can alter acinar morphogenesis (5.2.1 Altering the sugar-source available alters MCF-10A acinar morphogenesis when grown in DMEM media). I therefore examined the effect of glycolytic inhibitors in the MCF-10A model.

5.4.1 2-deoxyglucose

2-deoxyglucose is a glucose analogue where the 2-hydroxyl group has been replaced by a hydrogen. Taken into the cell by glucose transporters it is subsequently phosphorylated by the first enzyme in the glycolysis pathway, hexokinase, to form 2-deoxyglucose-6-phosphate. 2-deoxyglucose-6-phosphate cannot undergo further glycolysis and becomes trapped intracellularly. 2-deoxyglucose and 2-deoxyglucose-6-phosphate can bind into the active sites of hexokinase and phosphoglucose isomerase, inhibiting glycolysis at an early stage (Table 11). Used in the Seahorse Analyser at a high concentration to fully inhibit glycolysis (100 mM), at lower concentrations 2-deoxyglucose and 2-deoxyglucose-6-phosphate compete for enzyme binding with glucose and glucose-6-phosphate respectively leading to partial inhibition of glycolysis.

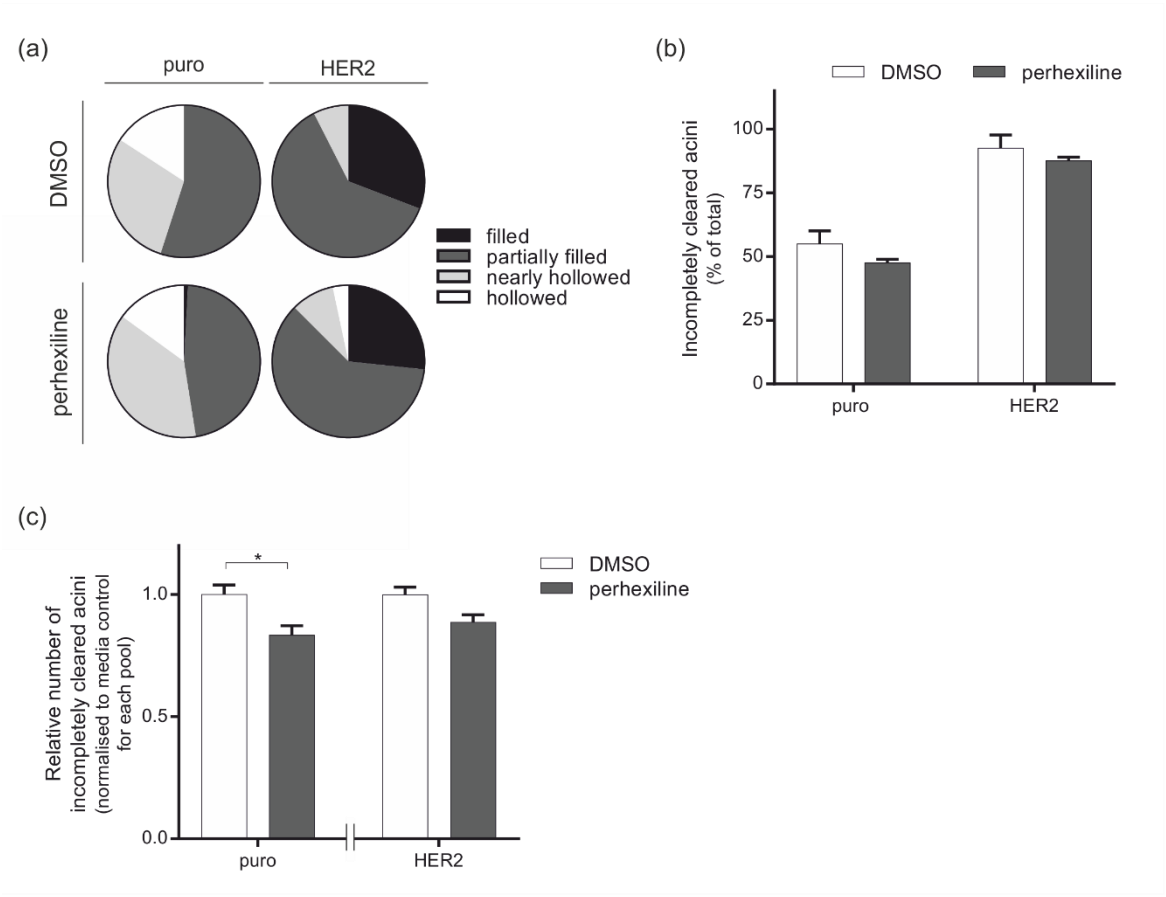

Figure 65 The effect of perhexiline on 3D acini

Acini were treated with DMSO (0.1%) or perhexiline (10 µM) every 2 days from day 6 of morphogenesis. At day 12 acini were fixed and stained with DAPI (red) and phalloidin-TRITC (green). Confocal microscopy was utilised to score luminal status; looking through all focal planes, acini were scored as filled, partially filled, nearly hollowed or completely hollowed. (a) Pie chart representation shows the proportion of acini scoring in each category from a representative experiment. (b) The number of acini scoring as incompletely cleared (filled or partially filled) in (a) was expressed as a percentage of the total acini scored. A minimum of 120 acini were scored for each condition across three replicates. Bar graphs represent the mean ± SEM from three technical repeats. (c) Combined data from three independent experiments shows the relative number of incompletely cleared acini in the presence of perhexiline compared to DMSO controls. Within an independent experiment values were adjusted for the total number of incompletely cleared acini for each pool. Adjusted values were normalised to the mean adjusted values for media across all three experiments. * $p \leq 0.05$ as determined by two-way ANOVA with Fisher's LSD test.

5.4.1.1 Metabolic consequences of 2-deoxyglucose treatment

Examining metabolic activity in 2D using the Seahorse Analyser, 2-deoxyglucose inhibited ECAR in a dose-dependent manner in both puro and HER2 cells (Figure 66a). No statistically significant differences were observed in ECAR following 100 mM 2-deoxyglucose injection (full glycolytic inhibition) although a trend towards decreasing ECAR was observed (Figure 66c). A dose-dependent inhibition of OCR was also observed (Figure 66b), while no statistically significant effects on OCR were seen following oligomycin (Figure 66d) or antimycinA and rotenone injections (Figure 66e).

I selected 10 mM 2-deoxyglucose for future experiments, a concentration that has been shown to inhibit cellular ATP in detached HER2 MCF-10A to levels observed in parental cells (Schafer, Grassian et al. 2009). This concentration resulted in a 0.52- and a 0.36-fold reduction in ECAR (Figure 66a) and a 0.18- and 0.07-fold reduction in OCR (Figure 66b) in puro and HER2 cells respectively.

5.4.1.2 The effect of 2-deoxyglucose treatment on 2D cultured cells

When examined over a 24 h and 48 h period 2-deoxyglucose significantly ($p \leq 0.01$) inhibited cell viability and ATP levels in both puro and HER2 cells grown in attachment and detachment (Figure 67). At 48 h following treatment puro cells show a 0.54- and a 0.42- fold reduction in cell viability in attached and detached conditions respectively when examined via an alamarBlue® assay which compared to a 0.25- and 0.33- fold reduction in viability in HER2 cells (Figure 67a). Examining ATP levels, 2-deoxyglucose treatment of attached and detached puro cells results in a 0.85- and 0.60-fold reduction in ATP respectively compared to a 0.49- and 0.43- fold reduction in HER2 (Figure 67b).

5.4.1.3 The effect of 2-deoxyglucose treatment on 3D acini

In acini 2-deoxyglucose treatment pushed puro towards a highly filled phenotype with a high percentage of acini presenting as incompletely cleared (Figure 68a,b,c); a significant ($p \leq 0.001$) 2.0-fold increase in the number of incompletely cleared acini was observed (Figure 68d). 2-deoxyglucose treatment on HER2 acini had no statistically significant effects on the luminal scoring of acini (Figure 68a,b,d) however acini appeared smaller (Figure 68c).

An alamarBlue® assay was carried out to assess acini viability following 2-deoxyglucose treatment (Figure 69). Viability was significantly ($p \leq 0.05$) reduced in both puro and HER2 acini following 2-deoxyglucose treatment with a 0.51- and a 0.69-fold reduction in viability in puro and HER2 respectively (Figure 69a). Consistent with previous observations (Figure 68c) HER2 acini appeared

smaller in the presence of 2-deoxyglucose (Figure 69b). Puro acini also appeared smaller, although the effect is less prominent. Taking the reduction in size, together with the alamarBlue® data, I suggest that 2-deoxyglucose is leading to cell cycle arrest before the onset of luminal clearing and either preventing or delaying the onset of clearing. I was interesting in addressing how glycolysis inhibition influenced luminal cell survival and I therefore tested inhibition of an additional glycolytic enzyme, lactate dehydrogenase.

5.4.2 Oxamate

Lactate dehydrogenase is a late stage step of glycolysis (Figure 4b) and can be targeted by oxamate (Table 11), a structural analogue of pyruvate and a well characterised inhibitor (Papaconstantinou and Colowick 1961, Papaconstantinou and Colowick 1961, Goldberg and Colowick 1965, Goldberg, Nitowsky et al. 1965).

5.4.2.1 Metabolic consequences of oxamate treatment

The metabolic consequences of oxamate treatment were examined in 2D using the Seahorse Analyser (Figure 70). Oxamate inhibited glycolysis in a dose-dependent manner; oxamate significantly ($p \leq 0.01$) inhibited ECAR in puro cells at all concentrations examined and at concentrations of 12.5 mM and above in HER2 cells (Figure 70a) while not statistically significantly altering ECAR following 100 mM 2-deoxyglucose injection (Figure 70c). Oxamate also inhibits OCR in a dose dependent manner (Figure 70b) while not affecting OCR following oligomycin (Figure 70d) or antimycinA and rotenone (Figure 70e) injections (except at 6.25 mM oxamate in HER2 cells where a significant ($p \leq 0.05$) decrease in OCR following oligomycin was observed). The extent of glycolytic inhibition was higher than the extent of mitochondrial inhibition; at the highest oxamate concentration (50 mM) oxamate resulted in a 0.56- and 0.54- fold reduction in glycolysis and a 0.25- and 0.27- fold reduction in mitochondrial ATP production in puro and HER2 cells respectively.

10 mM oxamate was taken forward for further experiments; this concentration resulted in a 0.46- and 0.48- fold reduction in glycolysis and a 0.16- and 0.20- fold reduction in mitochondrial ATP production in puro and HER2 cells respectively. This is the concentration where the extent of glycolysis inhibition began to plateau off.

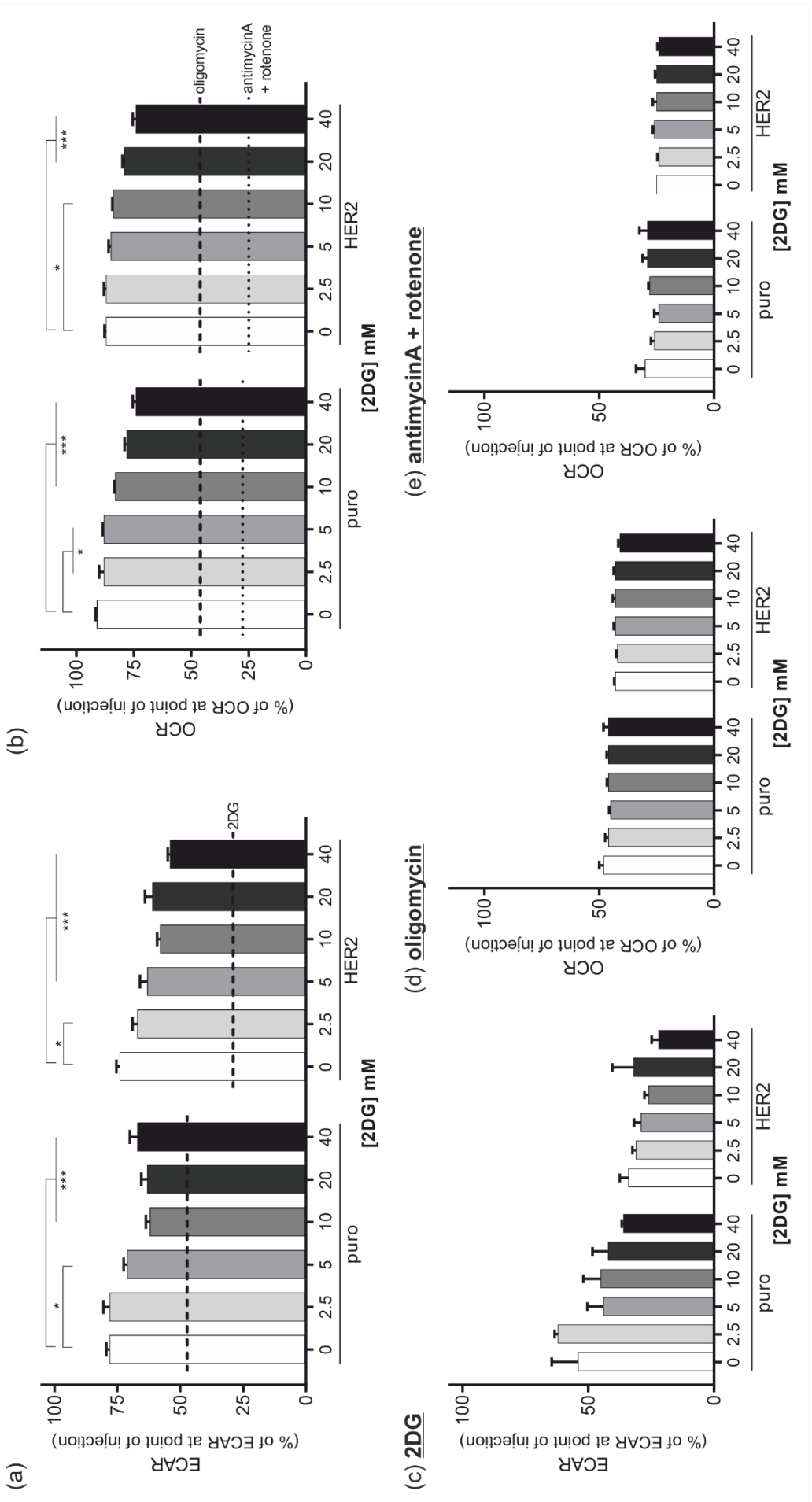
(a)
ECAR
(% of ECAR at point of injection)
100
75
50
25
0
*
***
*
***
2DG
0 2.5 5 10 20 40 0 2.5 5 10 20 40
puro
HER2
[2DG] mM
(b)
OCR
(% of OCR at point of injection)
100
75
50
25
0
*
***
*
***
oligomycin
antimycinA
+ rotenone
0 2.5 5 10 20 40 0 2.5 5 10 20 40
puro
HER2
[2DG] mM
(c) 2DG
ECAR
(% of ECAR at point of injection)
100
50
0
0 2.5 5 10 20 40 0 2.5 5 10 20 40
puro
HER2
[2DG] mM
(d) oligomycin
OCR
(% of OCR at point of injection)
100
50
0
0 2.5 5 10 20 40 0 2.5 5 10 20 40
puro
HER2
[2DG] mM
(e) antimycinA + rotenone
OCR
(% of OCR at point of injection)
100
50
0
0 2.5 5 10 20 40 0 2.5 5 10 20 40
puro
HER2
[2DG] mM

Figure 66 Metabolic responses to 2-deoxyglucose treatment

Cells (25,000 per well) were seeded into a Seahorse PET plate 18 h prior to experiment. The Seahorse Analyser simultaneously measured extracellular acidification rate (ECAR) and oxygen consumption rate (OCR) following injection of the stated 2-deoxyglucose (2DG) concentration. Following inhibitor treatment wells were injected with either 10 mM 2DG or 1 µM oligomycin followed by 1 µM antimycinA and 1 µM rotenone. All data was baselined to the values for ECAR and OCR at the point of injection of the drug (0 min). (a) ECAR following inhibitor treatment; dashed lines show the average ECAR for puro or HER2 cells following 2DG. Bar graphs represent the mean ± SEM from an independent experiment with four technical repeats. (b) OCR following 2-deoxyglucose treatment. Dashed lines show the average OCR for puro or HER2 cells following oligomycin injection; dotted lines show the average OCR for puro or HER2 cells following antimycinA and rotenone injection. Bar graphs represent the mean ± SEM from an independent experiment with four technical repeats. (c) ECAR following 10 mM 2DG; bar graphs represent the mean ± SEM from an independent experiment with two technical repeats. (d,e) OCR following oligomycin (d) followed by antimycinA and rotenone (e). Bar graphs represent the mean ± SEM from an independent experiment with two technical repeats. * $p \leq 0.05$, *** $p \leq 0.001$ as determined by a two-way ANOVA with Fisher's LSD test.

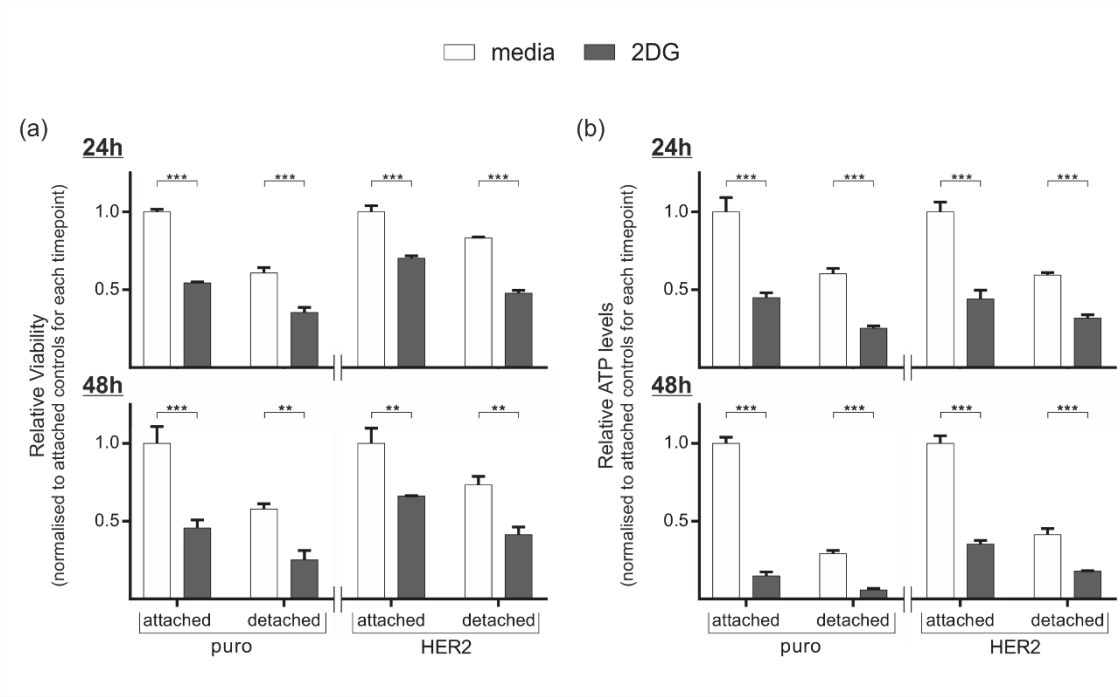

Figure 67 The effect of 2-deoxyglucose treatment on 2D cell viability

Cells (15,000 per well) were treated with media or 2-deoxyglucose (2DG) (10 mM) and seeded onto standard tissue culture plates (attached) or polyHEMA-coated plastic (detached) for 24 h or 48 h. (a) Cell viability was examined using alamarBlue® reagent which was added to conditions 6 h prior to data collection. (b) ATP levels were examined using the ATPlite assay. Fluorometric (a) or luminometric data (b) was normalised for experimental variation and expressed relative to the appropriate media control in attached conditions (puro or HER2). Bar graphs represent the mean ± SEM from three independent experiments each with three technical repeats. ** $p \leq 0.01$, *** $p \leq 0.001$ as determined by a two-way ANOVA with Fisher's LSD test.

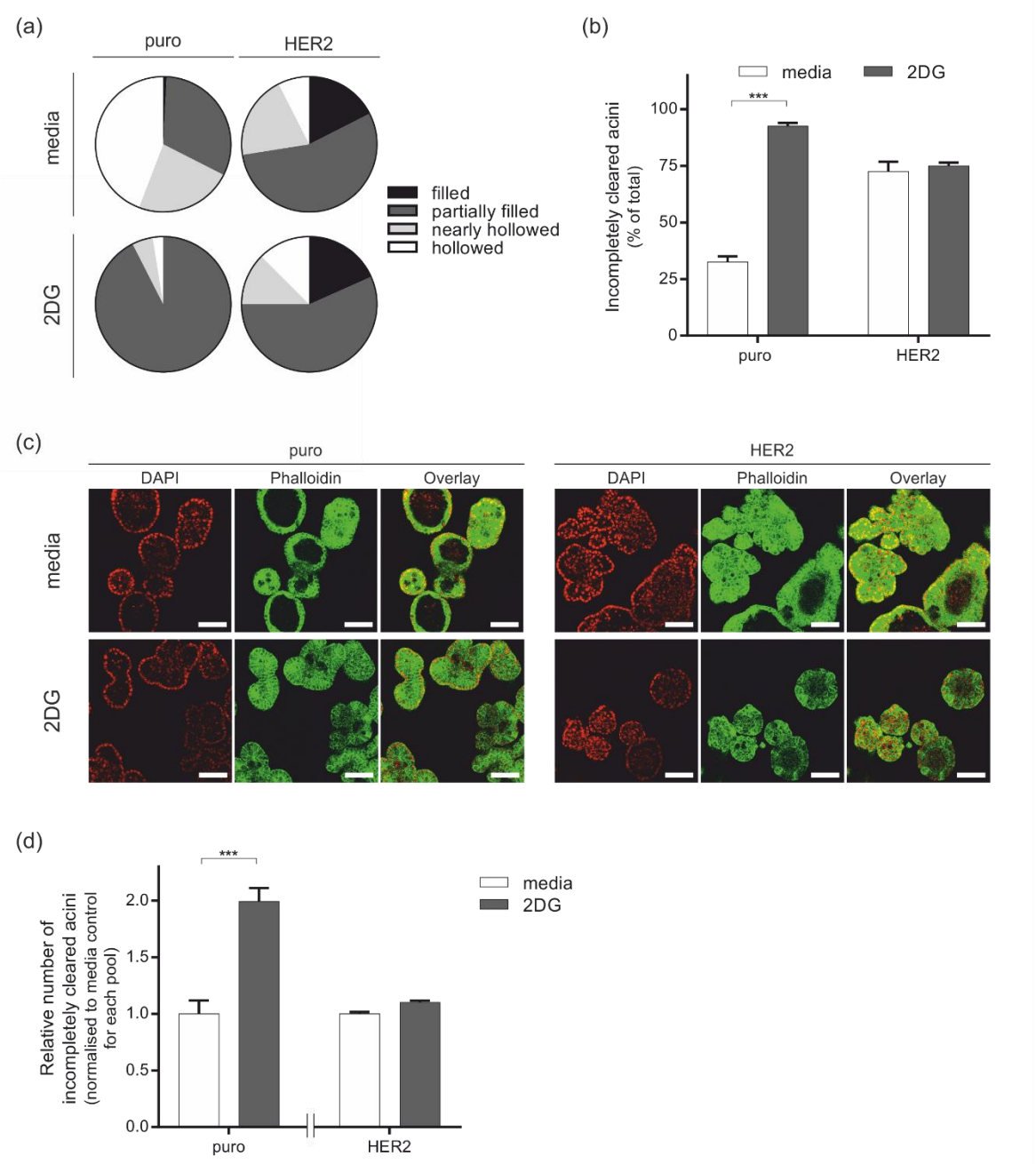

Figure 68 The effect of 2-deoxyglucose on 3D acini

Acini were treated with media or 2-deoxyglucose (2DG) (10 mM) every 2 days from day 6 of morphogenesis. At day 12 acini were fixed and stained with DAPI (red) and phalloidin-TRITC (green). Confocal microscopy was utilised to score luminal status; looking through all focal planes, acini were scored as filled, partially filled, nearly hollowed or completely hollowed. (a) Pie chart representation shows the proportion of acini scoring in each category from a representative experiment. (b) The number of acini scoring as incompletely cleared (filled or partially filled) in (a) was expressed as a percentage of the total acini scored. A minimum of 120 acini were scored for each condition across three replicates. Bar graphs represent the mean ± SEM from three technical repeats. (c) Representative confocal immunofluorescence images show the centre of acini following 2DG treatment; scale bars show 100µm. (d) Combined data from three independent experiments shows the relative number of incompletely cleared acini in the presence of 2DG compared to media controls. Within an independent experiment values were adjusted for the total number of incompletely cleared acini for each pool. Adjusted values were normalised to the mean adjusted values for media across all three experiments. *** $p \leq 0.001$ as determined by two-way ANOVA with Fisher's LSD test.

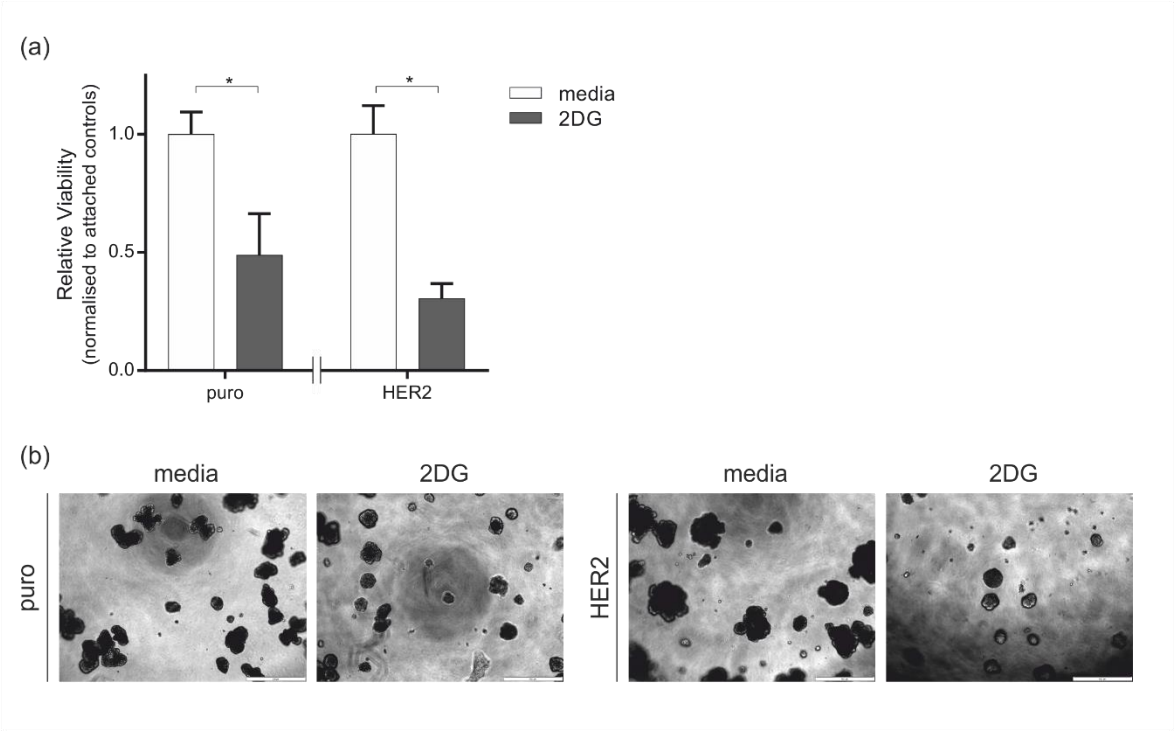

Figure 69 The effect of 2-deoxyglucose on 3D acini viability

Cells (200 per well) were seeded in 96-well plates which had been pre-coated with Matrigel and cultured in 3D for 12 days. Acini were treated with media or 2-deoxyglucose (2DG) (10 mM) every 2 days from day 6 of morphogenesis. (a) Cell viability was examined using alamarBlue® reagent which was added to conditions 6 h prior to data collection. Fluorometric data was adjusted for background, normalised for experimental variation and expressed relative to the appropriate media control (puro or HER2). Bar graphs represent the mean ± SEM from three independent experiments each with four technical repeats. (b) Representative phase contrast images of acini growing in 96-well plate show the reduced acini size following 2DG treatment; scale bars show 500 µm. * $p \leq 0.05$ as determined by a two-way ANOVA with Fisher's LSD test.

5.4.2.2 The effect of oxamate treatment on 2D cultured cells

Oxamate treatment had no effect on cell viability in attached or detached puro or HER2 cells when examined by an alamarBlue® assay at 24 h and 48 h except in HER2 attached cells at 24 h where oxamate treatment led to a significant ($p \leq 0.05$) decrease in viability (Figure 71a). In contrast, oxamate treatment significantly ($p \leq 0.05$) reduced ATP levels across all conditions examined (Figure 71b). Following 48 h treatment puro cells displayed a 0.53-fold reduction in ATP in both attached and detached conditions; this compared to a 0.52- fold reduction in ATP in attached HER2 cells and a 0.42-fold reduction in detached HER2 cells.

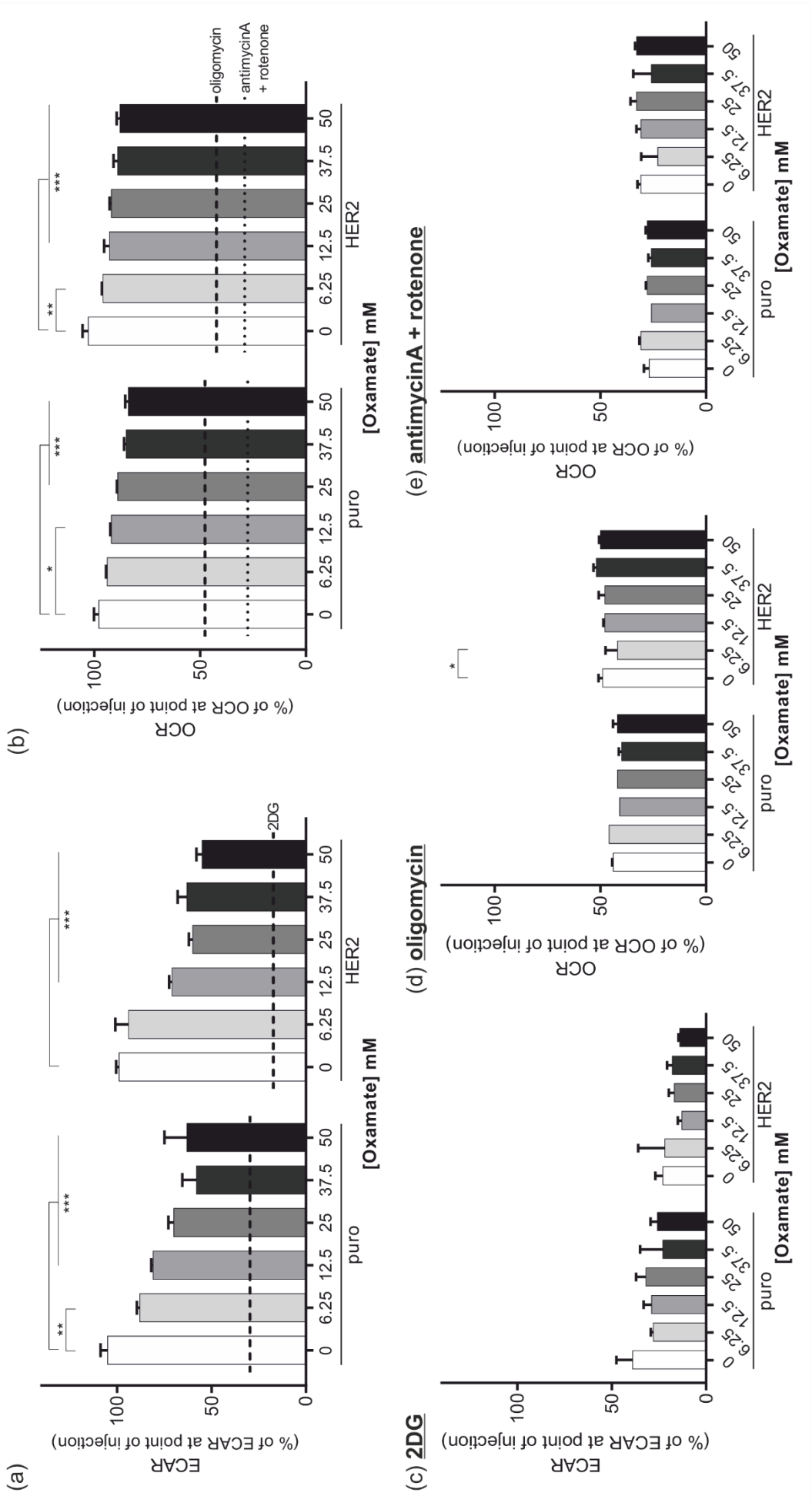
(a)
ECAR
(% of ECAR at point of injection)
100
50
0
**
***
***
2DG
0 6.25 12.5 25 37.5 50
puro
[Oxamate] mM
HER2
(b)
OCR
(% of OCR at point of injection)
oligomycin
antimycinA + rotenone
*
***
**
***
(c) 2DG
(d) oligomycin
(e) antimycinA + rotenone

Figure 70 Metabolic responses to oxamate treatment

Cells (25,000 per well) were seeded into a Seahorse PET plate 18 h prior to experiment. The Seahorse Analyser simultaneously measured extracellular acidification rate (ECAR) and oxygen consumption rate (OCR) following injection of the stated oxamate concentration. Following oxamate treatment, wells were injected with either 100 mM 2-deoxyglucose (2DG) or 1 µM oligomycin followed by 1 µM antimycinA and 1 µM rotenone. All data was baselined to the values for ECAR and OCR at the point of injection of the drug (0 min). (a) ECAR following oxamate treatment; dashed lines show the average ECAR for puro or HER2 cells following 2DG. Bar graphs represent the mean ± SEM from an independent experiment with four technical repeats. (b) OCR following oxamate treatment. Dashed lines show the average OCR for puro or HER2 cells following oligomycin injection; dotted lines show the average OCR for puro or HER2 cells following antimycinA and rotenone injection. Bar graphs represent the mean ± SEM from an independent experiment with four technical repeats. (c) ECAR following 2DG; bar graphs represent the mean ± SEM from an independent experiment with two technical repeats. (d,e) OCR following oligomycin (d) followed by antimycinA and rotenone (e). Bar graphs represent the mean ± SEM from an independent experiment with two technical repeats. * $p \leq 0.05$, ** $p \leq 0.01$; *** $p \leq 0.001$ as determined by a two-way ANOVA with Fisher's LSD test.

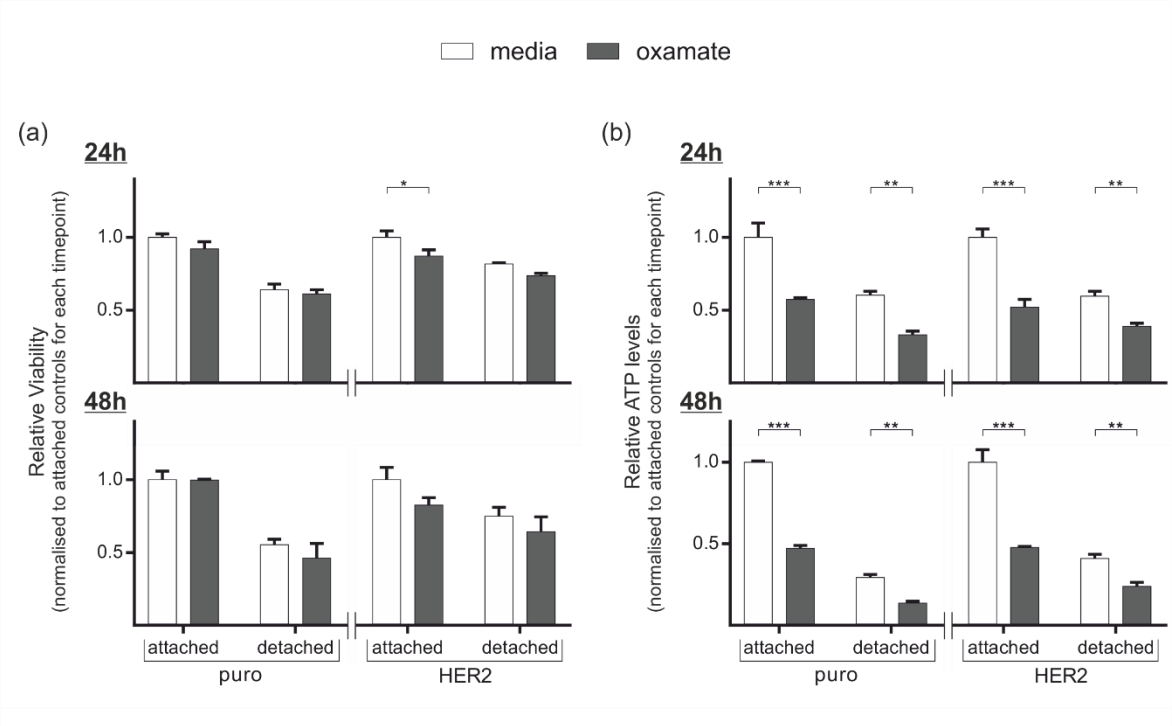

Figure 71 The effect of oxamate treatment on 2D cell viability

Cells (15,000 per well) were treated with media or oxamate (25 mM) and seeded onto standard tissue culture plates (attached) or polyHEMA-coated plastic (detached) for 24 h or 48 h. (a) Cell viability was examined using alamarBlue® reagent which was added to conditions 6 h prior to data collection. (b) ATP levels were examined using the ATPlite assay. Fluorometric (a) or luminometric data (b) was normalised for experimental variation and expressed relative to the appropriate media control in attached conditions (puro or HER2). Bar graphs represent the mean ± SEM from three independent experiments, each with three technical repeats. * $p \leq 0.05$, ** $p \leq 0.01$, *** $p \leq 0.001$ as determined by a two-way ANOVA with Fisher's LSD test.

5.4.2.3 The effect of oxamate treatment on 3D acini

Oxamate treatment results in acini scoring with a more hollowed phenotype (Figure 72a,b,c). Within an independent experiment a reduced number of puro acini scored as incompletely cleared following oxamate treatment, while treatment of HER2 resulted in a statistically significant ($p \leq 0.01$) reduction in incompletely cleared acini (Figure 72b). Combined data normalised for experimental differences in filling showed a statistically significant ($p \leq 0.01$) 0.28- and 0.21- fold reduction in incompletely cleared puro and HER2 acini respectively (Figure 72d).

When examining acini viability using an alamarBlue® assay no statistically significant differences were seen in oxamate-treated acini compared to media controls (Figure 73). HER2 acini showed a 0.08-fold reduction in viability following oxamate treatment but this did not reach statistical significance.

5.4.3 FX11

Oxamate is not a selective lactate dehydrogenase inhibitor (Thornburg, Nelson et al. 2008) and I have shown that oxamate also inhibits mitochondrial activity in MCF-10A (Figure 70b). The drug FX11 is a small molecule, selective active site inhibitor of lactate dehydrogenase A (Table 11) (Deck, Royer et al. 1998, Yu, Deck et al. 2001, Le, Cooper et al. 2010) and was tested as a more selective inhibitor than oxamate for examining glycolytic inhibition of MCF-10A.

5.4.3.1 Metabolic consequences of FX11 treatment

The metabolic consequences of FX11 treatment were examined using the Seahorse Analyser (Figure 74). FX11 has been shown to have a Ki of 8 μM when characterised using purified human liver lactate dehydrogenase A and 9 μM FX11 has statistically significant effects cellular metabolism when examined in P493 cells (Le, Cooper et al. 2010). I therefore selected concentrations either side of 9 μM for analysis.

Examining glycolysis, FX11 had variable effects on ECAR (Figure 74a); in puro cells, 9 μM FX11 statistically significantly ($p \leq 0.001$) increased ECAR compared to controls while higher concentrations statistically significantly ($p \leq 0.05$) decreased ECAR. Similarly lower concentrations of FX11 (2.25 μM, 9 μM) statistically significantly ($p \leq 0.01$) increased ECAR in HER2 cells while statistically significantly ($p \leq 0.001$) inhibiting ECAR at 36 μM. No statistically significant differences in ECAR were seen following 2-deoxyglucose injection (Figure 74c).

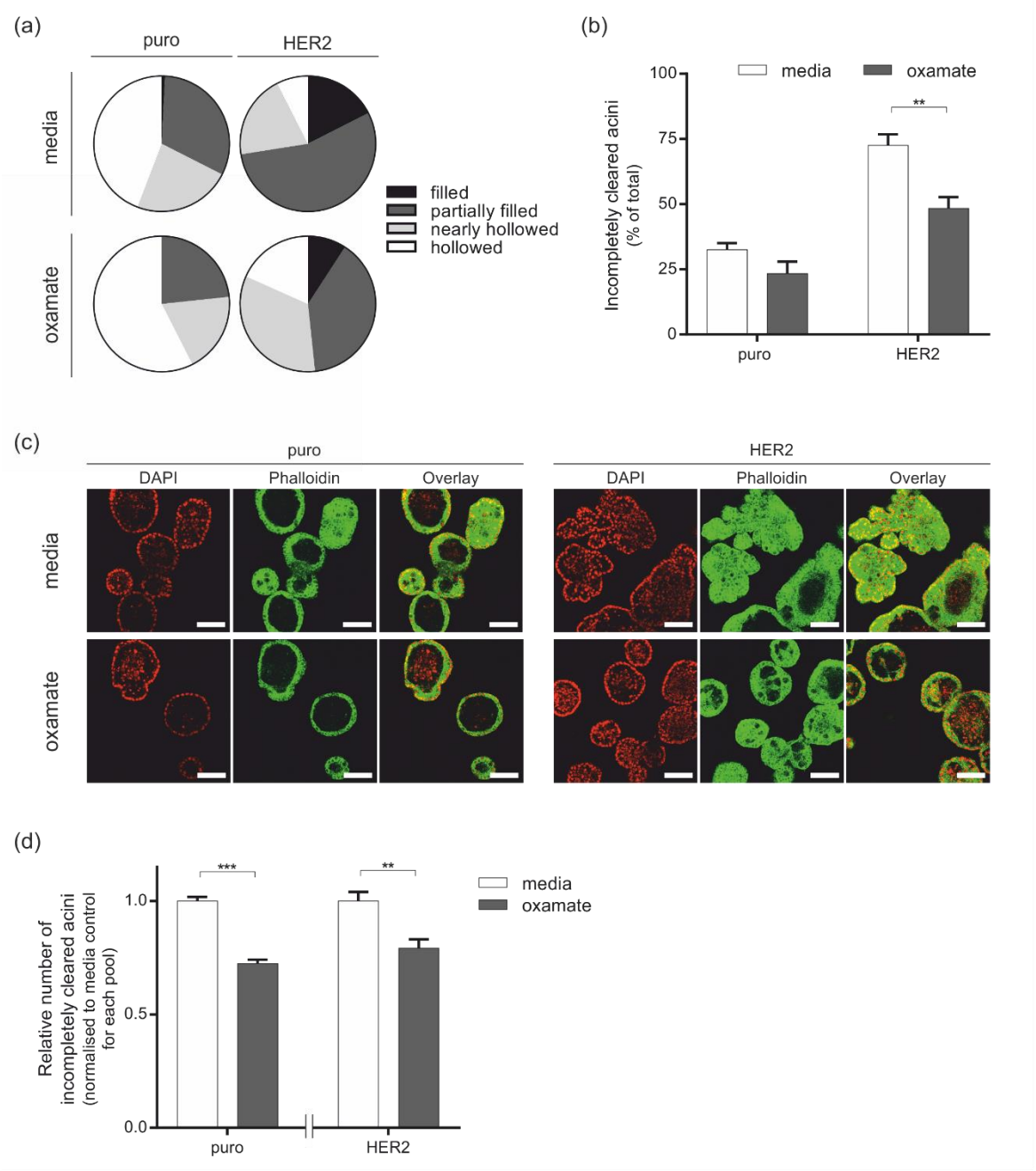

Figure 72 The effect of oxamate on 3D acini

Acini were treated with media or oxamate (25 mM) every 2 days from day 6 of morphogenesis. At day 12 acini were fixed and stained with DAPI (red) and phalloidin-TRITC (green). Confocal microscopy was utilised to score luminal status; looking through all focal planes, acini were scored as filled, partially filled, nearly hollowed or completely hollowed. (a) Pie chart representation shows the proportion of acini scoring in each category from a representative experiment. (b) The number of acini scoring as incompletely cleared (filled or partially filled) in (a) was expressed as a percentage of the total acini scored. A minimum of 120 acini were scored for each condition across three replicates. Bar graphs represent the mean ± SEM from three technical repeats. (c) Representative confocal immunofluorescence images show the centre of acini following oxamate treatment; scale bars show 100µm. (d) Combined data from three independent experiments shows the relative number of incompletely cleared acini in the presence of oxamate compared to media controls. Within an independent experiment values were adjusted for the total number of incompletely cleared acini for each pool. Adjusted values were normalised to the mean adjusted values for media across all three experiments. ** $p \leq 0.01$, *** $p \leq 0.001$ as determined by two-way ANOVA with Fisher's LSD test.

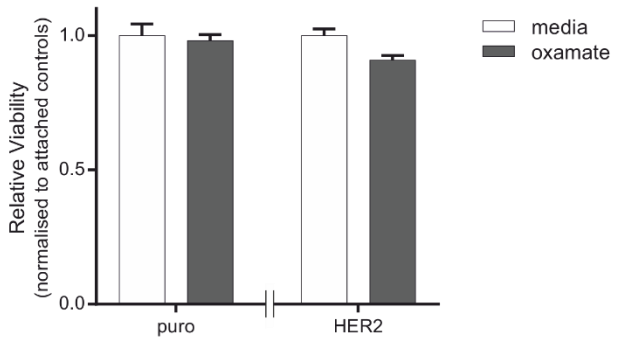

Figure 73 The effect of oxamate on 3D acini viability

Cells (200 per well) were seeded in 96-well plates which had been pre-coated with Matrigel and cultured in 3D for 12 days. Acini were treated with media or oxamate (25 mM) every 2 days from day 6 of morphogenesis. Cell viability was examined using alamarBlue® reagent which was added to conditions 6 h prior to data collection. Fluorometric data was adjusted for background, normalised for experimental variation and expressed relative to the appropriate media control (puro or HER2). Bar graphs represent the mean ± SEM from three independent experiments each with four technical repeats.

Variable effects on OCR were also observed following FX11 treatment with lower concentrations of FX11 statistically significantly ($p \leq 0.05$) increasing OCR (9 µM FX11 in puro cells, 2.25 µM, 4.5 µM and 9 µM FX11 in HER2 cells) and higher concentrations statistically significantly decreasing OCR (Figure 74). At low concentrations of FX11 (≤ 9 µM) the OCR following oligomycin injection was statistically significantly ($p \leq 0.01$) increased, but no statistically significant differences were seen at the highest concentrations (Figure 74d). 9 µM FX11 also statistically significantly increases OCR following antimycinA and rotenone treatment (Figure 74e).

From this data it is difficult to come to a conclusion on the metabolic action of FX11 and it suggests that FX11 is having an off target effects on cellular metabolism. Regardless I opted to pursue the treatment of cells with 9 µM FX11 – the concentration used in the literature (Le, Cooper et al. 2010).

5.4.3.2 The effect of FX11 treatment on 2D cultured cells

When examined in an alamarBlue® assay FX11 treatment had no statistically significant effects on cell viability in puro or HER2 cells cultured in attached or detached conditions, over a 24 h or 48 h period (Figure 75a). Similarly, FX11 had no statistically significant effects on ATP levels when examined in the same setting except in HER2 cells following 48 h of treatment (Figure 75b).

5.4.3.3 The effect of FX11 treatment on 3D acini

Within a single experiment FX11 treatment of acini resulted in a less filled phenotype (Figure 76a,b) with a significantly ($p \leq 0.05$) reduced number of acini presenting as incompletely cleared (Figure 76b). Combining data from three independent experiments, FX11 treatment resulted in a significant ($p \leq 0.001$) 0.25- fold reduction in the number of incompletely cleared puro acini compared to a significant ($p \leq 0.001$) 0.19-fold reduction observed in HER2 acini (Figure 76c).

5.4.4 Iodoacetic acid

As a final investigation into the role of glycolysis in acinar morphogenesis I examined the effect of a fourth glycolytic inhibitor, iodoacetic acid, on MCF-10A. Iodoacetic acid is an alkylating agent used in the literature for glycolysis inhibition due to its irreversible inhibition of glyceraldehyde-3-phosphate dehydrogenase (GAPDH) (Table 11) (Sabri and Ochs 1971, Loreck, Galarraga et al. 1987, Bickler and Kelleher 1992, Gemba, Oshima et al. 1994, Solem, Koebmann et al. 2003, Schmidt and Dringen 2009). GAPDH catalyses the sixth step of glycolysis (Figure 4a) and iodoacetic acid prevents glycolysis downstream of glyceraldehyde-3-phosphate.

5.4.4.1 Metabolic consequences of iodoacetic acid

The metabolic consequences of iodoacetic acid were examined using the Seahorse analyser (Figure 77). Concentrating on glycolysis, lower concentrations of iodoacetic acid had no statistically significant effects on ECAR while higher concentrations of iodoacetic acid statistically significantly ($p \leq 0.001$) inhibit ECAR (concentrations of 100 µM and above in puro cells and concentrations of 50 µM and above in HER2 cells) (Figure 77a). In puro cells these high concentrations of iodoacetic acid also statistically significantly ($p \leq 0.05$) inhibit ECAR following 2-deoxyglucose injection (Figure 77c).

Looking at mitochondrial activity, iodoacetic acid had no statistically significant effects on OCR except in HER2 cells at 100 µM where iodoacetic acid had a small but statistically significant ($p \leq 0.01$) increase in OCR (Figure 77b). Iodoacetic acid had no statistically significant effects on OCR following oligomycin (Figure 77d) or antimycinA and rotenone injections (Figure 77e) except in HER2 cells following oligomycin injection where 25 µM iodoacetic acid statistically significantly ($p \leq 0.05$) decreases OCR.

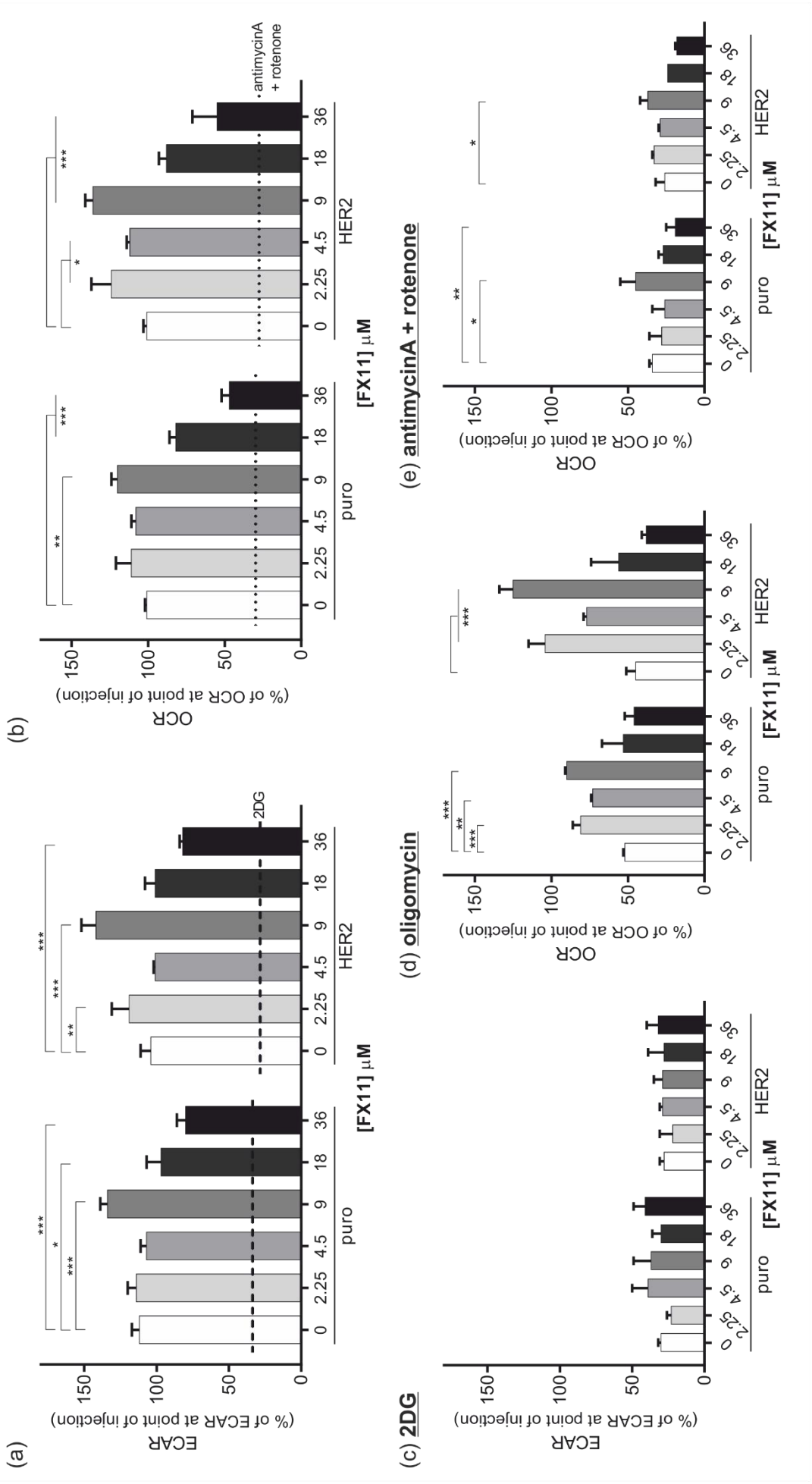
(a)
ECAR
(% of ECAR at point of injection)
0
50
100
150
2DG
puro
HER2
[FX11] μM
0
2.25
4.5
9
18
36
(b)
OCR
(% of OCR at point of injection)
antimycinA
+ rotenone
(c) 2DG
(d) oligomycin
(e) antimycinA + rotenone

Figure 74 Metabolic responses to FX11 treatment

Cells (25,000 per well) were seeded into a Seahorse PET plate 18 h prior to experiment. The Seahorse Analyser simultaneously measured extracellular acidification rate (ECAR) and oxygen consumption rate (OCR) following injection of the stated FX11 concentration. Following FX11 treatment, wells were injected with either 100 mM 2-deoxyglucose (2DG) or 1 µM oligomycin followed by 1 µM antimycinA and 1 µM rotenone. All data was baselined to the values for ECAR and OCR at the point of injection of the drug (0 min). (a) ECAR following FX11 treatment; dashed lines show the average ECAR for puro or HER2 cells following 2DG. Bar graphs represent the mean ± SEM from an independent experiment with four technical repeats. (b) OCR following FX11 treatment. Dashed lines show the average OCR for puro or HER2 cells following oligomycin injection; dotted lines show the average OCR for puro or HER2 cells following antimycinA and rotenone injection. Bar graphs represent the mean ± SEM from an independent experiment with four technical repeats. (c) ECAR following 2DG; bar graphs represent the mean ± SEM from an independent experiment with two technical repeats. (d,e) OCR following oligomycin (d) followed by antimycinA and rotenone (e). Bar graphs represent the mean ± SEM from an independent experiment with two technical repeats. * $p \leq 0.05$, ** $p \leq 0.01$; *** $p \leq 0.001$ as determined by a two-way ANOVA with Fisher's LSD test.

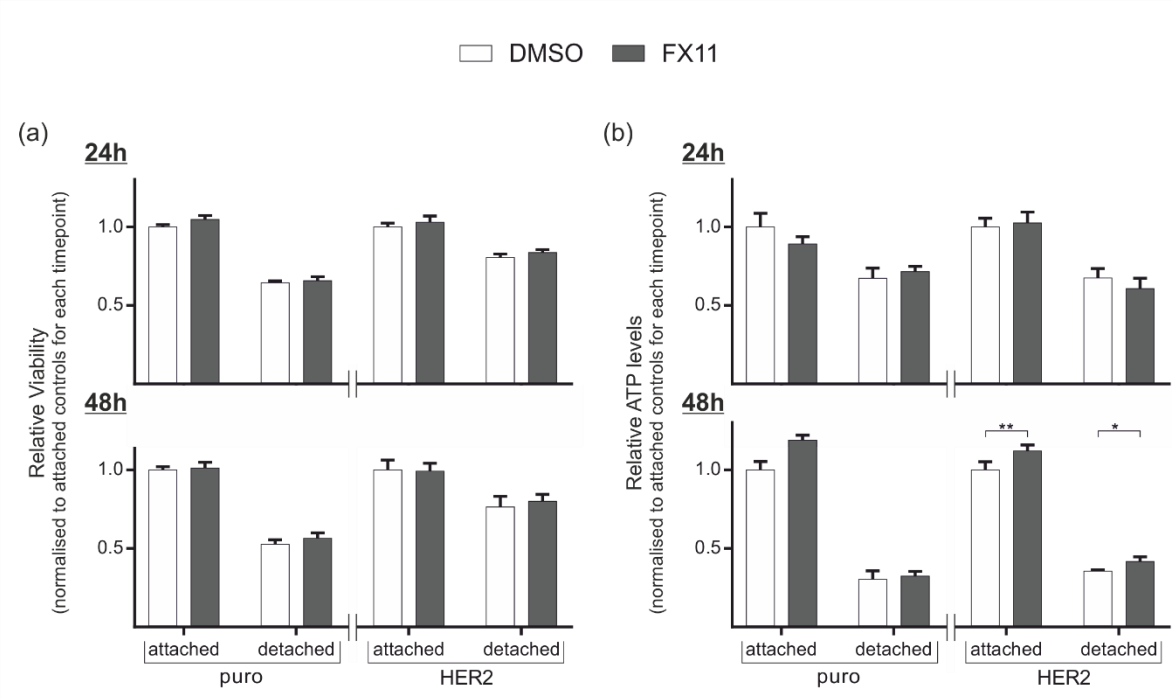

Figure 75 The effect of FX11 treatment on 2D cell viability

Cells (15,000 per well) were treated with media or FX11 (9 µM) and seeded onto standard tissue culture plates (attached) or polyHEMA-coated plastic (detached) for 24 h or 48 h. (a) Cell viability was examined using alamarBlue® reagent which was added to conditions 6 h prior to data collection. (b) ATP levels were examined using the ATPlite assay. Fluorometric (a) or luminometric data (b) was normalised for experimental variation and expressed relative to the appropriate media control in attached conditions (puro or HER2). Bar graphs represent the mean ± SEM from three independent experiments each with three technical repeats. * $p \leq 0.05$, ** $p \leq 0.01$ as determined by a two-way ANOVA with Fisher's LSD test.

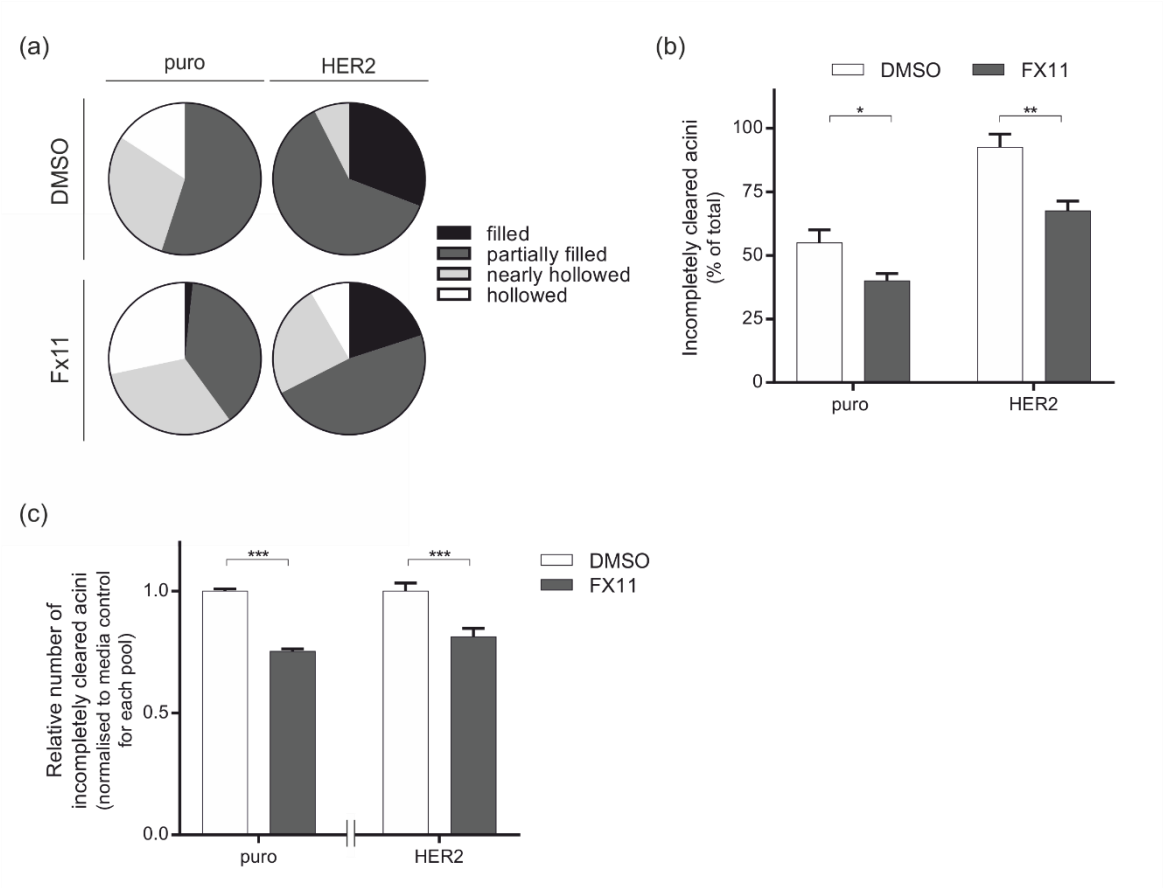

Figure 76 The effect on FX11 on 3D acini

Acini were treated with DMSO or FX11 (9 µM) every 2 days from day 6 of morphogenesis. At day 12 acini were fixed and stained with DAPI and phalloidin-TRITC. Confocal microscopy was utilised to score luminal status; looking through all focal planes, acini were scored as filled, partially filled, nearly hollowed or completely hollowed. (a) Pie chart representation shows the proportion of acini scoring in each category from a representative experiment. (b) The number of acini scoring as incompletely cleared (filled or partially filled) in (a) was expressed as a percentage of the total acini scored. A minimum of 120 acini were scored for each condition across three replicates. Bar graphs represent the mean ± SEM from three technical repeats. (c) Combined data from three independent experiments shows the relative number of incompletely cleared acini in the presence of FX11 compared to DMSO controls. Within an independent experiment, values were adjusted for the total number of incompletely cleared acini for each pool. Adjusted values were normalised to the mean adjusted values for media across all three experiments. * $p \leq 0.05$, ** $p \leq 0.01$, *** $p \leq 0.001$ as determined by two-way ANOVA with Fisher's LSD test.

Higher concentrations of iodoacetic acid interfered with non-glycolytic acidification making them undesirable for use in assays. Because of the differences in exposure time in 2D versus 3D culture I decided to carry out an acini experiment examining the effect of 12.5 µM, 25 µM and 50 µM of iodoacetic acid on acini development, despite not seeing inhibition of glycolysis at these concentrations.

5.4.4.2 The effect of iodoacetic acid treatment on 3D acini

At 12.5 µM and 25 µM iodoacetic acid treatment led to an increase in the percentage of incompletely cleared acini (Figure 78b). Scores could not be taken for 50 µM iodoacetic acid as acini were dead (Figure 78a) and failed to stain.

5.5 Inhibition of complex I of the electron transport chain

Having examined the consequences of FAO and glycolysis inhibition I sought to examine how manipulation of mitochondrial respiration would influence acinar morphogenesis.

5.5.1 Metformin

Metformin is a biguanide and an inhibitor of complex I of the electron transport chain with anti-tumourigenic properties (Table 11) (Wheaton, Weinberg et al. 2014). I examined whether this drug had anti-tumourigenic effects within the MCF-10A model.

5.5.1.1 Metabolic consequences of metformin treatment

The glycolytic and mitochondrial responses to metformin were examined in a Seahorse assay (Figure 79). Examining glycolysis, metformin had no statistically significant effects on ECAR at the concentrations tested (Figure 79a) with no statistically significant differences in ECAR following 2-deoxyglucose injection (Figure 79c). Similarly no statistically significant differences in OCR were seen in all conditions examined (Figure 79b,d,e).

5.5.1.2 The effect of metformin treatment on 3D acini

Metformin is a polar and hydrophilic compound raising the question of whether metformin can enter the cells over the length of the Seahorse assay; this could explain the lack of metabolic response to the drug in this setting. Based on findings relating to mammosphere formation in MCF-7 cells following 50 µM metformin treatment (unpublished work by Pardis Arvinrad, Jeremy Blaydes laboratory) I decided to examine the effect of 50 µM metformin on acini (Figure 80). If the lack of an effect of metformin on cell metabolism is due to a lack of drug update over the short exposure, the longer period of the 3D assay should be sufficient to allow metformin to enter into the cell. 50 µM metformin treatment had no statistically significant effect on acinar luminal status.

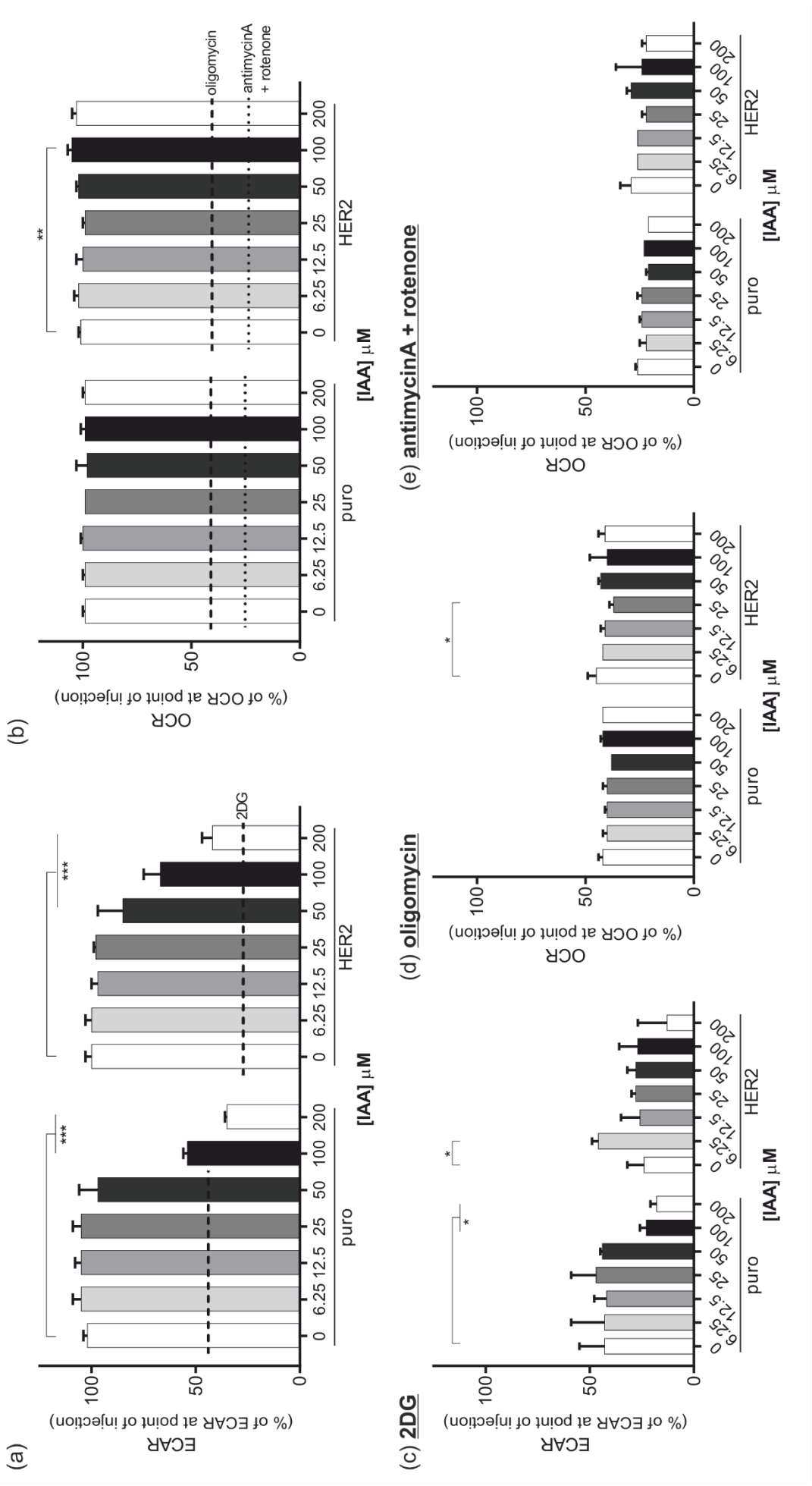
(a)
ECAR
(% of ECAR at point of injection)
100
50
0
***
***
2DG
0 6.25 12.5 25 50 100 200 0 6.25 12.5 25 50 100 200
puro
HER2
[IAA] µM
(b)
OCR
(% of OCR at point of injection)
100
50
0
**
oligomycin
antimycinA
+ rotenone
0 6.25 12.5 25 50 100 200 0 6.25 12.5 25 50 100 200
puro
HER2
[IAA] µM
(c) 2DG
ECAR
(% of ECAR at point of injection)
100
50
0
*
*
0 6.25 12.5 25 50 100 200 0 6.25 12.5 25 50 100 200
puro
HER2
[IAA] µM
(d) oligomycin
OCR
(% of OCR at point of injection)
100
50
0
*
0 6.25 12.5 25 50 100 200 0 6.25 12.5 25 50 100 200
puro
HER2
[IAA] µM
(e) antimycinA + rotenone
OCR
(% of OCR at point of injection)
100
50
0
0 6.25 12.5 25 50 100 200 0 6.25 12.5 25 50 100 200
puro
HER2
[IAA] µM

Figure 77 Metabolic responses to iodoacetic acid treatment

Cells (25,000 per well) were seeded into a Seahorse PET plate 18 h prior to experiment. The Seahorse Analyser simultaneously measured extracellular acidification rate (ECAR) and oxygen consumption rate (OCR) following injection of the stated iodoacetic acid (IAA) concentration. Following IAA treatment wells were injected with either 100 mM 2-deoxyglucose (2DG) or 1 µM oligomycin followed by 1 µM antimycinA and 1 µM rotenone. All data was baselined to the values for ECAR and OCR at the point of injection of the drug (0 min). (a) ECAR following IAA treatment; dashed lines show the average ECAR for puro or HER2 cells following 2DG. Bar graphs represent the mean ± SEM from an independent experiment with four technical repeats. (b) OCR following IAA treatment. Dashed lines show the average OCR for puro or HER2 cells following oligomycin injection; dotted lines show the average OCR for puro or HER2 cells following antimycinA and rotenone injection. Bar graphs represent the mean ± SEM from an independent experiment with four technical repeats. (c) ECAR following 2DG; bar graphs represent the mean ± SEM from an independent experiment with two technical repeats. (d,e) OCR following oligomycin (d) followed by antimycinA and rotenone (e). Bar graphs represent the mean ± SEM from an independent experiment with two technical repeats. * $p \leq 0.05$, ** $p \leq 0.01$; *** $p \leq 0.001$ as determined by a two-way ANOVA with Fisher's LSD test.

5.5.2 Phenformin

Phenformin is another biguanide known to inhibit complex I of the electron transport chain (Table 11) which is both more potent and more lipophilic than metformin (Sogame, Kitamura et al. 2009, Segal, Yasmeen et al. 2011, Appleyard, Murray et al. 2012). I therefore examined the metabolic responses of puro and HER2 cells to phenformin (Figure 81). Janzer *et al.* used a 30-fold lower concentration of phenformin compared to metformin to treat breast cancer stem cells (Janzer, German et al. 2014); while both drugs inhibited citric acid cycle intermediates, phenformin did so to a stronger extent. Lower concentrations of phenformin were therefore tested than those examined when titrating metformin due to the more potent activity of phenformin. The highest concentration of metformin tested previously (200 µM) was included in this experiment for comparison.

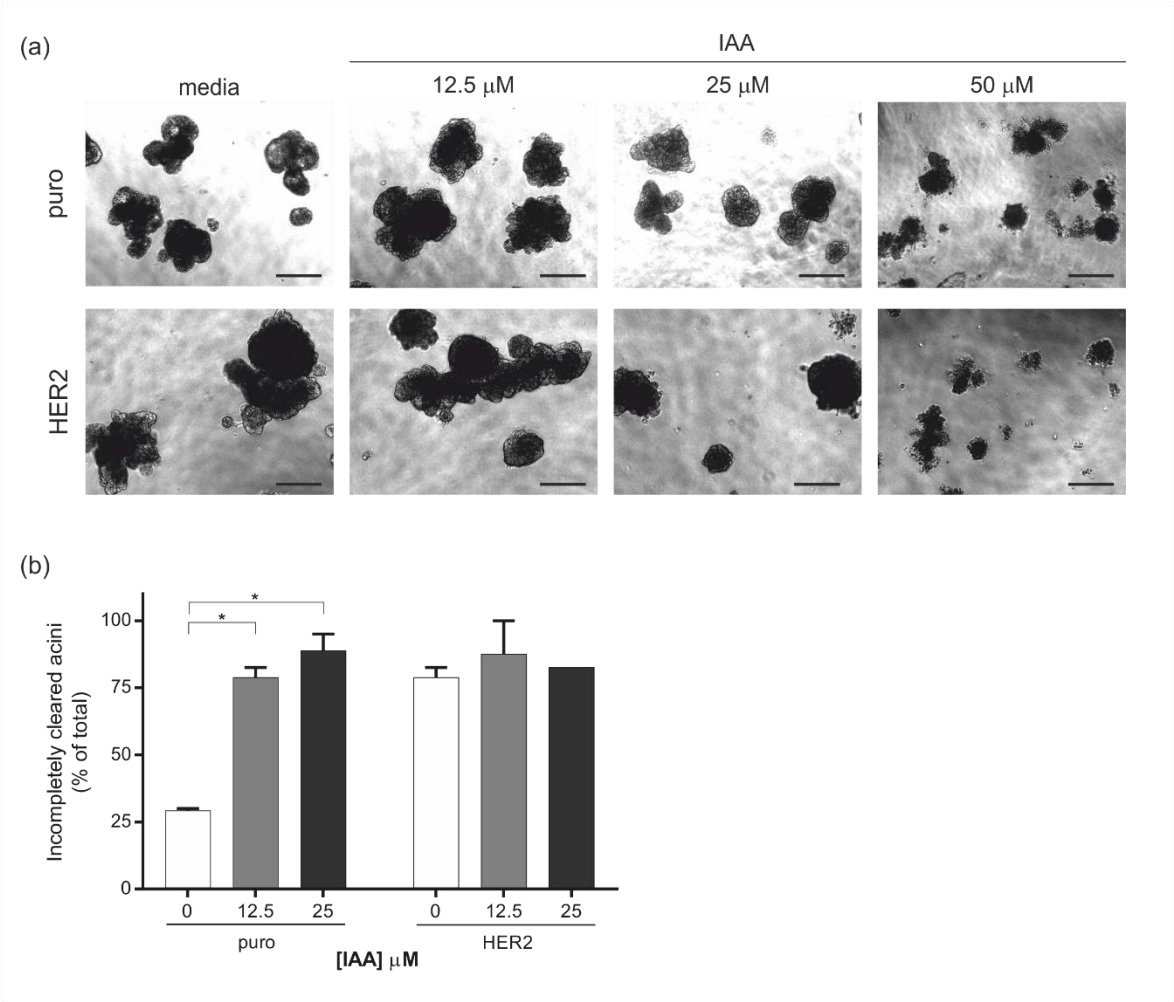

Figure 78 The effect of iodoacetic acid on 3D acini

Acini were treated with media or iodoacetic acid (IAA) every 2 days from day 6 of morphogenesis. (a) Representative phase-contrast images showing acini following IAA treatment. (b) At day 12 acini were fixed and stained with DAPI and phalloidin-TRITC. Confocal microscopy was utilised to score luminal status; looking through all focal planes, acini were scored as filled, partially filled, nearly hollowed or completely hollowed. The number of acini scoring as incompletely cleared (filled or partially filled) was expressed as a percentage of the total acini scored. A minimum of 80 acini were scored for each condition across two independent experiments each with a single technical repeat. Bar graphs represent the mean ± SEM from two independent experiments. * $p \leq 0.05$ as determined by two-way ANOVA with Fisher's LSD test.

5.5.2.1 Metabolic consequences of phenformin treatment

Examining glycolysis, low concentrations of phenformin (1-8 μM) resulted in a small but statistically significant ($p \leq 0.05$) reduction in ECAR in puro cells, with an average 0.09-fold reduction in ECAR, while higher concentrations had no statistically significant effects (Figure 81a). 200 μM metformin also resulted in a 0.09-fold reduction in ECAR in puro cells. In comparison, phenformin has no statistically significant effects on ECAR in HER2 cells except at 32 μM phenformin where ECAR was statistically significantly ($p \leq 0.05$) increased. Following 2-deoxyglucose injection metformin led to a statistically significant ($p \leq 0.05$) increase in ECAR in puro cells while phenformin had no statistically significant effects (Figure 81c). In contrast, in HER2 cells metformin had no statistically significant effect on ECAR following 2-deoxyglucose injection while phenformin led to a statistically significant ($p \leq 0.05$) decrease in ECAR.

Looking at mitochondrial activity, phenformin and 200 μM metformin had no statistically significant effects on OCR across all conditions examined (Figure 81b,d,e) except with 16 μM phenformin; 16 μM phenformin led to a statistically significant ($p \leq 0.01$) reduction in OCR following oligomycin (Figure 81d) and antimycinA and rotenone injections (Figure 81e). Inhibition of complex I by metformin or phenformin would be expected to inhibit oxygen consumption through inhibition of the electron transport chain (Bridges, Jones et al. 2014, Drahota, Palenickova et al. 2014) and as this has not been observed I did not pursue these inhibitors further.

5.6 Antioxidants attenuate luminal clearing

5.6.1 Vitamin C

The metabolic defect associated with ECM-detachment has been described by Schafer *et al*. to include a build-up of ROS (Schafer, Grassian et al. 2009, Davison, Durbin et al. 2013). ROS are primarily generated through oxidative phosphorylation (1.3.1.9 Reactive oxygen species: an inducer of oxidative stress) and can induce oxidative stress and cellular apoptosis if allowed to accumulate. I used the antioxidant Vitamin C to eliminate oxidative stress (Table 11) within MCF-10A to further examine the role of oxidative phosphorylation in acinar morphogenesis.

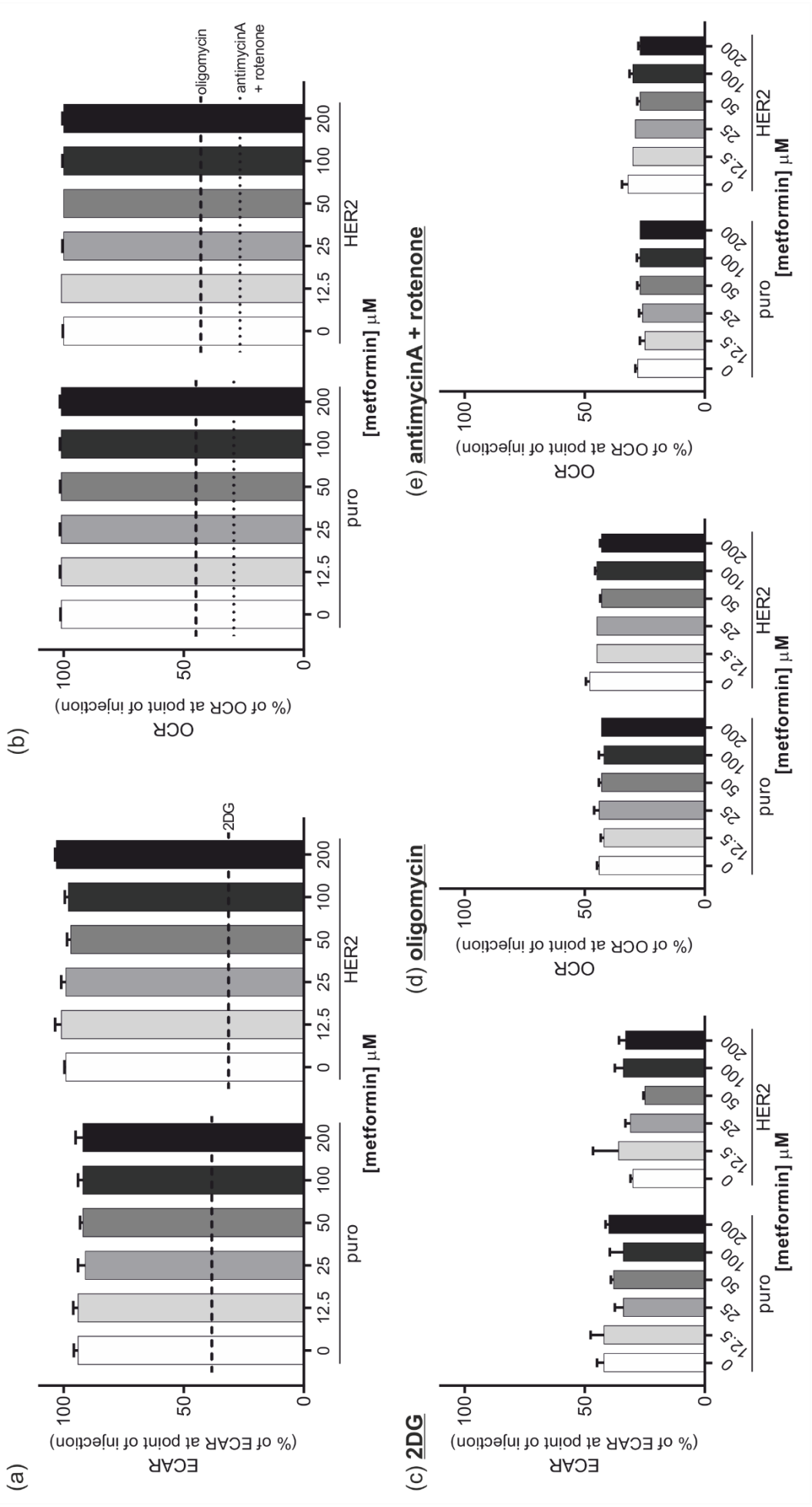
(a)
ECAR
(% of ECAR at point of injection)
2DG
puro
HER2
[metformin] µM
(b)
OCR
(% of OCR at point of injection)
oligomycin
antimycinA + rotenone
(c) 2DG
(d) oligomycin
(e) antimycinA + rotenone

Figure 79 Metabolic responses to metformin treatment

Cells (25,000 per well) were seeded into a Seahorse PET plate 18 h prior to experiment. The Seahorse Analyser simultaneously measured extracellular acidification rate (ECAR) and oxygen consumption rate (OCR) following injection of the stated metformin concentration. Following metformin treatment wells were injected with either 100 mM 2-deoxyglucose (2DG) or 1 µM oligomycin followed by 1 µM antimycinA and 1 µM rotenone. All data was baselined to the values for ECAR and OCR at the point of injection of the drug (0 min). (a) ECAR following metformin treatment; dashed lines show the average ECAR for puro or HER2 cells following 2DG. Bar graphs represent the mean ± SEM from an independent experiment with four technical repeats. (b) OCR following metformin treatment. Dashed lines show the average OCR for puro or HER2 cells following oligomycin injection; dotted lines show the average OCR for puro or HER2 cells following antimycinA and rotenone injection. Bar graphs represent the mean ± SEM from an independent experiment with four technical repeats. (c) ECAR following 2DG; bar graphs represent the mean ± SEM from an independent experiment with two technical repeats. (d,e) OCR following oligomycin (d) followed by antimycinA and rotenone (e). Bar graphs represent the mean ± SEM from an independent experiment with two technical repeats.

5.6.1.1 Metabolic consequences of Vitamin C treatment

The metabolic consequences of Vitamin C treatment were examined using the Seahorse Analyser (Figure 82). Looking at glycolysis in puro and HER2 cells there was a trend towards Vitamin C reducing ECAR in a dose-dependent manner but statistical significance ($p \leq 0.05$) is only reached at 2 mM Vitamin C (Figure 82a). Similarly a trend towards Vitamin C reducing ECAR was observed following 2-dexoyglucose injection (Figure 82c); statistical significance ($p \leq 0.05$) was reached for puro cells at 0.125 mM, 0.5 mM, 1mM and 2mM and in HER2 cells at 0.5 mM and 2 mM. Looking at mitochondrial activity, Vitamin C increased OCR at high concentrations with statistical significance ($p \leq 0.001$) reached at 2 mM Vitamin C in puro cells and at concentrations of 0.5 mM and above in HER2 cells (Figure 82b); however increases in OCR following oligomycin (Figure 82d) and antimycinA and rotenone (Figure 82e) were also observed at these concentrations.

I examined the effect of 500 µM Vitamin C on puro and HER2 cells; this concentration suppresses tamoxifen-induced cell death in MCF-7 cells (Subramani, Yeap et al. 2014).

5.6.1.2 The effect of Vitamin C treatment on 2D cultured cells

The consequences of Vitamin C treatment on cell viability and ATP levels was assessed in attached and detached cells over a 24 h and 48 h period (Figure 83). As determined by an alamarBlue® assay, Vitamin C treatment had no statistically significant effects on cell viability except in detached puro cells at 24 h where Vitamin C significantly ($p \leq 0.01$) increased cell viability (Figure 83a). Similarly ATP levels were not statistically significantly altered except in attached puro cells at 48 h where Vitamin C significantly ($p \leq 0.01$) reduced cellular ATP (Figure 83b).

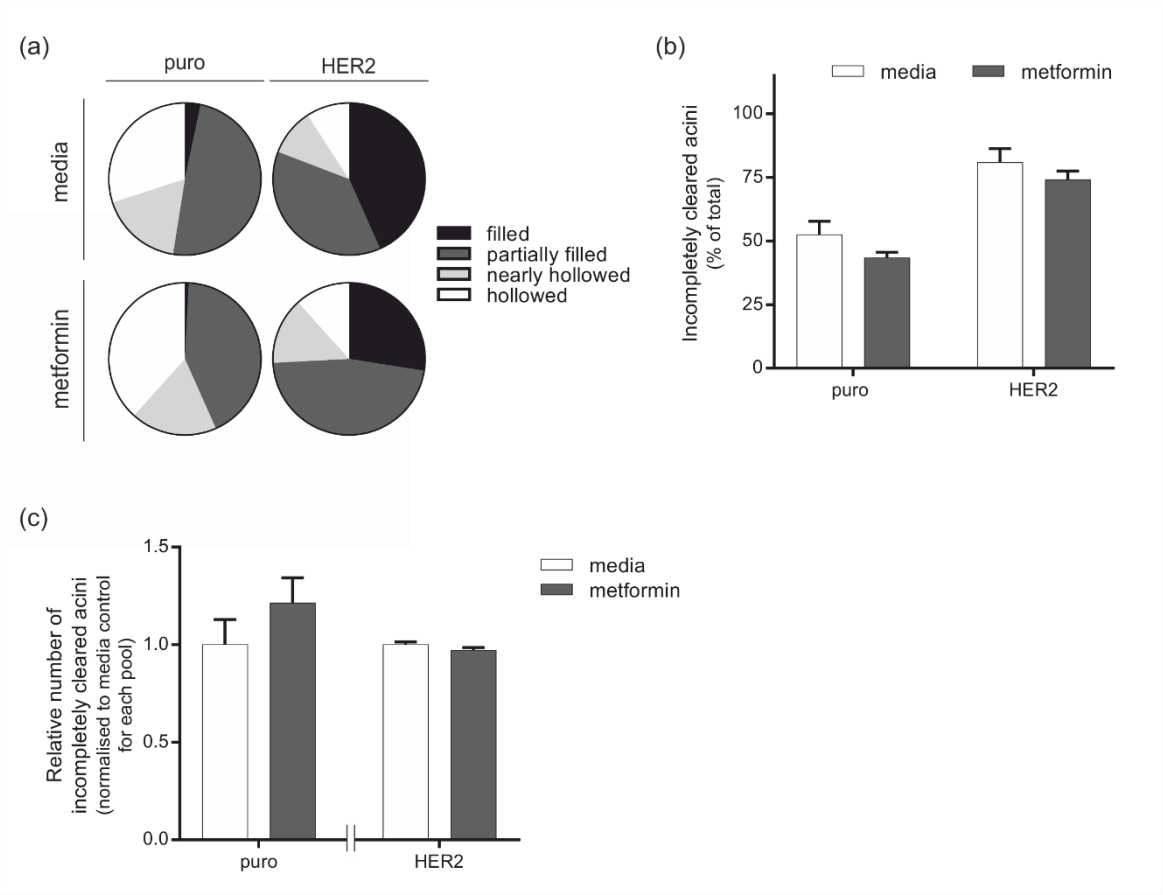

Figure 80 The effect of metformin on 3D acini

Acini were treated with media or metformin (50 µM) every 2 days from day 6 of morphogenesis. At day 12 acini were fixed and stained with DAPI and phalloidin-TRITC. Confocal microscopy was utilised to score luminal status; looking through all focal planes, acini were scored as filled, partially filled, nearly hollowed or completely hollowed. (a) Pie chart representation shows the proportion of acini scoring in each category from a representative experiment. (b) The number of acini scoring as incompletely cleared (filled or partially filled) in (a) was expressed as a percentage of the total acini scored. A minimum of 120 acini were scored for each condition across three replicates. Bar graphs represent the mean ± SEM from three technical repeats. (c) Combined data from three independent experiments shows the relative number of incompletely cleared acini in the presence of metformin compared to media controls. Within an independent experiment values were adjusted for the total number of incompletely cleared acini for each pool. Adjusted values were normalised to the mean adjusted values for media across all three experiments.

5.6.1.3 The effect of Vitamin C treatment on 3D acini

The effect of Vitamin C treatment on the luminal status of puro and HER2 acini was examined (Figure 84). Vitamin C treatment results in a statistically significant ($p \leq 0.01$) difference in the luminal status of puro acini (Figure 84a,b) with a 1.42-fold increase in the number of acini scoring as incompletely cleared following treatment (Figure 84c). An increase in the number of HER2 acini scoring as filled was also observed following treatment of Vitamin C (Figure 84a) although statistical significance was not reached (Figure 84b,c).

5.7 Dichloroacetate transforms controls into a more cancerous state

To further investigate the role of mitochondrial respiration in MCF-10A acinar morphogenesis I examined the effect of dichloroacetate treatment.

5.7.1 Dichloroacetate

Dichloroacetate is able to reactivate the citric acid cycle in cancer cells, reversing the suppression of oxidative phosphorylation (Table 11) (Bonnet, Archer et al. 2007). Acting through inhibition of pyruvate dehydrogenase kinase, which phosphorylates pyruvate dehydrogenase to inactive it, dichloroacetate indirectly activates pyruvate dehydrogenase and increases mitochondrial pyruvate metabolism.

5.7.1.1 Metabolic consequences of dichloroacetate treatment

The metabolic consequences of dichloroacetate were examined using a Seahorse assay (Figure 85). Dichloroacetate led to an increase in ECAR compared to media control in both puro and HER2 cells (Figure 85a), however an increase in ECAR in the presence of dichloroacetate was also seen following 2-deoxyglucose injections (Figure 85c) suggesting that this increase in ECAR is not a consequence of increase glycolytic activity. If I look at the pH of wells immediately following dichloroacetate injection I can see that dichloroacetate is increasing the pH of samples in a dose-dependent manner (Figure 86); alterations in ECAR may be a consequence of the drug injection into the media and not due to an effect of DCA on the cells.

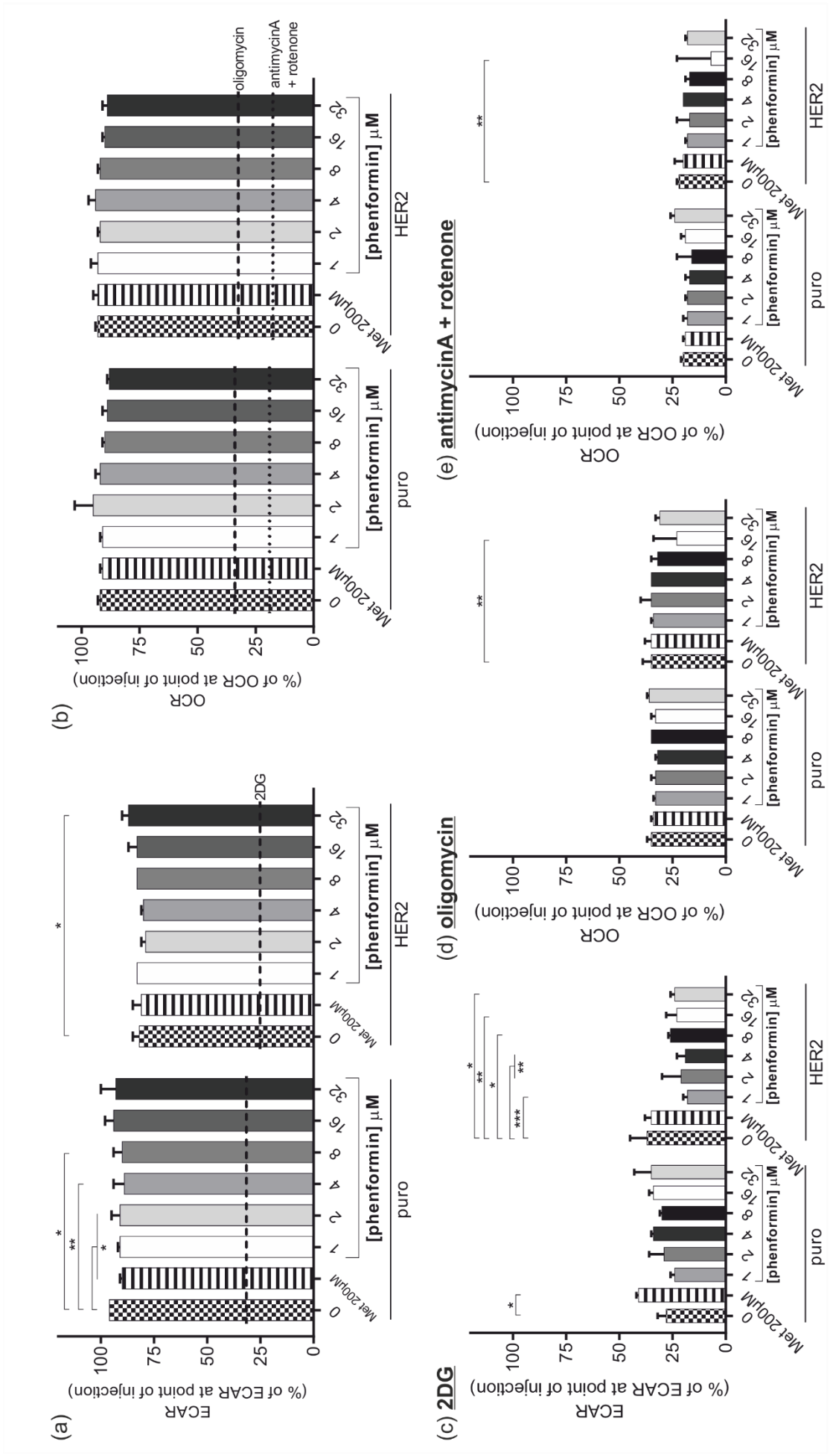
(a)
ECAR
(% of ECAR at point of injection)
2DG
Met 200µM
[phenformin] µM
puro
HER2
(b)
OCR
(% of OCR at point of injection)
oligomycin
antimycinA + rotenone
(c) 2DG
(d) oligomycin
(e) antimycinA + rotenone

Figure 81 Metabolic responses to phenformin treatment

Cells (25,000 per well) were seeded into a Seahorse PET plate 18 h prior to experiment. The Seahorse Analyser simultaneously measured extracellular acidification rate (ECAR) and oxygen consumption rate (OCR) following injection of 200 µM metformin or the stated phenformin concentration. Following inhibitor treatment wells were injected with either 100 mM 2-deoxyglucose (2DG) or 1 µM oligomycin followed by 1 µM antimycinA and 1 µM rotenone. All data was baselined to the values for ECAR and OCR at the point of injection of the drug (0 min). (a) ECAR following metformin or phenformin treatment; dashed lines show the average ECAR for puro or HER2 cells following 2DG. Bar graphs represent the mean ± SEM from an independent experiment with four technical repeats. (b) OCR following metformin or phenformin treatment. Dashed lines show the average OCR for puro or HER2 cells following oligomycin injection; dotted lines show the average OCR for puro or HER2 cells following antimycinA and rotenone injection. Bar graphs represent the mean ± SEM from an independent experiment with four technical repeats. (c) ECAR following 2DG; bar graphs represent the mean ± SEM from an independent experiment with two technical repeats. (d,e) OCR following oligomycin (d) followed by antimycinA and rotenone (e). Bar graphs represent the mean ± SEM from an independent experiment with two technical repeats. * $p \leq 0.05$, ** $p \leq 0.01$; *** $p \leq 0.001$ as determined by a two-way ANOVA with Fisher's LSD test.

Looking at mitochondrial activity, dichloroacetate significantly ($p \leq 0.001$) increases OCR (Figure 85b) in both puro and HER2 cells. At high concentrations of the inhibitor dichloroacetate does significantly affect OCR following oligomycin (Figure 85d) suggesting that there is an effect on proton leak. However, the extent of upregulation following oligomycin is less than seen in presence of dichloroacetate alone; for example there is a 1.20-fold increase in OCR following oligomycin in puro cells treated with 10 mM dichloroacetate compared to a 1.60-fold increase presence of 10 mM dichloroacetate alone (Figure 85b,d). Following antimycinA and rotenone injections no statistically significant differences in OCR are observed in puro cells in the presence of dichloroacetate, while HER2 cells show a statistically significant ($p \leq 0.05$) increase in OCR at 2.5 mM dichloroacetate and a decrease in OCR at 10 mM dichloroacetate (Figure 85e).

10 mM dichloroacetate was taken forward as the concentration for future experiments; this concentration induces a reduction in ECAR and an increase in OCR in melanoma cell lines without inducing high levels of apoptosis (Abildgaard, Dahl et al. 2014). In the Seahorse assay 10 mM dichloroacetate induced a 1.60-fold and a 1.63-fold increase in OCR in puro and HER2 cells respectively (Figure 85b).

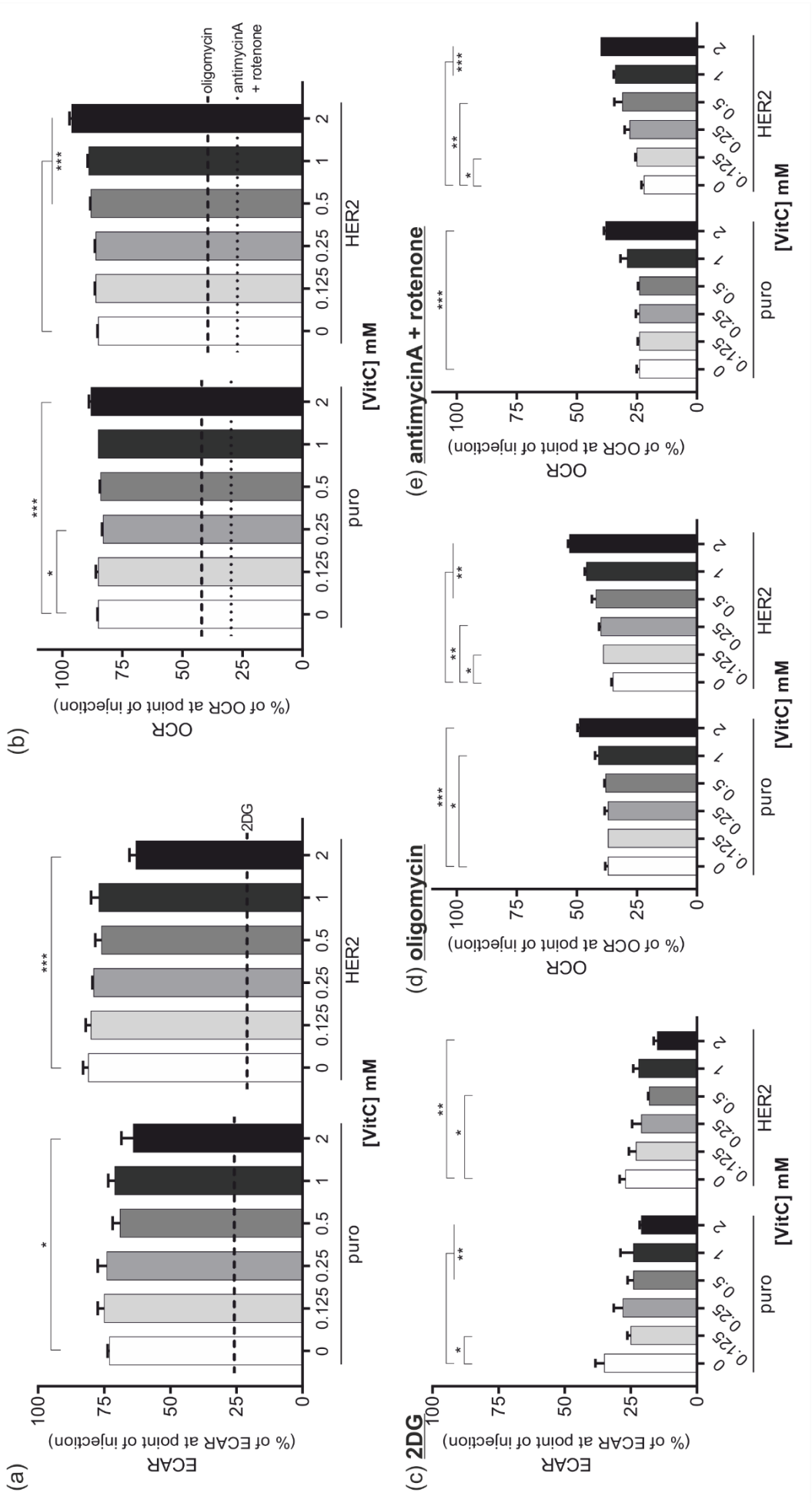
(a)
ECAR
(% of ECAR at point of injection)
2DG
puro
HER2
[VitC] mM
(b)
OCR
(% of OCR at point of injection)
oligomycin
antimycinA + rotenone
(c) 2DG
(d) oligomycin
(e) antimycinA + rotenone

Figure 82 Metabolic responses to Vitamin C treatment

Cells (25,000 per well) were seeded into a Seahorse PET plate 18 h prior to experiment. The Seahorse Analyser simultaneously measured extracellular acidification rate (ECAR) and oxygen consumption rate (OCR) following injection of the stated Vitamin C (VitC) concentration. Following Vit C treatment wells were injected with either 100 mM 2-deoxyglucose (2DG) or 1 µM oligomycin followed by 1 µM antimycinA and 1 µM rotenone. All data was baselined to the values for ECAR and OCR at the point of injection of the drug (0 min). (a) ECAR following VitC treatment; dashed lines show the average ECAR for puro or HER2 cells following 2DG. Bar graphs represent the mean ± SEM from an independent experiment with four technical repeats. (b) OCR following VitC treatment. Dashed lines show the average OCR for puro or HER2 cells following oligomycin injection; dotted lines show the average OCR for puro or HER2 cells following antimycinA and rotenone injection. Bar graphs represent the mean ± SEM from an independent experiment with four technical repeats. (c) ECAR following 2DG; bar graphs represent the mean ± SEM from an independent experiment with two technical repeats. (d,e) OCR following oligomycin (d) followed by antimycinA and rotenone (e). Bar graphs represent the mean ± SEM from an independent experiment with two technical repeats. * $p \leq 0.05$, ** $p \leq 0.01$; *** $p \leq 0.001$ as determined by a two-way ANOVA with Fisher's LSD test.

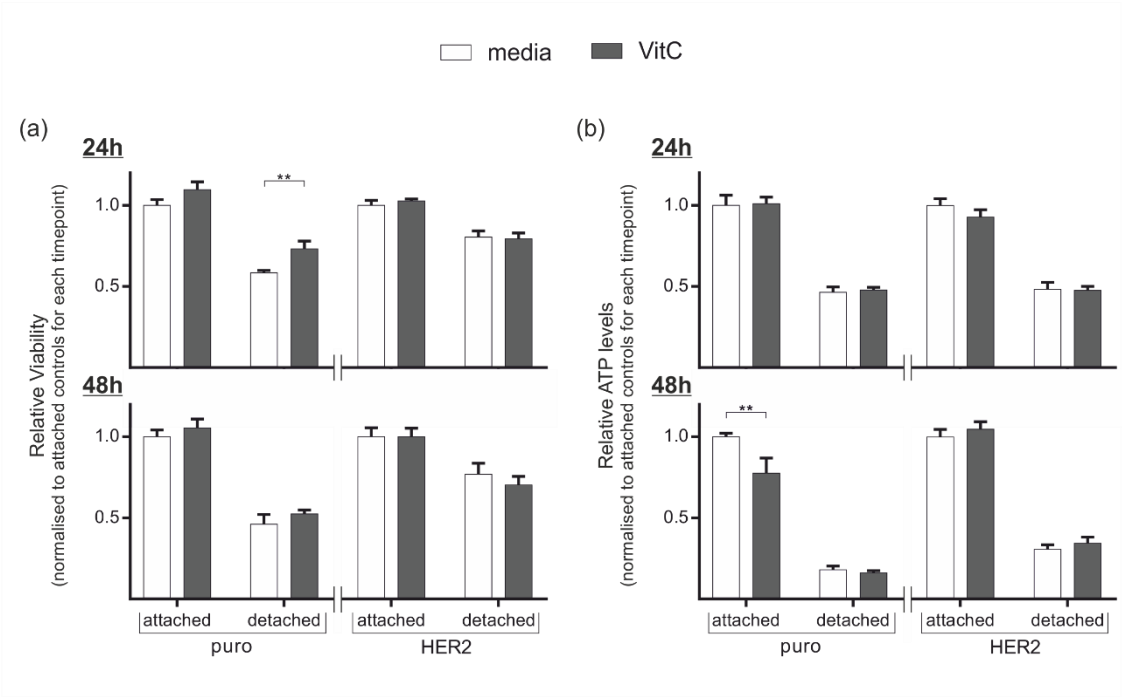

Figure 83 The effect of Vitamin C treatment on 2D cell viability

Cells (15,000 per well) were treated with media or Vitamin C (Vit C) (500 µM) and seeded onto standard tissue culture plates (attached) or polyHEMA-coated plastic (detached) for 24 or 48 h. (a) Cell viability was examined using alamarBlue® reagent which was added to conditions 6 h prior to data collection. (b) ATP levels were examined using the ATPlite assay. Fluorometric (a) or luminometric data (b) was normalised for experimental variation and expressed relative to the appropriate media control in attached conditions (puro or HER2). Bar graphs represent the mean ± SEM from three independent experiments each with three technical repeats. ** $p \leq 0.01$ as determined by a two-way ANOVA with Fisher's LSD test.

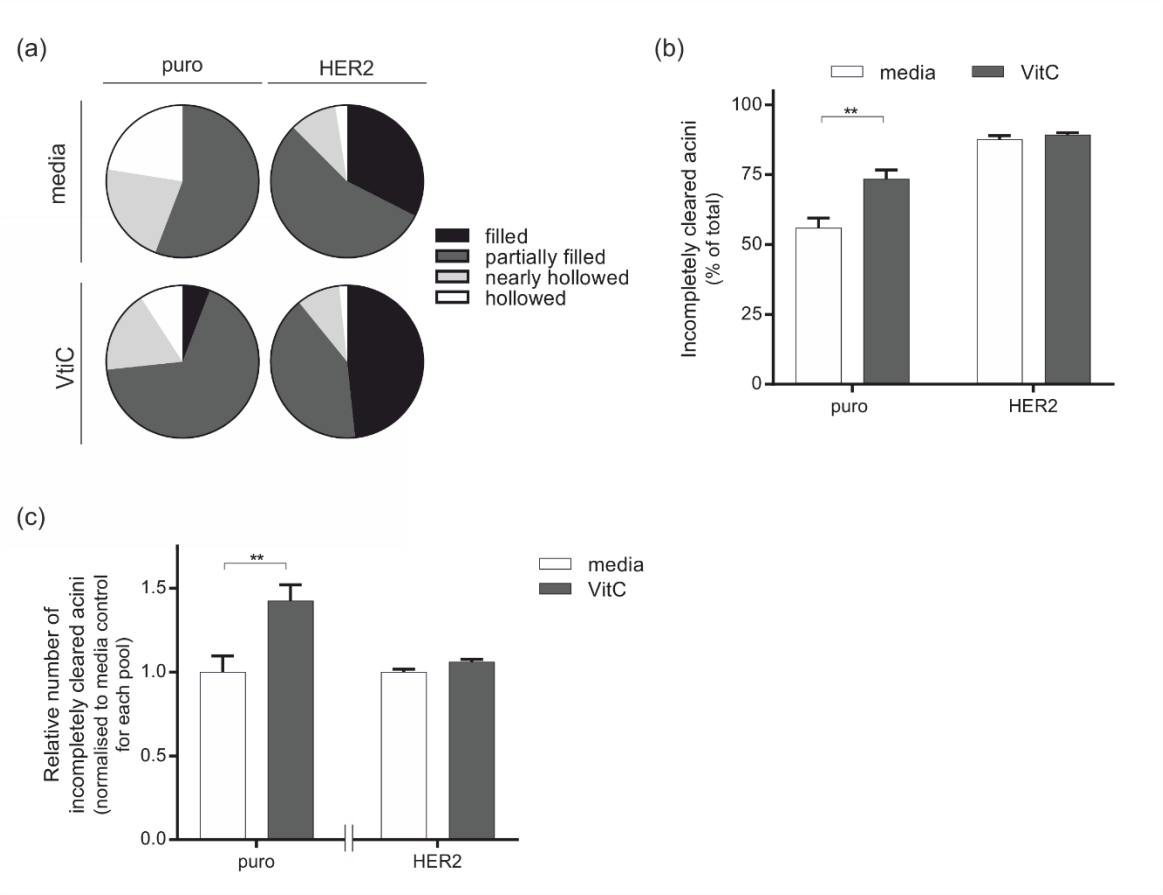

Figure 84 The effect of Vitamin C on 3D acini

Acini were treated with media or Vitamin C (VitC) (500 µM) every 2 days from day 6 of morphogenesis. At day 12 acini were fixed and stained with DAPI and phalloidin-TRITC. Confocal microscopy was utilised to score luminal status; looking through all focal planes, acini were scored as filled, partially filled, nearly hollowed or completely hollowed. (a) Pie chart representation shows the proportion of acini scoring in each category from a representative experiment. (b) The number of acini scoring as incompletely cleared (filled or partially filled) in (a) was expressed as a percentage of the total acini scored. A minimum of 120 acini were scored for each condition across three replicates. Bar graphs represent the mean ± SEM from three technical repeats. (c) Combined data from three independent experiments shows the relative number of incompletely cleared acini in the presence of VitC compared to media controls. Within an independent experiment values were adjusted for the total number of incompletely cleared acini for each pool. Adjusted values were normalised to the mean adjusted values for media across all three experiments. ** $p \leq 0.01$ as determined by two-way ANOVA with Fisher's LSD test.

5.7.1.2 The effect of dichloroacetate on 2D viability

To examine the effect of dichloroacetate on 2D cultured cells, cell viability and intracellular ATP levels were examined over a 24 h and 48 h period in attached and detached cells (Figure 87). When examined by an alamarBlue® assay, dichloroacetate had no statistically significant effects on puro or HER2 cells (Figure 87a). Similiarly, dichloroacetate had no statistically significant effects on puro or HER2 cells except at 48 h in HER2 attached cells where dichloroacetate statistically significantly ($p \leq 0.05$) reduced ATP levels (Figure 87b).

5.7.1.3 The effect of dichloroacetate on 3D acini

Dichloroacetate pushed acini towards a more filled phenotype (Figure 88a,b,c). Puro acini scored as 86% incompletely cleared in the presence of dichloroacetate, a statistically significant ($p \leq 0.001$) increase compared to 31% of incompletely cleared acini in the presence of media alone (Figure 88b). When combining data from three experiments a statistically significant ($p \leq 0.001$) 2.10-fold increase in incompletely cleared puro acini was observed following dichloroacetate treatment (Figure 88d). In contrast, a 1.10-fold increase in incompletely cleared acini was observed in HER2 acini following dichloroacetate treatment which did not reach statistical significance.

The day 12 time point used to assess the role of dichloroacetate in luminal clearing is a relatively early time point of morphogenesis when interested in the luminal clearing program. To further assess the role of dichloroacetate I examined the effect of dichloroacetate treatment on puro acini at day 16 of morphogenesis (Figure 89); this will allow me to examine whether dichloroacetate is simply delaying or fully preventing luminal clearing in this model.

Similarly to results seen at day 12 of morphogenesis, dichloroacetate leads to a statistically significant ($p \leq 0.001$) increase in the percentage of incompletely cleared acini (Figure 89a,b) with a 2.80-fold increase in the number of incompletely cleared acini in the presence of dichloroacetate compared to media alone (Figure 89c).

In addition to the effects observed on luminal clearing a different morphology was observed in puro acini treated with dichloroacetate (Figure 89c). This was examined further by monitoring acinar morphology (Figure 90). A highly branched acinar phenotype was observed in puro acini treated with dichloroacetate (Figure 90a) with a statistically significant ($p \leq 0.05$) 49% increase in the number of atypical acini compared to media controls (Figure 90b). Dichloroacetate treatment had no statistically significant effects on the number of atypical HER2 acini compared to media controls but acini did appear larger with dichloroacetate treatment (Figure 90a).

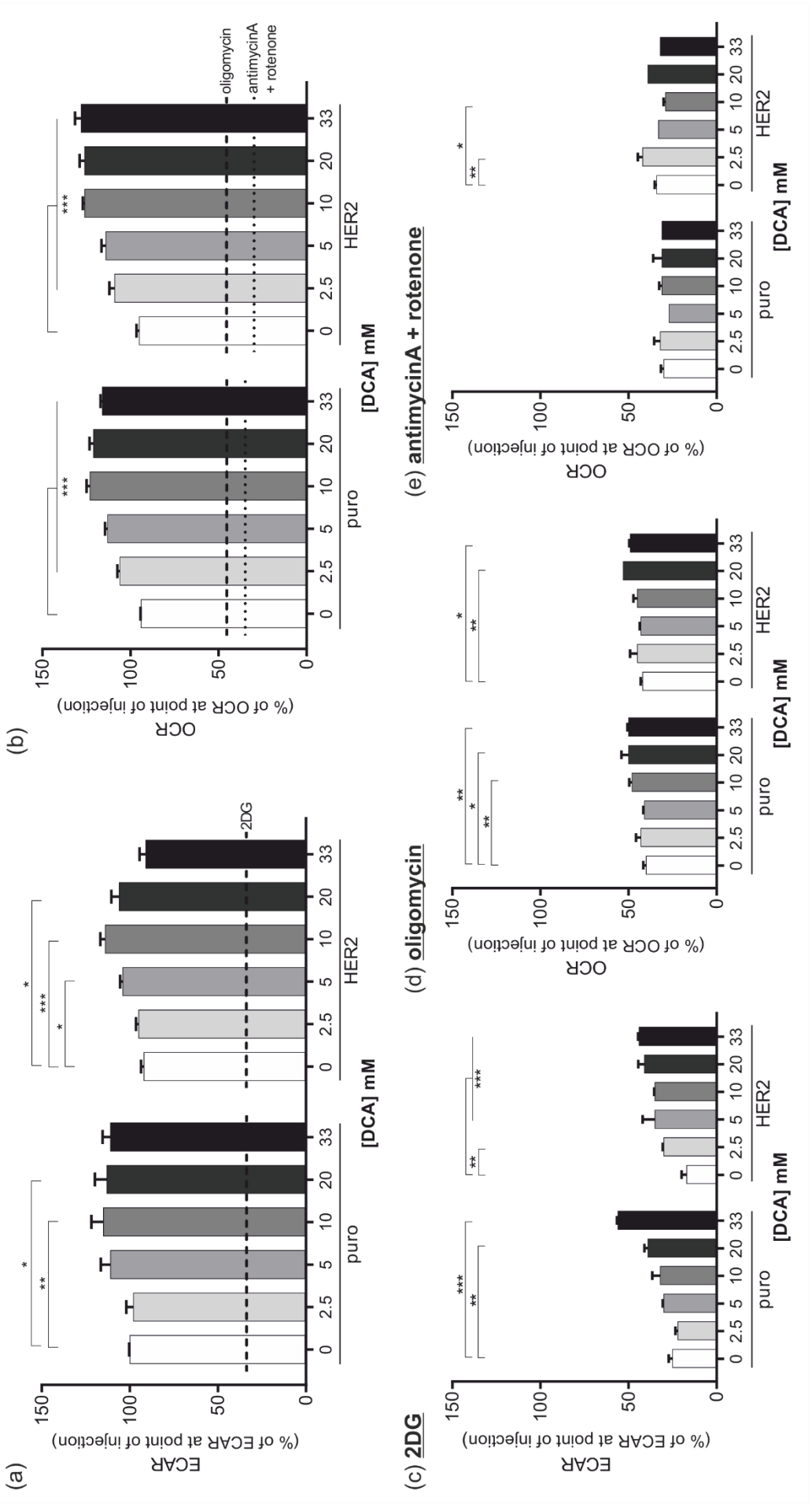
(a)
ECAR
(% of ECAR at point of injection)
2DG
puro
HER2
[DCA] mM
(b)
OCR
(% of OCR at point of injection)
oligomycin
antimycinA + rotenone
(c) 2DG
(d) oligomycin
(e) antimycinA + rotenone

Figure 85 Metabolic responses to dichloroacetate treatment

Cells (25,000 per well) were seeded into a Seahorse PET plate 18 h prior to experiment. The Seahorse Analyser simultaneously measured extracellular acidification rate (ECAR) and oxygen consumption rate (OCR) following injection of the stated dichloroacetate (DCA) concentration. Following DCA treatment, wells were injected with either 100 mM 2-deoxyglucose (2DG) or 1 µM oligomycin followed by 1 µM antimycinA and 1 µM rotenone. All data was baselined to the values for ECAR and OCR at the point of injection of the drug (0 min). (a) ECAR following DCA treatment; dashed lines show the average ECAR for puro or HER2 cells following 2DG. Bar graphs represent the mean ± SEM from an independent experiment with four technical repeats. (b) OCR following DCA treatment. Dashed lines show the average OCR for puro or HER2 cells following oligomycin injection; dotted lines show the average OCR for puro or HER2 cells following antimycinA and rotenone injection. Bar graphs represent the mean ± SEM from an independent experiment with four technical repeats. (c) ECAR following 2DG; bar graphs represent the mean ± SEM from an independent experiment with two technical repeats. (d,e) OCR following oligomycin (d) followed by antimycinA and rotenone (e). Bar graphs represent the mean ± SEM from an independent experiment with two technical repeats. * $p \leq 0.05$, ** $p \leq 0.01$; *** $p \leq 0.001$ as determined by a two-way ANOVA with Fisher's LSD test.

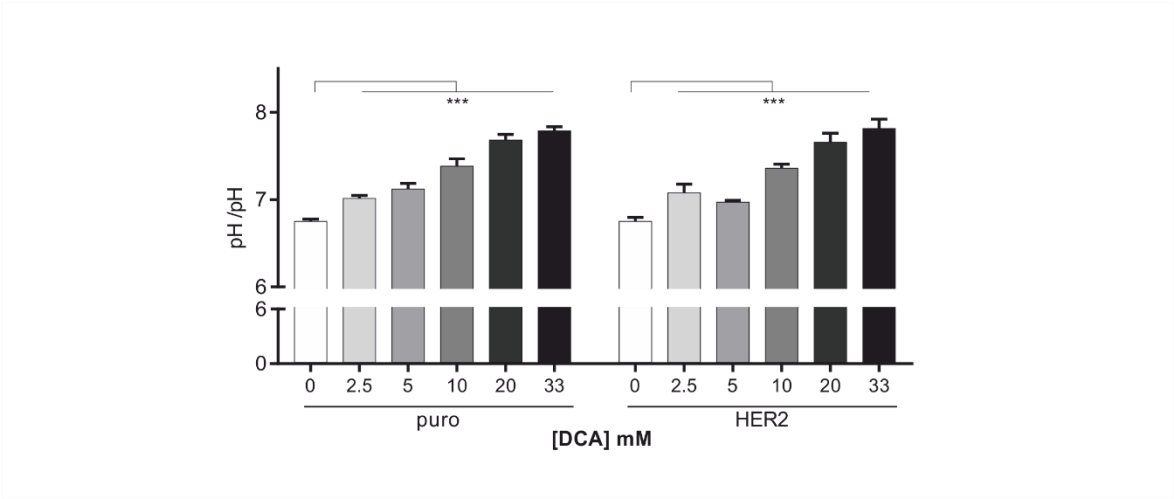

Figure 86 Dichloroacetate injection in a Seahorse assay increases the pH of wells in a dose dependent manner

Cells (25,000 per well) were seeded into Seahorse PET plate 18 h prior to experiment. Data shows the pH of wells immediately following injection of the stated dichloroacetate (DCA) concentration as measured by the Seahorse Analyser. Bar graphs represent the mean ± SEM from an independent experiment with four technical repeats. *** $p \leq 0.001$ as determined by a two-way ANOVA with Fisher's LSD test.

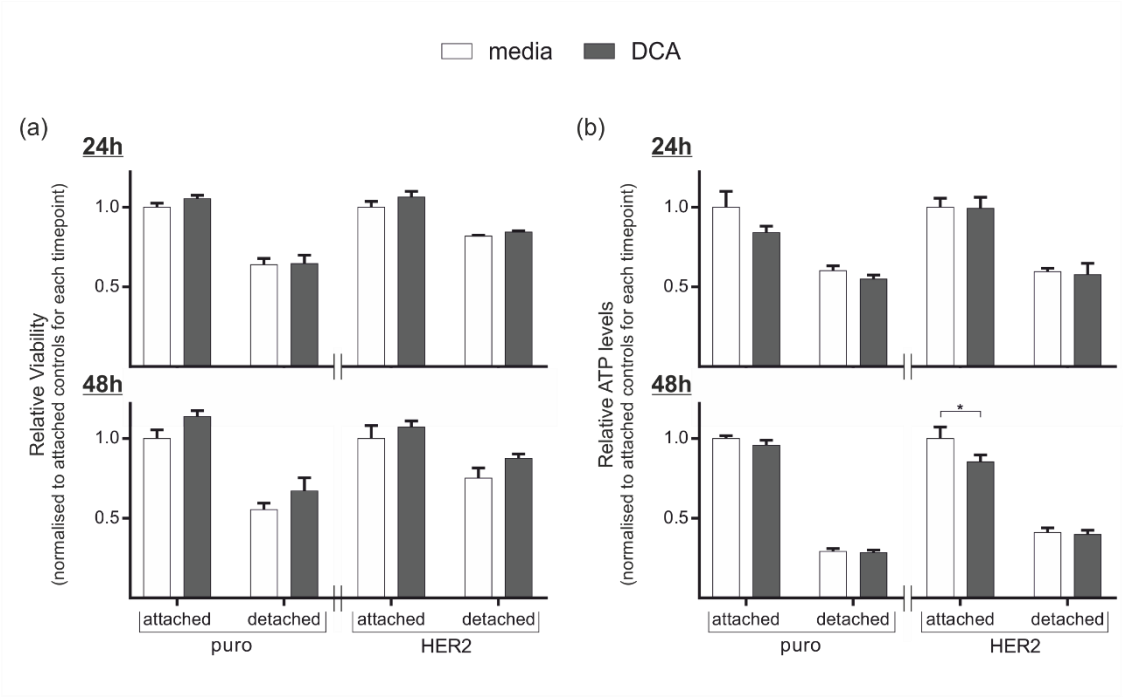

Figure 87 The effect of dichloroacetate on 2D cell viability

Cells (15,000 per well) were treated with media or dichloroacetate (DCA) (10 mM) and seeded onto standard tissue culture plates (attached) or polyHEMA-coated plastic (detached) for 24 h or 48 h. (a) Cell viability was examined using alamarBlue® reagent which was added to conditions 6 h prior to data collection. (b) ATP levels were examined using the ATPlite assay. Fluorometric (a) or luminometric data (b) was normalised for experimental variation and expressed relative to the appropriate media control in attached conditions (puro or HER2). Bar graphs represent the mean ± SEM from three independent experiments, each with three technical repeats. * $p \leq 0.05$ as determined by a two-way ANOVA with Fisher's LSD test.

An alamarBlue® assay was utilised to monitor viability in dichloroacetate-treated acini (Figure 91). Dichloroacetate resulted in a 1.12- and 1.07- fold increase in viability in puro and HER2 cells respectively but this did not reach statistical significance.

5.7.2 Autophagy and dichloroacetate

Dichloroacetate has been shown to induce autophagy in colorectal cancer cell lines (Gong, Peng et al. 2013, Lin, Hill et al. 2014), a cellular process that can promote cell survival in matrix-detached MCF-10A cells (Fung, Lock et al. 2008). I therefore hypothesised that the dichloroacetate-induced phenotype of luminal filling was a consequence of protective autophagy induction.

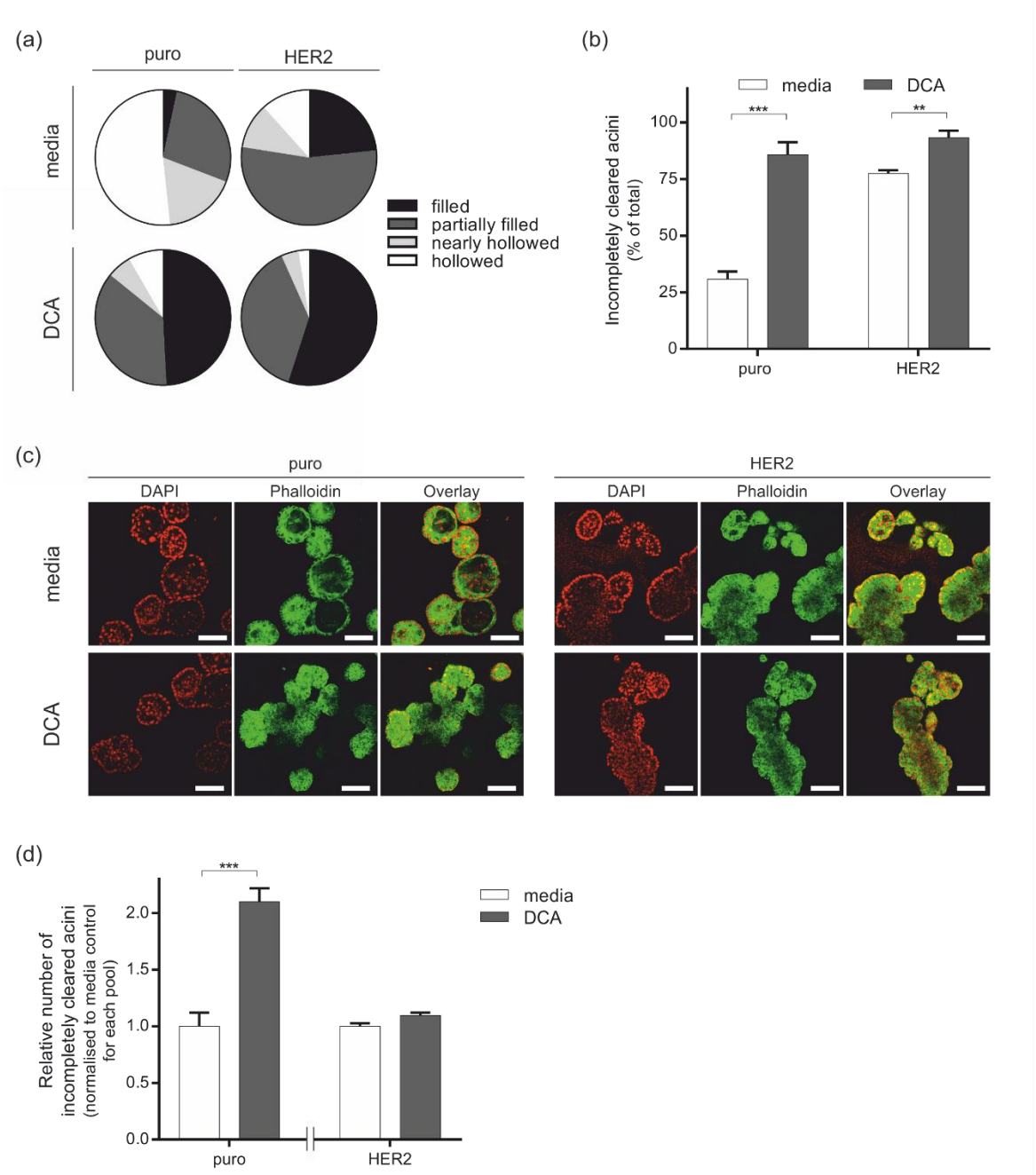

Figure 88 The effect of dichloroacetate on 3D acini at an early morphogenesis time point

Acini were treated with media or dichloroacetate (DCA) (10 mM) every 2 days from day 6 of morphogenesis. At day 12 acini were fixed and stained with DAPI (red) and phalloidin-TRITC (green). Confocal microscopy was utilised to score luminal status; looking through all focal planes, acini were scored as filled, partially filled, nearly hollowed or completely hollowed. (a) Pie chart representation shows the proportion of acini scoring in each category from a representative experiment. (b) The number of acini scoring as incompletely cleared (filled or partially filled) in (a) was expressed as a percentage of the total acini scored. A minimum of 120 acini were scored for each condition across three replicates. Bar graphs represent the mean ± SEM from three technical repeats. (c) Representative confocal immunofluorescence images show the centre of acini following DCA treatment; scale bars show 100µm. (d) Combined data from three independent experiments shows the relative number of incompletely cleared acini in the presence of DCA compared to media controls. Within an independent experiment, values were adjusted for the total number of incompletely cleared acini for each pool. Adjusted values were normalised to the mean adjusted values for media across all three experiments. ** $p \leq 0.01$, *** $p \leq 0.001$ as determined by two-way ANOVA with Fisher's LSD test.

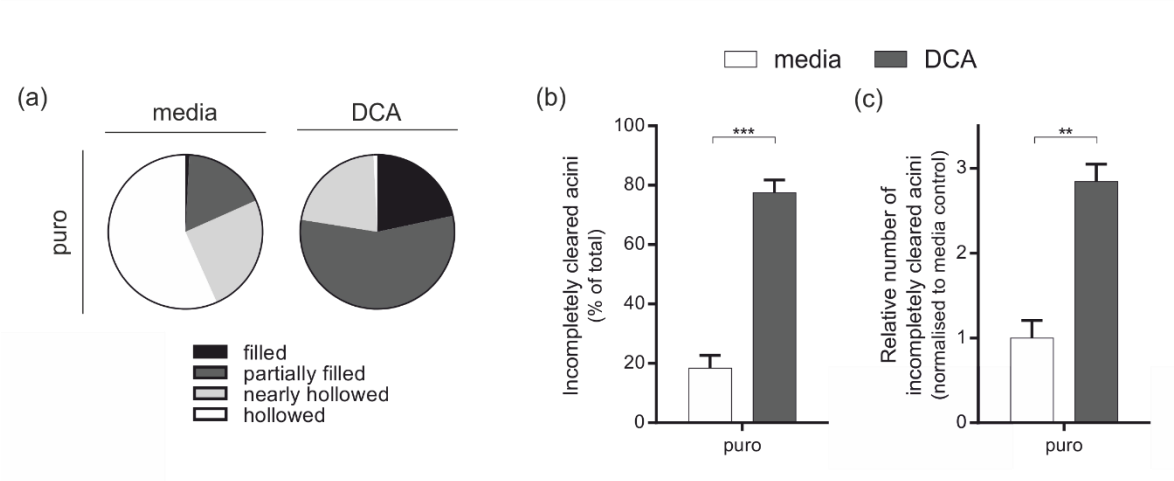

Figure 89 The effect of dichloroacetate on 3D acini at a late morphogenesis time point

Acini were treated with media or dichloroacetate (DCA) (10 mM) every 2 days from day 6 of morphogenesis. At day 16 acini were fixed and stained with DAPI and phalloidin-TRITC. Confocal microscopy was utilised to score luminal status; looking through all focal planes, acini were scored as filled, partially filled, nearly hollowed or completely hollowed. (a) Pie chart representation shows the proportion of acini scoring in each category from a representative experiment. (b) The number of acini scoring as incompletely cleared (filled or partially filled) in (a) was expressed as a percentage of the total acini scored. A minimum of 120 acini were scored for each condition across three replicates. Bar graphs represent the mean ± SEM from three technical repeats. (c) Combined data from three independent experiments shows the relative number of incompletely cleared acini in the presence of DCA compared to media controls. Within an independent experiment values were adjusted for the total number of incompletely cleared acini. Adjusted values were normalised to the mean adjusted values for media across all three experiments. ** $p \leq 0.01$, *** $p \leq 0.001$ as determined by paired t-test.

To examine whether dichloroacetate-induced luminal filling is a consequence of autophagy I included autophagy inhibitors with dichloroacetate treated acini from day 6 of morphogenesis. Within a single experiment dichloroacetate statistically significantly ($p \leq 0.01$) increased the number of acini scoring as incompletely cleared compared to media controls (Figure 92a,b) consistent with previous results (Figure 88). While chloroquine statistically significantly ($p \leq 0.05$) reduced the number of incompletely cleared acini in acini treated with media alone, the addition of chloroquine in dichloroacetate-treated acini had no statistically significant effects on the scoring of acini. When combining data from three independent experiments chloroquine caused a reduction in incompletely cleared acini in both media- and dichloroacetate- treated acini but this did not reach statistical significance (Figure 92c). The fold-increase in incompletely cleared acini upon dichloroacetate treatment was 2.1-fold in the absence of and 3.0-fold in the presence of chloroquine.

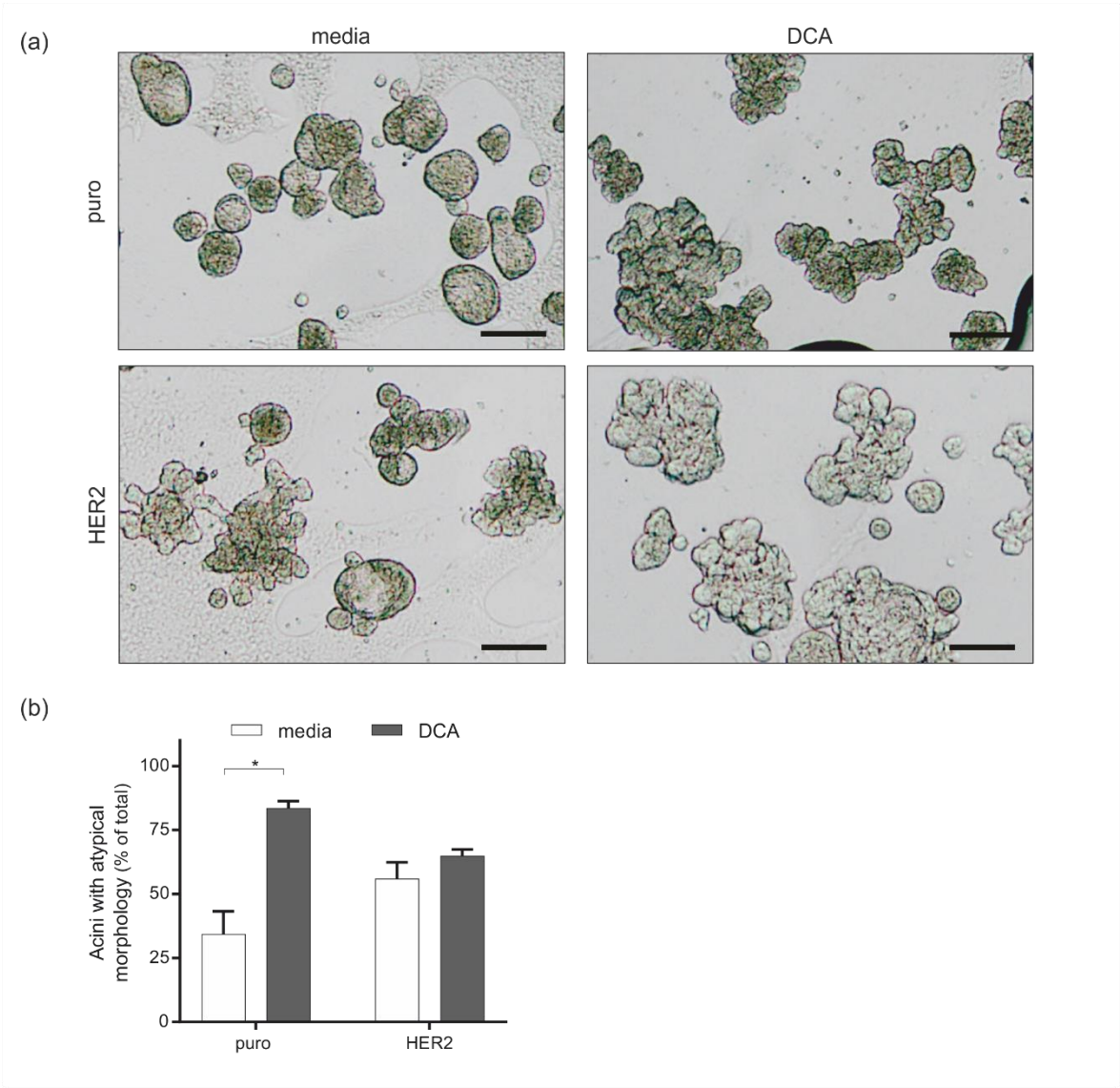

Figure 90 The effect of dichloroacetate on 3D acinar morphology

Acini were treated with media or dichloroacetate (DCA) (10 mM) every 2 days from day 6 of morphogenesis. At day 12 acini were fixed directly to minimise acini loss in wash steps (2% PFA final concentration) and mounted. High resolution pictures covering the entire slide were captured and all acini within a chamber scored manually. (a) Representative phase contrast images of acinar morphology are shown; scale bars show 200 µm. (b) Morphology was scored as normal or atypical, where atypical includes multiacinar, branching and non-rounded acini. The number of acini scoring as atypical was expressed as a percentage of the total acini scored. A minimum of 110 acini were present in each well. Bar graphs represent the mean ± SEM from three independent experiments each with three technical repeats. $p \leq 0.05$ as determined by two-way ANOVA with Fisher's LSD test.

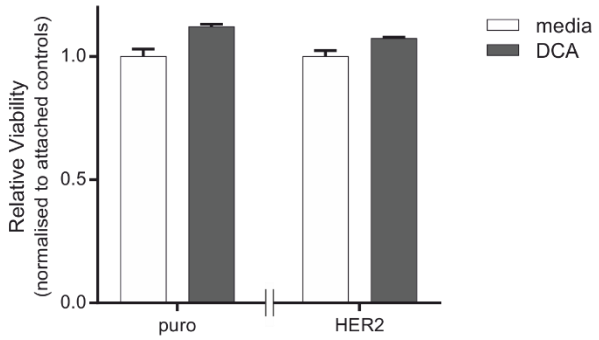

Figure 91 The effect of dichloroacetate on 3D cell viability

Cells (200 per well) were seeded in 96-well plates which had been pre-coated with Matrigel and cultured in 3D for 12 days. Acini were treated with media or dichloroacetate (DCA) (10 mM) every 2 days from day 6 of morphogenesis. Cell viability was examined using alamarBlue® reagent which was added to conditions 6 h prior to data collection. Fluorometric data was adjusted for background, normalised for experimental variation and expressed relative to the appropriate media control (puro or HER2). Bar graphs represent the mean ± SEM from three independent experiments, each with four technical repeats.

5.8 Discussion

This study examined the role of metabolism in acinar morphogenesis using the MCF-10A model of the healthy breast and a HER2-driven model of early breast cancer. My data demonstrates the sensitivity of the MCF-10A model to media composition. In addition through treatment of MCF-10A acini with metabolic inhibitors, summarised in Table 11, I have shown the importance of FAO for HER2-driven transformation and, secondly, highlighted a role for glycolysis in survival upon ECM-detachment. Finally, in contrast to the predicted hypothesis, dichloroacetate pushed control acini towards a highly transformed phenotype.

HER2 overexpression alters the metabolism of MCF-10A cells

I have shown that HER2 cells display statistically significantly enhanced glycolysis and downregulated mitochondrial respiration in 2D (Figure 51) suggesting that HER2 overexpression promotes a switch towards a more glycolytic phenotype. This is consistent with data from Zhao *et al.* who show that HER2 overexpression in MCF-7 and MDA-MB-435 leads to increased glycolysis through lactate dehydrogenase upregulation (Zhao, Zhou et al. 2009); note that MDA-MB-435 cells have been used here as a breast cancer model but have been shown to be derived from a M14 melanoma cell line (Rae, Creighton et al. 2007).

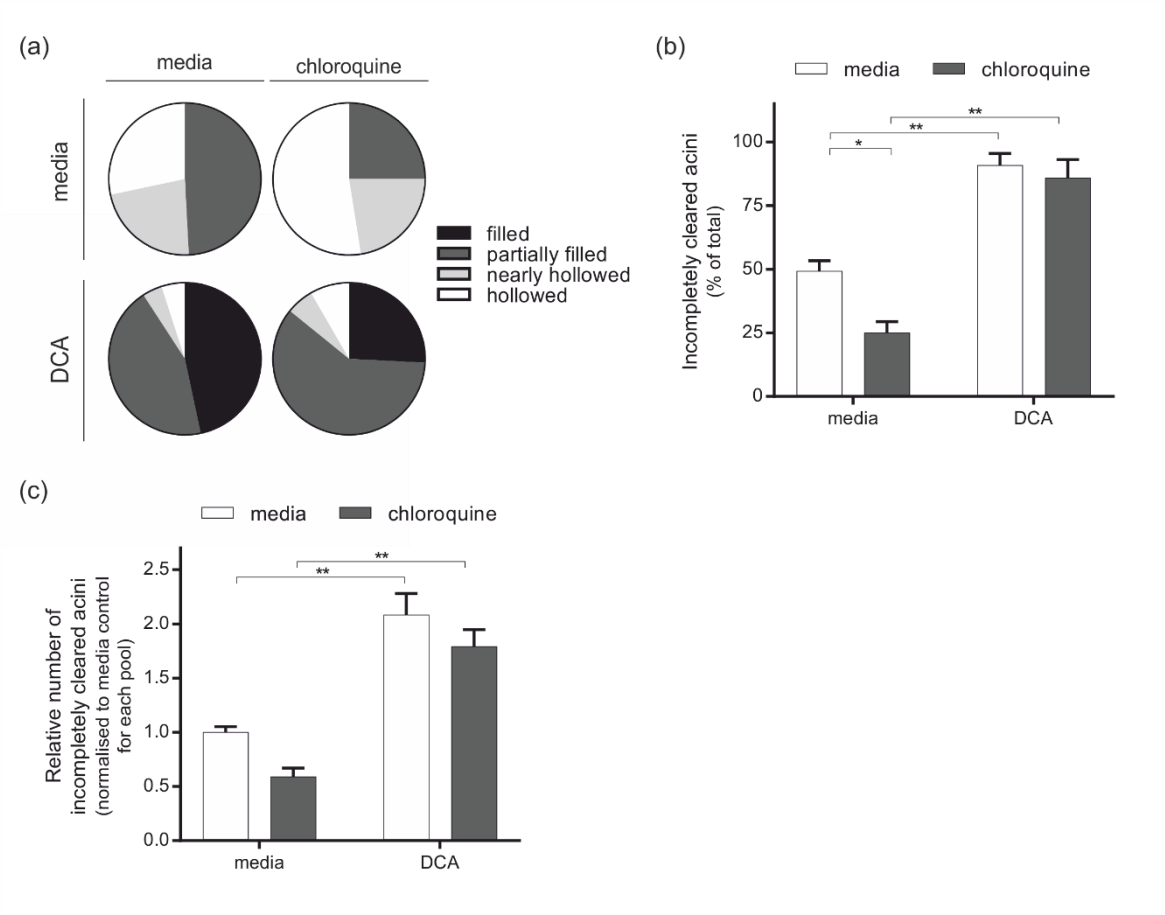

Figure 92 The effect of dichloroacetate and chloroquine on 3D acini

Acini were treated with media or dichloroacetate (DCA) (10 mM) with or without chloroquine (20 µM) every 2 days from day 6 of morphogenesis. At day 12 acini were fixed and stained with DAPI and phalloidin-TRITC. Confocal microscopy was utilised to score luminal status; looking through all focal planes, acini were scored as filled, partially filled, nearly hollowed or completely hollowed. (a) Pie chart representation shows the proportion of acini scoring in each category from a representative experiment. (b) The number of acini scoring as incompletely cleared (filled or partially filled) in (a) was expressed as a percentage of the total acini scored. A minimum of 120 acini were scored for each condition across three replicates. Bar graphs represent the mean ± SEM from three technical repeats. (c) Combined data from three independent experiments shows the relative number of incompletely cleared acini in the presence of chloroquine, DCA or a combination of chloroquine and DCA compared to media control. Within an independent experiment values were adjusted for the total number of incompletely cleared acini. Adjusted values were normalised to the mean adjusted values for media across all three experiments. * $p \leq 0.05$, ** $p \leq 0.01$ as determined by two-way ANOVA with Fisher's LSD test.

Examining the 2D metabolism of HER2 cells in more detail, I examined ATP levels in attached cells and observed no statistically significant increase following HER2 overexpression (Figure 52); this indicates that despite changes in the way HER2 cells utilise energy the overall generation of ATP is unchanged. AlamarBlue® was used to examine cell viability in this setting. The alamarBlue® reagent utilises the natural reducing power of the cell to reduce the active ingredient of alamarBlue® (resazurin) which is a non-fluorescent, cell-permeable molecule. Within the cell resazurin is reduced to a molecule with bright red fluorescence. Resazurin is continuously reduced in metabolically active cells providing a quantitative measurement of viability (Nakayama, Caton et al. 1997). In attached cells HER2 overexpression did not alter alamarBlue® readings suggesting that HER2 does not affect the reducing ability of a cell in this setting.

Using alamarBlue® I showed that detachment reduced cell viability within a 24 h timeframe and this reduction in viability was more enhanced by 48 h. This reduction in viability is consistent with epithelial cells which are dependent on survival signalling from the ECM for their survival and undergo anoikis upon detachment (Meredith, Fazeli et al. 1993, Frisch and Francis 1994). HER2 overexpression resulted in a smaller reduction in viability than puro cells at both 24 h and 48 h detachment. ATP levels were also reduced in detachment and this reduction was higher at 48 h than 24 h, consistent with previous reports (Schafer, Grassian et al. 2009). However at 24 h HER2 overexpression did not statistically significantly alter ATP levels compared to puro in contrast to what was described by Schafer *et al.* in their model (Schafer, Grassian et al. 2009). Nonetheless by 48 h HER2 overexpression resulted in a significant increase in ATP levels in detachment. Taken together this work supports previous findings that HER2 overexpression enhances cell viability and promotes ATP production in ECM-detached cells. This could be a result of increased glycolysis, although I have not tested this in these experiments.

I also used the alamarBlue® reagent to assess the cell viability of 3D acini and showed that HER2-overexpression results in a small, non-statistically significant increase in viability compared to puro (Figure 53). AlamarBlue® is also described by manufacturers as a proliferation assay, and such a use has been reported in the literature (Song, Zhou et al. 2008, Tong, Lu et al. 2010, Zhang, Wu et al. 2011). This use assumes all live cells have the same intracellular reducing power and, in the case of acini, I would expect that the larger, filled HER acini would have more cells than in puro acini resulting in an increased alamarBlue® reading. This is not what I have seen which may indicate that HER2 acini have an attenuated reducing power compared to puro. However, even though the same number of puro and HER2 cells are seeded initially this does not mean that they form acini at the same frequency; without counting the acini numbers in this system it is not possible to state whether HER2 is altering the reducing ability of the cells or there are simply the same number of cells overall leading to a matched ability to reduce resazurin.

Table 11 Summary of the key findings relating to metabolic manipulation of MCF-10A

Pathway	Drug (conc.)	Target	Expected action	Effect of treatment						Notes
				Metab.		2D		3D		
				Gly.	Mito.	Viability	ATP	Clearing	Atypical	
Fatty acid oxidation (FAO)	Etomoxir (100 µM)	CPT-1 (Eistetter and Wolf 1986). Catalyses formation of acyl-carnitine from acyl-coA and carnitine to allow passage of long chain fatty acids into the mitochondria	↓ long chain FAO	↑	↓	(↑)	—	↑	↓	HER2 acini more sensitive to etomoxir treatment than puro.
	Perhexiline (10 µM)	CPT-1 (Kennedy, Unger et al. 1996). Catalyses formation of acyl-carnitine from acyl-coA and carnitine to allow passage of long chain fatty acids into the mitochondria	↓ long chain FAO	—	(↑)	—	—	(↑)	n.e	Perhexiline did not influence metabolism in the same way as etomoxir at 10 µM. In acini I did not observe discolouration of the media as was observed with etomoxir treatment.
	Perhexiline (25 µM)			↑	↑	n.e	n.e	X	n.e	
Glycolysis	2-deoxyglucose (10 mM)	Competes with glucose and glucose-6-phosphate for enzyme binding, competitively inhibiting hexokinase and phosphoglucose isomerase	↓	↓	↓	↓	↓	↓	(↓)	Acini are noticeably smaller – I suggest that acini have undergone cell arrest before the onset of luminal clearing
	Oxamate (25 mM)	Lactate dehydrogenase (Goldberg and Colowick 1965)	↓	↓	↓	—	↓	↑	n.e	
	FX11 (9 µM)	Lactate dehydrogenase (Deck, Royer et al. 1998, Yu, Deck et al. 2001, Le, Cooper et al. 2010)	↓	↑	↑	—	—	↑	n.e	No clear effect on metabolism across dose response – unclear how FX11 is acting
	Iodoacetic acid (12.5 - 50 µM)	Glyceraldehyde-3-phosphate dehydrogenase (Sabri and Ochs 1971, Loreck, Galarraga et al. 1987)	↓	—	—	n.e	n.e	↓	↑	A non-specific, alkylating agent. Higher concentrations of iodoacetic acid interfered with non-glycolytic acidification.

Continued.

Pathway	Drug (conc.)	Target	Expected action	Effect treatment						Notes
				Metab.		2D		3D		
				Gly.	Mito.	Viability	ATP	Clearing	Atypical	
Electron transport	Metformin (50 µM)	Complex I of electron transport chain (Wheaton, Weinberg et al. 2014)	↓ mito.	—	—	n.e	n.e	—	n.e	No apparent metabolic consequences of metformin treatment
	Phenformin	Complex I of electron transport chain (Appleyard, Murray et al. 2012)	↓ mito	—	—	n.e	n.e	n.e	n.e	No apparent metabolic consequences of phenformin treatment
Oxidative stress	Vitamin C (500 µM)	Reactive oxygen species (ROS)	↓ oxidative stress	—	—	—	—	↓	n.e	Findings consistent with hypothesis that ROS drive luminal clearing in acini model
Mito. activity	Dichloroacetate (10 mM)	Pyruvate dehydrogenase (Bonnet, Archer et al. 2007)	↑ mito.	n.e	↑	—	—	↓	↑	Phenotype does not appear to work through induction of autophagy

Table 11 Summary of the key findings relating to metabolic manipulation of MCF-10A

Conc. = concentration; Metab. = metabolism; Gly. = glycolysis; Mito. = mitochondrial; ↑ = increase; (↑) = some evidence of increase;↓ = decrease; — = no clear effects; X = dead; n.e = not examined.

Media composition is important for acinar morphogenesis

The use of glucose- or fructose- adapted cells to study the role of glycolysis in cultured cells is a model that has been well utilised in our laboratory group (Figure 54). Birts *et al.* used this model to show the role of upregulated glycolysis on the CtBP-driven maintenance of mitotic fidelity (Birts, Nijjar et al. 2013). Secondly, unpublished microarray data from glucose- versus fructose-adapted MCF-7 cells demonstrate that glycolysis can have marked effects on the gene expression program in breast cancer, including genes relating to metabolism. I hoped the culture of glucose- or fructose- adapted acini would allow me to examine the long term consequences of metabolic alterations on acinar morphogenesis.

I began by growing cells in glucose- or fructose-DMEM – the media type used within the laboratory for studies of these types. However I observed a highly transformed phenotype when cells were grown in glucose-DMEM (Figure 55). Although it lacked Ham's F12, glucose-DMEM was meant to mimic standard MCF-10A assay media. DMEM lacks a few components provided by Ham's F12 including some amino acids and vitamins and has a higher glucose concentration compared to a DMEM/Ham's F12 mix (25 mM compared to 17.5 mM). To examine whether the transformed phenotype was a consequence of the lack of Ham's F12 I moved to using a glucose-free Biowest DMEM – F12 media to which I was able to add back either glucose or fructose. While 2D cultures grew at a comparable rate acini did not form typically in 3D culture (Figure 56, Figure 57). I had switched to a different supplier of DMEM – F12 media as the standard supplier media was not available in a glucose-free form. While standard MCF-10A media and glucose free Biowest DMEM – F12 media should be directly comparable on a component level I suggest that there is some sort of difference in media preparation that is unfavourable for acinar morphogenesis. The observation that glucose-DMEM acini have a different phenotype to fructose-DMEM acini does, however, highlights the importance of glycolytic metabolism in acinar morphogenesis.

Experimental rationale for metabolic inhibitor investigations

In this chapter, I report the use of a panel of metabolic inhibitors (Table 11) to examine the role of metabolism in acinar morphogenesis. I was interested in the role of metabolism in luminal clearing and therefore treated acini from day 6 of morphogenesis. This time point was selected because it is a late enough time point to allow formation of the acini, as I did not want to interfere with acini formation itself, but is before the onset of luminal clearing. By using a panel of inhibitors that targeted different metabolic pathways, I hoped that findings relating to each pathway would complement each other and allow me to build up a picture of how the different metabolic pathways cooperate to influence luminal clearing in MCF-10A acini. The following drugs

were tested simultaneously; etomoxir, 2-deoxyglucose, oxamate, metformin, Vitamin C and dichloroacetate. Two glycolytic inhibitors (2-deoxyglucose and oxamate) were included because they target the first and last stages of the pathway respectively, which could have different phenotypic consequences. Perhexiline and FX11 were added to the panel following analysis of etomoxir and oxamate treated acini respectively, with the aim to confirm my findings relating to inhibition of CPT-1 (etomoxir and perhexiline) and lactate dehydrogenase (oxamate, FX11). Phenformin was added to the panel when I was unable to show any metabolic consequences of metformin treatment, to attempt to examine electron transport chain inhibition in the acini model. As glycolytic inhibition using different enzyme targets was having the opposite effect on acinar morphogenesis (2-deoxyglucose versus oxamate), I added a fourth drug targeting glycolysis, iodoacetic acid, to try and build a clearer picture of how glycolysis influences acinar morphogenesis.

Fatty acid oxidation provides a survival advantage to extracellular matrix-detached cells in MCF-10A acini

CPT-1 is upregulated in a variety of tumours including the breast (Qu, Zeng et al. 2016) where its expression has been linked to tumorigenic properties including proliferation (Gatza, Silva et al. 2014), survival (Pucci, Zonetti et al. 2016) and resistance to metabolic stress (Zaugg, Yao et al. 2011). Targeting of this rate-limiting step of FAO (Drynan, Quant et al. 1996) through inhibitors such as etomoxir and perhexiline (Eistetter and Wolf 1986, Kennedy, Unger et al. 1996) can attenuate this pathway. I have used these inhibitors to examine the role of FAO in luminal clearing within the MCF-10A acini model. CPT-1 inhibition prevents the transport of long chain fatty acid molecules from the cytoplasm to the mitochondrial matrix; acyl-coA molecules of 10 carbons or less are still able to cross the inner mitochondrial membrane so these inhibitors have no effect on oxidation of short chain fatty acids.

Etomoxir

Metabolically etomoxir inhibited mitochondrial ATP production in a dose-dependent manner (Figure 58). This is to be expected as the products of FAO feed into the electron transport chain. Other metabolic pathways such as glycolysis and the citric acid cycle can still contribute to mitochondrial ATP production; however I observed high levels of inhibition of mitochondrial ATP production following etomoxir treatment indicating that MCF-10A cells utilise FAO for the majority of their mitochondrial ATP production. In addition to inhibition of mitochondrial activity I also observed an increase in glycolysis which plateaus at higher etomoxir concentrations. This upregulation of glycolysis is likely to be a compensatory mechanism in order to maintain sufficient ATP levels for cellular function in the presence of FAO inhibition. The plateau probably occurs

because cells hit their glycolytic capacity – to test this I would need to examine ECAR following an oligomycin injection (to completely inhibit mitochondrial ATP synthase activity) to determine the maximal glycolytic rate.

In 2D culture etomoxir leads to a small, statistically non-significant reduction in ATP levels except in attached HER2 cells following 48 h treatment where ATP levels were increased (Figure 59). In this setting cells were able to maintain cellular ATP at levels similar to controls despite FAO inhibition. This suggests that the upregulation of glycolysis upon etomoxir treatment is able to maintain ATP production at levels comparable to controls. Examining viability in an alarmarBlue® assay, etomoxir led to a small increase in viability which reached statistical significance in certain conditions. This indicates that etomoxir is not having a negative impact on viability in 2D culture.

In 3D etomoxir pushed puro and HER2 acini towards a less transformed phenotype with more acini presenting with a hollowed phenotype (Figure 60). This indicates that FAO can promote cell survival in luminal, ECM-detached MCF-10A cells supporting findings from Carracedo *et al.* who show that tumour-suppressor driven luminal filling is FAO-dependent (Carracedo, Weiss et al. 2012). Etomoxir treatment of HER2 acini reversed HER2-driven filling to an extent where HER2 acini were more cleared than puro controls, implicating a strong dependence of HER2 cells on FAO for luminal cell survival. HER2-overexpression has been shown to reduce FAO in both attached and detached MCF-10A but residual FAO still contributes significantly to ATP production in detached cells (Schafer, Grassian et al. 2009). The lower basal levels of FAO in HER2-overexpressing cells may explain the increased dependence on this pathway.

In addition to driving luminal clearing etomoxir treatment also attenuated the HER2-driven branching, atypical structure (Figure 61). The observation that etomoxir treatment leads to the formation of spherical HER2 acini implicates FAO in the development of these atypical structures.

Using the alamarBlue® reagent to examine cell viability in 3D acini following etomoxir treatment, I observed a statistically significant increase in viability in puro acini compared to media-treated cells and no difference in viability in HER2 acini (Figure 62). In etomoxir treated acini, where luminal cell death is enhanced, I would expect to see a reduction in alamarBlue® readings if this reagent is giving a quantitative reading of the number of cells. This would be particularly pronounced for HER2 acini where there was an average 0.85-fold reduction in the number of filled acini. On the assumption that acini treated with etomoxir have less cells in their acini the observation that viability is not altered when examined using alamarBlue® suggests that etomoxir treatment is enhancing the reducing ability of cells so that, even though there is a reduction in the number of cells, the level of conversion of resazurin to its reduced, fluorescent form is still comparable to acini treated with media alone.

Perhexiline

I hoped to confirm findings relating to the role of FAO in acinar morphogenesis by using a second CPT-1 inhibitor, perhexiline. Low concentrations of perhexiline were found to increase mitochondrial activity (Figure 63); this is in contrast to etomoxir which inhibited mitochondrial activity across all concentrations tested. It is possible that these concentrations of perhexiline are inhibiting FAO but a compensatory upregulation of other metabolic pathways which can feed NADH and $FADH_2$ into the electron transport chain lead to an upregulation of mitochondrial activity. At higher concentrations of perhexiline inhibition of mitochondrial activity was observed but these concentrations also interfered with values following 2-deoxyglucose, oligomycin or antimycinA and rotenone suggesting the inhibitor is interfering with non-glycolytic acidification, proton leak or non-mitochondrial respiration respectively and making it an undesirable agent at these concentrations due to unintentional effects.

Despite not being able to find a concentration of perhexiline that mimicked the metabolic activity of 100 µM etomoxir I decided to pursue the use of perhexiline for FAO inhibition in the acini model. Examining the effect of 10 µM perhexiline on 2D cell viability in attached and detached conditions, perhexiline had no clear effects on viability when examined using an alamarBlue® assay (Figure 64). Examining ATP levels there was a trend towards a decrease in ATP levels in the presence of perhexiline although statistical significance was not reached. Perhexiline is behaving similarly to etomoxir in this experimental setting. However in 3D 10 µM perhexiline treatment did not have the same effect on acini as 100 µM etomoxir (Figure 65). Perhexiline treatment led to a small reduction in the percentage of puro acini scoring as incompletely cleared within independent experiments which only reached statistical significance when data, normalised for experimental drift in luminal filling, was combined from three independent experiments. In contrast perhexiline had no effect on HER2 acini.

The effects of perhexiline on acini may not be comparable to the effects of etomoxir because 10 µM perhexiline was not seen to inhibit OCR while 100 µM etomoxir significantly reduced mitochondrial activity (Figure 63). In addition to this data from the short, 2D culture setting of the Seahorse assay 100 µM etomoxir treatment of 3D acini led to a discolouration of the media following culture at 37 °C in a CO_2 humidified chamber, with media gaining a strong yellow colour over a period of 2 days. Yellow media is consistent with acidification of the media and is indicative of a high glycolytic rate (which produces free protons resulting in acidification). In comparison 10 µM perhexiline led to a minimal change in media colour over the same period, suggesting that perhexiline is not having the same effects as etomoxir on cell metabolism at the concentration tested. Taken together these observations indicate that 10 µM perhexiline is not a high enough

concentration to induce the same level of CPT-1 inhibition that is achieved with 100 μM etomoxir; I did not find a concentration of perhexiline which had the same activity as etomoxir for a direct comparison. While I did try to increase the concentration of perhexiline used in 3D I found that 25 μM perhexiline killed acini.

Glycolytic inhibition influences acinar morphogenesis

Cancer cells upregulate glycolysis to facilitate biomass generation in order to meet the increased demand for growth and proliferation (Vander Heiden, Cantley et al. 2009). Exploitation of this effect has already been utilised in the clinic for diagnostic purposes through metabolic positron emission tomography imaging (Zhu, Lee et al. 2011, Zhu, Marcus et al. 2012) highlighting the potential of this pathway as a target for anti-cancer therapeutics. Through inhibition of glycolysis it is proposed cancer cells will be forced to switch back to mitochondrial metabolism leading to ROS generation. Having already shown that modification of glycolysis by use of glucose- and fructose- adapted MCF-10A can alter morphogenesis (Figure 55) I sought to examine the effect of glycolytic inhibitors in my model of the healthy and transformed breast. Some of these inhibitors are receiving attention as potential anti-cancer therapeutic agents.

Based on data from Schafer *et al.* who show that HER2-driven rescue of the ATP defect observed upon detachment is dependent on enhanced glucose uptake (Schafer, Grassian et al. 2009) I hypothesised that glycolytic inhibitors would drive luminal clearing in HER2 acini. As metabolic pathways exist in tight equilibrium with each other the flux of metabolism into other pathways can be altered following glycolytic inhibition. Examining multiple inhibitors targeting different parts of the glycolytic pathway helps to minimise the chance that any phenotype of inhibition is a consequence of the intended target and not an indirect effect of another metabolic pathway being altered.

2-deoxyglucose

Investigations began with 2-deoxyglucose, a competitive inhibitor of the first two steps of glycolysis. The metabolic consequences of this compound are well defined, and is used extensively in Seahorse assays at high concentrations (100 mM) to fully inhibit glycolysis. In the Seahorse assay I saw a dose-dependent inhibition of glycolysis in the presence of 2-deoxyglucose, as expected, and to a lesser extent mitochondrial activity (Figure 66). As previously highlighted the Seahorse metabolic assay is not directly comparable to 3D assays because of the length of exposure to the drug. This is particularly relevant for 2-deoxyglucose where the drug gets trapped intracellularly as it is phosphorylated, leading to the intracellular concentration of the inhibitor accumulating over time. It is therefore very difficult to predict the extent of inhibition on

glycolysis for this inhibitor. I selected 10 mM 2-dexoyglucose, the concentration shown to reverse HER2-driven rescue of ATP levels in detached conditions (Schafer, Grassian et al. 2009).

In 2D assay 2-deoxyglucose significantly inhibits both viability and ATP levels across all conditions examined (Figure 67). The inhibition of ATP levels at 24 h in HER2 detached cells treated with 2-deoxyglucose is consistent with findings from Schafer *et al.* (Schafer, Grassian et al. 2009). At 48 h puro cells appear more sensitive to 2-deoxyglucose than HER2 cells with a higher fold reduction in viability and ATP; this suggests that puro cells are more dependent on glycolysis for survival and ATP production.

In 3D 2-deoxyglucose led to an increase in the number of incompletely cleared puro acini with the majority of acini failing to undergo luminal clearing (Figure 68). HER2 acini treated with 2-deoxyglucose scored similarly to controls, however in both puro and HER2 acini the size of acini appeared to be reduced. This was particularly prominent in HER2 acini where acini were smaller and spherical compared to the typically large, branching structures (Figure 69b). In the 3D alamarBlue® assay 2-deoxyglucose led to a significant reduction in viability (Figure 69a). This is consistent with a reduction in cell number and/or cell size which would fit with the smaller acini structures.

In contrast to my proposed hypothesis that glycolysis inhibition will inhibit cell survival in detached conditions, in this setting I are seeing that 2-deoxyglucose is promoting transformation in my model of the healthy breast. Taking the viability data and the observations around acini size together I propose that 2-deoxyglucose is leading to cell arrest in this setting. Instead of driving luminal cell survival cells appear to be growth arresting before the onset of luminal clearing and are not proceeding through the morphogenesis program at all.

Lactate dehydrogenase inhibitors - Oxamate

Inhibition of lactate dehydrogenase by the pyruvate analogue oxamate had the expected consequences on glycolytic metabolism, inhibiting ECAR in a dose-dependent manner (Figure 70). I also saw, to a lesser extent, an inhibition on mitochondrial activity. Oxamate is a non-specific inhibitor and has been shown to also inhibit pyruvate entry into the mitochondria (Halestrap 1975, Martin-Requero, Ayuso et al. 1986), aspartate aminotransferase (Thornburg, Nelson et al. 2008) and pyruvate carboxylation (required for gluconeogenesis) (Martin-Requero, Ayuso et al. 1986, Martin-Requero, Ayuso et al. 1986). Aspartate aminotransferase catalyses the conversion of oxaloacetate and glutamate to aspartate and α-ketoglutarate and is required to shuttle electrons from glycolysis-derived cytoplasmic NADH to mitochondrial NADH (Cederbaum, Lieber et al. 1973, Greenhouse and Lehninger 1976). The off-target inhibition of transport of pyruvate and NADH

into the mitochondria are most likely to explain the inhibition of mitochondrial activity observed in the presence of oxamate.

In 2D oxamate had no statistically significant effects on cell viability but I did observe a statistically significant inhibition of ATP levels (Figure 71). An inhibition of ATP in 2D culture is consistent with the inhibition of glycolysis and mitochondrial metabolism seen in the Seahorse assay. Over the length of this assay (48 h) oxamate is not influencing the viability of cells suggesting that the metabolic consequences of 10 mM oxamate treatment are tolerated at this dose.

In acini oxamate treatment results in a less transformed phenotype, with a statistically significant reduction in the number of incompletely cleared acini in both puro and HER2 (Figure 72). This data supports findings from 2D culture where glucose uptake and utilisation is shown to be important for HER2-driven rescue of ATP following detachment (Schafer, Grassian et al. 2009). In 3D I have shown that glycolysis inhibition in HER2 acini, which inhibited ATP production in 2D, attenuates HER2-driven filling. This is the first time that the role of glycolysis in ECM-detachment has been examined directly in MCF-10A acini. This reduction in luminal clearing did not correlate with a reduction in alamarBlue® readings (Figure 73), contrary to expectations if alamarBlue® readings are assumed to be a quantitative read out of cell number.

Lactate dehydrogenase inhibitors – FX11

Due to off target effects of oxamate, I cannot conclude that the effect of this inhibitor on acinar transformation is a direct consequence of lactate dehydrogenase inhibition. To provide evidence to support or exclude the hypothesis that lactate dehydrogenase inhibition may promote luminal clearing, I sought to examine the effect of the inhibitor FX11 on acini. This inhibitor is described in the literature as a specific inhibitor of lactate dehydrogenase (Deck, Royer et al. 1998, Yu, Deck et al. 2001, Le, Cooper et al. 2010). When I examined this drug in the Seahorse analyser I saw some variable and unexpected consequences of FX11 on cellular metabolism (Figure 74). At 9 µM FX11 I saw an increase in ECAR in both puro and HER2 cells, even though this is the concentration used by Le *et al.* to inhibit glycolysis in P493 human lymphoma B cells (Le, Cooper et al. 2010). An upregulation of ECAR is inconsistent with inhibition of lactate dehydrogenase which would reduce the production of free protons. In addition at concentrations of 2.25-9 µM FX11 significantly increased OCR compared to media controls following oligomycin injection. This suggests that FX11 is interfering with proton leak causing basal respiration that is not coupled to ATP production; this is often a sign of mitochondrial damage. Nevertheless I still opted to pursue the use of FX11 in acini to find further evidence to support the finding that lactate dehydrogenase inhibition through oxamate treatment promotes anti-tumorigenic properties.

In the 2D setting 9 µM FX11 had no effect on alamarBlue® reagents over a 48 h period (Figure 75). This suggests that if FX11 is inducing mitochondrial damage this is not sufficient to alter viability over a 48 h period. In acini FX11 had the same phenotypic consequences as oxamate pushing acini towards a less transformed phenotype (Figure 76). In puro acini treatment resulted in a 0.28-fold and 0.25-fold reduction in incompletely cleared acini following oxamate and FX11 respectively. HER2 acini were less sensitive to the inhibitors with a 0.21-fold and 0.18-fold reduction following oxamate and FX11. Although both oxamate and FX11 appear to have non-specific effects on metabolism the similarity in 3D phenotypes following treatment implicates the common target, lactate dehydrogenase, is driving this phenotype.

Iodoacetic acid

Iodoacetic acid has been used to study the effect of GAPDH inhibition on cell phenotype (Sabri and Ochs 1971, Loreck, Galarraga et al. 1987, Bickler and Kelleher 1992, Gemba, Oshima et al. 1994, Solem, Koebmann et al. 2003, Schmidt and Dringen 2009) but in my setting I did not see ECAR inhibition without also seeing inhibition of ECAR following 2-deoxyglucose injection (Figure 77); this is suggestive that iodoacetic acid is also interfering with non-glycolytic acidification. While lower concentrations of iodoacetic acid did not interfere with non-glycolytic acidification they also had no inhibition on glycolysis. However, as the short term experiment does not accurately mimic long term exposure to a drug I decided to examine the effect of 12.5 µM, 25 µM and 50 µM iodoacetic acid. At low concentrations iodoacetic acid induced luminal filling in control acini while not affecting HER2 acini (Figure 78) and at higher concentrations induced acini death. As an alkylating agent iodoacetic acid interacts with any exposed cysteine residues making it highly unspecific. Over a six day exposure to iodoacetic acid I might predict that iodoacetic acid would have had time to interact with numerous cysteine residues in cellular proteins which would have unpredictable consequences.

Interfering with mitochondrial respiration had variable consequences on acinar morphogenesis depending on the target of inhibition

Metformin and phenformin

Metformin and phenformin are biguanides which inhibit complex I of the electron transport chain and interfere with mitochondrial membrane potential leading to an inhibition of oxygen consumption (Sogame, Kitamura et al. 2009, Bridges, Jones et al. 2014, Drahota, Palenickova et al. 2014, Miskimins, Ahn et al. 2014, Wheaton, Weinberg et al. 2014). This would be proposed to inhibit oxidative phosphorylation however in the Seahorse assay I found no evidence of OCR inhibition following treatment of metformin or phenformin (Figure 79, Figure 81). This could be a

consequence of the short term exposure of the drugs and their inability to enter the cell over the duration of the assay, even though phenformin is more lipophilic than metformin. While the Seahorse assay is very short term I did test 50 μM metformin on 3D acini (Figure 80); this concentration has phenotypic consequences in MCF-7 cells. With a 6 day exposure to metformin acini were the same as media treated controls. Metformin and phenformin have been used on a derivative of the MCF-10A line where they have phenotypic consequences over a 24 h period (Janzer, German et al. 2014) indicating that MCF-10A cells are sensitive to metformin. I did not see a change in luminal status in the presence of 50 μM metformin, suggesting metformin does not influence cell survival following detachment when examined in this setting.

Antioxidant treatment – Vitamin C

ROS are present exclusively in centrally localised cells of a developing acini and, when combined with Bcl-2 overexpression, ROS neutralisation leads to increased luminal filling (Schafer, Grassian et al. 2009, Davison, Durbin et al. 2013). Vitamin C is a naturally occurring antioxidant which typically reacts with and neutralises ROS and was used to further examine the role of ROS in MCF-10A acini.

Metabolically Vitamin C significantly altered both ECAR and OCR (Figure 82). ECAR was decreased in a dose-dependent manner but a similar decrease in ECAR following 2-deoxyglucose was also seen suggesting that the effects are from non-glycolytic alterations. Similarly OCR was increased in the presence of Vitamin C but so were readings following oligomycin and antimycinA and rotenone suggesting that these effects are from non-mitochondrial O_2 consumption.

In the 2D viability assay Vitamin C had no real effect on alamarBlue® readings or ATP levels (Figure 83). However in 3D Vitamin C treatment statistically significantly increased luminal filling in puro controls (Figure 84). This suggests that ROS are having a role in luminal clearing in puro acini which can be attenuated through antioxidant treatment, supporting previous findings (Schafer, Grassian et al. 2009, Davison, Durbin et al. 2013). Bim-regulated anoikis is also driving clearing within the MCF-10A setting (Reginato, Mills et al. 2005) and at the single day 12 time point I am unable to conclude that Vitamin C is sufficient to fully overcome luminal filling; it may just be delaying the onset of clearing. In the HER2 model Vitamin C had no statistically significant effects on luminal filling although HER2 acini are highly filled already.

Dichloroacetate promotes a highly transformed phenotype in control acini

Dichloroacetate, an indirect activator of pyruvate dehydrogenase, forces pyruvate back into the mitochondria (Bonnet, Archer et al. 2007). Through reactivation of the citric acid cycle, and downstream the electron transport chain, it is hypothesised that dichloroacetate will induce

cancer cell death through cellular stress due to enhanced ROS production as a consequence of increased mitochondrial activity. I hypothesised that, in my model, activation of pyruvate dehydrogenase would induce luminal cell death in HER2 acini by reversing the HER2 driven attenuation of ROS.

Metabolically dichloroacetate increases mitochondrial activity in a dose-dependent manner, as expected, but this plateaus at higher dichloroacetate concentrations (Figure 85). The plateau could be because dichloroacetate has reached its maximal inhibition of pyruvate dehydrogenase kinase or, alternatively, because cells have reached their maximal mitochondrial capacity. An injection of FCCP following dichloroacetate can be used to confirm that cells have met their mitochondrial capacity. Dichloroacetate is an acid and, while the drug was prepared at pH 7.4 prior to injection, its injection altered the cellular pH of wells (Figure 86); this makes it difficult to assess the effect of dichloroacetate on glycolysis as the change in pH upon dichloroacetate injection will have altered ECAR. However the changes in pH are still within a viable cell range so I can be confident that data relating to OCR is a reflection of the drug's activity and not the change in pH.

While in 2D dichloroacetate had no statistically significant effects on cell viability or ATP levels in puro and HER2 cells in detachment (Figure 87), I showed that dichloroacetate had highly statistically significant effects on the survival of ECM-detached cells within the MCF-10A model (Figure 88, Figure 89). Puro cells were transformed to a highly filled phenotype with 86% of acini scoring as incompletely cleared at day 12 of morphogenesis (Figure 88); this transformation was not a temporal delay in the onset of luminal clearing as puro acini still scored as incompletely cleared at day 16 (Figure 89). Dichloroacetate has had the opposite effect to our proposed hypothesis and has promoted cell survival in ECM-detached luminal cells. In the HER2 acini dichloroacetate had limited effects, proposed to be because they are already highly transformed and display a high level of filling in the absence of inhibitor.

Examining dichloroacetate treated acini in the presence of alamarBlue® inhibitor treatment leads to a non-statistically significant increase in the relative cell viability (Figure 91). As discussed previously this result is not consistent if it is assumed that alamarBlue® gives a quantitative read out of cell viability; in this setting I would expect the larger, branching, filled structures observed following dichloroacetate treatment in puro acini (Figure 90) to display a substantial increase in alamarBlue® readings. Taken together with alamarBlue® data from 3D acini treated with etomoxir (Figure 62) and oxamate (Figure 73) I propose that alamarBlue® is not a good read out of cell number in this setting. Unlike as described for puro versus HER2 acini where I do not know if the number of acini between puro and HER2 is different, here the acini are seeded in the absence of

inhibitor so similar readings from within an individual pooled population cannot be a result of there being a reduced number of acini forming initially. The unexpected result could be because inhibitors interfere with the reducing ability of a cell or, alternatively, the assay does not have an appropriate level of sensitivity within the setting examined.

As stated dichloroacetate treatment resulted in large, branching acini in the puro model (Figure 90). Similarly as described for luminal clearing dichloroacetate did not increase the percentage of HER2 acini scoring as atypical, which already score highly for this phenotype, but they did appear increased in size. This data suggests that dichloroacetate treatment can interfere with the acinar morphogenesis program resulting in a different morphology. Taken together with the finding that etomoxir can reverse the HER2-driven branching phenotype this implicates metabolism in the mechanism driving acinar morphology. While the atypical structure has been widely reported in the literature following HER2-overexpression in MCF-10A (Muthuswamy, Li et al. 2001, Debnath, Mills et al. 2002, Reginato, Mills et al. 2005), and the gross atypical morphology marks a more transformed phenotype, little is known about the mechanism driving the changes in morphology. Kenny *et al.* characterised atypical morphologies as having reduced cell-cell adhesions (Kenny, Lee et al. 2007). Consistent with this observation a downregulation of E-cadherin was observed in Bag-1L-overexpressing Bag-1L/A and Bag-1L/B stable clones with the extent of downregulation inversely correlating with the number of atypical acini. In addition HER2 overexpression has also been shown to lead to E-cadherin downregulation in MCF-10A (Kim, Yong et al. 2009). The observation that metabolic inhibition can alter acinar morphology shows that metabolism influences cellular signalling and suggests that its manipulation can influence morphology through signalling which influences pathways such as cell-cell adhesion.

Dichloroacetate does not work through autophagy induction

I was interested in examining how dichloroacetate is driving luminal cell survival and I began mechanistic investigations by looking at autophagy. This was based on findings that dichloroacetate could induce protective autophagy in colorectal cells (Gong, Peng et al. 2013, Lin, Hill et al. 2014), leading me to hypothesis that dichloroacetate could induce protective autophagy in ECM-detached luminal MCF-10A cells promoting their survival. Autophagy occurs in luminal MCF-10A cells (Debnath, Mills et al. 2002) and has been shown to promote luminal cell survival which is reversible by autophagy inhibition (Fung, Lock et al. 2008). I used chloroquine treatment of acini to examine the role of autophagy in my model of the healthy breast and in dichloroacetate-induced luminal filling.

Puro acini treated with chloroquine displayed a reduction in luminal filling (Figure 92), consistent with previous findings (Fung, Lock et al. 2008), but this did not reach statistical significance when

combining data from three independent experiments. When dichloroacetate treatment was combined with chloroquine there were no statistically significant effects on luminal clearing compared to dichloroacetate treatment alone. The observation that dichloroacetate induces cell survival in the presence of autophagy inhibition indicates that dicholoroacetate promotes transformation in a mechanism that is independent of autophagy. In addition chloroquine treatment in the presence of dichloroacetate results in a smaller fold-decrease in incompletely cleared acini compared to in the presence of media alone. This suggests that dichloroacetate is able to protect from cell death upon detachment even in the presence of autophagy inhibition. Autophagy inhibitors are not completely specific and I therefore tested a second autophagy inhibitor, 3-methyladenine, to confirm my results. This inhibitor targets a different part of autophagy inhibiting autophagosome formation (through PI3K inhibition) while chloroquine impairs lysosomal acidification (preventing fusion between the autophagosome and the lysosome). However the concentration of DMSO required to use 3-methyladenine at an appropriate concentration led to acini cell death, so I could not use this inhibitor in this setting.

Conclusion

Metabolism has an important role in the acinar morphogenesis program of MCF-10A acini. I have been unable to show clear metabolic consequences of treatment with the inhibitors metformin, phenformin and iodoacetic acid and the consequences of perhexiline and FX11 are not well defined. However I have shown clear, dose-dependent metabolic responses to 2-deoxyglucose, etomoxir, oxamate, Vitamin C and dichloroacetate treatment. These inhibitors also had clear effects on acinar morphogenesis. Inhibition of fatty acid oxidation (etomoxir) or glycolysis (oxamate) can reverse HER2-driven luminal filling while antioxidant treatment (Vitamin C) can attenuate clearing in non-transformed controls. Additionally, contrary to expectations, dichloroacetate treatment of non-transformed controls was shown to induce a highly transformed phenotype which included a branching, atypical morphology. While metabolic interference has previously been shown to interfere with cell survival in ECM-detachment, this data expands on findings and is the first time that metabolic manipulation has been reported to also influence acinar morphology.

Chapter 6: The role of metabolism in HMEC acinar morphogenesis

Work presented in Chapter 5: 'The role of metabolism in MCF-10A acinar morphogenesis' highlighted a role for metabolism in MCF-10A acinar morphogenesis. Manipulation of metabolism through inhibitors was able to influence cell survival in ECM-detached luminal cells and, in some cases, alter acinar morphology. I felt it important to explore these findings in a second experimental model.

Human mammary epithelial cells (HMEC) are isolated from healthy, adult female breast tissue and can be cultured in 3D where they form acini structures. I sought to use this setting to further examine some of our most interesting findings relating to etomoxir, 2-deoxyglucose, oxamate and dichloroacetate treatment.

6.1 HMEC cells can be cultured on top of Matrigel® to form 3D acini

For these investigations I aimed to set up a system where I could culture HMEC in 3D in an analogous way to my MCF-10A acini. HMEC were seeded in chamber slides onto a layer of polymerised Matrigel® in growth medium (MEGM™ BulletKit™) supplemented with 2% Matrigel®. Representative images of the time course of HMEC acinar morphogenesis show that HMEC successfully form acini in these conditions (Figure 93a). At day two of morphogenesis no clear acini structures were identifiable (data not shown) but by day four spherical acini had formed. Between day four and day eight these structure grew in size, remaining spherical and of a similar size up to day 14 of morphogenesis. Acini underwent luminal clearing as they progressed through morphogenesis moving from a filled to hollowed phenotype (Figure 93b,c). At day four of morphogenesis 99% of acini scored as incompletely cleared which was reduced to 11% at day 14. The majority of luminal clearing occured between day six and 10 of morphogenesis with 67% of acini progressing out of the incompletely cleared category over this time period. I had successfully set up and characterised a system for growing HMEC acini which could be used for investigations.

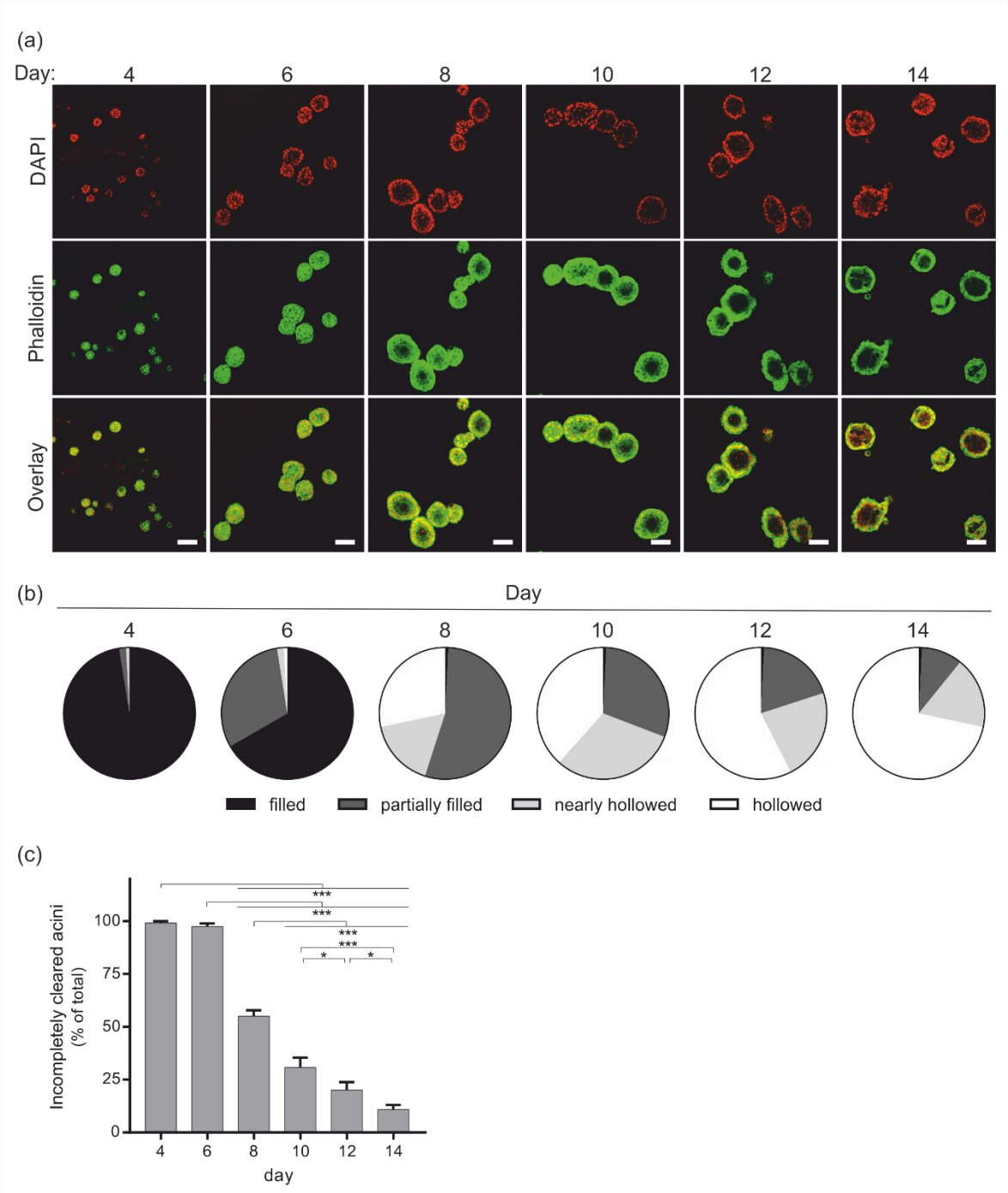

Figure 93 Time course of HMEC acinar morphogenesis

All HMEC acini were seeded together (day 0), fixed at the indicated time point and stained with DAPI (red) and phalloidin-TRITC (green). (a) Representative confocal immunofluorescence images show the centre of HMEC acini at the indicated time point of morphogenesis; scale bars show 100 µm. (b) Confocal microscopy was utilised to score luminal status. Looking through all focal planes, acini were scored as filled, partially filled, nearly hollowed or completely hollowed. Pie chart representation shows the proportions of acini scoring in each category at the indicated time point. (c) The number of acini scoring as incompletely cleared (filled or partially filled) was expressed as a percentage of the total acini scored. Data are from an independent experiment with three technical repeats. Bar graphs represent the mean ± SEM. A minimum of 120 acini were scored for each condition across three chambers. * $p \leq 0.05$, *** $p \leq 0.001$ as determined by one-way ANOVA with Fisher's LSD test.

6.2 Dichloroacetate does not affect HMEC acinar morphogenesis

Parental HMEC undergo high levels of luminal clearing across a small window of time in the absence of an inhibitor which could make identification of any acceleration of the luminal clearing program difficult; I therefore begun investigations by examining the effect of dichloroacetate, an inhibitor which induced luminal filling in non-transformed MCF-10A acini.

The effect of dichloroacetate on the luminal clearing and morphology of HMEC acini was examined using the same drug concentrations and treatment time points from the MCF-10A work (day 12 of morphogenesis). In this setting dichloroacetate had no statistically significant effects on the morphogenesis of acini (Figure 94). Within a single experiment dichloroacetate-treated acini scored as 18% incompletely cleared compared to 17% in media alone (Figure 94b). When combining data from three independent experiments dichloroacetate was shown to induce a 0.19-fold reduction in the number of incompletely cleared acini although this did not reach statistical significance (Figure 94c). Acini presented with a spherical structure upon dichloroacetate treatment with 7% of dichloroacetate-treated acini scoring as atypical compared to 17% of media only controls, although this reduction in atypical acini was not statistically significant (Figure 94e).

6.3 Generation and characterisation of HMEC puro and HMEC HER2

To examine the metabolic inhibitors which accelerated luminal clearing in MCF-10A within the HMEC acini model I generated HMEC with a delayed or attenuated luminal clearing program. Based on findings from MCF-10A (Muthuswamy, Li et al. 2001, Pradeep, Zeisel et al. 2012, Papadakis, Barker et al. 2016) I hypothesised that HER2 overexpression in HMEC would generate filled acinar structures.

6.3.1 Generation of HER2-overexpressing HMEC

A pooled population of HMEC overexpressing HER2 (denoted HMEC HER2) were generated by retroviral infection using a pBABEpuro-ErbB2 vector. A pooled clone using an empty pBABEpuro construct was generated as an experimental control (denoted HMEC puro). HER2 overexpression was confirmed by immunofluorescence (Figure 95). HER2 protein was not detected in HMEC puro cells under these experimental conditions. Across the HER2 population HER2 staining is positive in the nucleus and cytoplasm with more intense staining observed at the periphery of cells.

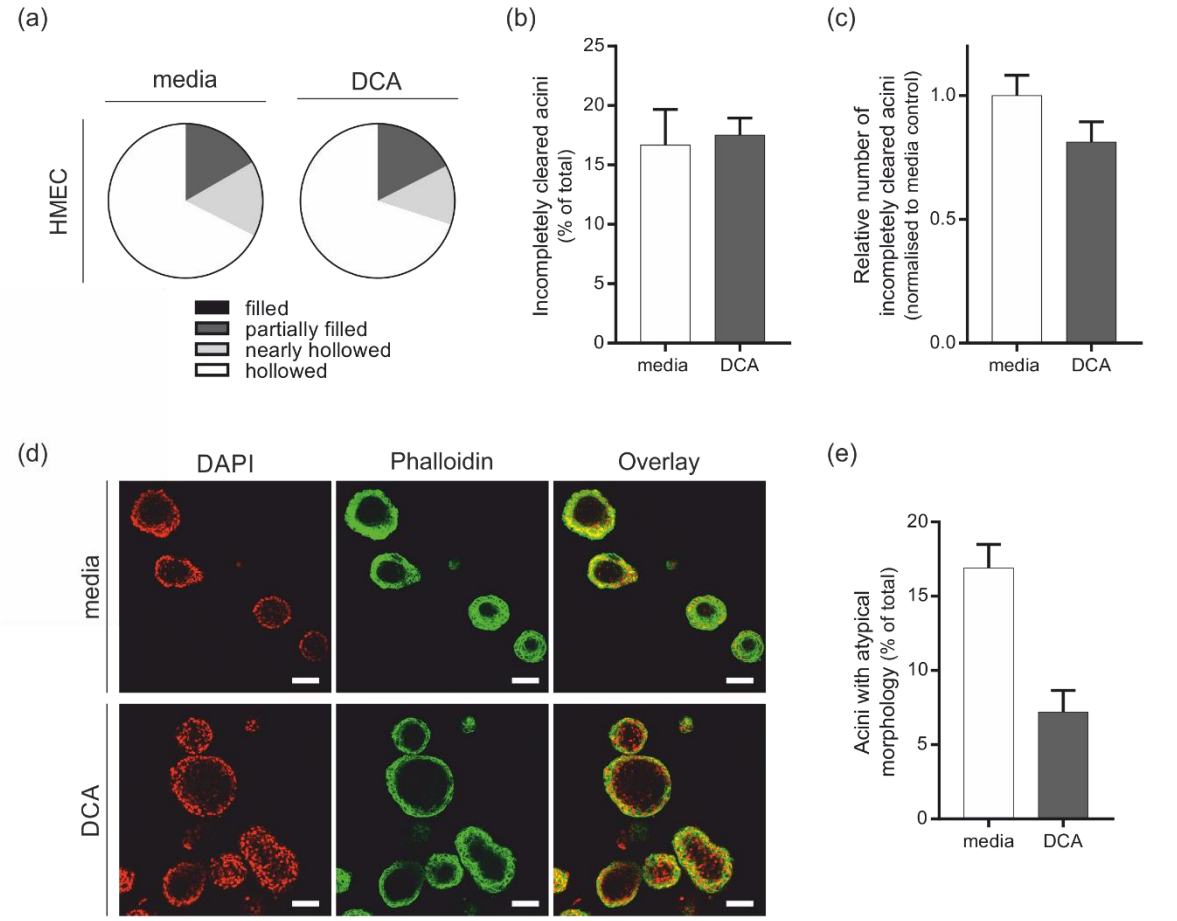

Figure 94 The effect of dichloroacetate on HMEC acini

HMEC acini were treated with media or dichloroacetate (DCA) (10 mM) every 2 days from day 6 of morphogenesis. At day 12 acini were fixed and stained with DAPI (red) and phalloidin-TRITC (green) (a-d) or fixed directly to minimise acini loss in wash steps (2% PFA final concentration) and mounted (e). (a) Confocal microscopy was utilised to score luminal status; looking through all focal planes, acini were scored as filled, partially filled, nearly hollowed or completely hollowed. Pie chart representation shows the proportion of acini scoring in each category from a representative experiment. (b) The number of acini scoring as incompletely cleared (filled or partially filled) in (a) was expressed as a percentage of the total acini scored. Bar graphs represent the mean ± SEM from three technical repeats; a minimum of 120 acini were scored for each condition across three replicates. (c) Combined data from three independent experiments shows the relative number of incompletely cleared acini in the presence of DCA compared to media controls. Within an independent experiment values were adjusted for the total number of incompletely cleared acini for each pool. Adjusted values were normalised to the mean adjusted values for media across all three experiments. (d) Representative confocal immunofluorescence images show the centre of HMEC acini at day 12 of morphogenesis; scale bars show 100 µm. (e) High resolution pictures covering the entire slide were captured and all acini within a chamber scored manually. Morphology was scored as normal or atypical, where atypical includes multiacinar, branching and non-rounded acini. The number of acini scoring as atypical was expressed as a percentage of the total acini scored. A minimum of 86 acini were present in each well. Bar graphs represent the mean ± SEM from three independent experiments each with three technical repeats.

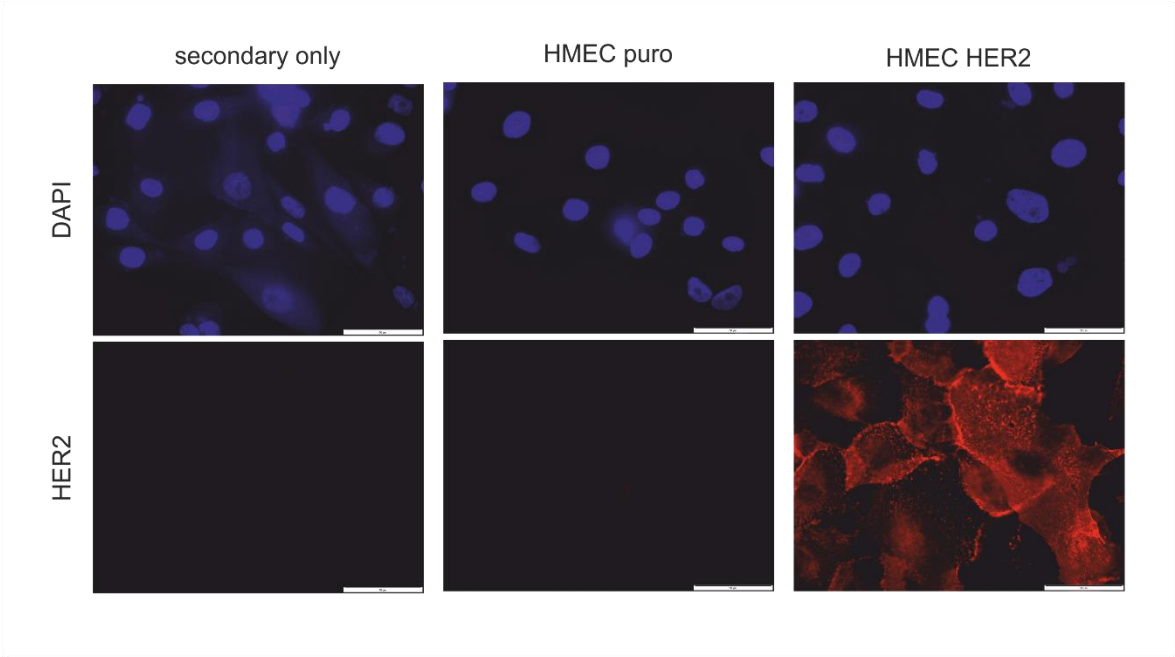

Figure 95 HER2 abundance and localisation in HMEC HER2

Representative images of immunofluorescence staining for HER2 (red) and DAPI counterstain (blue) in monolayer cultures; scale bars show 50 µm.

6.3.2 Characterisation of HER2-overexpressing HMEC

HER2-overexpressing cells were grown in 3D and scored for luminal status and morphology at day 12 of morphogenesis (Figure 96). Acini were hollowed (Figure 96c) with HER2-overexpression resulting in a non-statistically significant difference in luminal status compared to controls; 14% of HMEC HER2 scored as incompletely cleared acini compared to 14% in HMEC puro (Figure 96a,b). Additionally HER2 acini were spherical in structure (Figure 96c,d). HER2-overexpression resulted in a non-statistically significant difference in morphology scoring as 11% atypical compared to 12% in HMEC puro.

Although HER2 overexpression did not have the expected consequences on HMEC morphogenesis, I decided to pursue investigations into the consequences of etomoxir, 2-deoxyglucose, oxamate and dichloroacetate within this model. In the MCF-10A model, Bcl-2 overexpression is unable to prevent luminal clearing unless ROS production is limited by a second manipulation (Schafer, Grassian et al. 2009, Davison, Durbin et al. 2013). It may be that HER2 overexpression alone is insufficient to attenutate luminal clearing in HMEC acini but has a phenotypic consequence when combined with metabolic inhibition.

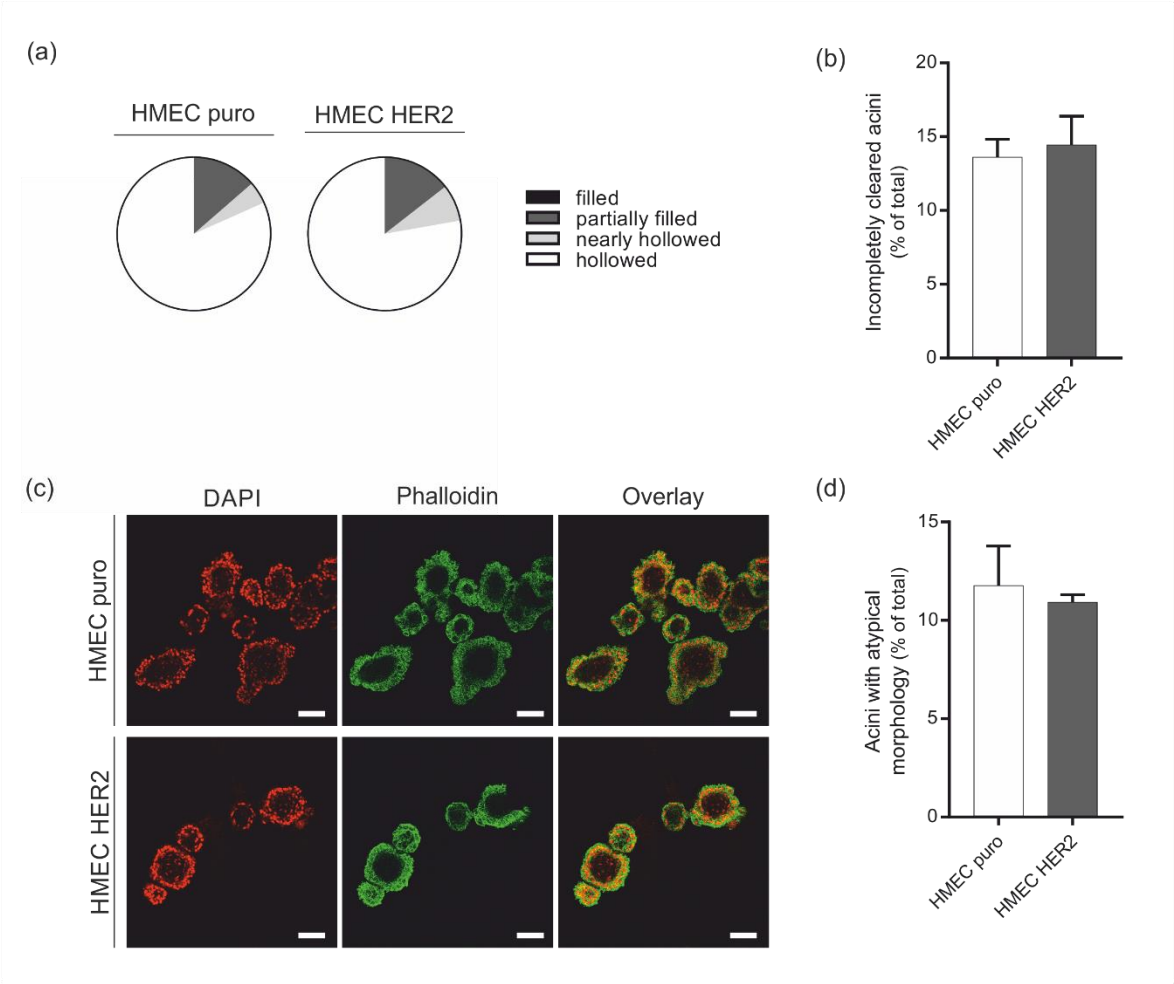

Figure 96 The effect of HER2 overexpression in 3D HMEC

HMEC acini were cultured for 12 days and stained with DAPI (red) and phalloidin-TRITC (green) (a-c) or fixed directly to minimise acini loss in wash steps (2% PFA final concentration) and mounted (d). (a) Confocal microscopy was utilised to score luminal status; looking through all focal planes, acini were scored as filled, partially filled, nearly hollowed or completely hollowed. Pie chart representation shows the proportions of acini scoring in each category. (b) The number of acini scoring as incompletely cleared (filled or partially filled) was expressed as a percentage of the total acini scored. A minimum of 120 acini were scored for each condition within an independent experiment, across three chambers. (c) Representative confocal immunofluorescence images show the centre of HMEC acini at day 12 of morphogenesis; scale bars show 100 µm. (d) High resolution pictures covering the entire slide were captured and all acini within a chamber scored manually. Morphology was scored as normal or atypical, where atypical includes multiacinar, branching and non-rounded acini. The number of acini scoring as atypical was expressed as a percentage of the total acini scored. A minimum of 134 acini were present in each well. Bar graphs represent the mean ± SEM from three independent experiments, each with three technical repeats.

6.4 The effect of metabolic inhibitors on HMEC acini

I tested the effect of etomoxir, 2-deoxyglucose, oxamate and dichloroacetate on luminal clearing in HMEC puro and HMEC HER2 using the same drug concentrations and treatment time points from the MCF-10A work (day 12 of morphogenesis). Representative images show the effect of these inhibitors on luminal status (Figure 97).

In this setting etomoxir led to an increase in the percentage of incompletely cleared acini which reached statistical significance ($p \leq 0.01$) in HMEC puro (Figure 98). The fold-increase in the number of incompletely cleared acini was 1.80-fold in HMEC puro and 1.49-fold in HMEC HER2 (Figure 98c). Etomoxir treatment resulted in the typical spherical structure observed in parental HMEC in both controls and HER2-overexpressing acini (Figure 97).

2-deoxyglucose acini also maintained the typical spherical structure however these acini were noticeably smaller (Figure 97) and exhibited a highly filled phenotype (Figure 98). Within a single experiment acini scored as 74% and 85% incompletely clearing in HMEC puro and HMEC HER2 respectively, compared to 13% and 18% respectively in media controls (Figure 98a,b). When combining data from three independent experiments a statistically significant ($p \leq 0.001$) over 6-fold increase in the number of incompletely cleared acini was seen following 2-deoxyglucose treatment compared to media alone (Figure 98c).

Oxamate treatment resulted in spherical acinar structures characteristic of controls (Figure 97) which scored similarly to media controls when examining luminal status (Figure 98a); HMEC puro scored as 13% incompletely cleared following oxamate treatment while HMEC HER2 scored as 18% incompletely cleared (Figure 98b). There was no statistically significant difference in the relative number of incompletely cleared acini in HMEC puro or HMEC HER2 when compared to media controls (Figure 98c).

Dichloroacetate treatment also resulted in spherical structures (Figure 97) with hollowed lumens (Figure 98). No statistically significant differences in the scoring of dichloroacetate-treated HMEC puro or HMEC HER2 were seen compared to media controls (Figure 98b,c).

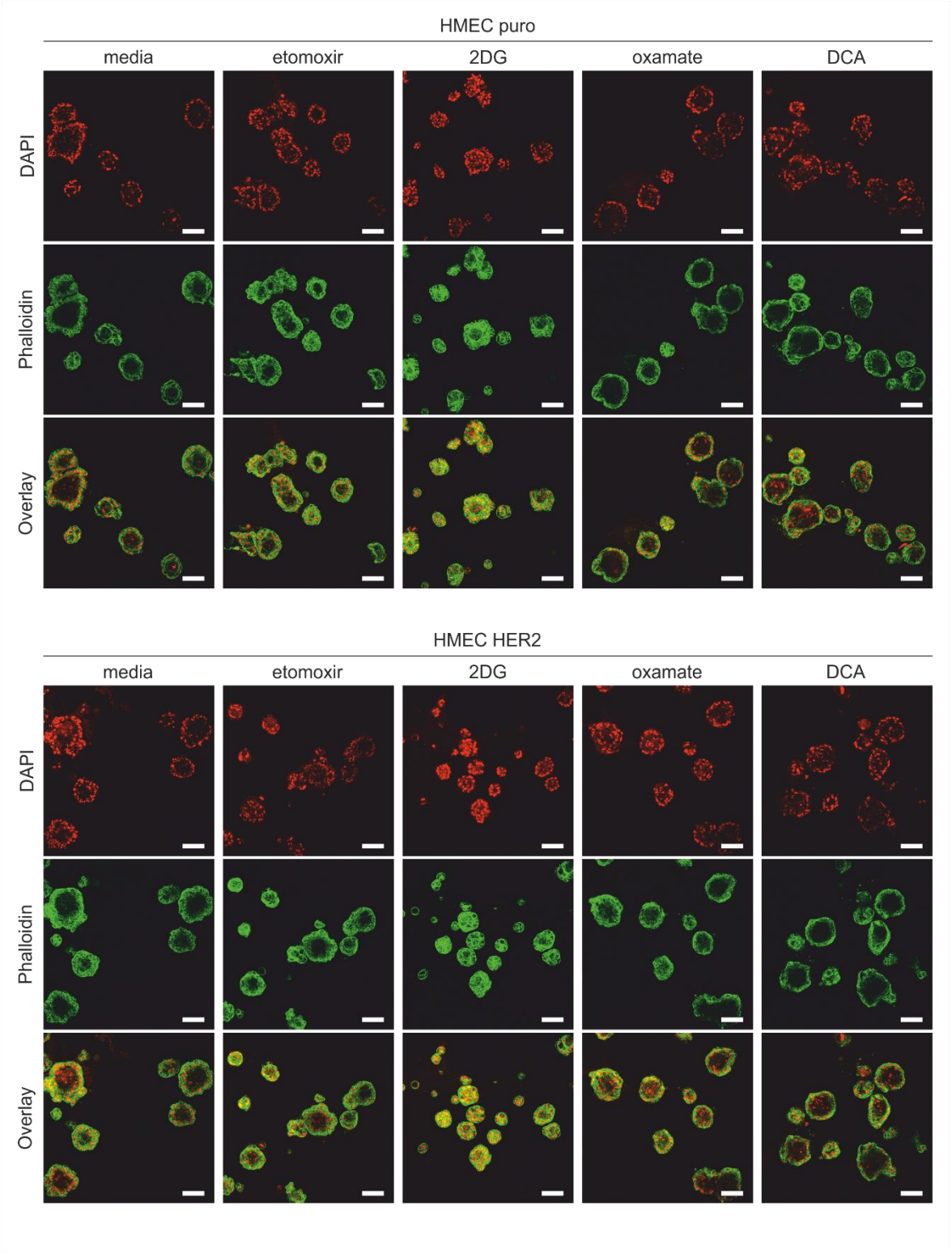

Figure 97 Representative images show the effect of metabolic inhibitors on HMEC acini

HMEC acini were treated with media or metabolic inhibitors every 2 days from day 6 of morphogenesis. At day 12 acini were fixed and stained with DAPI (red) and phalloidin-TRITC (green). Representative confocal immunofluorescence images show the effect of 100 µM etomoxir, 10 mM 2-deoxyglucose (2DG), 25 mM oxamate or 10 mM dichloroacetate (DCA) on luminal status. Images show the centre of acini; scale bars show 100 µm.

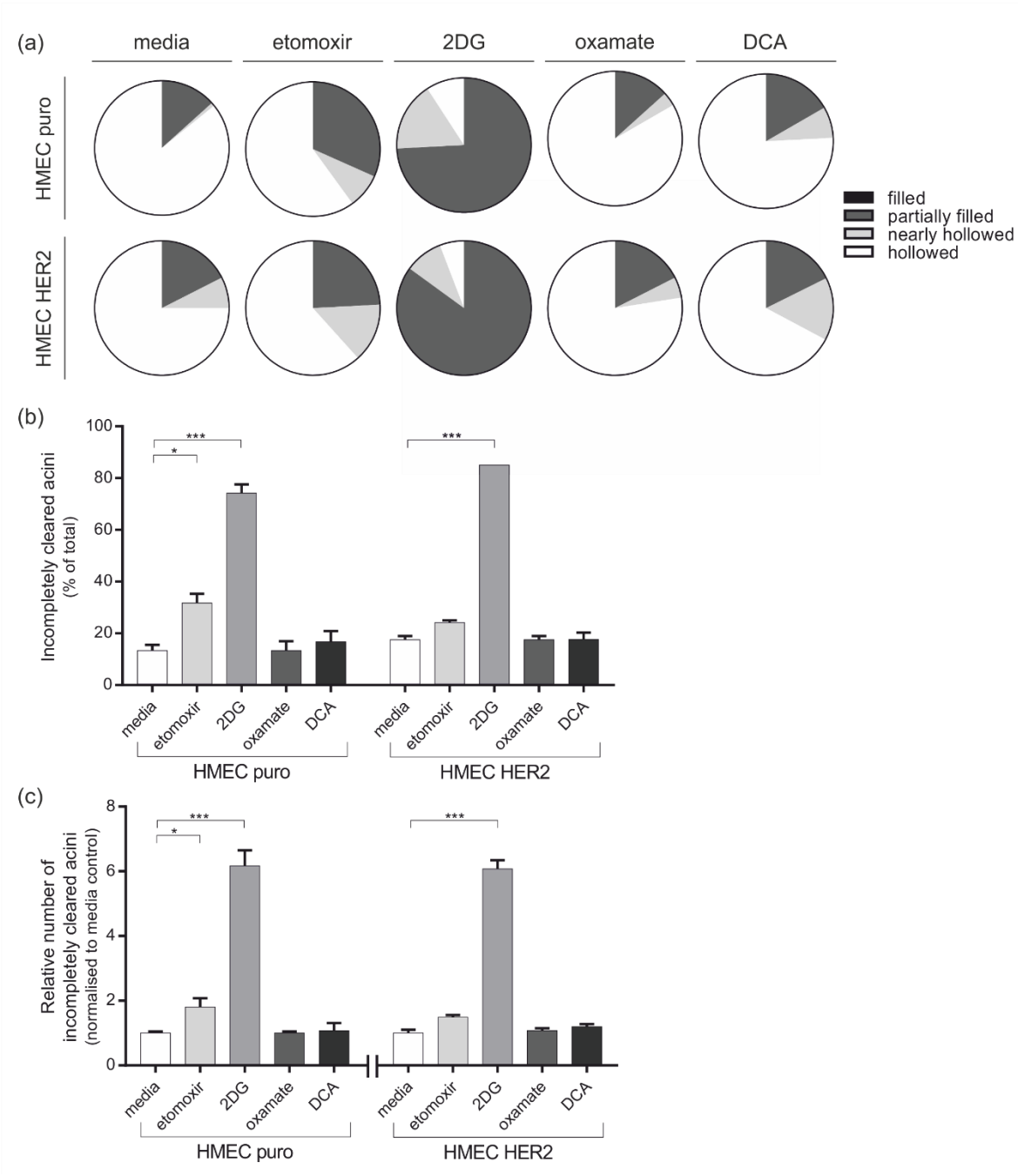

Figure 98 The effect of metabolic inhibitors on HMEC acini

HMEC acini were treated with media or 100 µM etomoxir, 10 mM 2-deoxyglucose (2DG), 25 mM oxamate or 10 mM dichloroacetate (DCA) every 2 days from day 6 of morphogenesis. At day 12 acini were fixed and stained with DAPI and phalloidin-TRITC. Confocal microscopy was utilised to score luminal status; looking through all focal planes, acini were scored as filled, partially filled, nearly hollowed or completely hollowed. (a) Pie chart representation shows the proportion of acini scoring in each category from a representative experiment. (b) The number of acini scoring as incompletely cleared (filled or partially filled) in (a) was expressed as a percentage of the total acini scored. A minimum of 120 acini were scored for each condition across three replicates. Bar graphs represent the mean ± SEM from three technical repeats. (c) Combined data from three independent experiments shows the relative number of incompletely cleared acini in the presence of metabolic inhibitors compared to media controls. Within an independent experiment values were adjusted for the total number of incompletely cleared acini for each pool. Adjusted values were normalised to the mean adjusted values for media across all three experiments. * $p \leq 0.05$, *** $p \leq 0.001$ as determined by two-way ANOVA with Fisher's LSD test.

6.5 Culture of acini in different media influences their morphogenesis

Results in HMEC do not match those observed in MCF-10A acini, although I have not included MCF-10A as a positive control in this setting. The media used in these two culture settings differs; HMEC have so far been grown in MEGM™ BulletKit™ growth medium (HMEC media) while MCF-10A are typically cultured in MCF-10A assay media (MCF-10A media). I examined HMEC acini alongside MCF-10A acini and also examined how each cell type would grow in the other cell type's media (Figure 99).

HMEC behaved as originally characterised in their standard HMEC media with no statistically significant differences in the percentage of incompletely cleared HMEC puro and HMEC HER2 acini (Figure 99a) or the percentage of atypical acini (Figure 99b). Similarly, MCF-10A acini behaved as previously described in their MCF-10A media (Figure 32) with HER2-overexpression statistically significantly ($p \leq 0.001$) increasing the percentage of incompletely cleared acini (Figure 99a) and the percentage of atypical acini compared to controls (Figure 99b).

When HMEC are grown in MCF-10A media acini presented as hollowed and there was no statistically significant difference in the percentage of incompletely cleared acini in parental or pooled populations compared to HMEC media (Figure 99a). Examining morphology, MCF-10A assay media statistically significantly ($p \leq 0.05$) increased the percentage of HMEC acini scoring as atypical compared to HMEC media in HMEC puro and HMEC HER2 (Figure 99b). HER2 overexpression in HMEC acini cultured in the presence of MCF-10A media did not statistically significantly increase the percentage of atypical acini compared to controls. Looking at the number of acini formed, a statistically significant ($p \leq 0.01$) decrease in the number of acini was observed in HMEC acini cultured in MCF-10A assay media compared to HMEC media with over a 0.6-fold reduction observed in all three conditions (Figure 99c).

The growth of MCF-10A in HMEC media results in a statistically significant ($p \leq 0.01$) increase in the percentage of incompletely cleared (Figure 99a) and atypical (Figure 99b) puro and HER2 acini compared to culture in MCF-10A assay media. Puro acini presented with a filled phenotype with 98% of acini incompletely cleared and this score is not statistically significantly different than the score for HER2 (Figure 99a). Puro acini present with 54% of atypical acini with HER2 scoring as statistically significantly ($p \leq 0.001$) higher at 63% atypical (Figure 99b).

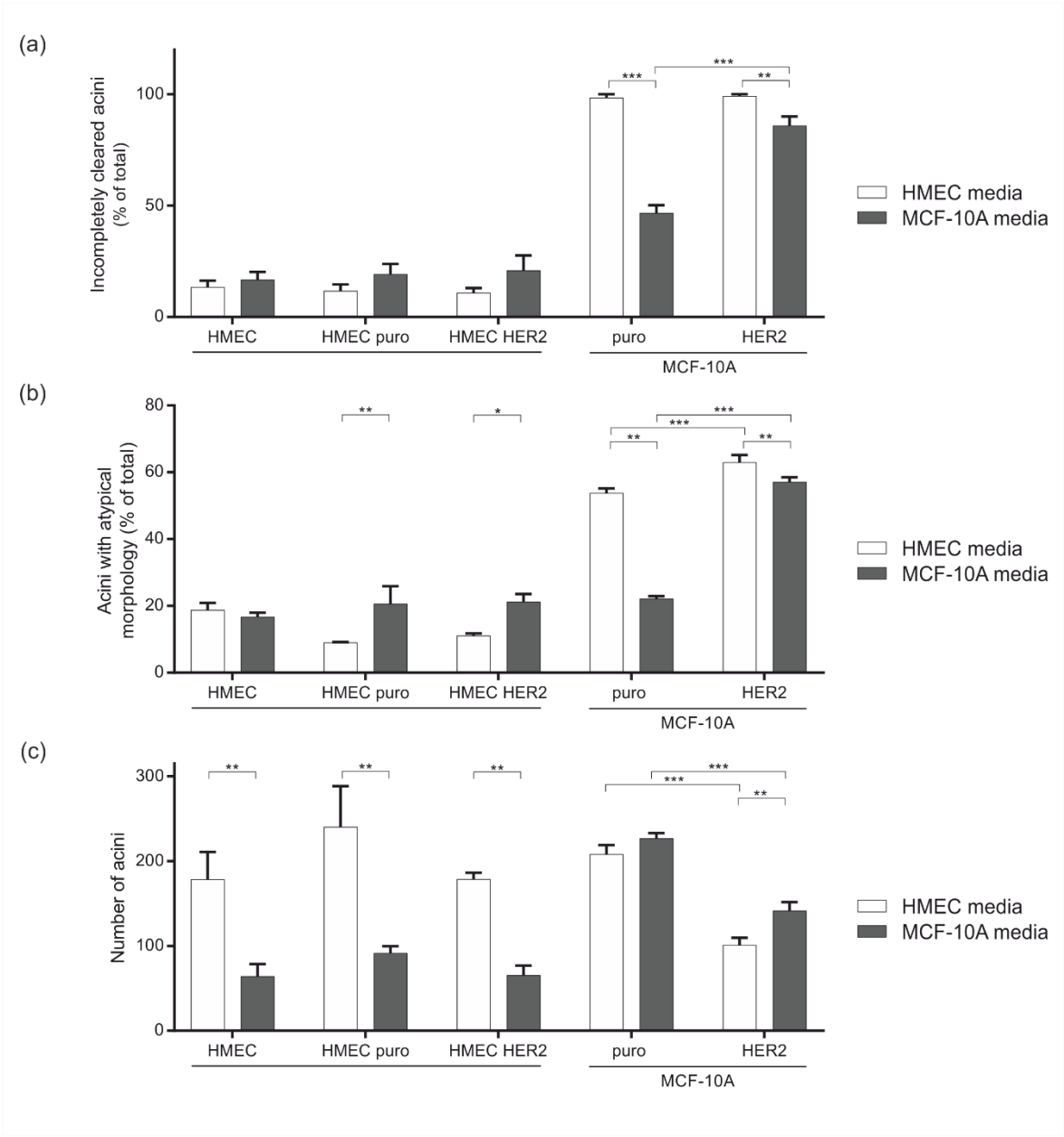

Figure 99 The effect of media on HMEC and MCF-10A morphogenesis

All HMEC (HMEC, HMEC puro, HMEC HER2) or MCF-10A acini (puro, HER2) were seeded together (day 0) in HMEC media (white bars) or MCF-10A assay media (grey bars). At day 12 acini were fixed and stained with DAPI and phalloidin-TRITC (a) or fixed directly to minimise acini loss in wash steps (2% PFA final concentration) and mounted (b,c). (a) Confocal microscopy was utilised to score luminal status. Looking through all focal planes, acini were scored as filled, partially filled, nearly hollowed or completely hollowed. The number of acini scoring as incompletely cleared (filled or partially filled) was expressed as a percentage of the total acini scored. A minimum of 120 acini were scored for each condition across three chambers. (b) High resolution pictures covering the entire slide were captured and all acini within a chamber scored manually. Morphology was scored as normal or atypical, where atypical includes multiacinar, branching and non-rounded acini. The number of acini scoring as atypical was expressed as a percentage of the total acini scored. A minimum of 35 acini were present in each well. Bar graphs represent the mean ± SEM from three independent experiments each with three technical repeats. * $p \leq 0.05$, ** $p \leq 0.01$, *** $p \leq 0.001$ as determined by a two-way ANOVA with Fisher's LSD test.

6.6 Discussion

The work presented in this chapter further examine the findings in MCF-10A acini relating to dichloroacetate, etomoxir, 2-deoxyglucose and oxamate treatment within a second system. While HMEC acini were found to culture in 3D in an analogous way to MCF-10A acini, HER2-overexpression did not result in luminal filling in this setting. Dichloroacetate and oxamate treatment had no effects on acinar morphogenesis, while etomoxir and 2-deoxyglucose promoted filling (Table 12). In addition metabolic manipulation did not alter the external morphology of HMEC acini.

A second system to examine the role of metabolism in 3D acini

Cell lines such as MCF-10A contain genetic modifications and are prone to genotypic and phenotypic instability even with regular characterisation and replacement from cryopreserved stocks. It is therefore important that scientists examine findings in a second setting. Often this is another cell line but ideally it is in primary tissue. Here I have used human mammary epithelial cells (HMEC); these are isolated from healthy breast tissue and were purchased as cryopreserved stocks from Lonza. To complete this work I needed to confirm that HMEC can be cultured on a layer of Matrigel® to form acini ('on top' assay). HMEC formed spherical acini which underwent luminal clearing within a similar time frame to MCF-10A acini (Figure 93), enabling me to examine the effect of HER2-overexpression and/or metabolic inhibition on acinar morphogenesis in a second, experimentally similar setting.

HER2 overexpression in HMEC acini does not attenuate luminal clearing

In order to examine the effect of metabolic inhibitors that are proposed to accelerate luminal clearing I needed to generate a HMEC model with a delayed or attenuated luminal clearing program. Luminal clearing in HMEC acini occurred over a short window in parentals with the majority of clearing occurring between days six and 10 (Figure 93). At day 12 of morphogenesis HMEC acini had progressed further through the luminal clearing program than MCF-10A acini with a smaller percentage of acini presenting as incompletely cleared (Figure 99). Selecting a time point which would allow me to confidently confirm or disprove a role for a metabolic inhibitor in accelerating luminal clearing would have been difficult. I instead looked to generate HER2-overexpressing HMEC which, based on findings from MCF-10A (Muthuswamy, Li et al. 2001, Pradeep, Zeisel et al. 2012, Papadakis, Barker et al. 2016), were hypothesised to have a filled luminal phenotype.

Table 12 Summary table comparing findings relating to metabolic manipulation of MCF-10A and HMEC acini

Drug	Pathway	Effects in acini				Notes
		MCF-10A		HMEC		
		Clearing	Atypical	Clearing	Atypical	
Etomoxir	FAO	↑	↓	↓	n.e	
2-deoxyglucose	Glycolysis	↓	↓	↓	n.e	Acini noticeably smaller
Oxamate	Glycolysis	↑	n.e	—	n.e	
Dichloroacetate	Activation of mitochondrial activity	↓	↑	—	—	

↑ = increase;↓ = decrease; — = no clear effects; n.e = not examined.

Despite successful generation of a HER2-overexpressing pooled population through retroviral infection (Figure 95) HMEC HER2 acini were not statistically significantly different to controls when examined at day 12 of morphogenesis (Figure 96). This occurred even in an experiment where HER2 MCF-10A were present providing a positive control for luminal filling (Figure 99). Based on my characterisation of the HMEC acinar time course (Figure 93), day 12 of morphogenesis is a relatively early time point following luminal clearing. In the MCF-10A model HER2-overexpression is able to fully delay luminal clearing and I would therefore expect to see a strong phenotype in HMEC HER2. Even if HER2 overexpression was only promoting short-term survival in ECM-detached luminal cells I would still expect to have seen this at day 12. In addition, HER2-overexpression has not altered acinar morphogenesis (Figure 96). It is possible that MCF-10A cells contain a transformation that is insufficient alone to alter acinar morphogenesis but when combined with HER2-overexpression results in the high level of transformation. This transformation may not be present in HMEC explaining why HMEC HER2 have the same acinar phenotype as controls.

Dicholoroacetate does not alter HMEC acinar morphogenesis

In the HMEC setting, dichloroacetate had no statistically significant effects on acinar morphogenesis, with luminal filling and external morphology unaltered (Figure 94). This is in contrast to what I observed in puro MCF-10A where dichloroacetate pushed acini towards to filled phenotype with a branching morphology (Figure 88, Figure 89, Figure 90). Similarly to as described for HER2, it is possible that an additional transformation is required in combination with

dichloroacetate treatment to lead to a transformed phenotype. Additionally dichloroacetate had no statistically significant effects on acinar morphogenesis of HMEC HER2. This highlights that HER2-overexpression combined with dichloroacetate is also insufficient to drive a filled phenotype.

Etomoxir attenuates luminal clearing in HMEC puro acini

Based on findings in MCF-10A relating to the role of fatty acid oxidation in luminal cell survival (5.3 Inhibition of fatty acid oxidation accelerates luminal clearing and attenuates HER2-driven luminal filling) (Schafer, Grassian et al. 2009, Carracedo, Weiss et al. 2012) I sought to examine the consequences of etomoxir treatment on HMEC acini.

In contrast to findings from MCF-10A where fatty acid oxidation inhibition accelerates luminal clearing (Figure 60), etomoxir treatment leads to an increase in the percentage of incompletely clearing acini in HMEC puro and HMEC HER2 reaching statistical significance in HMEC puro (Figure 98). The observation that fatty acid oxidation inhibition is attenuating clearing suggests that fatty acid oxidation is promoting apoptosis in ECM-detached luminal cells in this setting. HMEC HER2 are less sensitive to etomoxir treatment displaying a smaller fold-increase in the relative number of incompletely cleared acini; this could indicate that HER2-overexpression is influencing metabolism in HMEC acini so that cells are less responsive to fatty acid oxidation inhibition. It should be noted, however, that these changes in luminal clearing, although reaching statistical significance in HMEC puro, are not occurring in the majority of acini with over 58% of acini remaining hollowed.

The effect of glycolysis inhibition on HMEC acinar morphogenesis

In MCF-10A acini I propose that 2-deoxyglucose treatment leads to cell cycle arrest before the onset of luminal clearing leading to a filled phenotype in acini which are smaller in size than media controls. Similarly, in HMEC acini 2-deoxyglucose treatment led to acini which scored as partially filled (Figure 98) and were smaller in size than controls when assessed by eye (Figure 97). This supports the hypothesis I suggested for MCF-10A which is that 10 mM 2-deoxyglucose treatment promotes cell cycle arrest in acini and, subsequently, do not proceed further through the program. This suggests a strong dependence on glucose metabolism for cell cycle progression in MCF-10A and HMEC.

Lactate dehydrogenase inhibition in MCF-10A acini promoted luminal clearing. I examined this finding in HMEC acini using oxamate. Oxamate treatment of HMEC puro and HMEC HER2 had no statistically significant effects on luminal clearing (Figure 98). At day 12 of morphogenesis the vast majority of acini are already hollowed, which makes identification of an acceleration in the

program difficult when looking at this time point. I cannot say with confidence whether oxamate treatment accelerates clearing in HMEC from this data.

Metabolic manipulation does not alter HMEC acinar morphology

Based on evidence that metabolic manipulation can alter acinar morphology in MCF-10A acini I also monitored the external morphology of treated HMEC acini. In MCF-10A dichloroacetate treatment led to a highly branched external morphology (Figure 89) while etomoxir treatment of HER2-overexpressing acini led to a reversal of the branching, atypical phenotype (Figure 60). However in HMEC I did not see any effect of inhibitors on acinar morphology (Figure 94, Figure 97). While changes relating to morphology in MCF-10A acini correlated with the inhibitors effects on luminal filling, this was not the case in HMEC acini. For example, while etomoxir can attenuate luminal clearing, I did not see any evidence of an increased number of branching structures when assessed by eye (Figure 97), although this has not been investigated fully using our protocol for morphology scoring. Taken together these observations suggest that metabolic manipulation does not have an effect on HMEC acinar morphology in this setting.

Attempts to culture HMEC and MCF-10A acini in experimentally identical conditions

The findings relating to HER2-overexpression and metabolic manipulation of HMEC acini differ from those seen in MCF-10A. While the general experimental set up of the HMEC acini culture system was analogous to the MCF-10A system, I used the MEGM^{TM} mammary epithelial cell growth medium instead of MCF-10A assay media. These media share similarities in supplements including hydrocortisone, insulin and epidermal growth factor. Epidermal growth factor, which I know to be essential for acini formation in MCF-10A cells (data not shown), is present at 3 ng/ml in HMEC media compared to 5 ng/ml in MCF-10A 3D assay media. While MCF-10A assay media contains 2% horse serum, MEGM^{TM} mammary epithelial cell growth medium is serum-free and instead contains bovine pituitary extract to support the long term culture of HMEC (Hammond, Ham et al. 1984). HMEC media also lacks cholera toxin, and HMEC acini undergo luminal clearing despite the absence of cholera toxin which is a requirement for luminal clearing in MCF-10A acini (Nedvetsky, Kwon et al. 2012).

The differences in media composition make direct comparison between the two systems less than ideal, and these differences could account for the different phenotypes observed. I therefore explored whether HMEC could be cultured in MCF-10A media and vice versa. Growth of acini in the other cell type's media did result in statistically significant differences (Figure 99).

Looking at culture of MCF-10A in the HMEC media, culture in HMEC media resulted in a highly filled phenotype in puro acini and there was no longer a statistical significance difference in the

percentage of incompletely cleared acini following HER2-overexpression (Figure 99). This reduction in luminal clearing is probably due to the absence of cholera toxin and makes HMEC media an inappropriate culture condition to study HMEC alongside MCF-10A. While cholera toxin could potentially be added to HMEC media there was also a statistically significant increase in the percentage of atypical MCF-10A acini cultured in HMEC media compared to MCF-10A media.

When HMEC were cultured in MCF-10A assay media the luminal status of HMEC acini was not statistically significantly altered (Figure 99). While the number of acini scoring as atypical in HMEC puro and HMEC HER2 was statistically increased in culture with MCF-10A assay media compared to HMEC media, the overall percentage of atypical acini was still relatively low at approximately 20%. It should be noted that the number of acini formed in MCF-10A assay media is significantly lower than the number formed in HMEC media. These culture conditions could therefore be considered for further investigations, although one may want to increase the seeding density of cells. It should be noted, however, that even when HMEC are cultured in MCF-10A media HER2-overexpression did not promote luminal filling. This result cannot, therefore, be explained by a difference in media composition which alters HER2s activity.

Conclusion

To summarise I have shown that HER2-overexpression or metabolic manipulation do not influence HMEC acini in the same way as MCF-10A acini (Table 12). Although oxamate and dichloroacetate did not statistically significantly alter acinar morphogenesis in this setting, etomoxir and 2-deoxyglucose attenuated luminal clearing. Schafer *et al.* have shown that, similarly to MCF-10A cells, HMEC do display an ATP defect upon detachment (Schafer, Grassian et al. 2009) implicating metabolism in the luminal cell clearing program of HMEC acini. This data suggests that the mechanism that contribute to ATP production in ECM-detached cells may differ between HMEC and MCF-10A.

Chapter 7: Overexpression of a metabolic sensor interferes with MCF-10A acinar morphogenesis

The prior work in this thesis focuses on enzymes directly involved in metabolism; however, metabolism can also affect phenotype through its impact on metabolism-regulated transcription factors. The work described in this chapter focuses on such a family, the CtBPs (1.4 C-terminal Binding Proteins (CtBPs)).

CtBP proteins are coded for by two genes in vertebrates, CtBP1 and CtBP2, and alternative splicing of CtBP1 or CtBP2 mRNA generates two isoforms of each family member which are all highly homologous (Katsanis and Fisher 1998). Functioning predominantly as transcriptional regulators (Chinnadurai 2007), CtBPs are co-repressors that recruit DNA binding proteins and DNA modifying enzymes. NADH-dependent dimerisation leads to activation of their transcriptional regulatory function (Figure 14) making their activity regulated by the metabolic state of a cell. In a highly glycolytic cell, such as a cancerous one, the resulting higher levels of NADH will increase the transcriptional regulatory activity of these proteins, resulting in altered gene expression. Many of the genes targeted by CtBPs are implicated in tumour progression (Table 1).

In Chapter 5: 'The role of metabolism in MCF-10A acinar morphogenesis' I report that manipulation of metabolism within the vector control (puro) and HER2-overexpressing (HER2) MCF-10A acini models can influence cell survival in ECM-detached luminal cells. Based on the function of CtBPs as a metabolic sensors I could predict that manipulation of CtBP in this setting could also influence acinar morphogenesis. In this work I present data demonstrating that inhibition or overexpression of CtBPs can influence cell survival in ECM-detached conditions.

7.1 The CtBP inhibitor MTOB accelerates the luminal apoptosis program, promoting luminal clearing.

4-Methylthio-2-oxobutanoic acid (MTOB) is an inhibitor of CtBPs (Achouri, Noel et al. 2007, Straza, Paliwal et al. 2010, Di, Byun et al. 2013) and I used this to examine the consequences of CtBP inhibition on puro and HER2 cells in 2D and 3D culture. 4 mM MTOB was used as this concentration displaces CtBP2 from the promoter region of the CtBP-target gene Bik (Straza, Paliwal et al. 2010) and has been used extensively in the Jeremy Blaydes laboratory for studies relating to CtBP.

7.1.1 The effect of MTOB treatment on 2D cultured cells

In a 2D cell viability assay MTOB treatment led to a statistically significant ($p \leq 0.05$) increase in cell viability at 24 h in puro and HER2 cells in both attached and detached conditions (Figure 100a). While attached cells showed no statistically significant differences in viability at 48 h, both puro and HER2 cells showed an increase in viability in detached cells in the presence of MTOB but statistical significance ($p \leq 0.05$) was only reached in puro cells. Examining ATP levels MTOB treatment resulted in no statistically significant differences in ATP at 24 h in all conditions examined (Figure 100b). At 48 h both puro and HER2 cells showed an increase in ATP in detached cells at 48 h in the presence of MTOB but statistical significance ($p \leq 0.05$) was only reached in puro cells.

7.1.2 The effect of MTOB treatment on 3D acini

Acini were treated from day 6 of morphogenesis before the onset of luminal clearing, with 4 mM MTOB. MTOB treatment pushed acini towards a more hollowed phenotype (Figure 101a,c). Within a single experiment just 17% of puro and 34% of HER2 presented as incompletely cleared compared to 33% and 73% of controls respectively (Figure 101b). Looking at the relative number of incompletely cleared acini from combining three independent experiments MTOB statistically significantly ($p \leq 0.05$) reduced the number of incompletely cleared puro acini to less than 50% of controls. While significance was not reached for HER2, MTOB reduced the number of incompletely cleared HER2 acini to approximately 75% of controls (Figure 101d).

7.1.3 Metabolic consequences of MTOB treatment

MTOB is also the final compound of the methionine salvage pathway that converts the polyamine by-product methylthioadenosine to adenine and methionine. As a metabolic intermediate in the methionine salvage pathway, and as I have previously shown that interfering with metabolic pathways can alter the morphogenesis program of acini (Chapter 5: 'The role of metabolism in MCF-10A acinar morphogenesis') I examined the consequences of MTOB treatment on cell metabolism. If MTOB treatment influences the metabolism of the cells it is difficult to ascertain whether the effect of MTOB is due to metabolic suppression/activation or due to CtBP inhibition. A dose-response experiment to MTOB treatment was carried out using the Seahorse analyser to examine the effect of MTOB on glycolytic and mitochondrial respiration (Figure 102).

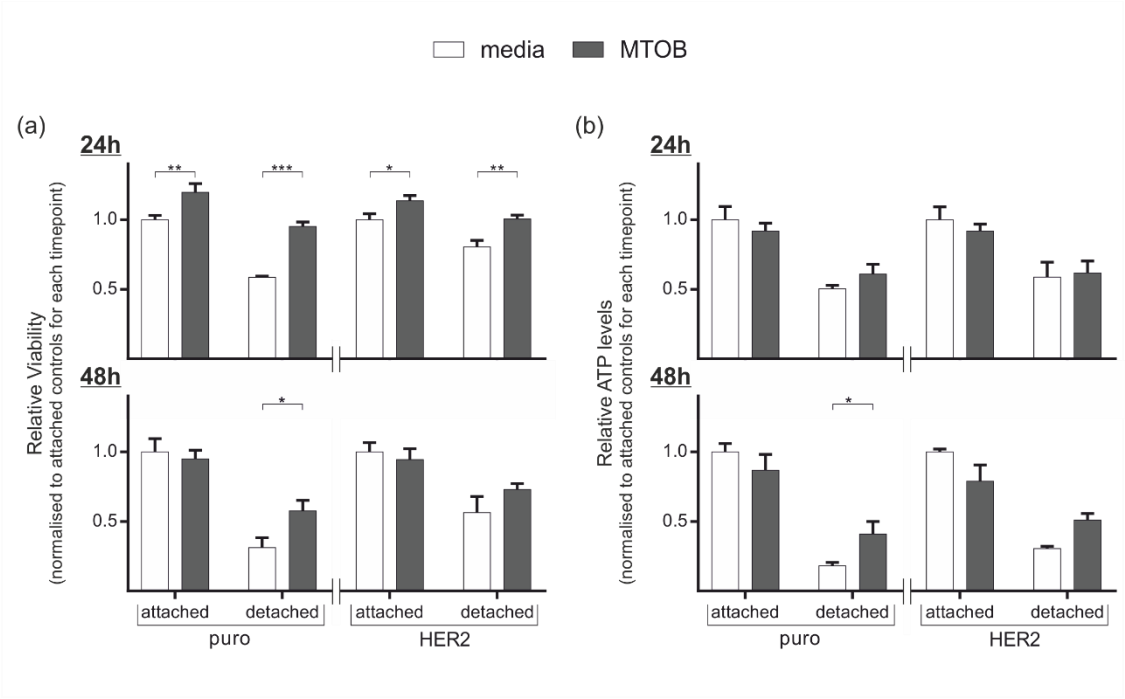

Figure 100 The CtBP inhibitor MTOB influences cell viability in 2D culture

Cells (15,000 per well) were treated with media or methylthio-2-oxobutyric acid (MTOB, 4 mM) and seeded onto standard tissue culture plates (attached) or polyHEMA-coated plastic (detached) for 24 h or 48 h. (a) Cell viability was examined using alamarBlue® reagent which was added to conditions 6 h prior to data collection. (b) ATP levels were examined using the ATPlite assay. Fluorometric (a) or luminometric data (b) was normalised for experimental variation and expressed relative to the appropriate vector control in attached conditions (puro or HER2). Bar graphs represent the mean ± SEM from three independent experiments each with three technical repeats. * $p \leq 0.05$, ** $p \leq 0.01$, *** $p \leq 0.001$ as determined by a two-way ANOVA with Fisher's LSD test.

While a statistically significant ($p \leq 0.05$) difference in glycolytic respiration (ECAR) is observed in puro cells with 1 mM and 16 mM MTOB and in HER2 cells at 4 mM MTOB, the pattern of the response is not consistent across puro and HER2 and is not a dose-dependent response (Figure 102a). Similarly a statistically significant ($p \leq 0.05$) difference in mitochondrial respiration (OCR) is observed in puro cells with 2 mM, 4 mM and 8 mM MTOB but, again, this effect is not observed in HER2 and there is limited evidence of a dose-dependent response (Figure 102b). These changes are relatively small with a 1.27, 1.13- and 1.13- fold increase in mitochondrial ATP production with 2 mM, 4 mM and 8 mM MTOB respectively. The lack of a dose-dependent response, the observation that the pattern of response is not replicated in HER2 cells compared to puro cells and because many of these changes are small, although significance was gained, suggests that these changes may not be biologically significant.

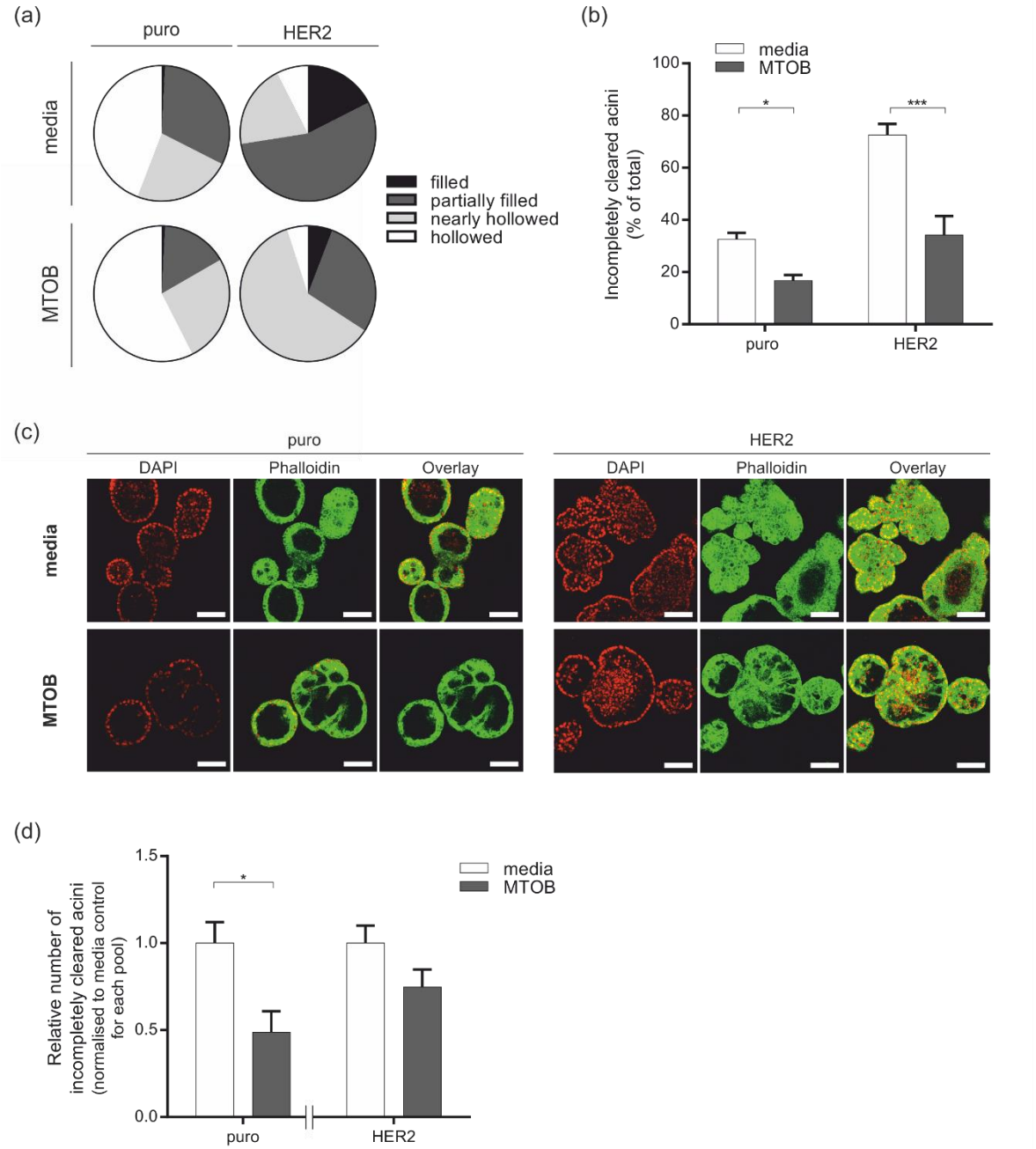

Figure 101 The CtBP inhibitor MTOB can accelerate luminal clearing

Acini were treated with media or methylthio-2-oxobutyric acid (MTOB, 4 mM) every 2 days from day 6 of morphogenesis. At day 12 acini were fixed and stained with DAPI (red) and phalloidin-TRITC (green). Confocal microscopy was utilised to score luminal status; looking through all focal planes, acini were scored as filled, partially filled, nearly hollowed or completely hollowed. (a) Pie chart representation shows the proportion of acini scoring in each category from a representative experiment. (b) The number of acini scoring as incompletely cleared (filled or partially filled) in (a) was expressed as a percentage of the total acini scored. A minimum of 120 acini were scored for each condition across three replicates. Bar graphs represent the mean ± SEM from three technical repeats. (c) Representative confocal immunofluorescence images show the centre of acini following MTOB treatment; scale bars show 100 µm. (d) Combined data from three independent experiments shows the relative number of incompletely cleared acini in the presence of MTOB compared to media controls. Within an independent experiment values were adjusted for the total number of incompletely cleared acini for each pool. Adjusted values were normalised to the mean adjusted values for media across all three experiments. * $p \leq 0.05$, *** $p \leq 0.001$ as determined by two-way ANOVA with Fisher's LSD test.

The dose-dependent response experiment assesses short-term metabolic responses to stimuli (1 h in the presence of drug). This is in contrast to the long-term exposure to MTOB present during 3D acini experiments where the drug is present for six days. I therefore sought to assess metabolic responses to a longer exposure to the drug (72 h total). Cells were plated into dishes overnight before refeeding with media in the absence or presence of 4 mM MTOB. After a 48 h treatment cells were trypsinised and counted before plating into a V3-PS XF96 cell culture microplate overnight. Cells which had been exposed to MTOB were plated in fresh media with 4 mM MTOB. While cells treated with media alone plated on the microplate as expected I observed rounded detached cells settled at the bottom of wells containing MTOB treated cells when observed down the microscope (data not shown). These cells were lost following the required washes needed for the Seahorse assay so I could not proceed with this experiment.

While there is still some uncertainty as to the exact mechanism of action of the MTOB inhibitor my findings relating to 3D acini suggest that CtBP inhibition may inhibit cell survival following ECM-detachment. To further examine the role of CtBP proteins in cell survival following ECM-detachment I produced dual pooled populations of puro- or HER2- overexpressing CtBP2 wildtype or functional mutants.

7.2 Overexpression of CtBP2 delays the luminal apoptosis program

7.2.1 Generation of CtBP2-overexpressing puro- or HER2- dual pooled populations

Dual pooled populations of puro or HER2 cells overexpressing different CtBP2 variants were generated by retroviral infection. Dual populations overexpressing CtBP2 were denoted puro CtBP2 and HER2 CtBP2. Experimental controls containing an empty pBABEneo construct were produced and denoted puro neo or HER2 neo. Two dual populations overexpressing functional mutants were produced; the CtBP2 G189A mutant which contains a mutation in the NADH binding site (Mirnezami, Campbell et al. 2003, Thio, Bonventre et al. 2004) and the CtBP2 H321L mutant which contains a mutation in the dehydrogenase domain (Thio, Bonventre et al. 2004). The G189A NADH-binding mutant is expected to be dimerisation-inactive resulting in monomeric CtBP activity while the H312L mutant is hypothesised to keep CtBP in an NADH-bound, dimeric state. The dual populations overexpressing the CtBP2 G189A mutant were denoted puro G189A and HER2 G189A and the populations overexpressing the CtBP2 H321L mutant denoted puro H321L and HER2 H321L.

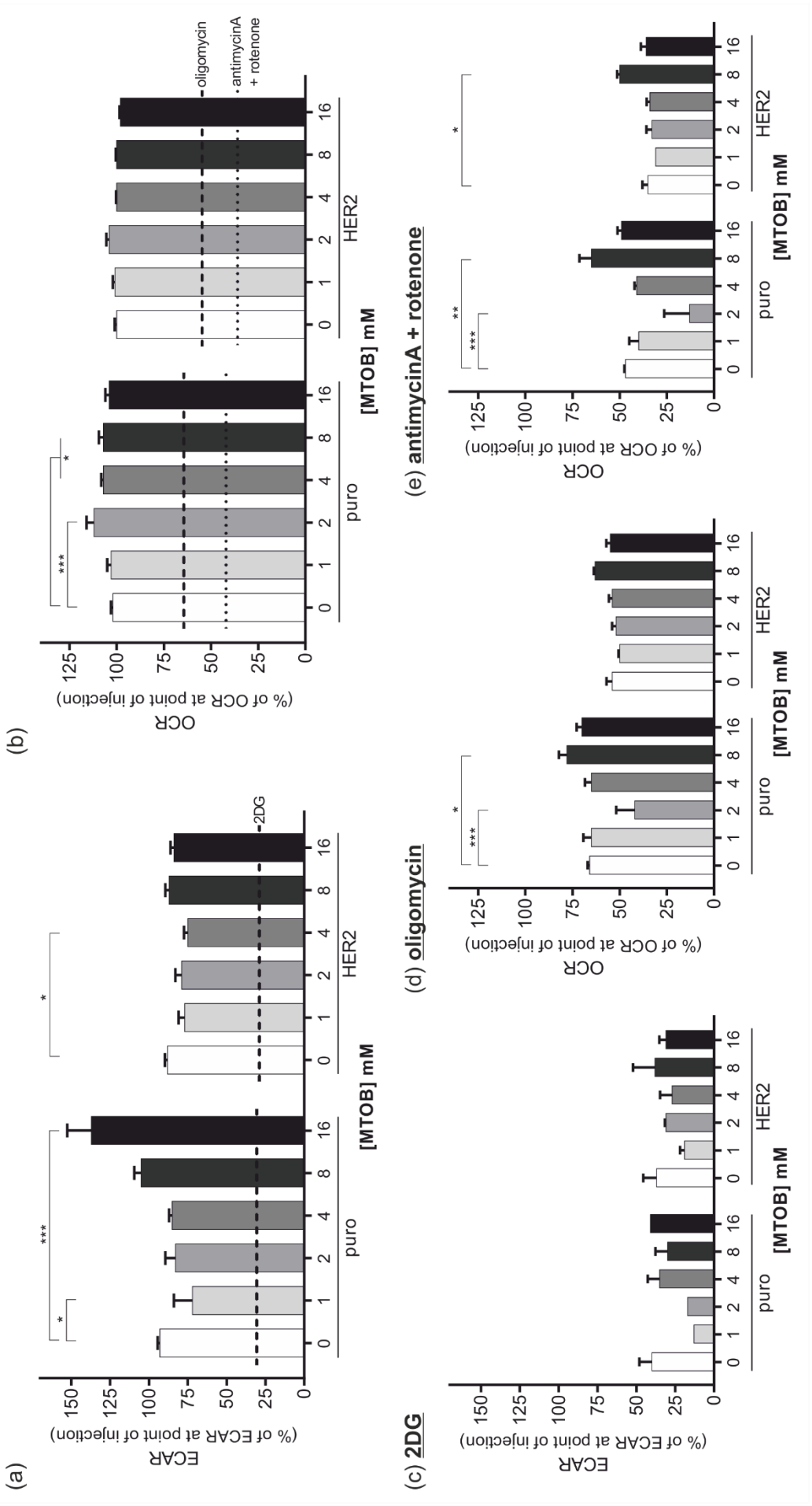
(a)
ECAR
(% of ECAR at point of injection)
2DG
puro
HER2
[MTOB] mM
(b)
OCR
(% of OCR at point of injection)
oligomycin
antimycinA + rotenone
(c) 2DG
(d) oligomycin
(e) antimycinA + rotenone

Figure 102 Metabolic responses to MTOB treatment

Cells (25,000 per well) were seeded into Seahorse PET plate 18 h prior to experiment. The Seahorse Analyser simultaneously measured extracellular acidification rate (ECAR) and oxygen consumption rate (OCR) following injection of the stated methylthio-2-oxobutyric acid (MTOB, 4 mM) concentration. Following MTOB treatment wells were injected with either 100 mM 2-deoxyglucose (2DG) or 1 µM oligomycin followed by 1 µM antimycinA and 1 µM rotenone. All data was baselined to the values for ECAR and OCR at the point of injection of the drug (0 min). (a) ECAR following MTOB treatment; dashed lines show the average ECAR for puro or HER2 cells following 2DG. Bar graphs represent the mean ± SEM from an independent experiment with four technical repeats. (b) OCR following MTOB treatment. Dashed lines show the average OCR for puro or HER2 cells following oligomycin injection; dotted lines show the average OCR for puro or HER2 cells following antimycinA and rotenone injection. Bar graphs represent the mean ± SEM from an independent experiment with four technical repeats. (c) ECAR following 2DG; bar graphs represent the mean ± SEM from an independent experiment with two technical repeats. (d,e) OCR following oligomycin (d) followed by antimycinA and rotenone (e). Bar graphs represent the mean ± SEM from an independent experiment with two technical repeats. * $p \leq 0.05$, ** $p \leq 0.01$; *** $p \leq 0.001$ as determined by a two-way ANOVA with Fisher's LSD test.

In each of the CtBP2 vectors used the CtBP2 coding region also codes for a myc- and 6-His-proteins tag at the C-terminus. The BD Biosciences Purified Mouse Anti-CtBP2 antibody recognises the C-terminus of CtBP2 and we propose that it recognises the extreme C-terminus as it has been shown that the addition of a 6-His-tag prevents binding of this antibody (unpublished data, Jeremy Blaydes laboratory). The nature of the exogenous CtBP2 containing a 6-His-tag and being unrecognisable by a CtBP2 antibody allows me to individually examine endogenous and exogenous CtBP2 expression levels.

Examining the puro dual pooled populations, exogenous CtBP2 staining is not present in puro neo controls but stains strongly with nuclear localisation in all three CtBP2-overexpressing populations (puro CtBP2, puro G189A and puro H321L) (Figure 103). CtBP2 overexpression is heterogeneous across each population consistent with a pooled population. In all three dual pools CtBP2 staining is not present in 100% of the populations.

In the HER2 dual pooled populations exogenous CtBP2 staining is not present in HER2 neo controls but stains with nuclear localisation in all three CtBP2-overexpressing populations (HER2 CtBP2, HER2 G189A and HER2 H321L) (Figure 104). As observed for puro populations CtBP2 overexpression is heterogeneous and is not present in 100% of the population. In both puro H321L (Figure 103) and HER2 H321L dual populations (Figure 104) CtBP2 overexpression is lower than the other CtBP2 variants.

I also examined endogenous levels of both CtBP2 and CtBP1 in the CtBP2-overexpressing dual pools. Endogenous CtBP2 (Figure 105) and CtBP1 (Figure 106) staining levels are homogeneous

and nuclear across all dual populations and at the same levels in dual pools overexpressing CtBP2 variants as seen in controls.

7.2.2 Characterisation of CtBP2-overexpressing dual pooled populations in 2D culture

I sought to characterise the effect of CtBP2 overexpression in 2D culture, examining colony forming efficiency and cell viability and ATP in attached and detached conditions. Overexpression of CtBP2 in puro resulted in a statistically significantly higher ($p \leq 0.05$) colony forming efficiency compared to neo control with 90% of puro CtBP2 cells seeded forming colonies compared to 73% of puro neo (Figure 107). This phenotype was not observed in CtBP2 mutant-overexpressing dual pools puro G189A and puro H321L. Puro G189A had a statistically significantly decreased ($p \leq 0.05$) colony forming efficiency compared to puro neo and puro CtBP2 with 58% of cells forming colonies. Puro H321L had a 65% colony forming efficiency, a non-statistically significant decrease in efficiency compared to controls and a statistically significant ($p \leq 0.01$) decrease compared to overexpression of wildtype CtBP2. HER2 pooled populations had a lower colony forming efficiency than puro and wildtype- or mutant- CtBP2 overexpression had no statistically significant effects on the colony forming efficiency.

The effect of CtBP2 overexpression on cell survival in 2D was examined using alamarBlue® and an ATP assay. Cells were plated on standard tissue culture treated (attached) or polyHEMA-coated (detached) plastic and cell viability examined at 24 and 48 h. Examining viability detachment led to a decrease in the relative viability of cells across all eight dual pool (Figure 108a); the fold-reduction in viability was more pronounced at 48 h compared to 24 h consistent with previous alamarBlue® data relating to detachment (Figure 52). In addition, the relative decrease in cell viability in detachment was less pronounced in HER2-overexpressing populations compared to puro.

CtBP2 overexpression had little effect on the relative viability of cells except for in HER2-overexpressing dual pools where CtBP2 overexpression statistically significantly increased ($p \leq 0.05$) cell viability in detachment; this was observed at 24 h and 48 h. Overexpression of the G189A mutant in this condition had no statistically significant effects on cell viability, while overexpression of the H321L mutant increased viability compared to neo which was statistically significant ($p \leq 0.05$) at 48 h.

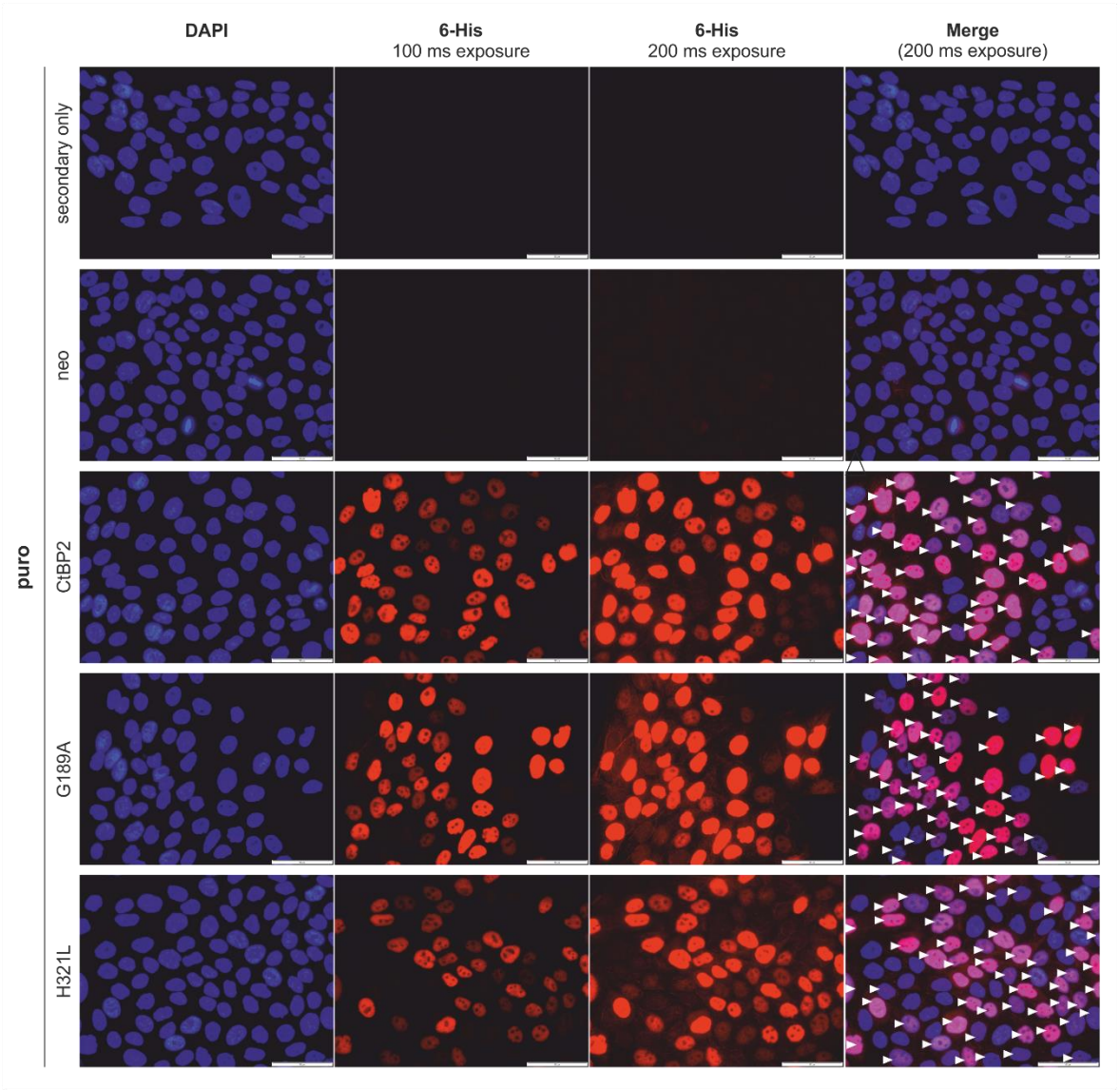

Figure 103 Exogenous CtBP2 abundance and localisation in puro MCF-10A dual retroviral pooled populations

Representative images of immunofluorescence staining for 6-His (red) and DAPI counterstain (blue) in monolayer cultures. White triangles in merge images indicate cells that stain positive for 6-His; scale bars show 50 µm.

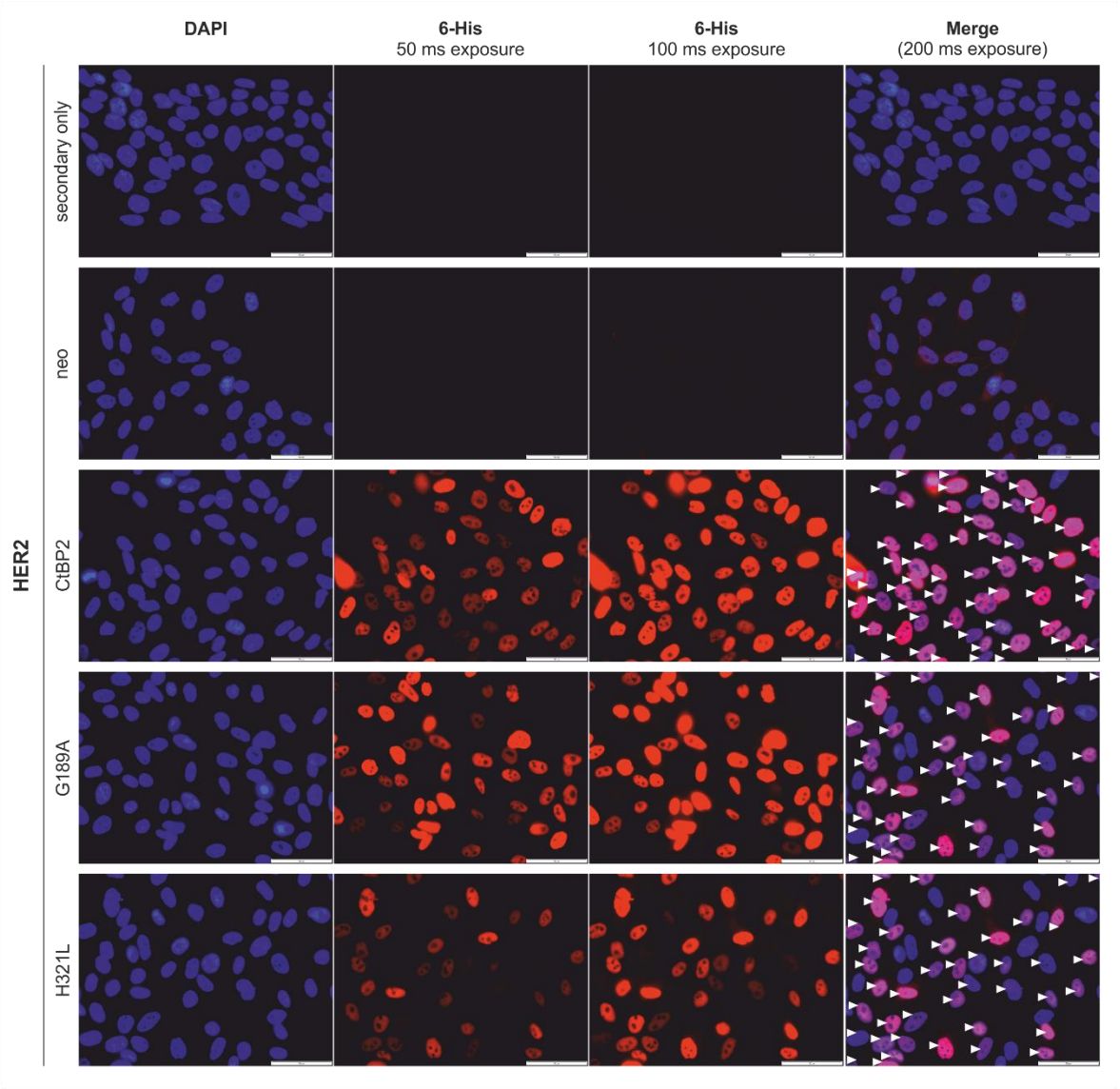

Figure 104 Exogenous CtBP2 abundance and localisation in HER2 MCF-10A dual retroviral pooled populations

Representative images of immunofluorescence staining for 6-His (red) and DAPI counterstain (blue) in monolayer cultures. White triangles in merge images indicate cells that stain positive for 6-His; scale bars show 50 µm.

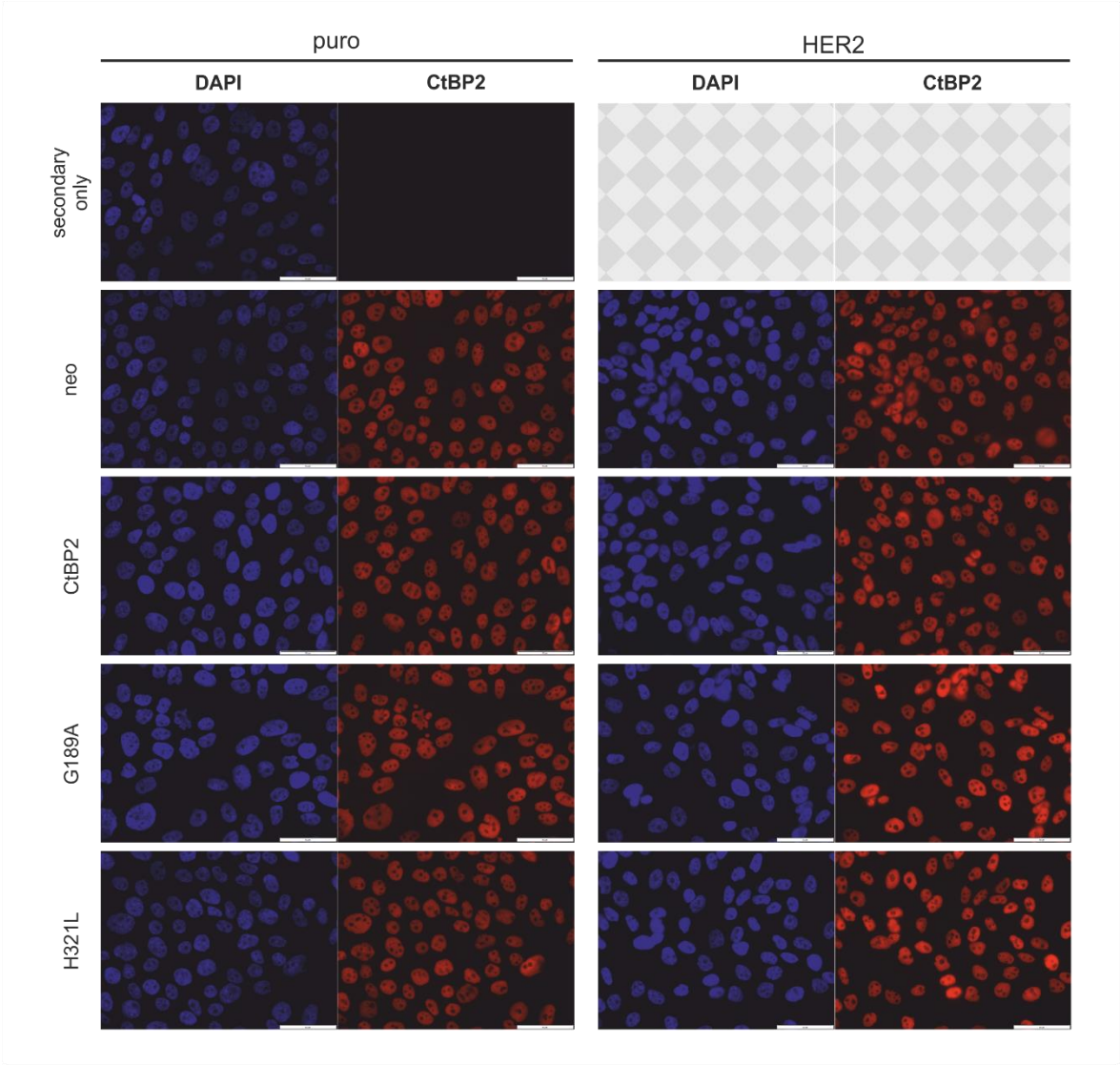

Figure 105 Endogenous CtBP2 abundance and localisation in puro MCF-10A dual retroviral pooled populations

Representative images of immunofluorescence staining for CtBP2 (red) and DAPI counterstain (blue) in monolayer cultures; scale bars show 50 µm.

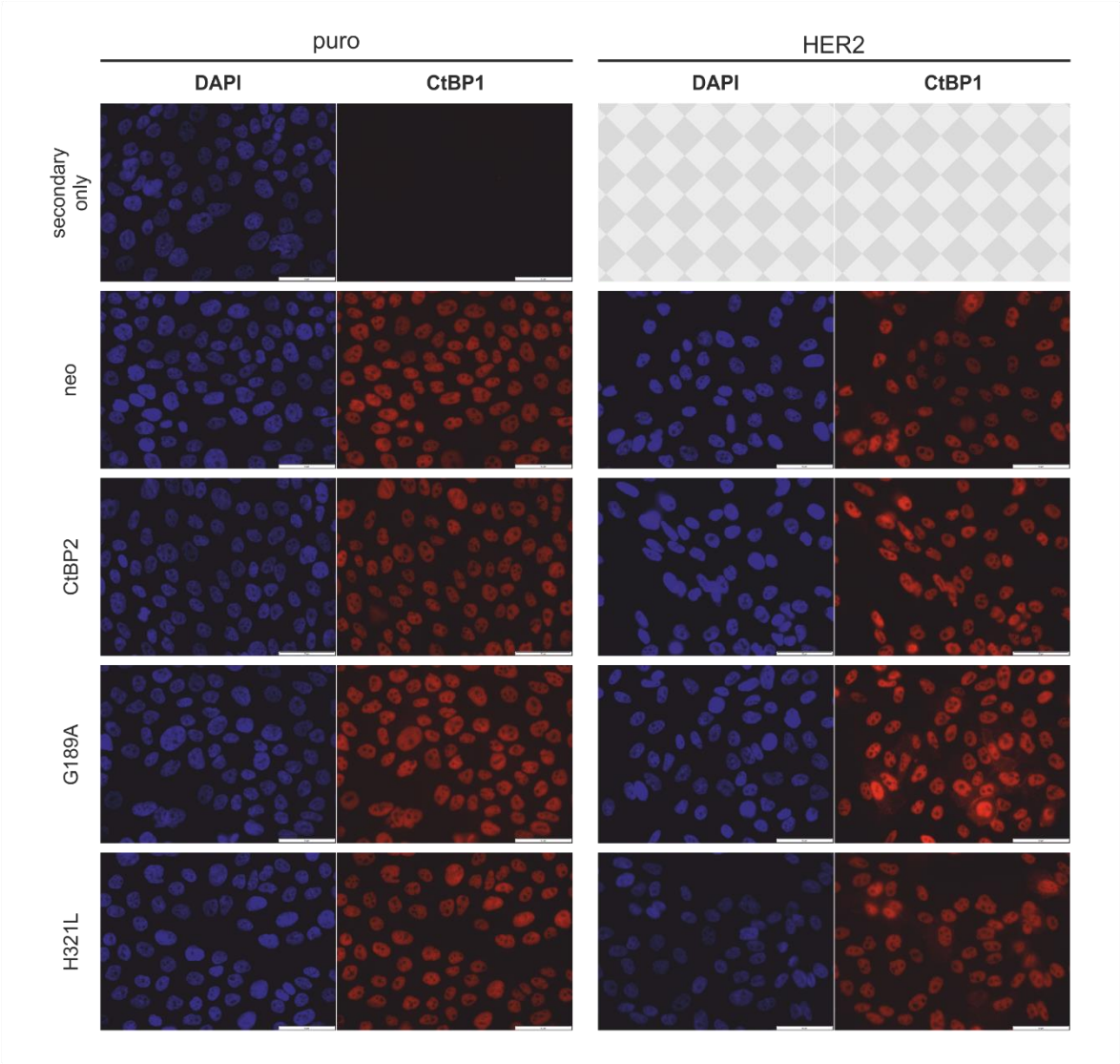

Figure 106 Endogenous CtBP1 abundance and localisation in puro MCF-10A dual retroviral pooled populations

Representative images of immunofluorescence staining for CtBP1 (red) and DAPI counterstain (blue) in monolayer cultures; scale bars show 50 µm.

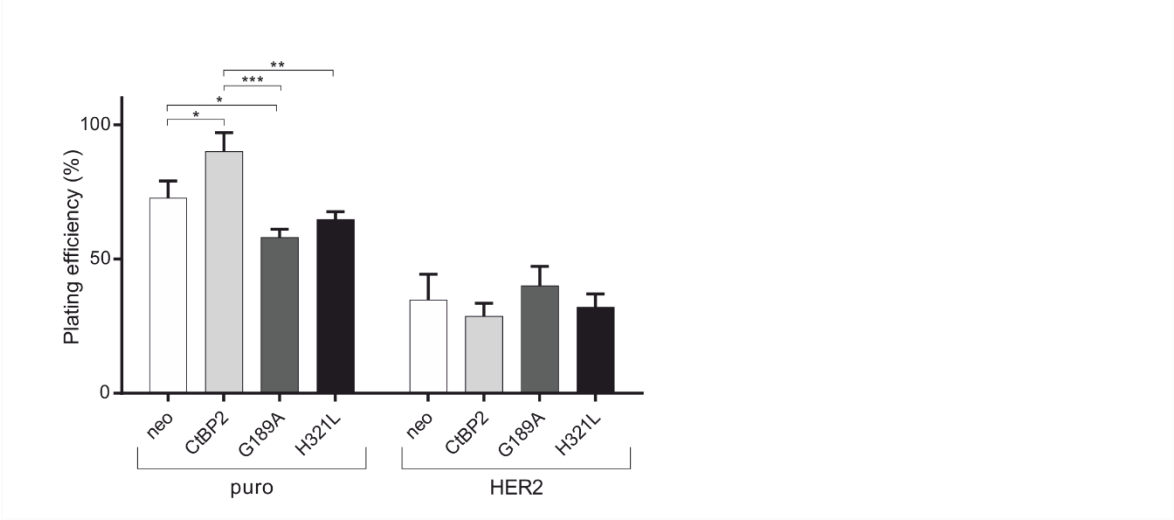

Figure 107 Effect of CtBP2 overexpression on 2D MCF-10A culture

The colony-forming efficiency of MCF-10A dual pools was assessed in a clonogenic assay and expressed as the plating efficiency. Bar graphs represent the mean ± SEM from three independent experiments each with three technical repeats. * $p \leq 0.05$, ** $p \leq 0.01$, *** $p \leq 0.001$ as determined by two-way ANOVA with Fisher's LSD test.

Examining cellular ATP, detachment led to a decrease in the relative ATP levels across all eight dual pool with the fold-reduction in ATP more pronounced at 48 h compared to 24 h (Figure 108b). Wildtype- or mutant- CtBP2 overexpression resulted in inhibition of ATP in certain attached conditions. Overexpression of the G189A mutant resulted in a statistically significant ($p \leq 0.01$) decrease in ATP levels in attached puro and HER2 cells at 24 h. Overexpression of the H321L mutant resulted in a statistically significant ($p \leq 0.05$) decrease in ATP levels in attached puro cells at 24 h. HER2 CtBP2 showed a statistical significant decrease ($p \leq 0.01$) in ATP levels at 48 h in attached conditions.

7.2.3 Characterisation of CtBP2-overexpressing dual pooled populations in 3D culture

The role of CtBP2 in ECM-detachment was examined using the MCF-10A acinar model of breast morphogenesis. Cells were cultured in 3D for 12 or 16 days and their luminal status and gross external morphology monitored by microscopy. At day 12 of morphogenesis the majority of parental acini have undergone luminal clearing and display a hollowed lumen (Debnath, Muthuswamy et al. 2003). Luminal apoptosis begins around day eight so day 12 is a relatively early time point to examine luminal clearing and should be a sufficient time point to monitor if CtBP2 provides a short-term protection from ECM-detachment. Looking at the later time point of day 16 allows me to examine whether this protection is more long-term.

Examining morphology at day 16 of morphogenesis, control dual pools (puro neo and HER2 neo) behaved as expected with puro neo acini adopting the spherical acini structure observed in parental acini (Debnath, Muthuswamy et al. 2003) and HER2 neo acini displaying an increase in the number of atypical structures (Figure 109a,b) (Muthuswamy, Li et al. 2001, Papadakis, Barker et al. 2016). Wildtype- or mutant- CtBP2 overexpression did not statistically significantly alter the percentage of atypical acini in either puro or HER2 dual pooled populations (Figure 109b).

Looking at luminal status control dual pools (puro neo and HER2 neo) continued to behave as expected. At day 12 of morphogenesis the majority of puro neo acini had undergone luminal clearing with only 37% of acini presenting as incompletely cleared (Figure 110a,b). In contrast HER2 neo acini presented with 79% of acini scoring as incompletely cleared. By day 16 of morphogenesis the number of incompletely cleared acini in both puro neo and HER2 neo had dropped but HER2 neo still had a higher percentage of incompletely cleared acini compared to puro neo (64% compared to 24%) (Figure 110c).

At day 12 of morphogenesis, overexpression of CtBP2 in the puro population (puro CtBP2) resulted in a statistically significant ($p \leq 0.001$) 1.42-fold increase in the percentage of incompletely cleared acini compared to control (puro neo) (Figure 110b). However, by day 16 of morphogenesis, while overexpression of CtBP2 resulted in a similar 1.42-fold increase in the percentage of incompletely cleared acini compared to control, statistical significance was lost (Figure 110c).

Puro G189A and puro H312L behaved similarly to puro CtBP2 when compared to puro neo with mutant CtBP2 overexpression resulting in statistically significant ($p \leq 0.001$) 1.52- and 1.71- fold increases in the percentage of incompletely cleared acini respectively compared to puro neo at day 12 of morphogenesis (Figure 110b). The percentage of incompletely cleared acini at day 16 of morphogenesis remained higher in mutant CtBP2-overexpressing puro populations compared to neo control but statistical significance was lost (Figure 110c), likewise to the behaviour of wildtype CtBP2 at this time point. At day 12 of morphogenesis, but not day 16, the percentage of incompletely cleared puro H321L acini was statistically significantly increased compared to puro CtBP2 ($p \leq 0.01$) and puro G189A ($p \leq 0.05$).

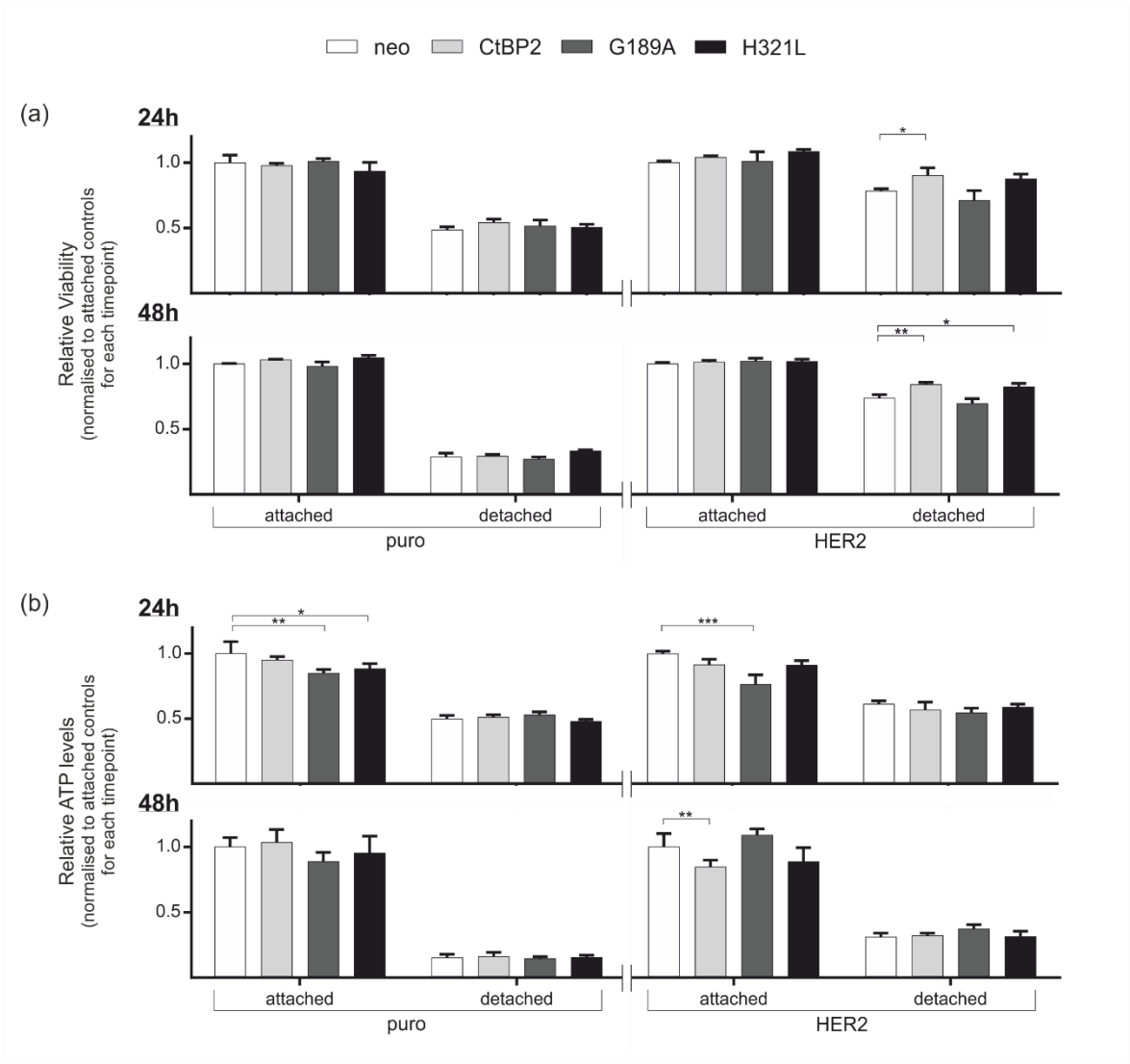

Figure 108 Effect of CtBP2 overexpression on cell viability in attachment and detachment

Cells (15,000 per well) were seeded onto standard tissue culture plates (attached) or polyHEMA-coated plastic (detached) for 24 h or 48 h. (a) Cell viability was examined using alamarBlue® reagent which was added to conditions 6 h prior to data collection. (b) ATP levels were examined using the ATPlite assay. Fluorometric (a) or luminometric data (b) was normalised for experimental variation and expressed relative to the appropriate vector control in attached conditions (puro neo or HER2 neo). Bar graphs represent the mean ± SEM from three independent experiments each with three technical repeats. * $p \leq 0.05$, ** $p \leq 0.01$, *** $p \leq 0.001$ as determined by a two-way ANOVA with Fisher's LSD test.

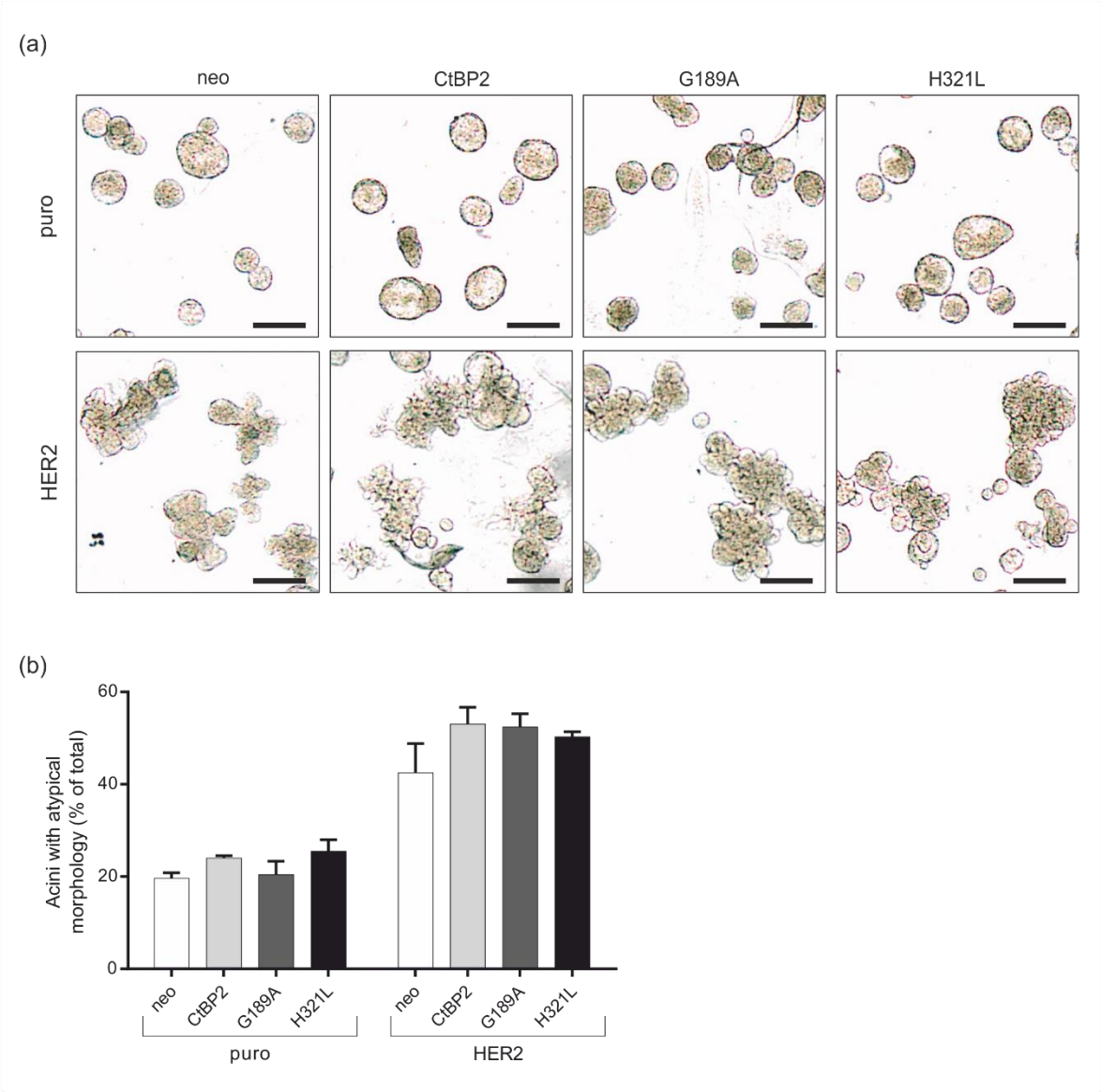

Figure 109 CtBP2 overexpression does not alter the external morphology of puro or HER2 acini

Acini were cultured for 16 days, fixed directly to minimise acini loss in wash steps (2% PFA final concentration) and mounted. High resolution pictures covering the entire slide were captured and all acini within a chamber scored manually. (a) Representative images of acini morphology are shown; scale bars show 200 µm. (b) Morphology was scored as normal or atypical, where atypical includes multiacinar, branching and non-rounded acini. The number of acini scoring as atypical was expressed as a percentage of the total acini scored. A minimum of 120 acini were present in each well. Bar graphs represent the mean ± SEM from three independent experiments each with three technical repeats.

In the HER2 dual populations wildtype CtBP2 overexpression had no statistical significant effects on the percentage of incompletely cleared acini compared to vector control at either day 12 or day 16 of morphogenesis (Figure 110b,c). At day 12 of morphogenesis HER2 G189A and HER2 H321L did not score statistically significantly differently to HER2 neo, although HER2 H321L displayed a statistically significant ($p \leq 0.01$) decrease in the percentage of incompletely cleared acini compared to HER2 CtBP2 and HER2 G189A (Figure 110b). At day 16 of morphogenesis HER2 G189A acini had a statistically significant ($p \leq 0.05$) increase in the percentage of incompletely cleared acini compared to HER2 neo and this was also statistically significantly ($p \leq 0.05$) increased compared to HER2 CtBP2 (Figure 110c).

7.3 CtBP2-driven luminal filling can be reversed by a CtBP inhibitor

To confirm that the effects of CtBP2 overexpression on luminal clearing in puro were a direct result of CtBP2 overexpression I used the CtBP inhibitor MTOB to reverse the phenotype (Figure 111). MTOB was added to acini cultures from day six of morphogenesis. As previously observed, wildtype- or mutant- CtBP2 overexpression in the presence of media alone resulted in a statistically significant ($p \leq 0.05$) increase in the percentage of incompletely cleared acini compared to neo control (Figure 111b). Combining data from three independent experiments there was a statistically significant ($p \leq 0.01$) 1.35-fold increase in the number of incompletely cleared acini in puro CtBP2 compared to puro neo in the presence of media alone (Figure 111c). G189A or H321L overexpression also led to a statistically significant ($p \leq 0.001$) 1.55- or 1.57-fold increase respectively in the number of incompletely cleared acini in the presence of media alone compared to puro neo.

Following MTOB treatment all four dual populations scored with a more hollowed phenotype than their respective population treated with media alone (Figure 111a). Puro neo acini displayed a 0.44-fold reduction in the number of incompletely cleared acini following MTOB treatment (Figure 111c) consistent with findings examining the effect of MTOB on the single puro pooled population (Figure 101).

CtBP overexpression in MTOB-treated acini only resulted in a 1.11-fold increase in the percentage of incompletely cleared acini compared to neo control which was not statistically significant (Figure 111c); this compares to the statistically significant 1.35-fold increase observed following CtBP2 overexpression in the presence of media alone. Consistent with this MTOB treatment in puro G189A and puro H312L resulted in smaller fold-increases in the number of incompletely cleared acini compared to puro neo than was observed in acini treated with media alone, and no statistically significant differences was observed compared to puro CtBP2.

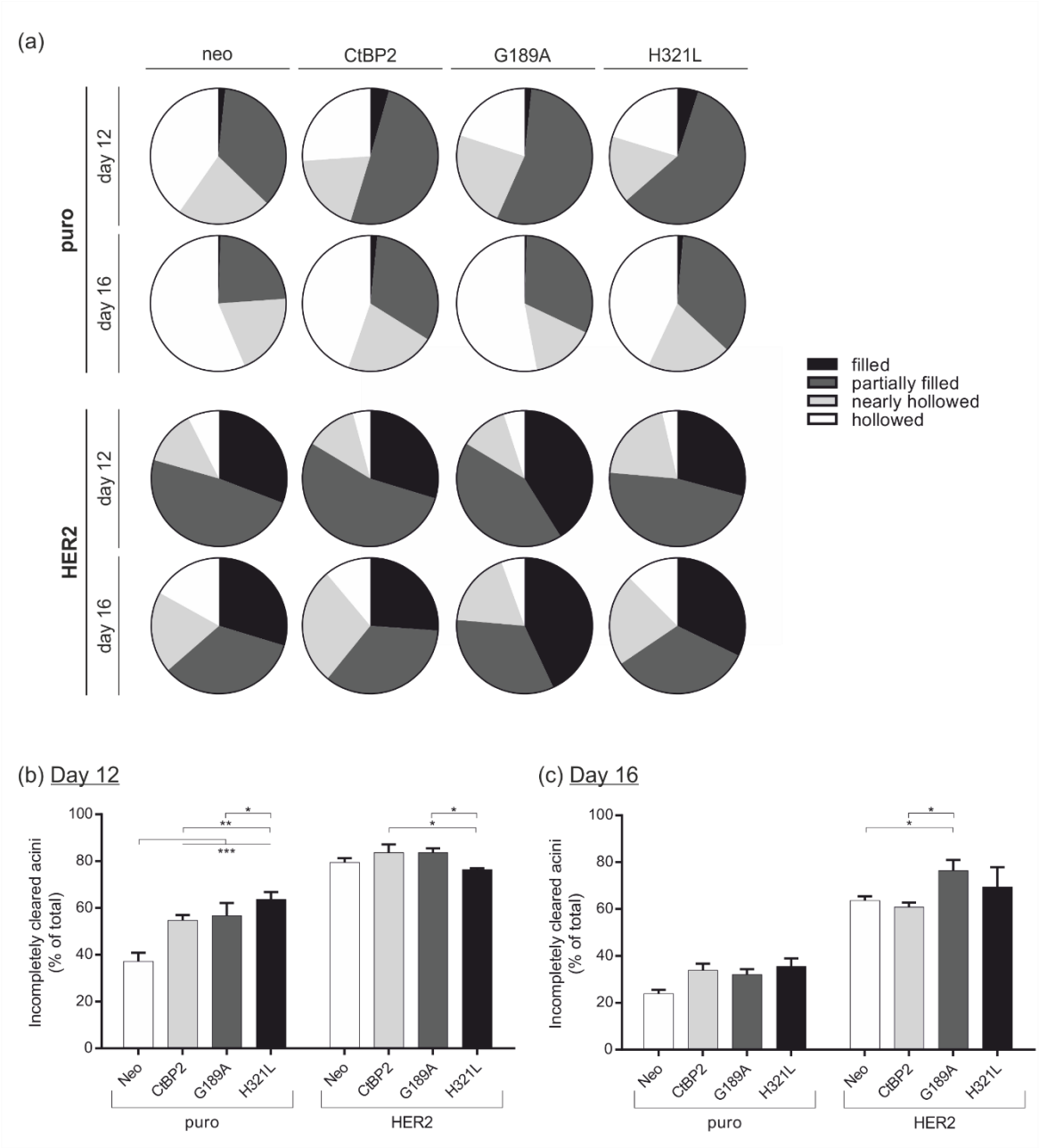

Figure 110 CtBP2 overexpression causes a delay in the onset of luminal clearing in puro dual pooled populations

Acini were cultured for the indicated number of days and stained with DAPI and phalloidin-TRITC. Confocal microscopy was utilised to score luminal status; looking through all focal planes, acini were scored as filled, partially filled, nearly hollowed or completely hollowed. (a) Pie chart representation shows the proportions of acini scoring in each category. The number of acini scoring as incompletely cleared (filled or partially filled) at day 12 (b) or day 16 (c) of morphogenesis was expressed as a percentage of the total acini scored. Bar graphs represent the mean ± SEM from three independent experiments each with three technical repeats. A minimum of 120 acini were scored for each condition within an independent experiment across triplicate wells. * $p \leq 0.05$, ** $p \leq 0.01$, *** $p \leq 0.001$ as determined by a two-way ANOVA with Fisher's LSD test.

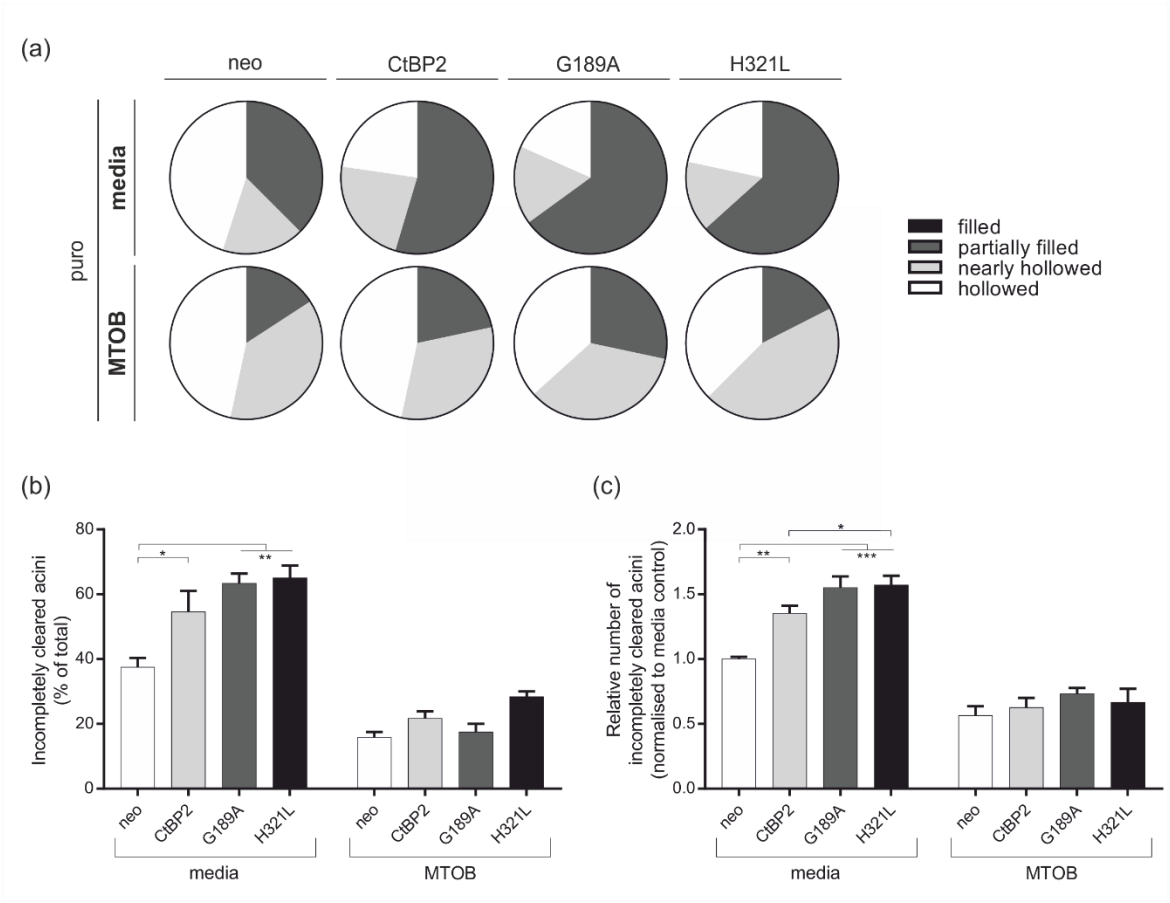

Figure 111 CtBP inhibition reverses CtBP2-driven filling in puro dual populations

Puro dual population acini were treated with media or methylthio-2-oxobutyric acid (MTOB, 4 mM) every 2 days from day 6 of morphogenesis. At day 12 acini were fixed and stained with DAPI and phalloidin-TRITC. Confocal microscopy was utilised to score luminal status; looking through all focal planes, acini were scored as filled, partially filled, nearly hollowed or completely hollowed. (a) Pie chart representation shows the proportions of acini scoring in each category from an independent experiment. (b) The number of acini scoring as incompletely cleared (filled or partially filled) was expressed as a percentage of the total acini scored. Bar graphs represent the mean ± SEM from an independent experiment with three technical repeats. A minimum of 120 acini were scored for each condition across triplicate wells. (c) Individual experiments were adjusted for experimental drift in the total luminal filling. Data was expressed relative to media condition in neo. Bar graphs represent the mean ± SEM from three independent experiments each with three technical repeats. * $p \leq 0.05$, ** $p \leq 0.01$, *** $p \leq 0.001$ as determined by a two-way ANOVA with Fisher's LSD test.

7.4 Discussion

This study examined the role of the intracellular metabolism sensor, CtBP2, in acinar morphogenesis using the MCF-10A model of the healthy breast and the HER2-driven model of early breast cancer. Findings from CtBP inhibition experiments and CtBP2-overexpressing populations showed a role for CtBP in promoting luminal cell survival in the MCF-10A model.

The CtBP inhibitor MTOB promotes luminal clearing

The CtBP inhibitor MTOB is a member of the α-keto acids family and was discovered in a search for potential substrates for the dehydrogenase activity of CtBP1 (Achouri, Noel et al. 2007). The catalytic efficiency of CtBP1 in the presence of MTOB was much higher than in the presence of other α-keto acids tested, suggesting that MTOB is a good substrate for CtBP dehydrogenase activity. Examining the crystal structure of CtBP in the presence of MTOB, MTOB sits in the active site adjacent to the NAD^+ consistent with MTOB acting as a substrate which can be reduced by NADH (Hilbert, Grossman et al. 2014). This would be expected to dissociate CtBP dimers and could be the mechanism by which MTOB suppresses CtBP activity. This is consistent with the findings that MTOB can inhibit transcriptional repression of CtBP-target genes (Straza, Paliwal et al. 2010, Di, Byun et al. 2013). As repression is an NADH-dependent function, the MTOB-inhibition of repression implies that MTOB is acting by attenuating dimerization.

In 2D MTOB increased viability in all conditions at 24 h while increasing viability in detached cells at 48 h (Figure 100). I also observed an increase in ATP in detached puro and HER2 cells at 48 h. This suggests that MTOB treatment may provide a level of protection from cell death following ECM-detachment. However, in the 3D acini setting I saw a different effect; MTOB accelerated luminal clearing resulting in a reduction in the number of incompletely cleared acini which indicates that MTOB attenuates survival in ECM-detached, luminal cells (Figure 101).

Due to MTOBs role in the methionine salvage pathway I also examined the metabolic consequences of this inhibitor in the short term Seahorse analyser (Figure 102). In this setting MTOB treatment had no clear metabolic consequences on glycolytic or mitochondrial activity. I also tried to do a long-term exposure to MTOB in the 2D setting however, following 48 h MTOB treatment, cells failed to plate onto a microplate. This is indicative that MTOB treatment prevents cells from plating onto V3-PS plastic; whether it is the MTOB pre-treatment or the presence of MTOB during re-plating that determines this inability to plate cannot be determined from this experimental set up.

While I cannot be certain that the phenotypic consequences of MTOB treatment are a direct result of CtBP inhibition, the short term Seahorse assay data (Figure 102) suggests that MTOB is

not having a metabolic effect. Assuming that MTOB is acting as a CtBP inhibitor in the 3D acini this supports a role for the metabolic sensors CtBPs in luminal cell survival in ECM-detached conditions. To further support a role of CtBPs in ECM-detached cells, I successfully generated dual pooled populations overexpressing CtBP2 (Figure 103, Figure 104).

Dual pooled populations overexpressing exogeneous CtBP2 do not have altered levels of endogenous CtBPs

In the puro and HER2 dual pooled populations CtBP2 is present in all three CtBP2-overexpressing populations (CtBP2, G189A and H321L) with nuclear localisation (Figure 103, Figure 104). This nuclear localisation is consistent with overexpression of the CtBP2 protein (Zhao, Subramanian et al. 2006). Staining was heterogeneous across the populations, consistent with a pooled population, and staining was not positive in 100% of cells. The negative staining for CtBP2 in certain cells may be due to the sensitivity of immunofluorescence staining in this setting or because CtBP2 is not present in these cells.

In isoform-specific CtBP knockdown experiments we have observed an upregulation of the untargeted isoform (unpublished data, Jeremy Blaydes group) suggesting a compensatory feedback loop exists between the two isoforms. It was therefore important for me to examine endogenous CtBP2 (Figure 105) and CtBP1 (Figure 106) levels in MCF-10A cells overexpressing CtBP2. Both CtBP1 and CtBP2 were localised to the nucleus suggesting that the cellular function of these proteins in MCF-10A relate to their nuclear functions. Homogeneous staining of CtBP2 and CtBP1 within puro neo and HER2 neo controls is consistent with homogeneous expression of a protein within a genetically identical population. Endogenous levels of CtBP2 and CtBP1 were not altered in CtBP2-overexpressing dual populations compared to controls, indicating that exogenous CtBP2 overexpression was not interfering with endogenous levels of these proteins. In addition, comparing puro neo to HER2 neo shows that HER2 overexpression does not alter levels of CtBPs.

CtBP2 overexpression increases the colony-forming efficiency of MCF-10A cells

A colony-forming assay was carried out to characterise the 2D consequences of CtBP2 overexpression (Figure 107). In puro cells wildtype, but not mutant, CtBP2 overexpression resulted in a statistically significant increase in the plating efficiency. The CtBP2 G189A mutant contains a mutation in the NADH-binding site (Thio, Bonventre et al. 2004) which makes it NADH-insensitive. This should therefore reduce the transcriptional repressor activity of CtBP2 but CtBP proteins do, however, have activity as monomers and this monomeric activity should be higher (Mirnezami, Campbell et al. 2003). The reversal of the CtBP2-driven phenotype in the presence of

the G189A functional mutant could suggest that the phenotype is driven by the dimeric form of CtBP2. However the H321L mutant also reversed the phenotype; this mutant has a mutation in the catalysis domain of the dehydrogenase domain (Thio, Bonventre et al. 2004) and is proposed to maintain a dimeric form of CtBP2 due to its inability to oxidise NADH to NAD^+. Based on the assumed function of the two mutants the reversal of the wildtype phenotype by both mutants is contradictory. It should be noted that the H321L mutant is not overexpressed to the same extent as the wildtype or G189A mutant in these populations (Figure 103).

HER2 dual populations had a lower colony forming efficiency than puro with wildtype- or mutant-CtBP2 overexpression having no statistically significant effects on plating efficiency. A reduced colony forming efficiency in HER2-overexpressing MCF-10A cells is consistent with previous findings (data not shown). The absence of an increase in plating efficiency in CtBP2-overexpressing HER2 compared to HER2 neo suggests that CtBP2 is unable to promote colony formation in the presence of HER2 overexpression.

The role of CtBP2 overexpression in cell survival in ECM-detached conditions

In 2D attached cells there is not a clear role for CtBP2 overexpression in influencing cell survival or cellular ATP levels (Figure 108). There is, however, evidence that CtBP2 overexpression in HER2 detached conditions statistically significantly increases cell viability when examined using an alamarBlue® assay suggesting that CtBP2 may provide a protection from ECM-detachment.

CtBP2 overexpression can delay the onset of luminal clearing in the MCF-10A acini model

I have shown previously that the acinar morphogenesis program is extremely sensitive to manipulation. In generating dual pooled populations I have increased the likelihood that I have introduced mutations in a single pooled population; the dual population has undergone two rounds of genetic manipulation and antibiotic selection. It was therefore important for me to confirm that the pBABEneo empty vector controls are behaving as expected (Figure 109, Figure 110). Puro neo behaved as parental acini with hollowed lumens and spherical structures (Debnath, Muthuswamy et al. 2003). HER2 neo behaved characteristically of HER2-overexpressing acini with filled structures and presentation of branching structures (Muthuswamy, Li et al. 2001, Debnath, Mills et al. 2002, Reginato, Mills et al. 2005, Papadakis, Barker et al. 2016).

In puro acini CtBP2 overexpression resulted in a statistically significant increase in the percentage of incompletely cleared acini at day 12 of morphogenesis, but significance was lost when examining the later time point of day 16. This implicates CtBP2 in promoting luminal cell survival but this delay is only temporal as clearing eventually occurred. This data fits with the data relating

to MTOB treatment of puro where I saw the reverse phenotype – CtBP inhibition accelerating luminal clearing (Figure 101). Furthermore treatment of CtBP2-overexpressing acini with MTOB reversed the CtBP2-driven luminal filling at day 12 of morphogenesis (Figure 111). Taken together this data supports a role for CtBP2 in cell survival in ECM-detached conditions.

When overexpressing the G189A or H321L mutants in puro, these acini scored similarly to wildtype CtBP2 with no statistically significant differences in the number of incompletely cleared acini (Figure 109). As MTOB is able to accelerate luminal clearing, and MTOB is proposed to inhibit NADH-dimerisation, I might expect that the G189A mutant would have similar effects to MTOB and accelerate luminal clearing while H321L would promote filling. The role of the G189A mutant in the literature is clear, inhibiting NADH-dimerisation of CtBP (Mirnezami, Campbell et al. 2003, Thio, Bonventre et al. 2004, Birts, Nijjar et al. 2013). If I had seen a reversal of the CtBP2-driven phenotype of filling in the presence of this mutant then I could conclude that the dimeric form of CtBP2 is important in driving the phenotype. However, the fact that the mutant is behaving as the controls leads me to question whether it is the monomer function that is important or, alternatively, the mutant is not as inactivating as I expected. As this is an overexpression situation, if the G189A mutant is not completely inactivated then the presence of more CtBP2 overall could mean that there is more overall CtBP2 activity.

In contrast to the G189A mutant the H321L mutant is less well characterised. While suggested to prevent dehydrogenase activity, which is hypothesised to keep CtBP in an NADH-bound, dimeric form, investigations into the catalytically inactive mutants has indicated that mutations in this region can inhibit NADH binding (unpublished data, Jeremy Blaydes group). Using a H321Q mutant equivalent in the CtBP1 isoform it was shown that CtBP failed to bind NADH. The function of the H321L mutant may therefore be different to expected. It should be noted that glutamine (Q) has a larger side chain than leucine (L), so it is possible that the glutamine mutation is a more disruptive to NADH binding than leucine.

It is important to highlight that endogenous CtBP is still present in this setting. The presence of wildtype CtBP1 and CtBP2 could be minimising the effect of a mutant. The CtBP2 overexpressed in this system contains silent mutations that makes it resistant to a custom siRNA which targets both CtBP1 and CtBP2 isoforms which gave me the opportunity to examine the role of mutant CtBP2 overexpression in the absence of CtBP2 knockdown. However transfection of puro with control siRNA using INTERFERin® (Polyplus transfection, Source BioScience, Nottingham, UK) resulted in highly filled acini structures at day 12 of morphogenesis (data not shown). This further highlights the sensitivity of acini morphogenesis to manipulation which has been discussed previously. The

shift in the morphogenesis program following transfection meant our knockdown experiments were not suitable for interpretation.

In HER2 acini wildtype CtBP2 overexpression had no effects on luminal clearing (Figure 110). This is likely to be a consequence of the fact that HER2 overexpression alone results in a high level of transformation and fully prevents luminal clearing, while CtBP2 overexpression appears to only led to a delay. At day 12 mutant CtBP2-overexpressing pooled populations did not score statistically differently to controls however, at day 16 the G189A mutant led to a statistically significant increase in the percentage of incompletely cleared acini compared to neo control and CtBP2 wildtype; this suggests that the G189A mutant can further support a complete inhibition of luminal clearing when combined with HER2 overexpression.

CtBP2 overexpression does not influence acinar morphology

I have found evidence to show that metabolic manipulation can also influence the external morphology of acini (Chapter 5 'The role of metabolism in MCF-10A acinar morphogenesis'). I therefore asked whether overexpression of CtBP2 will drive a change in morphology (Figure 109). However in this setting CtBP2 had no effect on the morphology of puro or HER2 acini.

Conclusion

To summarise manipulation of a metabolic sensor, CtBP, can influence acinar morphogenesis. In the MCF-10A model of the healthy breast CtBP inhibition (using MTOB) accelerated luminal clearing. In addition CtBP2 overexpression was shown to delay luminal clearing which was reversible by treatment with a CtBP inhibitor. This data supports findings presented in previous chapters highlighting a role for metabolism in cell survival in ECM-detached condition.

Chapter 8: Final Discussion

This thesis examines the role of Bag-1, HER2 and metabolism in cell survival following ECM-detachment. As stated in section 1.9 Outline of Study and Aims I set out to examine the following using the MCF-10A model of the breast duct:

- How Bag-1 influences luminal clearing, and the role of individual Bag-1 isoforms in this setting.
- How metabolism influences cell survival in ECM-detached cells.
- The role of HER2 in driving the metabolic changes that support development of filled, atypical MCF-10A acini.

The role of Bag-1 in luminal clearing

I utilised the MCF-10A acini model to examine the role of Bag-1 in initiating premalignant changes in the breast. The interest in this protein comes from studies showing that Bag-1 is frequently overexpressed in breast cancer, including early stages of the disease (Takayama, Krajewski et al. 1998, Brimmell, Burns et al. 1999, Tang, Shehata et al. 1999, Turner, Krajewski et al. 2001, Tang, Beck et al. 2004), which may implicate this protein in driving breast cancer development. In addition proof-of-principle studies have demonstrated that Bag-1 can influence breast cancer cell growth *in vitro* (Sharp, Crabb et al. 2009, Sharp, Cutress et al. 2009, Enthammer, Papadakis et al. 2013) and *in vivo* (Kudoh, Knee et al. 2002).

Contrary to work by Anderson *et al.* and our findings in the Bag-1L/A and Bag-1L/B stably transfected clones, Bag-1 was able to delay, but not fully prevent, luminal clearing in the retroviral pooled populations (Figure 50) (Anderson, Sutherland et al. 2010, Papadakis, Barker et al. 2016). As discussed in Chapter 4: 'The role of isoform-specific Bag-1S- or Bag-1L- overexpression on MCF-10A acinar morphogenesis' the use of pooled populations should minimise the chance of a phenotype which was not a direct consequence of Bag-1 overexpression being observed. I suggest that the MCF-10A/EcoR line used in the Anderson *et al.* study (Anderson, Sutherland et al. 2010) and the Bag-1L/A and Bag-1L/B clones (Papadakis, Barker et al. 2016) contain additional transformations that do not relate to Bag-1 overexpression which, when combined with Bag-1 overexpression, are driving the observed phenotypes. This highlights one of the disadvantages of cell line usage for the study of disease and emphasises the importance of good practice to minimise genotypic and phenotypic instability with regular characterisation and replacement of cell lines from cryopreserved stocks (discussed in section 1.2.1 Cell lines and primary tissue).

Although the data has not been reported here, I also attempted siRNA-mediated knockdown of Bag-1 using DharmaFECT1 (Thermo scientific, United Kingdom) to try to reverse the Bag-1L-driven atypical morphology reported in the Bag-1L/A and Bag-1L/B stable clones. I used a ON-TARGETplus SMART pool Bag-1 siRNA which would target all isoforms of Bag-1, endogenous and exogenous. Knockdown experiments proved challenging for a number of reasons. As mentioned, the Bag-1 siRNA targets all isoforms of Bag-1 while I was trying to examine the Bag-1L isoform specifically. In addition, knockdown must be carried out on 2D culture; while I was interesting in examining how Bag-1 influences later time points of acinar morphogenesis (cell survival in ECM-detachment and the gross morphology of a developed acini), knockdown of Bag-1 before acini are seeded may influence the early stages of morphogenesis. Thirdly, it is difficult to predict the efficiency and duration of Bag-1 knockdown in the 3D setting. While it is possible to collect lysates from 3D acini, it is technically challenging and requires a very high number of acini which meant that carrying out a timecourse of Bag-1 levels in 3D acini following knockdown was not feasible. Finally, transfection interfered with normal acinar morphogenesis and acini transfected with control siRNA had a more filled phenotype than non-transfected acini at day 12 of morphogenesis. As discussed in Chapter 7: Overexpression of a metabolic sensor interferes with MCF-10A acinar morphogenesis, INTERFERin®-based transfection also interfered with the morphogenesis of control transfected acini. These factors made knockdown experiments very difficult to interpret.

Despite the discrepancy in the extent of the Bag-1 protein's ability to influence acinar morphogenesis I have shown a role for Bag-1 in providing a protection from luminal clearing; this function was not isoform specific with both Bag-1S and Bag-1L overexpression inducing the phenotype. This finding supports the suggestion that Bag-1 overexpression is as an early transformation event which contributes to breast cancer initiation; Bag-1 overexpression is likely to contribute to tumorigenesis, at least in part, through its interaction with Raf-1 (Wang, Takayama et al. 1996, Song, Takeda et al. 2001) which drives MAPK signalling (Kermer, Krajewska et al. 2002, Anderson, Sutherland et al. 2010, Papadakis, Barker et al. 2016) and can repress Bim-regulated anoikis (Reginato, Mills et al. 2003, Anderson, Sutherland et al. 2010).

The role of HER2 in acinar transformation

The observation that cancer cells deregulate their cellular energetics has led to its inclusion as one of the ten hallmarks of cancer, implicating these changes as essential for cancer development and progression. (Figure 12) (Hanahan and Weinberg 2011). In line with this strategies to therapeutically target metabolism for cancer treatment have gained interest (Pelicano, Martin et al. 2006, Carracedo, Cantley et al. 2013). I used MCF-10A acini to study the role of metabolism in

the survival of luminal breast cells. Overexpression of HER2 in this model, an oncogene already implicated in driving metabolic changes associated with transformation (Schafer, Grassian et al. 2009), leads to filled acini structures which are phenotypically similar to early breast cancer; this allowed me to examine how oncogenes may influence metabolism to promote tumourigenesis.

While exploring our findings in MCF-10A acini in more detail using a second experimental model, HMECs, we found that HER2 overexpression was insufficient to drive transformation of HMEC acini (Figure 96). The MCF-10A cell line is considered a healthy breast line although it was isolated from a patient with fibrocystic disease and contains modest genetic modifications typical of cultured breast epithelial cells (Yaswen and Stampfer 2002) including loss of $p16^{INK4a}$ (Elenbaas, Spirio et al. 2001). $p16^{INK4a}$ is involved in cell cycle regulation, inhibiting progression from G1 phase to S phase, and is frequently described as a tumour suppressor gene (Liggett and Sidransky 1998, Rocco and Sidransky 2001, Ohtani, Yamakoshi et al. 2004, Romagosa, Simonetti et al. 2011). The presence of genetic modifications, such as loss of a tumour suppressor gene, highlights a limitation of using the MCF-10A cell line for modelling the healthy breast. The existence of mutations in MCF-10A, compared to HMEC which are isolated from the healthy adult female breast and should therefore contain minimal genetic modifications, could explain why I observed differences across the two models.

Media composition can influence acinar morphogenesis

Work comparing HMEC to MCF-10A also highlights the importance of media composition in contributing to certain cellular phenotypes (Figure 99). I also observed this with the MCF-10A cell line grown in DMEM alone (Figure 54) or in Biowest DMEM – F12 media (Figure 55, Figure 56). Medium is optimised to support the long term propagation and culture of cell lines and contains serum, growth factors and metabolites which can all influence cellular signalling. This is another limitation of using cell lines and highlights that the media composition should be a consideration when planning experiments. It also suggests that care should be taken when directly comparing findings taken from cell lines grown in different media types, as different media types add an additional level of variability to the system. Such variables need to be controlled as much as possible to ensure validity in the data generated.

3D models are important for the study of breast tumourigenesis

Although I have discussed some limitations of the MCF-10A cell line the work I have presented here has successfully utilised MCF-10A acini to further understand the role of Bag-1, HER2 and metabolism in breast tumourigenesis. Many of the phenotypes reported in this thesis relate to 3D characteristics which may not have been observed when studying traditional 2D culture. For

example findings relating to acinar morphology would not have been seen in 2D and, in addition, many of the metabolic inhibitors tested had limited effects on cell viability when examined in a 2D assay but had the ability to alter transformation in 3D. This emphasises the importance of using 3D models to investigate cancer initiation and progression.

Targeting FAO for cancer therapies

In addressing questions relating to the role of metabolism in cell transformation and cell survival in ECM-detached conditions I have shown that HER2 overexpression drives changes in cell metabolism (Figure 51, Figure 52) and that targeting these changes can attenuate transformation (Table 11). In particular I have shown that HER2 MCF-10A are more dependent on FAO than controls and that targeting this phenotype with the CPT-1 inhibitor etomoxir can completely reverse the HER2-driven phenotype of luminal filling (Figure 60). This data is consistent with other studies suggesting that targeting of FAO has potential for anticancer therapeutics because cancer cells utilise FAO for the generation of NADPH (to neutralise oxidative stress) and as a source of ATP production in conditions of metabolic stress (Schafer, Grassian et al. 2009, Carracedo, Cantley et al. 2013); targeting of this pathway should attenuate a cancer cells ability to meet these two cellular demands, inhibiting survival. Many pharmacological inhibitors of FAO have been pursued for treatment of heart disease and as a consequence there are a few compounds which have already been approved for human use (Lionetti, Stanley et al. 2011). CPT-1 specifically is considered a good target because this is the rate limiting step and in also upregulated in a variety of cancers, including breast (Gatza, Silva et al. 2014, Qu, Zeng et al. 2016), where it promotes cell survival (Zaugg, Yao et al. 2011, Pucci, Zonetti et al. 2016). While etomoxir was retired from early phase trials due to hepatotoxicity, perhexiline is currently approved for human use in Australia and Asia for the treatment of heart disease.

Targeting glycolysis for cancer therapy

I have also shown that targeting glycolysis has potential for cancer therapies. Inhibition of the Warburg effect will attenuate biomass generation impeding a cancer cells ability to grow and proliferate. Targeting of lactate dehydrogenase with oxamate or FX11, although note the exact target of FX11 is unclear, promoted luminal clearing within the MCF-10A model (Figure 72, Figure 76). Although oxamate is an unlikely therapeutic agent these findings support the development of specific, pharmacologically relevant inhibitors of lactate dehydrogenase for cancer therapeutics. By inhibiting lactate dehydrogenase it is expected that pyruvate will be forced to enter the citric acid cycle, reactivating the mitochondria and promoting cell death through enhanced ROS.

Although 2-deoxyglucose appeared to attenuate luminal clearing in the MCF-10A and HMEC acini models (Figure 68, Figure 98) promoting a transformed phenotype, I propose that these acini have arrested at an early time point before the onset of clearing. This suggests that 2-deoxyglucose treatment can promote cell cycle arrest and is consistent with other studies on the function of 2-deoxyglucose in solid tumours, although these studies also showed evidence of cytotoxicity (Maher, Krishan et al. 2004, Muley, Olinger et al. 2015). The structurally similar fluorescent analogue, fluoro-deoxy-glucose, is used widely for metabolic positron emission tomography scanning for the detection and diagnosis of cancer (Zhu, Lee et al. 2011) highlighting the potential of 2-deoxyglucose for cancer therapies and supporting early phase clinical trials of this compound which have already shown that it can be tolerated (Singh, Banerji et al. 2005, Raez, Papadopoulos et al. 2013).

Dicholoroacetate promoted cell transformation

Not all the inhibitors had the intended effects on MCF-10A acini. The indirect activator of pyruvate dehydrogenase, dichloroacetate, has received a lot of press attention due to its apparent anti-tumourigenic properties. This is an off-patent drug which can be self-prescribed by cancer sufferers. This small molecule is widely used for the treatment of lactic acidosis where it is well tolerated and has been tested in early phase cancer trials (Michelakis, Sutendra et al. 2010, Dunbar, Coats et al. 2014). It is expected that, through activation of pyruvate dehydrogenase, pyruvate is forced into the citric acid cycle reactivating the mitochondria and attenuating the Warburg effect. Consistent with this dichloroacetate promotes apoptosis and increased ROS production in cancer cells *in vitro* while inhibiting tumour growth *in vivo* (Bonnet, Archer et al. 2007). However in MCF-10A acini dichloroacetate had transforming effects on the control model of the healthy breast (Figure 87, Figure 88, Figure 89). This finding was not replicated in the HMEC acini which suggests that dichloroacetate-induced transformation requires other premalignant changes which are present in MCF-10A but not in HMEC. Even so, its existence in the MCF-10A model highlights the importance of further studies into the phenotypic consequences of metabolic manipulation in both healthy and cancerous tissues. There is a high level of cross talk between each metabolic pathway and this complexity must not be overlooked when attempting to target any of these pathways for therapies.

Metabolic sensor manipulation can also influence transformation

In addition to therapeutic targeting of metabolism I have shown that the metabolic sensor CtBP can also be targeted in cancer. Overexpression of CtBP2 in MCF-10A provided a protection from luminal clearing and promoted transformation (Figure 110). In a highly glycolytic cell, such as a cancerous one, the high ratio of NADH to NAD^+ would be expected to promote CtBP-dimerisation

and therefore activation of CtBP co-regulatory transcriptional complexes. Many of the transcriptional targets of CtBP are associated with tumourigenic properties (Table 1) and the observation that its overexpression promotes transformation in the MCF-10A model is in line with the hypothesis that CtBPs have a role in tumourigenesis. Use of the CtBP inhibitor MTOB attenuated the CtBP-driven transformation in MCF-10A and supports the development of CtBP inhibitors for cancer therapies (Figure 111). This is in line with other proof-of-principle studies from the Jeremy Blaydes laboratory examining the role of CtBPs in breast tumourigenesis (Birts, Harding et al. 2010) and supports the further development of CtBP inhibitors. A cyclic peptide, CP61, inhibits CtBP dimerisation *in vitro* (Birts, Nijjar et al. 2013) and provides a good starting point for the development of pharmacologically relevant CtBP-specific agents for targeting cancer.

The advantages of targeting metabolism

Targeting of metabolism for cancer therapy will not only provide new treatment options, which can help combat the occurrence of resistance, but it is hoped that such an approach will have limited off-target effects on healthy tissue. This relies on the fact that the metabolic pathways being targeted are deregulated in cancer cells compared to healthy tissue. While other non-transformed cell types undergo metabolic transformations, such as highly proliferative cells which also upregulate glycolysis (Vander Heiden, Cantley et al. 2009), targeting of two pathways simultaneously would allow lower inhibitor doses to be used. This would limit toxicity and would also minimise the development of resistance. Dual therapies require mutation(s) which target both the pathways being pharmacologically altered in order to develop resistance, reducing the frequency of occurrence.

Final remarks

The key findings of this thesis are that, although the MCF-10A cell line has its limitations, I have successfully utilised the MCF-10A acini 3D model of the breast to improve understanding of the phenotypic changes that contribute to breast tumourigenesis; such changes observed in 3D may not always be seen when using traditional 2D culture techniques. I have generated data to further support a role of Bag-1 in cell survival which may be an early transforming event in breast cancer initiation. In addition I have shown that cell metabolism can influence cell survival and induce cell signalling through a metabolic sensor which can further influence transformation. Interpretation of data collected using the MCF-10A cell line has been enhanced by extension of some of the work to primary HMEC derived acini. Finally the use of 3D models has furthered our understanding of how targeting of metabolism, either directly or through inhibition of CtBPs, has therapeutic potential in breast cancer.

References

Abildgaard, C., C. Dahl, A. L. Basse, T. Ma and P. Guldberg (2014). "Bioenergetic modulation with dichloroacetate reduces the growth of melanoma cells and potentiates their response to BRAFV600E inhibition." J Transl Med **12**: 247.

Achouri, Y., G. Noel and E. Van Schaftingen (2007). "2-Keto-4-methylthiobutyrate, an intermediate in the methionine salvage pathway, is a good substrate for CtBP1." Biochem Biophys Res Commun **352**(4): 903-906.

Afentakis, M., M. Dowsett, I. Sestak, J. Salter, T. Howell, A. Buzdar, J. Forbes and J. Cuzick (2013). "Immunohistochemical BAG1 expression improves the estimation of residual risk by IHC4 in postmenopausal patients treated with anastrazole or tamoxifen: a TransATAC study." Breast Cancer Res Treat **140**(2): 253-262.

Agnantis, N. K., M. Fatourous, I. Arampatzis, E. Briasoulis, E. V. Ignatiadou, E. Paraskevaidis and D. Roukous (2004). "Carcinogenesis of Breast Cancer: Advances and Applications." Gastric and Breast Cancer.

Al-Hajj, M., M. S. Wicha, A. Benito-Hernandez, S. J. Morrison and M. F. Clarke (2003). "Prospective identification of tumorigenic breast cancer cells." Proc Natl Acad Sci U S A **100**(7): 3983-3988.

Alberti, S., J. Demand, C. Esser, N. Emmerich, H. Schild and J. Hohfeld (2002). "Ubiquitylation of BAG-1 suggests a novel regulatory mechanism during the sorting of chaperone substrates to the proteasome." J Biol Chem **277**(48): 45920-45927.

Anderson, L. R., R. L. Sutherland and A. J. Butt (2010). "BAG-1 overexpression attenuates luminal apoptosis in MCF-10A mammary epithelial cells through enhanced RAF-1 activation." Oncogene **29**(4): 527-538.

Antoniou, A., P. D. Pharoah, S. Narod, H. A. Risch, J. E. Eyfjord, J. L. Hopper, N. Loman, H. Olsson, O. Johannsson, A. Borg, B. Pasini, P. Radice, S. Manoukian, D. M. Eccles, N. Tang, E. Olah, H. Anton-Culver, E. Warner, J. Lubinski, J. Gronwald, B. Gorski, H. Tulinius, S. Thorlacius, H. Eerola, H. Nevanlinna, K. Syrjakoski, O. P. Kallioniemi, D. Thompson, C. Evans, J. Peto, F. Lalloo, D. G. Evans and D. F. Easton (2003). "Average risks of breast and ovarian cancer associated with BRCA1 or BRCA2 mutations detected in case Series unselected for family history: a combined analysis of 22 studies." Am J Hum Genet **72**(5): 1117-1130.

Appleyard, M. V., K. E. Murray, P. J. Coates, S. Wullschleger, S. E. Bray, N. M. Kernohan, S. Fleming, D. R. Alessi and A. M. Thompson (2012). "Phenformin as prophylaxis and therapy in breast cancer xenografts." Br J Cancer **106**(6): 1117-1122.

Athanassiadou, P., D. Grapsa, M. Gonidi, A. M. Athanassiadou, A. Tsipis and E. Patsouris (2009). "CD24 expression has a prognostic impact in breast carcinoma." Pathol Res Pract **205**(8): 524-533.

Avruch, J., A. Khokhlatchev, J. M. Kyriakis, Z. Luo, G. Tzivion, D. Vavvas and X. F. Zhang (2001). "Ras activation of the Raf kinase: tyrosine kinase recruitment of the MAP kinase cascade." Recent Prog Horm Res **56**: 127-155.

Bannister, A. J. and T. Kouzarides (2011). "Regulation of chromatin by histone modifications." Cell Res **21**(3): 381-395.

Berg, J. M., J. L. Tymoczko and L. Stryer (2007). Biochemistry, W. H. Freeman and Company.

References

Berger, M. S., G. W. Locher, S. Saurer, W. J. Gullick, M. D. Waterfield, B. Groner and N. E. Hynes (1988). "Correlation of c-erbB-2 gene amplification and protein expression in human breast carcinoma with nodal status and nuclear grading." Cancer Res **48**(5): 1238-1243.

Bergman, L. M., C. N. Birts, M. Darley, B. Gabrielli and J. P. Blaydes (2009). "CtBPs promote cell survival through the maintenance of mitotic fidelity." Mol Cell Biol **29**(16): 4539-4551.

Bergman, L. M., L. Morris, M. Darley, A. H. Mirnezami, S. C. Gunatilake and J. P. Blaydes (2006). "Role of the unique N-terminal domain of CtBP2 in determining the subcellular localisation of CtBP family proteins." BMC Cell Biol **7**: 35.

Bickler, P. E. and J. A. Kelleher (1992). "Fructose-1,6-bisphosphate stabilizes brain intracellular calcium during hypoxia in rats." Stroke **23**(11): 1617-1622.

Birts, C. N., L. M. Bergman and J. P. Blaydes (2011). "CtBPs promote mitotic fidelity through their activities in the cell nucleus." Oncogene **30**(11): 1272-1280.

Birts, C. N., R. Harding, G. Soosaipillai, T. Halder, A. Azim-Araghi, M. Darley, R. I. Cutress, A. C. Bateman and J. P. Blaydes (2010). "Expression of CtBP family protein isoforms in breast cancer and their role in chemoresistance." Biol Cell **103**(1): 1-19.

Birts, C. N., S. K. Nijjar, C. A. Mardle, F. Hoakwie, P. J. Duriez, J. P. Blaydes and A. Tavassoli (2013). "A cyclic peptide inhibitor of C-terminal binding protein dimerization links metabolism with mitotic fidelity in breast cancer cells." Chemical Science **4**(8): 3046-3057.

Biswas, S. C. and L. A. Greene (2002). "Nerve growth factor (NGF) down-regulates the Bcl-2 homology 3 (BH3) domain-only protein Bim and suppresses its proapoptotic activity by phosphorylation." J Biol Chem **277**(51): 49511-49516.

Bollig-Fischer, A., T. G. Dewey and S. P. Ethier (2011). "Oncogene activation induces metabolic transformation resulting in insulin-independence in human breast cancer cells." PLoS One **6**(3): e17959.

Bonazzi, M., S. Spano, G. Turacchio, C. Cericola, C. Valente, A. Colanzi, H. S. Kweon, V. W. Hsu, E. V. Polishchuck, R. S. Polishchuck, M. Sallese, T. Pulvirenti, D. Corda and A. Luini (2005). "CtBP3/BARS drives membrane fission in dynamin-independent transport pathways." Nat Cell Biol **7**(6): 570-580.

Bonnet, S., S. L. Archer, J. Allalunis-Turner, A. Haromy, C. Beaulieu, R. Thompson, C. T. Lee, G. D. Lopaschuk, L. Puttagunta, S. Bonnet, G. Harry, K. Hashimoto, C. J. Porter, M. A. Andrade, B. Thebaud and E. D. Michelakis (2007). "A mitochondria-K+ channel axis is suppressed in cancer and its normalization promotes apoptosis and inhibits cancer growth." Cancer Cell **11**(1): 37-51.

Borowicz, S., M. Van Scoyk, S. Avasarala, M. K. Karuppusamy Rathinam, J. Tauler, R. K. Bikkavilli and R. A. Winn (2014). "The soft agar colony formation assay." J Vis Exp(92): e51998.

Breastcancer.org. "Genetics." Retrieved 13/12/2016, from http://www.breastcancer.org/risk/factors/genetics.

Bridges, H. R., A. J. Jones, M. N. Pollak and J. Hirst (2014). "Effects of metformin and other biguanides on oxidative phosphorylation in mitochondria." Biochem J **462**(3): 475-487.

Briknarova, K., S. Takayama, L. Brive, M. L. Havert, D. A. Knee, J. Velasco, S. Homma, E. Cabezas, J. Stuart, D. W. Hoyt, A. C. Satterthwait, M. Llinas, J. C. Reed and K. R. Ely (2001). "Structural analysis of BAG1 cochaperone and its interactions with Hsc70 heat shock protein." Nat Struct Biol **8**(4): 349-352.

Brimmell, M., J. S. Burns, P. Munson, L. McDonald, M. J. O'Hare, S. R. Lakhani and G. Packham (1999). "High level expression of differentially localized BAG-1 isoforms in some oestrogen receptor-positive human breast cancers." Br J Cancer **81**(6): 1042-1051.

Brown, R. S. and R. L. Wahl (1993). "Overexpression of Glut-1 glucose transporter in human breast cancer. An immunohistochemical study." Cancer **72**(10): 2979-2985.

Bukau, B., J. Weissman and A. Horwich (2006). "Molecular chaperones and protein quality control." Cell **125**(3): 443-451.

Burdall, S. E., A. M. Hanby, M. R. Lansdown and V. Speirs (2003). "Breast cancer cell lines: friend or foe?" Breast Cancer Res **5**(2): 89-95.

Cancer Research UK. Survival statistics for breast cancer Retrieved 18/06/2016, from http://www.cancerresearchuk.org/about-cancer/type/breast-cancer/treatment/statistics-and-outlook-for-breast-cancer.

Cancer Research UK. Breast cancer genes Retrieved 13/12/2016, from http://www.cancerresearchuk.org/about-cancer/type/breast-cancer/about/risks/breast-cancer-genes.

Canel, M., A. Serrels, M. C. Frame and V. G. Brunton (2013). "E-cadherin-integrin crosstalk in cancer invasion and metastasis." J Cell Sci **126**(Pt 2): 393-401.

Cardiff, R. D., M. R. Anver, B. A. Gusterson, L. Hennighausen, R. A. Jensen, M. J. Merino, S. Rehm, J. Russo, F. A. Tavassoli, L. M. Wakefield, J. M. Ward and J. E. Green (2000). "The mammary pathology of genetically engineered mice: the consensus report and recommendations from the Annapolis meeting." Oncogene **19**(8): 968-988.

Carracedo, A., L. C. Cantley and P. P. Pandolfi (2013). "Cancer metabolism: fatty acid oxidation in the limelight." Nat Rev Cancer **13**(4): 227-232.

Carracedo, A., D. Weiss, A. K. Leliaert, M. Bhasin, V. C. de Boer, G. Laurent, A. C. Adams, M. Sundvall, S. J. Song, K. Ito, L. S. Finley, A. Egia, T. Libermann, Z. Gerhart-Hines, P. Puigserver, M. C. Haigis, E. Maratos-Flier, A. L. Richardson, Z. T. Schafer and P. P. Pandolfi (2012). "A metabolic prosurvival role for PML in breast cancer." J Clin Invest **122**(9): 3088-3100.

Cederbaum, A. I., C. S. Lieber, D. S. Beattie and E. Rubin (1973). "Characterization of shuttle mechanisms for the transport of reducing equivalents into mitochondria." Arch Biochem Biophys **158**(2): 763-781.

Chen, J., J. Xiong, H. Liu, G. Chernenko and S. C. Tang (2002). "Distinct BAG-1 isoforms have different anti-apoptotic functions in BAG-1-transfected C33A human cervical carcinoma cell line." Oncogene **21**(46): 7050-7059.

Chen, S. and G. Parmigiani (2007). "Meta-analysis of BRCA1 and BRCA2 penetrance." J Clin Oncol **25**(11): 1329-1333.

Chinnadurai, G. (2002). "CtBP, an unconventional transcriptional corepressor in development and oncogenesis." Mol Cell **9**(2): 213-224.

Chinnadurai, G. (2007). "Transcriptional regulation by C-terminal binding proteins." Int J Biochem Cell Biol **39**(9): 1593-1607.

Chinnadurai, G. (2009). "The transcriptional corepressor CtBP: a foe of multiple tumor suppressors." Cancer Res **69**(3): 731-734.

References

Christofk, H. R., M. G. Vander Heiden, M. H. Harris, A. Ramanathan, R. E. Gerszten, R. Wei, M. D. Fleming, S. L. Schreiber and L. C. Cantley (2008). "The M2 splice isoform of pyruvate kinase is important for cancer metabolism and tumour growth." Nature **452**(7184): 230-233.

Clevenger, C. V., K. Thickman, W. Ngo, W. P. Chang, S. Takayama and J. C. Reed (1997). "Role of Bag-1 in the survival and proliferation of the cytokine-dependent lymphocyte lines, Ba/F3 and Nb2." Mol Endocrinol **11**(5): 608-618.

Coldwell, M. J., M. L. deSchoolmeester, G. A. Fraser, B. M. Pickering, G. Packham and A. E. Willis (2001). "The p36 isoform of BAG-1 is translated by internal ribosome entry following heat shock." Oncogene **20**(30): 4095-4100.

Comijn, J., G. Berx, P. Vermassen, K. Verschueren, L. van Grunsven, E. Bruyneel, M. Mareel, D. Huylebroeck and F. van Roy (2001). "The two-handed E box binding zinc finger protein SIP1 downregulates E-cadherin and induces invasion." Mol Cell **7**(6): 1267-1278.

Conklin, M. W. and P. J. Keely (2012). "Why the stroma matters in breast cancer: insights into breast cancer patient outcomes through the examination of stromal biomarkers." Cell Adh Migr **6**(3): 249-260.

Curtis, C., S. P. Shah, S. F. Chin, G. Turashvili, O. M. Rueda, M. J. Dunning, D. Speed, A. G. Lynch, S. Samarajiwa, Y. Yuan, S. Graf, G. Ha, G. Haffari, A. Bashashati, R. Russell, S. McKinney, M. Group, A. Langerod, A. Green, E. Provenzano, G. Wishart, S. Pinder, P. Watson, F. Markowetz, L. Murphy, I. Ellis, A. Purushotham, A. L. Borresen-Dale, J. D. Brenton, S. Tavare, C. Caldas and S. Aparicio (2012). "The genomic and transcriptomic architecture of 2,000 breast tumours reveals novel subgroups." Nature **486**(7403): 346-352.

Cutress, R. I. (2003). BAG-1 expression and function in breast cancer. Doctorate of Philosophy, University of Southampton.

Cutress, R. I., P. A. Townsend, A. C. Bateman, P. W. Johnson, K. Ryder, D. M. Barnes and G. Packham (2001). "BAG-1 immunostaining and survival in early breast cancer." J Clin Oncol **19**(16): 3706-3707.

Cutress, R. I., P. A. Townsend, M. Brimmell, A. C. Bateman, A. Hague and G. Packham (2002). "BAG-1 expression and function in human cancer." Br J Cancer **87**(8): 834-839.

Cutress, R. I., P. A. Townsend, A. Sharp, A. Maison, L. Wood, R. Lee, M. Brimmell, M. A. Mullee, P. W. Johnson, G. T. Royle, A. C. Bateman and G. Packham (2003). "The nuclear BAG-1 isoform, BAG-1L, enhances oestrogen-dependent transcription." Oncogene **22**(32): 4973-4982.

Davison, C. A., S. M. Durbin, M. R. Thau, V. R. Zellmer, S. E. Chapman, J. Diener, C. Wathen, W. M. Leevy and Z. T. Schafer (2013). "Antioxidant enzymes mediate survival of breast cancer cells deprived of extracellular matrix." Cancer Res **73**(12): 3704-3715.

De Matteis, M. A., M. Di Girolamo, A. Colanzi, M. Pallas, G. Di Tullio, L. J. McDonald, J. Moss, G. Santini, S. Bannykh, D. Corda and et al. (1994). "Stimulation of endogenous ADP-ribosylation by brefeldin A." Proc Natl Acad Sci U S A **91**(3): 1114-1118.

Debnath, J., K. R. Mills, N. L. Collins, M. J. Reginato, S. K. Muthuswamy and J. S. Brugge (2002). "The role of apoptosis in creating and maintaining luminal space within normal and oncogene-expressing mammary acini." Cell **111**(1): 29-40.

Debnath, J., S. K. Muthuswamy and J. S. Brugge (2003). "Morphogenesis and oncogenesis of MCF-10A mammary epithelial acini grown in three-dimensional basement membrane cultures." Methods **30**(3): 256-268.

Deck, L. M., R. E. Royer, B. B. Chamblee, V. M. Hernandez, R. R. Malone, J. E. Torres, L. A. Hunsaker, R. C. Piper, M. T. Makler and D. L. Vander Jagt (1998). "Selective inhibitors of human lactate dehydrogenases and lactate dehydrogenase from the malarial parasite Plasmodium falciparum." J Med Chem **41**(20): 3879-3887.

Deng, H., J. Liu, Y. Deng, G. Han, Y. G. Shellman, S. E. Robinson, J. J. Tentler, W. A. Robinson, D. A. Norris, X. J. Wang and Q. Zhang (2013). "CtBP1 is expressed in melanoma and represses the transcription of p16INK4a and Brca1." J Invest Dermatol **133**(5): 1294-1301.

Deng, Y., J. Liu, G. Han, S. L. Lu, S. Y. Wang, S. Malkoski, A. C. Tan, C. Deng, X. J. Wang and Q. Zhang (2010). "Redox-dependent Brca1 transcriptional regulation by an NADH-sensor CtBP1." Oncogene **29**(50): 6603-6608.

Di, L. J., J. S. Byun, M. M. Wong, C. Wakano, T. Taylor, S. Bilke, S. Baek, K. Hunter, H. Yang, M. Lee, C. Zvosec, G. Khramtsova, F. Cheng, C. M. Perou, C. R. Miller, R. Raab, O. I. Olopade and K. Gardner (2013). "Genome-wide profiles of CtBP link metabolism with genome stability and epithelial reprogramming in breast cancer." Nat Commun **4**: 1449.

Di, L. J., A. G. Fernandez, A. De Siervi, D. L. Longo and K. Gardner (2010). "Transcriptional regulation of BRCA1 expression by a metabolic switch." Nat Struct Mol Biol **17**(12): 1406-1413.

Drahota, Z., E. Palenickova, R. Endlicher, M. Milerova, J. Brejchova, M. Vosahlikova, P. Svoboda, L. Kazdova, M. Kalous, Z. Cervinkova and M. Cahova (2014). "Biguanides inhibit complex I, II and IV of rat liver mitochondria and modify their functional properties." Physiol Res **63**(1): 1-11.

Drynan, L., P. A. Quant and V. A. Zammit (1996). "Flux control exerted by mitochondrial outer membrane carnitine palmitoyltransferase over beta-oxidation, ketogenesis and tricarboxylic acid cycle activity in hepatocytes isolated from rats in different metabolic states." Biochem J **317 (Pt 3)**: 791-795.

Dunbar, E. M., B. S. Coats, A. L. Shroads, T. Langaee, A. Lew, J. R. Forder, J. J. Shuster, D. A. Wagner and P. W. Stacpoole (2014). "Phase 1 trial of dichloroacetate (DCA) in adults with recurrent malignant brain tumors." Invest New Drugs **32**(3): 452-464.

Eistetter, K. and H. P. O. Wolf (1986). "Etomoxir." Drugs of the Future **11**: 1034-1036.

Elenbaas, B., L. Spirio, F. Koerner, M. D. Fleming, D. B. Zimonjic, J. L. Donaher, N. C. Popescu, W. C. Hahn and R. A. Weinberg (2001). "Human breast cancer cells generated by oncogenic transformation of primary mammary epithelial cells." Genes Dev **15**(1): 50-65.

Enthammer, M., E. S. Papadakis, M. Salome Gachet, M. Deutsch, S. Schwaiger, K. Koziel, M. I. Ashraf, S. Khalid, G. Wolber, G. Packham, R. I. Cutress, H. Stuppner and J. Troppmair (2013). "Isolation of a novel thioflavin S-derived compound that inhibits BAG-1-mediated protein interactions and targets BRAF inhibitor-resistant cell lines." Mol Cancer Ther **12**(11): 2400-2414.

Farabegoli, F., M. H. Champeme, I. Bieche, D. Santini, C. Ceccarelli, M. Derenzini and R. Lidereau (2002). "Genetic pathways in the evolution of breast ductal carcinoma in situ." J Pathol **196**(3): 280-286.

Fjeld, C. C., W. T. Birdsong and R. H. Goodman (2003). "Differential binding of NAD+ and NADH allows the transcriptional corepressor carboxyl-terminal binding protein to serve as a metabolic sensor." Proc Natl Acad Sci U S A **100**(16): 9202-9207.

Fornaro, L., M. Lucchesi, C. Caparello, E. Vasile, S. Caponi, L. Ginocchi, G. Masi and A. Falcone (2011). "Anti-HER agents in gastric cancer: from bench to bedside." Nat Rev Gastroenterol Hepatol **8**(7): 369-383.

Frisch, S. M. and H. Francis (1994). "Disruption of epithelial cell-matrix interactions induces apoptosis." J Cell Biol **124**(4): 619-626.

Frixen, U. H., J. Behrens, M. Sachs, G. Eberle, B. Voss, A. Warda, D. Lochner and W. Birchmeier (1991). "E-cadherin-mediated cell-cell adhesion prevents invasiveness of human carcinoma cells." J Cell Biol **113**(1): 173-185.

Froesch, B. A., S. Takayama and J. C. Reed (1998). "BAG-1L protein enhances androgen receptor function." J Biol Chem **273**(19): 11660-11666.

Fung, C., R. Lock, S. Gao, E. Salas and J. Debnath (2008). "Induction of autophagy during extracellular matrix detachment promotes cell survival." Mol Biol Cell **19**(3): 797-806.

Gassler, C. S., T. Wiederkehr, D. Brehmer, B. Bukau and M. P. Mayer (2001). "Bag-1M accelerates nucleotide release for human Hsc70 and Hsp70 and can act concentration-dependent as positive and negative cofactor." J Biol Chem **276**(35): 32538-32544.

Gatza, M. L., G. O. Silva, J. S. Parker, C. Fan and C. M. Perou (2014). "An integrated genomics approach identifies drivers of proliferation in luminal-subtype human breast cancer." Nat Genet **46**(10): 1051-1059.

Gebauer, M., M. Zeiner and U. Gehring (1997). "Proteins interacting with the molecular chaperone hsp70/hsc70: physical associations and effects on refolding activity." FEBS Lett **417**(1): 109-113.

Gemba, T., T. Oshima and M. Ninomiya (1994). "Glutamate efflux via the reversal of the sodium-dependent glutamate transporter caused by glycolytic inhibition in rat cultured astrocytes." Neuroscience **63**(3): 789-795.

Gerdes, J., U. Schwab, H. Lemke and H. Stein (1983). "Production of a mouse monoclonal antibody reactive with a human nuclear antigen associated with cell proliferation." Int J Cancer **31**(1): 13-20.

Ginestier, C., M. H. Hur, E. Charafe-Jauffret, F. Monville, J. Dutcher, M. Brown, J. Jacquemier, P. Viens, C. G. Kleer, S. Liu, A. Schott, D. Hayes, D. Birnbaum, M. S. Wicha and G. Dontu (2007). "ALDH1 is a marker of normal and malignant human mammary stem cells and a predictor of poor clinical outcome." Cell Stem Cell **1**(5): 555-567.

Goldberg, E. B. and S. P. Colowick (1965). "The Role of Glycolysis in the Growth of Tumor Cells. 3. Lactic Dehydrogenase as the Site of Action of Oxamate on the Growth of Cultured Cells." J Biol Chem **240**: 2786-2790.

Goldberg, E. B., H. M. Nitowsky and S. P. Colowick (1965). "The Role of Glycolysis in the Growth of Tumor Cells. Iv. The Basis of Glucose Toxicity in Oxamate-Treated, Cultured Cells." J Biol Chem **240**: 2791-2796.

Gong, F., X. Peng, Y. Sang, M. Qiu, C. Luo, Z. He, X. Zhao and A. Tong (2013). "Dichloroacetate induces protective autophagy in LoVo cells: involvement of cathepsin D/thioredoxin-like protein 1 and Akt-mTOR-mediated signaling." Cell Death Dis **4**: e913.

Green, M. R. and J. Sambrook (2012). Molecular Cloning: A Laboratoy Manual, 2012 Cold Springs Harbor Laboratory Press.

Greenhouse, W. V. and A. L. Lehninger (1976). "Occurrence of the malate-aspartate shuttle in various tumor types." Cancer Res **36**(4): 1392-1396.

Grooteclaes, M., Q. Deveraux, J. Hildebrand, Q. Zhang, R. H. Goodman and S. M. Frisch (2003). "C-terminal-binding protein corepresses epithelial and proapoptotic gene expression programs." Proc Natl Acad Sci U S A **100**(8): 4568-4573.

Grooteclaes, M. L. and S. M. Frisch (2000). "Evidence for a function of CtBP in epithelial gene regulation and anoikis." Oncogene **19**(33): 3823-3828.

Guan, C., H. Shi, H. Wang, J. Zhang, W. Ni, B. Chen, S. Hou, X. Yang, A. Shen and R. Ni (2013). "CtBP2 contributes to malignant development of human esophageal squamous cell carcinoma by regulation of p16INK4A." J Cell Biochem **114**(6): 1343-1354.

Guerin, M., M. Gabillot, M. C. Mathieu, J. P. Travagli, M. Spielmann, N. Andrieu and G. Riou (1989). "Structure and expression of c-erbB-2 and EGF receptor genes in inflammatory and non-inflammatory breast cancer: prognostic significance." Int J Cancer **43**(2): 201-208.

Guzey, M., S. Takayama and J. C. Reed (2000). "BAG1L enhances trans-activation function of the vitamin D receptor." J Biol Chem **275**(52): 40749-40756.

Haga, Y., N. Miwa, S. Jahangeer, T. Okada and S. Nakamura (2009). "CtBP1/BARS is an activator of phospholipase D1 necessary for agonist-induced macropinocytosis." EMBO J **28**(9): 1197-1207.

Halestrap, A. P. (1975). "The mitochondrial pyruvate carrier. Kinetics and specificity for substrates and inhibitors." Biochem J **148**(1): 85-96.

Halestrap, A. P. (2012). "The mitochondrial pyruvate carrier: has it been unearthed at last?" Cell Metab **16**(2): 141-143.

Halestrap, A. P. and R. M. Denton (1974). "Specific inhibition of pyruvate transport in rat liver mitochondria and human erythrocytes by alpha-cyano-4-hydroxycinnamate." Biochem J **138**(2): 313-316.

Halestrap, A. P. and M. C. Wilson (2012). "The monocarboxylate transporter family--role and regulation." IUBMB Life **64**(2): 109-119.

Hammond, S. L., R. G. Ham and M. R. Stampfer (1984). "Serum-free growth of human mammary epithelial cells: rapid clonal growth in defined medium and extended serial passage with pituitary extract." Proc Natl Acad Sci U S A **81**(17): 5435-5439.

Hanahan, D. and R. A. Weinberg (2000). "The hallmarks of cancer." Cell **100**(1): 57-70.

Hanahan, D. and R. A. Weinberg (2011). "Hallmarks of cancer: the next generation." Cell **144**(5): 646-674.

Hansen, R. K. and M. J. Bissell (2000). "Tissue architecture and breast cancer: the role of extracellular matrix and steroid hormones." Endocr Relat Cancer **7**(2): 95-113.

Hickman, J. A., R. Graeser, R. de Hoogt, S. Vidic, C. Brito, M. Gutekunst, H. van der Kuip and I. P. Consortium (2014). "Three-dimensional models of cancer for pharmacology and cancer cell biology: capturing tumor complexity in vitro/ex vivo." Biotechnol J **9**(9): 1115-1128.

Hilbert, B. J., S. R. Grossman, C. A. Schiffer and W. E. Royer, Jr. (2014). "Crystal structures of human CtBP in complex with substrate MTOB reveal active site features useful for inhibitor design." FEBS Lett **588**(9): 1743-1748.

Hildebrand, J. D. and P. Soriano (2002). "Overlapping and unique roles for C-terminal binding protein 1 (CtBP1) and CtBP2 during mouse development." Mol Cell Biol **22**(15): 5296-5307.

References

Hinitt, C. A., J. Wood, S. S. Lee, A. C. Williams, J. L. Howarth, C. P. Glover, J. B. Uney and A. Hague (2010). "BAG-1 enhances cell-cell adhesion, reduces proliferation and induces chaperone-independent suppression of hepatocyte growth factor-induced epidermal keratinocyte migration." Exp Cell Res **316**(13): 2042-2060.

Hohfeld, J. and S. Jentsch (1997). "GrpE-like regulation of the hsc70 chaperone by the anti-apoptotic protein BAG-1." EMBO J **16**(20): 6209-6216.

Holliday, D. L., K. T. Brouilette, A. Markert, L. A. Gordon and J. L. Jones (2009). "Novel multicellular organotypic models of normal and malignant breast: tools for dissecting the role of the microenvironment in breast cancer progression." Breast Cancer Res **11**(1): R3.

Hong, C. S., N. A. Graham, W. Gu, C. Espindola Camacho, V. Mah, E. L. Maresh, M. Alavi, L. Bagryanova, P. A. Krotee, B. K. Gardner, I. S. Behbahan, S. Horvath, D. Chia, I. K. Mellinghoff, S. A. Hurvitz, S. M. Dubinett, S. E. Critchlow, S. K. Kurdistani, L. Goodglick, D. Braas, T. G. Graeber and H. R. Christofk (2016). "MCT1 Modulates Cancer Cell Pyruvate Export and Growth of Tumors that Co-express MCT1 and MCT4." Cell Rep **14**(7): 1590-1601.

Hovey, R. C., T. B. McFadden and R. M. Akers (1999). "Regulation of mammary gland growth and morphogenesis by the mammary fat pad: a species comparison." J Mammary Gland Biol Neoplasia **4**(1): 53-68.

Howlader N, Noone AM, Krapcho M, et al. (eds). SEER Cancer Statistics Review, 1975-2011, National Cancer Institute. Bethesda, MD, http://seer.cancer.gov/csr/1975_2011/ , based on November 2013 SEER data submission, posted to the SEER web site, April 2014.

Ignatoski, K. M., A. J. Lapointe, E. H. Radany and S. P. Ethier (1999). "erbB-2 overexpression in human mammary epithelial cells confers growth factor independence." Endocrinology **140**(8): 3615-3622.

Imbalzano, K. M., I. Tatarkova, A. N. Imbalzano and J. A. Nickerson (2009). "Increasingly transformed MCF-10A cells have a progressively tumor-like phenotype in three-dimensional basement membrane culture." Cancer Cell Int **9**: 7.

Jaganathan, H., J. Gage, F. Leonard, S. Srinivasan, G. R. Souza, B. Dave and B. Godin (2014). "Three-dimensional in vitro co-culture model of breast tumor using magnetic levitation." Sci Rep **4**: 6468.

Janzer, A., N. J. German, K. N. Gonzalez-Herrera, J. M. Asara, M. C. Haigis and K. Struhl (2014). "Metformin and phenformin deplete tricarboxylic acid cycle and glycolytic intermediates during cell transformation and NTPs in cancer stem cells." Proc Natl Acad Sci U S A **111**(29): 10574-10579.

Jiang, P., W. Du, X. Wang, A. Mancuso, X. Gao, M. Wu and X. Yang (2011). "p53 regulates biosynthesis through direct inactivation of glucose-6-phosphate dehydrogenase." Nat Cell Biol **13**(3): 310-316.

Kabbage, M. and M. B. Dickman (2008). "The BAG proteins: a ubiquitous family of chaperone regulators." Cell Mol Life Sci **65**(9): 1390-1402.

Kang, S. S., Y. K. Chun, M. H. Hur, H. K. Lee, Y. J. Kim, S. R. Hong, J. H. Lee, S. G. Lee and Y. K. Park (2002). "Clinical significance of glucose transporter 1 (GLUT1) expression in human breast carcinoma." Jpn J Cancer Res **93**(10): 1123-1128.

Katsanis, N. and E. M. Fisher (1998). "A novel C-terminal binding protein (CTBP2) is closely related to CTBP1, an adenovirus E1A-binding protein, and maps to human chromosome 21q21.3." Genomics **47**(2): 294-299.

Katz, M., I. Amit, A. Citri, T. Shay, S. Carvalho, S. Lavi, F. Milanezi, L. Lyass, N. Amariglio, J. Jacob-Hirsch, N. Ben-Chetrit, G. Tarcic, M. Lindzen, R. Avraham, Y. C. Liao, P. Trusk, A. Lyass, G. Rechavi, N. L. Spector, S. H. Lo, F. Schmitt, S. S. Bacus and Y. Yarden (2007). "A reciprocal tensin-3-cten switch mediates EGF-driven mammary cell migration." Nat Cell Biol **9**(8): 961-969.

Kennedy, J. A., S. A. Unger and J. D. Horowitz (1996). "Inhibition of carnitine palmitoyltransferase-1 in rat heart and liver by perhexiline and amiodarone." Biochem Pharmacol **52**(2): 273-280.

Kenny, P. A., G. Y. Lee, C. A. Myers, R. M. Neve, J. R. Semeiks, P. T. Spellman, K. Lorenz, E. H. Lee, M. H. Barcellos-Hoff, O. W. Petersen, J. W. Gray and M. J. Bissell (2007). "The morphologies of breast cancer cell lines in three-dimensional assays correlate with their profiles of gene expression." Mol Oncol **1**(1): 84-96.

Kermer, P., M. Krajewska, J. M. Zapata, S. Takayama, J. Mai, S. Krajewski and J. C. Reed (2002). "Bag1 is a regulator and marker of neuronal differentiation." Cell Death Differ **9**(4): 405-413.

Kim, I. Y., H. Y. Yong, K. W. Kang and A. Moon (2009). "Overexpression of ErbB2 induces invasion of MCF10A human breast epithelial cells via MMP-9." Cancer Lett **275**(2): 227-233.

Kim, T. K. and J. H. Eberwine (2010). "Mammalian cell transfection: the present and the future." Anal Bioanal Chem **397**(8): 3173-3178.

Knee, D. A., B. A. Froesch, U. Nuber, S. Takayama and J. C. Reed (2001). "Structure-function analysis of Bag1 proteins. Effects on androgen receptor transcriptional activity." J Biol Chem **276**(16): 12718-12724.

Kraus, M. H., N. C. Popescu, S. C. Amsbaugh and C. R. King (1987). "Overexpression of the EGF receptor-related proto-oncogene erbB-2 in human mammary tumor cell lines by different molecular mechanisms." EMBO J **6**(3): 605-610.

Kudoh, M., D. A. Knee, S. Takayama and J. C. Reed (2002). "Bag1 proteins regulate growth and survival of ZR-75-1 human breast cancer cells." Cancer Res **62**(6): 1904-1909.

Kullmann, M., J. Schneikert, J. Moll, S. Heck, M. Zeiner, U. Gehring and A. C. Cato (1998). "RAP46 is a negative regulator of glucocorticoid receptor action and hormone-induced apoptosis." J Biol Chem **273**(23): 14620-14625.

Kumar, V., J. E. Carlson, K. A. Ohgi, T. A. Edwards, D. W. Rose, C. R. Escalante, M. G. Rosenfeld and A. K. Aggarwal (2002). "Transcription corepressor CtBP is an NAD(+)-regulated dehydrogenase." Mol Cell **10**(4): 857-869.

Kunz-Schughart, L. A., J. P. Freyer, F. Hofstaedter and R. Ebner (2004). "The use of 3-D cultures for high-throughput screening: the multicellular spheroid model." J Biomol Screen **9**(4): 273-285.

Kuppuswamy, M., S. Vijayalingam, L. J. Zhao, Y. Zhou, T. Subramanian, J. Ryerse and G. Chinnadurai (2008). "Role of the PLDLS-binding cleft region of CtBP1 in recruitment of core and auxiliary components of the corepressor complex." Mol Cell Biol **28**(1): 269-281.

Le, A., C. R. Cooper, A. M. Gouw, R. Dinavahi, A. Maitra, L. M. Deck, R. E. Royer, D. L. Vander Jagt, G. L. Semenza and C. V. Dang (2010). "Inhibition of lactate dehydrogenase A induces oxidative stress and inhibits tumor progression." Proc Natl Acad Sci U S A **107**(5): 2037-2042.

Lee, J. M., S. Dedhar, R. Kalluri and E. W. Thompson (2006). "The epithelial-mesenchymal transition: new insights in signaling, development, and disease." J Cell Biol **172**(7): 973-981.

Lee, S. S., S. J. Crabb, N. Janghra, C. Carlberg, A. C. Williams, R. I. Cutress, G. Packham and A. Hague (2007). "Subcellular localisation of BAG-1 and its regulation of vitamin D receptor-mediated

transactivation and involucrin expression in oral keratinocytes: implications for oral carcinogenesis." Exp Cell Res **313**(15): 3222-3238.

Leers, M. P., W. Kolgen, V. Bjorklund, T. Bergman, G. Tribbick, B. Persson, P. Bjorklund, F. C. Ramaekers, B. Bjorklund, M. Nap, H. Jornvall and B. Schutte (1999). "Immunocytochemical detection and mapping of a cytokeratin 18 neo-epitope exposed during early apoptosis." J Pathol **187**(5): 567-572.

Lei, K. and R. J. Davis (2003). "JNK phosphorylation of Bim-related members of the Bcl2 family induces Bax-dependent apoptosis." Proc Natl Acad Sci U S A **100**(5): 2432-2437.

Levkowitz, G., H. Waterman, S. A. Ettenberg, M. Katz, A. Y. Tsygankov, I. Alroy, S. Lavi, K. Iwai, Y. Reiss, A. Ciechanover, S. Lipkowitz and Y. Yarden (1999). "Ubiquitin ligase activity and tyrosine phosphorylation underlie suppression of growth factor signaling by c-Cbl/Sli-1." Mol Cell **4**(6): 1029-1040.

Ley, R., K. Balmanno, K. Hadfield, C. Weston and S. J. Cook (2003). "Activation of the ERK1/2 signaling pathway promotes phosphorylation and proteasome-dependent degradation of the BH3-only protein, Bim." J Biol Chem **278**(21): 18811-18816.

Ley, R., K. E. Ewings, K. Hadfield, E. Howes, K. Balmanno and S. J. Cook (2004). "Extracellular signal-regulated kinases 1/2 are serum-stimulated "Bim(EL) kinases" that bind to the BH3-only protein Bim(EL) causing its phosphorylation and turnover." J Biol Chem **279**(10): 8837-8847.

Li, Z., F. U. Hartl and A. Bracher (2013). "Structure and function of Hip, an attenuator of the Hsp70 chaperone cycle." Nat Struct Mol Biol **20**(8): 929-935.

Liberali, P., E. Kakkonen, G. Turacchio, C. Valente, A. Spaar, G. Perinetti, R. A. Bockmann, D. Corda, A. Colanzi, V. Marjomaki and A. Luini (2008). "The closure of Pak1-dependent macropinosomes requires the phosphorylation of CtBP1/BARS." EMBO J **27**(7): 970-981.

Liggett, W. H., Jr. and D. Sidransky (1998). "Role of the p16 tumor suppressor gene in cancer." J Clin Oncol **16**(3): 1197-1206.

Lin, G., D. K. Hill, G. Andrejeva, J. K. Boult, H. Troy, A. C. Fong, M. R. Orton, R. Panek, H. G. Parkes, M. Jafar, D. M. Koh, S. P. Robinson, I. R. Judson, J. R. Griffiths, M. O. Leach, T. R. Eykyn and Y. L. Chung (2014). "Dichloroacetate induces autophagy in colorectal cancer cells and tumours." Br J Cancer **111**(2): 375-385.

Lin, Y., F. Lv, F. Liu, X. Guo, Y. Fan, F. Gu, J. Gu and L. Fu (2015). "High Expression of Pyruvate Kinase M2 is Associated with Chemosensitivity to Epirubicin and 5-Fluorouracil in Breast Cancer." J Cancer **6**(11): 1130-1139.

Lionetti, V., W. C. Stanley and F. A. Recchia (2011). "Modulating fatty acid oxidation in heart failure." Cardiovasc Res **90**(2): 202-209.

Liu, R., S. Takayama, Y. Zheng, B. Froesch, G. Q. Chen, X. Zhang, J. C. Reed and X. K. Zhang (1998). "Interaction of BAG-1 with retinoic acid receptor and its inhibition of retinoic acid-induced apoptosis in cancer cells." J Biol Chem **273**(27): 16985-16992.

Loreck, D. J., J. Galarraga, J. Van der Feen, J. M. Phang, B. H. Smith and C. J. Cummins (1987). "Regulation of the pentose phosphate pathway in human astrocytes and gliomas." Metab Brain Dis **2**(1): 31-46.

Luciano, F., A. Jacquel, P. Colosetti, M. Herrant, S. Cagnol, G. Pages and P. Auberger (2003). "Phosphorylation of Bim-EL by Erk1/2 on serine 69 promotes its degradation via the proteasome pathway and regulates its proapoptotic function." Oncogene **22**(43): 6785-6793.

Luders, J., J. Demand and J. Hohfeld (2000). "The ubiquitin-related BAG-1 provides a link between the molecular chaperones Hsc70/Hsp70 and the proteasome." J Biol Chem **275**(7): 4613-4617.

Luders, J., J. Demand, O. Papp and J. Hohfeld (2000). "Distinct isoforms of the cofactor BAG-1 differentially affect Hsc70 chaperone function." J Biol Chem **275**(20): 14817-14823.

Luftner, D., J. Mesterharm, C. Akrivakis, R. Geppert, P. E. Petrides, K. D. Wernecke and K. Possinger (2000). "Tumor type M2 pyruvate kinase expression in advanced breast cancer." Anticancer Res **20**(6D): 5077-5082.

Maher, J. C., A. Krishan and T. J. Lampidis (2004). "Greater cell cycle inhibition and cytotoxicity induced by 2-deoxy-D-glucose in tumor cells treated under hypoxic vs aerobic conditions." Cancer Chemother Pharmacol **53**(2): 116-122.

Manske, M. (2006). GENtle, a free multi-purpose molecular biology tool PhD thesis, Universität zu Köln.

Marani, M., T. Tenev, D. Hancock, J. Downward and N. R. Lemoine (2002). "Identification of novel isoforms of the BH3 domain protein Bim which directly activate Bax to trigger apoptosis." Mol Cell Biol **22**(11): 3577-3589.

Martin-Requero, A., M. S. Ayuso and R. Parrilla (1986). "Interaction of oxamate with the gluconeogenic pathway in rat liver." Arch Biochem Biophys **246**(1): 114-127.

Martin-Requero, A., M. S. Ayuso and R. Parrilla (1986). "Rate-limiting steps for hepatic gluconeogenesis. Mechanism of oxamate inhibition of mitochondrial pyruvate metabolism." J Biol Chem **261**(30): 13973-13978.

Medina, R. A. and G. I. Owen (2002). "Glucose transporters: expression, regulation and cancer." Biol Res **35**(1): 9-26.

Meiners, S., V. Brinkmann, H. Naundorf and W. Birchmeier (1998). "Role of morphogenetic factors in metastasis of mammary carcinoma cells." Oncogene **16**(1): 9-20.

Meredith, J. E., Jr., B. Fazeli and M. A. Schwartz (1993). "The extracellular matrix as a cell survival factor." Mol Biol Cell **4**(9): 953-961.

Merlo, G. R., F. Basolo, L. Fiore, L. Duboc and N. E. Hynes (1995). "p53-dependent and p53-independent activation of apoptosis in mammary epithelial cells reveals a survival function of EGF and insulin." J Cell Biol **128**(6): 1185-1196.

Michelakis, E. D., G. Sutendra, P. Dromparis, L. Webster, A. Haromy, E. Niven, C. Maguire, T. L. Gammer, J. R. Mackey, D. Fulton, B. Abdulkarim, M. S. McMurtry and K. C. Petruk (2010). "Metabolic modulation of glioblastoma with dichloroacetate." Sci Transl Med **2**(31): 31ra34.

Millar, E. K., L. R. Anderson, C. M. McNeil, S. A. O'Toole, M. Pinese, P. Crea, A. L. Morey, A. V. Biankin, S. M. Henshall, E. A. Musgrove, R. L. Sutherland and A. J. Butt (2009). "BAG-1 predicts patient outcome and tamoxifen responsiveness in ER-positive invasive ductal carcinoma of the breast." Br J Cancer **100**(1): 123-133.

Miller, F. R., H. D. Soule, L. Tait, R. J. Pauley, S. R. Wolman, P. J. Dawson and G. H. Heppner (1993). "Xenograft model of progressive human proliferative breast disease." J Natl Cancer Inst **85**(21): 1725-1732.

Mirnezami, A. H., S. J. Campbell, M. Darley, J. N. Primrose, P. W. Johnson and J. P. Blaydes (2003). "Hdm2 recruits a hypoxia-sensitive corepressor to negatively regulate p53-dependent transcription." Curr Biol **13**(14): 1234-1239.

Miskimins, W. K., H. J. Ahn, J. Y. Kim, S. Ryu, Y. S. Jung and J. Y. Choi (2014). "Synergistic anti-cancer effect of phenformin and oxamate." PLoS One **9**(1): e85576.

Mroz, E. A., A. H. Baird, W. A. Michaud and J. W. Rocco (2008). "COOH-terminal binding protein regulates expression of the p16INK4A tumor suppressor and senescence in primary human cells." Cancer Res **68**(15): 6049-6053.

Mueckler, M. and B. Thorens (2013). "The SLC2 (GLUT) family of membrane transporters." Mol Aspects Med **34**(2-3): 121-138.

Muley, P., A. Olinger and H. Tummala (2015). "2-Deoxyglucose induces cell cycle arrest and apoptosisin colorectal cancer cells independent of its glycolysis inhibition." Nutr Cancer **67**(3): 514-522.

Muthuswamy, S. K., D. Li, S. Lelievre, M. J. Bissell and J. S. Brugge (2001). "ErbB2, but not ErbB1, reinitiates proliferation and induces luminal repopulation in epithelial acini." Nat Cell Biol **3**(9): 785-792.

Nadler, Y., R. L. Camp, J. M. Giltnane, C. Moeder, D. L. Rimm, H. M. Kluger and Y. Kluger (2008). "Expression patterns and prognostic value of Bag-1 and Bcl-2 in breast cancer." Breast Cancer Res **10**(2): R35.

Nakayama, G. R., M. C. Caton, M. P. Nova and Z. Parandoosh (1997). "Assessment of the Alamar Blue assay for cellular growth and viability in vitro." J Immunol Methods **204**(2): 205-208.

Nardini, M., S. Spano, C. Cericola, A. Pesce, A. Massaro, E. Millo, A. Luini, D. Corda and M. Bolognesi (2003). "CtBP/BARS: a dual-function protein involved in transcription co-repression and Golgi membrane fission." EMBO J **22**(12): 3122-3130.

Nardini, M., D. Svergun, P. V. Konarev, S. Spano, M. Fasano, C. Bracco, A. Pesce, A. Donadini, C. Cericola, F. Secundo, A. Luini, D. Corda and M. Bolognesi (2006). "The C-terminal domain of the transcriptional corepressor CtBP is intrinsically unstructured." Protein Sci **15**(5): 1042-1050.

Nedvetsky, P. I., S. H. Kwon, J. Debnath and K. E. Mostov (2012). "Cyclic AMP regulates formation of mammary epithelial acini in vitro." Mol Biol Cell **23**(15): 2973-2981.

Niyaz, Y., M. Zeiner and U. Gehring (2001). "Transcriptional activation by the human Hsp70-associating protein Hap50." J Cell Sci **114**(Pt 10): 1839-1845.

Nollen, E. A., J. F. Brunsting, J. Song, H. H. Kampinga and R. I. Morimoto (2000). "Bag1 functions in vivo as a negative regulator of Hsp70 chaperone activity." Mol Cell Biol **20**(3): 1083-1088.

Norwood, S. L. (1990). "Fibrocystic breast disease. An update and review." J Obstet Gynecol Neonatal Nurs **19**(2): 116-121.

O'Connor, L., A. Strasser, L. A. O'Reilly, G. Hausmann, J. M. Adams, S. Cory and D. C. Huang (1998). "Bim: a novel member of the Bcl-2 family that promotes apoptosis." EMBO J **17**(2): 384-395.

National Office of Statistics (2012). "Breast Cancer: Incidence, Mortality and Survival, 2010." [Online]. Available from: www.ons.gov.uk/ons/dcp171780_280355.pdf [Accessed 12th July 2013].

Ohtani, N., K. Yamakoshi, A. Takahashi and E. Hara (2004). "The p16INK4a-RB pathway: molecular link between cellular senescence and tumor suppression." J Med Invest **51**(3-4): 146-153.

Olayioye, M. A., R. M. Neve, H. A. Lane and N. E. Hynes (2000). "The ErbB signaling network: receptor heterodimerization in development and cancer." EMBO J **19**(13): 3159-3167.

OpenStax. (2013, 16/07/2014). "Anatomy and Physiology of the Female Reproductive System." 5. Retrieved 26/08/2016, 2016, from http://cnx.org/contents/nMy6SWSQ@5/Anatomy-and-Physiology-of-the-.

Orton, R. J., O. E. Sturm, V. Vyshemirsky, M. Calder, D. R. Gilbert and W. Kolch (2005). "Computational modelling of the receptor-tyrosine-kinase-activated MAPK pathway." Biochem J **392**(Pt 2): 249-261.

Osborne, C. K., K. Hobbs and J. M. Trent (1987). "Biological differences among MCF-7 human breast cancer cell lines from different laboratories." Breast Cancer Res Treat **9**(2): 111-121.

Packham, G., M. Brimmell and J. L. Cleveland (1997). "Mammalian cells express two differently localized Bag-1 isoforms generated by alternative translation initiation." Biochem J **328 (Pt 3)**: 807-813.

Paik, S., S. Shak, G. Tang, C. Kim, J. Baker, M. Cronin, F. L. Baehner, M. G. Walker, D. Watson, T. Park, W. Hiller, E. R. Fisher, D. L. Wickerham, J. Bryant and N. Wolmark (2004). "A multigene assay to predict recurrence of tamoxifen-treated, node-negative breast cancer." N Engl J Med **351**(27): 2817-2826.

Pan, S., C. J. World, C. J. Kovacs and B. C. Berk (2009). "Glucose 6-phosphate dehydrogenase is regulated through c-Src-mediated tyrosine phosphorylation in endothelial cells." Arterioscler Thromb Vasc Biol **29**(6): 895-901.

Papaconstantinou, J. and S. P. Colowick (1961). "The role of glycolysis in the growth of tumor cells. I. Effects of oxamic acid on the metabolism of Ehrlich ascites tumor cells in vitro." J Biol Chem **236**: 278-284.

Papaconstantinou, J. and S. P. Colowick (1961). "The role of glycolysis in the growth of tumor cells. II. The effect of oxamic acid on the growth of HeLa cells in tissue culture." J Biol Chem **236**: 285-288.

Papadakis, E. S., C. R. Barker, H. Syed, T. Reeves, S. Schwaiger, H. Stuppner, J. Troppmair, J. P. Blaydes and R. I. Cutress (2016). "The Bag-1 inhibitor, Thio-2, reverses an atypical 3D morphology driven by Bag-1L overexpression in a MCF-10A model of ductal carcinoma in situ." Oncogenesis **5**: e215.

Parker, J. S., M. Mullins, M. C. Cheang, S. Leung, D. Voduc, T. Vickery, S. Davies, C. Fauron, X. He, Z. Hu, J. F. Quackenbush, I. J. Stijleman, J. Palazzo, J. S. Marron, A. B. Nobel, E. Mardis, T. O. Nielsen, M. J. Ellis, C. M. Perou and P. S. Bernard (2009). "Supervised risk predictor of breast cancer based on intrinsic subtypes." J Clin Oncol **27**(8): 1160-1167.

Pece, S., D. Tosoni, S. Confalonieri, G. Mazzarol, M. Vecchi, S. Ronzoni, L. Bernard, G. Viale, P. G. Pelicci and P. P. Di Fiore (2010). "Biological and molecular heterogeneity of breast cancers correlates with their cancer stem cell content." Cell **140**(1): 62-73.

Pelicano, H., D. S. Martin, R. H. Xu and P. Huang (2006). "Glycolysis inhibition for anticancer treatment." Oncogene **25**(34): 4633-4646.

Petros, A. M., E. T. Olejniczak and S. W. Fesik (2004). "Structural biology of the Bcl-2 family of proteins." Biochim Biophys Acta **1644**(2-3): 83-94.

Ponti, D., A. Costa, N. Zaffaroni, G. Pratesi, G. Petrangolini, D. Coradini, S. Pilotti, M. A. Pierotti and M. G. Daidone (2005). "Isolation and in vitro propagation of tumorigenic breast cancer cells with stem/progenitor cell properties." Cancer Res **65**(13): 5506-5511.

Pradeep, C. R., A. Zeisel, W. J. Kostler, M. Lauriola, J. Jacob-Hirsch, B. Haibe-Kains, N. Amariglio, N. Ben-Chetrit, A. Emde, I. Solomonov, G. Neufeld, M. Piccart, I. Sagi, C. Sotiriou, G. Rechavi, E. Domany, C. Desmedt and Y. Yarden (2012). "Modeling invasive breast cancer: growth factors propel progression of HER2-positive premalignant lesions." Oncogene **31**(31): 3569-3583.

Pucci, S., M. J. Zonetti, T. Fisco, C. Polidoro, G. Bocchinfuso, A. Palleschi, G. Novelli, L. G. Spagnoli and P. Mazzarelli (2016). "Carnitine palmitoyl transferase-1A (CPT1A): a new tumor specific target in human breast cancer." Oncotarget **7**(15): 19982-19996.

Puck, T. T. and P. I. Marcus (1956). "Action of x-rays on mammalian cells." J Exp Med **103**(5): 653-666.

Puthalakath, H. and A. Strasser (2002). "Keeping killers on a tight leash: transcriptional and post-translational control of the pro-apoptotic activity of BH3-only proteins." Cell Death Differ **9**(5): 505-512.

Qu, Q., F. Zeng, X. Liu, Q. J. Wang and F. Deng (2016). "Fatty acid oxidation and carnitine palmitoyltransferase I: emerging therapeutic targets in cancer." Cell Death Dis **7**: e2226.

Rae, J. M., C. J. Creighton, J. M. Meck, B. R. Haddad and M. D. Johnson (2007). "MDA-MB-435 cells are derived from M14 melanoma cells--a loss for breast cancer, but a boon for melanoma research." Breast Cancer Res Treat **104**(1): 13-19.

Raez, L. E., K. Papadopoulos, A. D. Ricart, E. G. Chiorean, R. S. Dipaola, M. N. Stein, C. M. Rocha Lima, J. J. Schlesselman, K. Tolba, V. K. Langmuir, S. Kroll, D. T. Jung, M. Kurtoglu, J. Rosenblatt and T. J. Lampidis (2013). "A phase I dose-escalation trial of 2-deoxy-D-glucose alone or combined with docetaxel in patients with advanced solid tumors." Cancer Chemother Pharmacol **71**(2): 523-530.

Ram, T. G., K. E. Kokeny, C. A. Dilts and S. P. Ethier (1995). "Mitogenic activity of neu differentiation factor/heregulin mimics that of epidermal growth factor and insulin-like growth factor-I in human mammary epithelial cells." J Cell Physiol **163**(3): 589-596.

Rechler, M. M. and S. P. Nissley (1985). "The nature and regulation of the receptors for insulin-like growth factors." Annu Rev Physiol **47**: 425-442.

Reginato, M. J., K. R. Mills, E. B. Becker, D. K. Lynch, A. Bonni, S. K. Muthuswamy and J. S. Brugge (2005). "Bim regulation of lumen formation in cultured mammary epithelial acini is targeted by oncogenes." Mol Cell Biol **25**(11): 4591-4601.

Reginato, M. J., K. R. Mills, J. K. Paulus, D. K. Lynch, D. C. Sgroi, J. Debnath, S. K. Muthuswamy and J. S. Brugge (2003). "Integrins and EGFR coordinately regulate the pro-apoptotic protein Bim to prevent anoikis." Nat Cell Biol **5**(8): 733-740.

Reitzer, L. J., B. M. Wice and D. Kennell (1979). "Evidence that glutamine, not sugar, is the major energy source for cultured HeLa cells." J Biol Chem **254**(8): 2669-2676.

Rijal, G. and W. Li (2016). "3D scaffolds in breast cancer research." Biomaterials **81**: 135-156.

Rocco, J. W. and D. Sidransky (2001). "p16(MTS-1/CDKN2/INK4a) in cancer progression." Exp Cell Res **264**(1): 42-55.

Romagosa, C., S. Simonetti, L. Lopez-Vicente, A. Mazo, M. E. Lleonart, J. Castellvi and S. Ramon y Cajal (2011). "p16(Ink4a) overexpression in cancer: a tumor suppressor gene associated with senescence and high-grade tumors." Oncogene **30**(18): 2087-2097.

Rucka, M. (2013). Metabolic regulation of tumour cell motility. Doctorate of Philosophy, University of Southampton.

Sabri, M. I. and S. Ochs (1971). "Inhibition of glyceraldehyde-3-phosphate dehydrogenase in mammalian nerve by iodoacetic acid." J Neurochem **18**(8): 1509-1514.

Santa-Maria, C. A., L. Nye, M. B. Mutonga, S. Jain and W. J. Gradishar (2016). "Management of Metastatic HER2-Positive Breast Cancer: Where Are We and Where Do We Go From Here?" Oncology (Williston Park) **30**(2): 148-155.

Sato-Tadano, A., T. Suzuki, M. Amari, K. Takagi, Y. Miki, K. Tamaki, M. Watanabe, T. Ishida, H. Sasano and N. Ohuchi (2013). "Hexokinase II in breast carcinoma: a potent prognostic factor associated with hypoxia-inducible factor-1alpha and Ki-67." Cancer Sci **104**(10): 1380-1388.

Schafer, Z. T., A. R. Grassian, L. Song, Z. Jiang, Z. Gerhart-Hines, H. Y. Irie, S. Gao, P. Puigserver and J. S. Brugge (2009). "Antioxidant and oncogene rescue of metabolic defects caused by loss of matrix attachment." Nature **461**(7260): 109-113.

Schmidt, M. M. and R. Dringen (2009). "Differential effects of iodoacetamide and iodoacetate on glycolysis and glutathione metabolism of cultured astrocytes." Front Neuroenergetics **1**: 1.

Schmitz, F., A. Konigstorfer and T. C. Sudhof (2000). "RIBEYE, a component of synaptic ribbons: a protein's journey through evolution provides insight into synaptic ribbon function." Neuron **28**(3): 857-872.

Schulz, J. B., D. Bremen, J. C. Reed, J. Lommatzsch, S. Takayama, U. Wullner, P. A. Loschmann, T. Klockgether and M. Weller (1997). "Cooperative interception of neuronal apoptosis by BCL-2 and BAG-1 expression: prevention of caspase activation and reduced production of reactive oxygen species." J Neurochem **69**(5): 2075-2086.

Independent UK Panel of Breast Cancer Screening (2012). "The benefits and harms of breast cancer screening: an independent review." The Lancet **380**.

Segal, E. D., A. Yasmeen, M. C. Beauchamp, J. Rosenblatt, M. Pollak and W. H. Gotlieb (2011). "Relevance of the OCT1 transporter to the antineoplastic effect of biguanides." Biochem Biophys Res Commun **414**(4): 694-699.

Shackleton, M., F. Vaillant, K. J. Simpson, J. Stingl, G. K. Smyth, M. L. Asselin-Labat, L. Wu, G. J. Lindeman and J. E. Visvader (2006). "Generation of a functional mammary gland from a single stem cell." Nature **439**(7072): 84-88.

Sharp, A., S. J. Crabb, P. W. Johnson, A. Hague, R. Cutress, P. A. Townsend, A. Ganesan and G. Packham (2009). "Thioflavin S (NSC71948) interferes with Bcl-2-associated athanogene (BAG-1)-mediated protein-protein interactions." J Pharmacol Exp Ther **331**(2): 680-689.

Sharp, A., S. J. Crabb, P. A. Townsend, R. I. Cutress, M. Brimmell, X. H. Wang and G. Packham (2004). "BAG-1 in carcinogenesis." Expert Rev Mol Med **6**(7): 1-15.

Sharp, A., R. I. Cutress, P. W. Johnson, G. Packham and P. A. Townsend (2009). "Short peptides derived from the BAG-1 C-terminus inhibit the interaction between BAG-1 and HSC70 and decrease breast cancer cell growth." FEBS Lett **583**(21): 3405-3411.

Shatkina, L., S. Mink, H. Rogatsch, H. Klocker, G. Langer, A. Nestl and A. C. Cato (2003). "The cochaperone Bag-1L enhances androgen receptor action via interaction with the NH2-terminal region of the receptor." Mol Cell Biol **23**(20): 7189-7197.

Shaw, F. L., H. Harrison, K. Spence, M. P. Ablett, B. M. Simoes, G. Farnie and R. B. Clarke (2012). "A detailed mammosphere assay protocol for the quantification of breast stem cell activity." J Mammary Gland Biol Neoplasia **17**(2): 111-117.

Shi, Y., F. Lan, C. Matson, P. Mulligan, J. R. Whetstine, P. A. Cole, R. A. Casero and Y. Shi (2004). "Histone demethylation mediated by the nuclear amine oxidase homolog LSD1." Cell **119**(7): 941-953.

Shi, Y., J. Sawada, G. Sui, B. Affar el, J. R. Whetstine, F. Lan, H. Ogawa, M. P. Luke and Y. Nakatani (2003). "Coordinated histone modifications mediated by a CtBP co-repressor complex." Nature **422**(6933): 735-738.

Siitonen, S. M., J. T. Kononen, H. J. Helin, I. S. Rantala, K. A. Holli and J. J. Isola (1996). "Reduced E-cadherin expression is associated with invasiveness and unfavorable prognosis in breast cancer." Am J Clin Pathol **105**(4): 394-402.

Singh, D., A. K. Banerji, B. S. Dwarakanath, R. P. Tripathi, J. P. Gupta, T. L. Mathew, T. Ravindranath and V. Jain (2005). "Optimizing cancer radiotherapy with 2-deoxy-d-glucose dose escalation studies in patients with glioblastoma multiforme." Strahlenther Onkol **181**(8): 507-514.

Slamon, D. J., G. M. Clark, S. G. Wong, W. J. Levin, A. Ullrich and W. L. McGuire (1987). "Human breast cancer: correlation of relapse and survival with amplification of the HER-2/neu oncogene." Science **235**(4785): 177-182.

Sogame, Y., A. Kitamura, M. Yabuki and S. Komuro (2009). "A comparison of uptake of metformin and phenformin mediated by hOCT1 in human hepatocytes." Biopharm Drug Dispos **30**(8): 476-484.

Sokol, E. S., D. H. Miller, A. Breggia, K. C. Spencer, L. M. Arendt and P. B. Gupta (2016). "Growth of human breast tissues from patient cells in 3D hydrogel scaffolds." Breast Cancer Res **18**(1): 19.

Solem, C., B. J. Koebmann and P. R. Jensen (2003). "Glyceraldehyde-3-phosphate dehydrogenase has no control over glycolytic flux in Lactococcus lactis MG1363." J Bacteriol **185**(5): 1564-1571.

Sondermann, H., C. Scheufler, C. Schneider, J. Hohfeld, F. U. Hartl and I. Moarefi (2001). "Structure of a Bag/Hsc70 complex: convergent functional evolution of Hsp70 nucleotide exchange factors." Science **291**(5508): 1553-1557.

Song, H. F., J. Zhou, K. Pan, Q. J. Wang, H. Wang, L. X. Huang, Y. Q. Li and J. C. Xia (2008). "[Antitumor effects and mechanisms of a dendritic cell vaccine which silenced SOCS1 by siRNA, stimulated by OK-432 and pulsed with lysate of HepG2 cells]." Ai Zheng **27**(7): 685-691.

Song, J., M. Takeda and R. I. Morimoto (2001). "Bag1-Hsp70 mediates a physiological stress signalling pathway that regulates Raf-1/ERK and cell growth." Nat Cell Biol **3**(3): 276-282.

Soule, H. D., T. M. Maloney, S. R. Wolman, W. D. Peterson, Jr., R. Brenz, C. M. McGrath, J. Russo, R. J. Pauley, R. F. Jones and S. C. Brooks (1990). "Isolation and characterization of a spontaneously immortalized human breast epithelial cell line, MCF-10." Cancer Res **50**(18): 6075-6086.

Spano, S., M. G. Silletta, A. Colanzi, S. Alberti, G. Fiucci, C. Valente, A. Fusella, M. Salmona, A. Mironov, A. Luini and D. Corda (1999). "Molecular cloning and functional characterization of brefeldin A-ADP-ribosylated substrate. A novel protein involved in the maintenance of the Golgi structure." J Biol Chem **274**(25): 17705-17710.

Stankiewicz, T. R., J. J. Gray, A. N. Winter and D. A. Linseman (2014). "C-terminal binding proteins: central players in development and disease." Biomol Concepts **5**(6): 489-511.

Staubert, C., O. J. Broom and A. Nordstrom (2015). "Hydroxycarboxylic acid receptors are essential for breast cancer cells to control their lipid/fatty acid metabolism." Oncotarget **6**(23): 19706-19720.

Straza, M. W., S. Paliwal, R. C. Kovi, B. Rajeshkumar, P. Trenh, D. Parker, G. F. Whalen, S. Lyle, C. A. Schiffer and S. R. Grossman (2010). "Therapeutic targeting of C-terminal binding protein in human cancer." Cell Cycle **9**(18): 3740-3750.

Subramani, T., S. K. Yeap, W. Y. Ho, C. L. Ho, A. R. Omar, S. A. Aziz, N. M. Rahman and N. B. Alitheen (2014). "Vitamin C suppresses cell death in MCF-7 human breast cancer cells induced by tamoxifen." J Cell Mol Med **18**(2): 305-313.

Subramanian, T. and G. Chinnadurai (2003). "Association of class I histone deacetylases with transcriptional corepressor CtBP." FEBS Lett **540**(1-3): 255-258.

Takaoka, A., M. Adachi, H. Okuda, S. Sato, A. Yawata, Y. Hinoda, S. Takayama, J. C. Reed and K. Imai (1997). "Anti-cell death activity promotes pulmonary metastasis of melanoma cells." Oncogene **14**(24): 2971-2977.

Takayama, S., D. N. Bimston, S. Matsuzawa, B. C. Freeman, C. Aime-Sempe, Z. Xie, R. I. Morimoto and J. C. Reed (1997). "BAG-1 modulates the chaperone activity of Hsp70/Hsc70." EMBO J **16**(16): 4887-4896.

Takayama, S., S. Krajewski, M. Krajewska, S. Kitada, J. M. Zapata, K. Kochel, D. Knee, D. Scudiero, G. Tudor, G. J. Miller, T. Miyashita, M. Yamada and J. C. Reed (1998). "Expression and location of Hsp70/Hsc-binding anti-apoptotic protein BAG-1 and its variants in normal tissues and tumor cell lines." Cancer Res **58**(14): 3116-3131.

Takayama, S., T. Sato, S. Krajewski, K. Kochel, S. Irie, J. A. Millan and J. C. Reed (1995). "Cloning and functional analysis of BAG-1: a novel Bcl-2-binding protein with anti-cell death activity." Cell **80**(2): 279-284.

Tang, S. C., J. Beck, S. Murphy, G. Chernenko, D. Robb, P. Watson and M. Khalifa (2004). "BAG-1 expression correlates with Bcl-2, p53, differentiation, estrogen and progesterone receptors in invasive breast carcinoma." Breast Cancer Res Treat **84**(3): 203-213.

Tang, S. C., N. Shehata, G. Chernenko, M. Khalifa and X. Wang (1999). "Expression of BAG-1 in invasive breast carcinomas." J Clin Oncol **17**(6): 1710-1719.

Thio, S. S., J. V. Bonventre and S. I. Hsu (2004). "The CtBP2 co-repressor is regulated by NADH-dependent dimerization and possesses a novel N-terminal repression domain." Nucleic Acids Res **32**(5): 1836-1847.

Thornburg, J. M., K. K. Nelson, B. F. Clem, A. N. Lane, S. Arumugam, A. Simmons, J. W. Eaton, S. Telang and J. Chesney (2008). "Targeting aspartate aminotransferase in breast cancer." Breast Cancer Res **10**(5): R84.

Tian, W. N., J. N. Pignatare and R. C. Stanton (1994). "Signal transduction proteins that associate with the platelet-derived growth factor (PDGF) receptor mediate the PDGF-induced release of glucose-6-phosphate dehydrogenase from permeabilized cells." J Biol Chem **269**(20): 14798-14805.

Tong, H. X., C. W. Lu, L. W. Wang, Q. S. Wang and J. H. Zhang (2010). "[Role of caspase-8 in TRAIL-induced apoptosis of neuroblastoma cell lines]." Zhongguo Dang Dai Er Ke Za Zhi **12**(11): 902-907.

Townsend, P. A., R. I. Cutress, C. J. Carroll, K. M. Lawrence, T. M. Scarabelli, G. Packham, A. Stephanou and D. S. Latchman (2004). "BAG-1 proteins protect cardiac myocytes from simulated

ischemia/reperfusion-induced apoptosis via an alternate mechanism of cell survival independent of the proteasome." J Biol Chem **279**(20): 20723-20728.

Townsend, P. A., R. I. Cutress, A. Sharp, M. Brimmell and G. Packham (2003). "BAG-1 prevents stress-induced long-term growth inhibition in breast cancer cells via a chaperone-dependent pathway." Cancer Res **63**(14): 4150-4157.

Townsend, P. A., R. I. Cutress, A. Sharp, M. Brimmell and G. Packham (2003). "BAG-1: a multifunctional regulator of cell growth and survival." Biochim Biophys Acta **1603**(2): 83-98.

Townsend, P. A., E. Dublin, I. R. Hart, R. H. Kao, A. M. Hanby, R. I. Cutress, R. Poulsom, K. Ryder, D. M. Barnes and G. Packham (2002). "BAG-i expression in human breast cancer: interrelationship between BAG-1 RNA, protein, HSC70 expression and clinico-pathological data." J Pathol **197**(1): 51-59.

Turner, B. C., S. Krajewski, M. Krajewska, S. Takayama, A. A. Gumbs, D. Carter, T. R. Rebbeck, B. G. Haffty and J. C. Reed (2001). "BAG-1: a novel biomarker predicting long-term survival in early-stage breast cancer." J Clin Oncol **19**(4): 992-1000.

Vander Heiden, M. G., L. C. Cantley and C. B. Thompson (2009). "Understanding the Warburg effect: the metabolic requirements of cell proliferation." Science **324**(5930): 1029-1033.

Vargo-Gogola, T. and J. M. Rosen (2007). "Modelling breast cancer: one size does not fit all." Nat Rev Cancer **7**(9): 659-672.

Varley, J. M., J. E. Swallow, W. J. Brammar, J. L. Whittaker and R. A. Walker (1987). "Alterations to either c-erbB-2(neu) or c-myc proto-oncogenes in breast carcinomas correlate with poor short-term prognosis." Oncogene **1**(4): 423-430.

Vinci, M., S. Gowan, F. Boxall, L. Patterson, M. Zimmermann, W. Court, C. Lomas, M. Mendiola, D. Hardisson and S. A. Eccles (2012). "Advances in establishment and analysis of three-dimensional tumor spheroid-based functional assays for target validation and drug evaluation." BMC Biol **10**: 29.

Vleminckx, K., L. Vakaet, Jr., M. Mareel, W. Fiers and F. van Roy (1991). "Genetic manipulation of E-cadherin expression by epithelial tumor cells reveals an invasion suppressor role." Cell **66**(1): 107-119.

Wang, H. G., S. Takayama, U. R. Rapp and J. C. Reed (1996). "Bcl-2 interacting protein, BAG-1, binds to and activates the kinase Raf-1." Proc Natl Acad Sci U S A **93**(14): 7063-7068.

Weaver, V. M. and M. J. Bissell (1999). "Functional culture models to study mechanisms governing apoptosis in normal and malignant mammary epithelial cells." J Mammary Gland Biol Neoplasia **4**(2): 193-201.

Weigelt, B., J. L. Peterse and L. J. van 't Veer (2005). "Breast cancer metastasis: markers and models." Nat Rev Cancer **5**(8): 591-602.

Weigert, R., M. G. Silletta, S. Spano, G. Turacchio, C. Cericola, A. Colanzi, S. Senatore, R. Mancini, E. V. Polishchuk, M. Salmona, F. Facchiano, K. N. Burger, A. Mironov, A. Luini and D. Corda (1999). "CtBP/BARS induces fission of Golgi membranes by acylating lysophosphatidic acid." Nature **402**(6760): 429-433.

Wheaton, W. W., S. E. Weinberg, R. B. Hamanaka, S. Soberanes, L. B. Sullivan, E. Anso, A. Glasauer, E. Dufour, G. M. Mutlu, G. S. Budigner and N. S. Chandel (2014). "Metformin inhibits mitochondrial complex I of cancer cells to reduce tumorigenesis." Elife **3**: e02242.

Wieduwilt, M. J. and M. M. Moasser (2008). "The epidermal growth factor receptor family: biology driving targeted therapeutics." Cell Mol Life Sci **65**(10): 1566-1584.

Willis, S. N., J. I. Fletcher, T. Kaufmann, M. F. van Delft, L. Chen, P. E. Czabotar, H. Ierino, E. F. Lee, W. D. Fairlie, P. Bouillet, A. Strasser, R. M. Kluck, J. M. Adams and D. C. Huang (2007). "Apoptosis initiated when BH3 ligands engage multiple Bcl-2 homologs, not Bax or Bak." Science **315**(5813): 856-859.

Wilson, J. E. (2003). "Isozymes of mammalian hexokinase: structure, subcellular localization and metabolic function." J Exp Biol **206**(Pt 12): 2049-2057.

Witcher, M., X. Yang, A. Pater and S. C. Tang (2001). "BAG-1 p50 isoform interacts with the vitamin D receptor and its cellular overexpression inhibits the vitamin D pathway." Exp Cell Res **265**(1): 167-173.

Yang, J. S., S. Y. Lee, S. Spano, H. Gad, L. Zhang, Z. Nie, M. Bonazzi, D. Corda, A. Luini and V. W. Hsu (2005). "A role for BARS at the fission step of COPI vesicle formation from Golgi membrane." EMBO J **24**(23): 4133-4143.

Yang, X., G. Chernenko, Y. Hao, Z. Ding, M. M. Pater, A. Pater and S. C. Tang (1998). "Human BAG-1/RAP46 protein is generated as four isoforms by alternative translation initiation and overexpressed in cancer cells." Oncogene **17**(8): 981-989.

Yang, X., Y. Hao, Z. Ding and A. Pater (2000). "BAG-1 promotes apoptosis induced by N-(4-hydroxyphenyl)retinamide in human cervical carcinoma cells." Exp Cell Res **256**(2): 491-499.

Yaswen, P. and M. R. Stampfer (2002). "Molecular changes accompanying senescence and immortalization of cultured human mammary epithelial cells." Int J Biochem Cell Biol **34**(11): 1382-1394.

Yawata, A., M. Adachi, H. Okuda, Y. Naishiro, T. Takamura, M. Hareyama, S. Takayama, J. C. Reed and K. Imai (1998). "Prolonged cell survival enhances peritoneal dissemination of gastric cancer cells." Oncogene **16**(20): 2681-2686.

Yoon, D. S., R. P. Wersto, W. Zhou, F. J. Chrest, E. S. Garrett, T. K. Kwon and E. Gabrielson (2002). "Variable levels of chromosomal instability and mitotic spindle checkpoint defects in breast cancer." Am J Pathol **161**(2): 391-397.

Younes, M., R. W. Brown, D. R. Mody, L. Fernandez and R. Laucirica (1995). "GLUT1 expression in human breast carcinoma: correlation with known prognostic markers." Anticancer Res **15**(6B): 2895-2898.

Yu, Y., J. A. Deck, L. A. Hunsaker, L. M. Deck, R. E. Royer, E. Goldberg and D. L. Vander Jagt (2001). "Selective active site inhibitors of human lactate dehydrogenases A4, B4, and C4." Biochem Pharmacol **62**(1): 81-89.

Zaugg, K., Y. Yao, P. T. Reilly, K. Kannan, R. Kiarash, J. Mason, P. Huang, S. K. Sawyer, B. Fuerth, B. Faubert, T. Kalliomaki, A. Elia, X. Luo, V. Nadeem, D. Bungard, S. Yalavarthi, J. D. Growney, A. Wakeham, Y. Moolani, J. Silvester, A. Y. Ten, W. Bakker, K. Tsuchihara, S. L. Berger, R. P. Hill, R. G. Jones, M. Tsao, M. O. Robinson, C. B. Thompson, G. Pan and T. W. Mak (2011). "Carnitine palmitoyltransferase 1C promotes cell survival and tumor growth under conditions of metabolic stress." Genes Dev **25**(10): 1041-1051.

Zeiner, M., M. Gebauer and U. Gehring (1997). "Mammalian protein RAP46: an interaction partner and modulator of 70 kDa heat shock proteins." EMBO J **16**(18): 5483-5490.

References

Zeiner, M. and U. Gehring (1995). "A protein that interacts with members of the nuclear hormone receptor family: identification and cDNA cloning." Proc Natl Acad Sci U S A **92**(25): 11465-11469.

Zeiner, M., Y. Niyaz and U. Gehring (1999). "The hsp70-associating protein Hap46 binds to DNA and stimulates transcription." Proc Natl Acad Sci U S A **96**(18): 10194-10199.

Zhang, J., L. Wu, M. X. Feng, P. Sexton, C. X. Bai, J. M. Qu, M. Merrilees and P. N. Black (2011). "Pulmonary fibroblasts from COPD patients show an impaired response of elastin synthesis to TGF-beta1." Respir Physiol Neurobiol **177**(3): 236-240.

Zhang, Q., D. W. Piston and R. H. Goodman (2002). "Regulation of corepressor function by nuclear NADH." Science **295**(5561): 1895-1897.

Zhang, Q., S. Y. Wang, A. C. Nottke, J. V. Rocheleau, D. W. Piston and R. H. Goodman (2006). "Redox sensor CtBP mediates hypoxia-induced tumor cell migration." Proc Natl Acad Sci U S A **103**(24): 9029-9033.

Zhao, L. J., M. Kuppuswamy, S. Vijayalingam and G. Chinnadurai (2009). "Interaction of ZEB and histone deacetylase with the PLDLS-binding cleft region of monomeric C-terminal binding protein 2." BMC Mol Biol **10**: 89.

Zhao, L. J., T. Subramanian, Y. Zhou and G. Chinnadurai (2006). "Acetylation by p300 regulates nuclear localization and function of the transcriptional corepressor CtBP2." J Biol Chem **281**(7): 4183-4189.

Zhao, Y. H., M. Zhou, H. Liu, Y. Ding, H. T. Khong, D. Yu, O. Fodstad and M. Tan (2009). "Upregulation of lactate dehydrogenase A by ErbB2 through heat shock factor 1 promotes breast cancer cell glycolysis and growth." Oncogene **28**(42): 3689-3701.

Zhu, A., D. Lee and H. Shim (2011). "Metabolic positron emission tomography imaging in cancer detection and therapy response." Semin Oncol **38**(1): 55-69.

Zhu, A., D. M. Marcus, H. K. Shu and H. Shim (2012). "Application of metabolic PET imaging in radiation oncology." Radiat Res **177**(4): 436-448.